Max-Planck-Institut für Meteorologie
Max Planck Institute for Meteorology

Examensarbeit Nr. 94

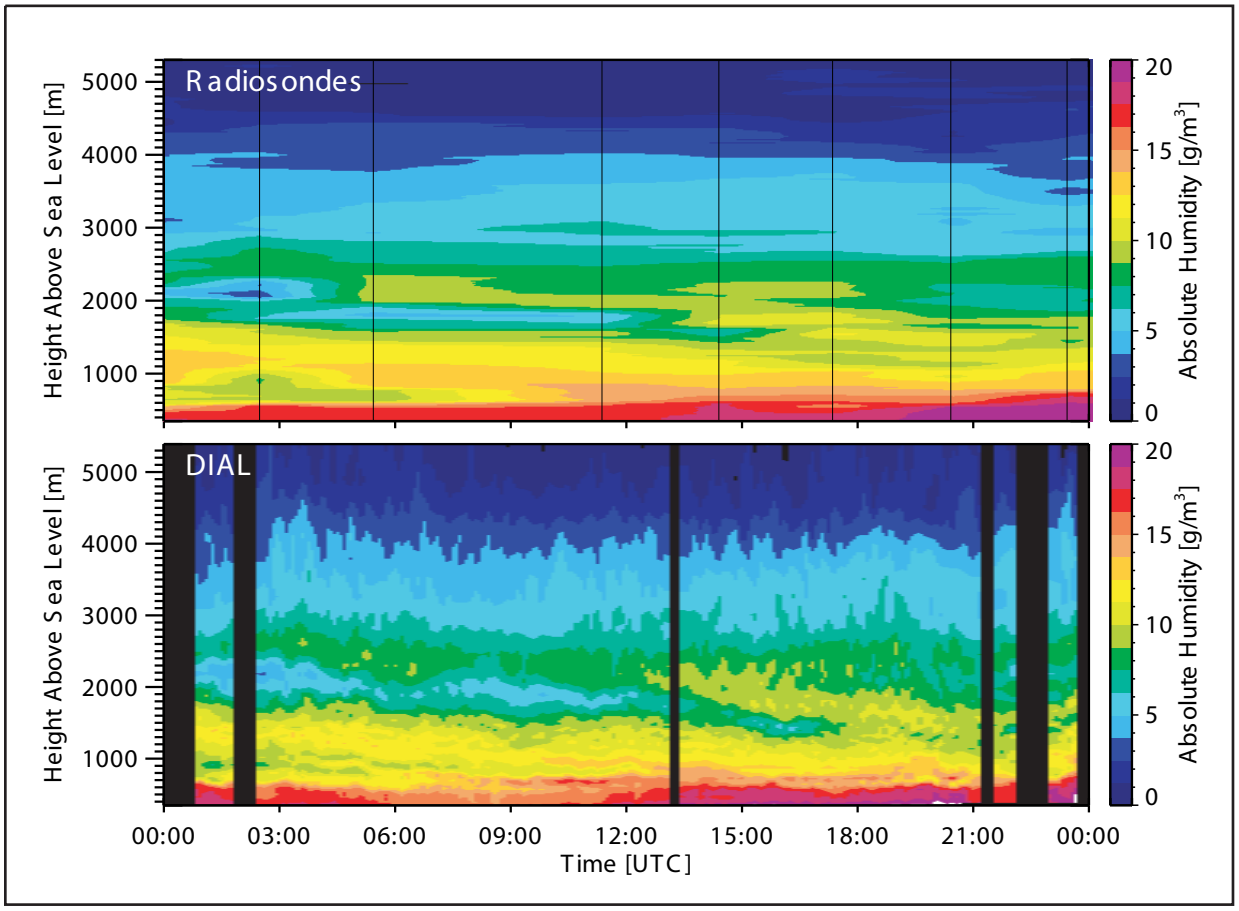

Application and Development of Water Vapor DIAL Systems

von

Klaus Ertel

Hamburg, Februar 2004

Dissertation zur Erlangung des Doktorgrades

Autor:

Klaus Ertel Max-Planck-Institut für Meteorologie

Max-Planck-Institut für Meteorologie
Bundesstrasse 53
D - 20146 Hamburg
Germany

Tel.: +49-(0)40-4 11 73-0
Fax: +49-(0)40-4 11 73-298
e-mail: <name>@dkrz.de
Web: www.mpimet.mpg.de

Application and Development of Water Vapor DIAL Systems

Dissertation
zur Erlangung des Doktorgrades
der Naturwissenschaften im Fachbereich
Geowissenschaften
der Universität Hamburg

vorgelegt von

Klaus Ertel

aus
Bad Neustadt a. d. Saale

Hamburg

2004

Als Dissertation angenommen vom Fachbereich Geowissenschaften
der Universität Hamburg
auf Grund der Gutachten von Dr. habil. Jens Bösenberg
und Prof. Dr. Hartmut Graßl

Hamburg den 6. Januar 2004

Prof. Dr. H. Schleicher
Dekan
des Fachbereichs Geowissenschaften

Abstract

Regarding weather and climate, water vapor is one of the most important atmospheric constituents. A precise knowledge of its highly variable distribution is therefore crucial for many applications such as climate monitoring or weather prediction. Water vapor lidars are the only instruments that can deliver continuous measurements of humidity profiles of high spatial and temporal resolution. As opposed to the Raman method, differential absorption lidar (DIAL) offers the advantages of good daytime performance and self-calibration.

In the course of this work, measurements were collected with an existing alexandrite laser based DIAL system during several field experiments. Among them was the Nauru99 campaign where a water vapor DIAL system was operated on board a ship for the first time. The data from the various campaigns yielded many interesting results, for example the confirmation of the development of an internal thermal boundary layer over the island of Nauru.

It became apparent however, that the quality of the measured data was not satisfactory. During the postprocessing of the data, many sources of systematic errors could be identified and partly eliminated. Such sources were errors in the calculation of the water vapor absorption cross section, errors in the determination of the signal baseline, and errors caused by an insufficient spectral quality of the emitted laser pulses.

Because of the quality problems, the high level of maintenance, and the large space and energy requirements associated with the old system, a new laser system was constructed. The best concept was found to be an injection seeded, gain-switched Ti:Sa ring laser. This new laser operates in the 820 nm wavelength region at a repetition rate of 50 Hz. Special features are the newly developed active stabilization scheme, the continuous monitoring of crucial parameters on a single shot basis, and the fact that no optical elements inside the laser cavity are needed, except the laser crystal itself. Achieved performance parameters are: pulse energy of 15 mJ, spectral purity of $99.97\,\%$, and shot-to-shot energy fluctuations of 1.6 %.

A preliminary DIAL system was constructed based on the new laser system and tested extensively during a field experiment in May/June 2003 at the German Weather Service's Lindenberg Observatory. The laser performance and the quality of the measured data were very satisfactory. Uninterrupted operation of up to 11.5 h could be achieved.

Zusammenfassung

Wasserdampf stellt in Bezug auf Wetter und Klima einen der wichtigsten Bestandteile der Atmosphäre dar. Die genaue Kenntnis der hochvariablen Verteilung von Wasserdampf ist deshalb für viele Anwendungen, wie z.B. Klima-Beobachtungen und Wettervorhersage von großer Bedeutung. Lidar-Systeme sind die einzigen Instrumente, die kontinuierliche Messungen von zeitlich und räumlich hoch aufgelösten Feuchte-Profilen liefern können. Im Gegensatz zur Raman-Methode bietet differentielles Absorptions-Lidar (DIAL) die Vorteile, dass es zum einen auch bei Tag gute Ergebnisse liefert und zum anderen selbst-kalibrierend ist.

Im Rahmen dieser Arbeit wurden mit einem bereits existierenden, auf einem Alexandrit-Laser aufbauenden DIAL-System Messungen im Rahmen mehrerer Feldexperimente getätigt. Eines davon war die Nauru99-Kampagne, während der erstmalig Wasserdampf-DIAL Messungen an Bord eines Schiffes durchgeführt wurden. Die verschiedenen Kampagnen erbrachten viele interessante Ergebnisse, z. B. konnte die Bildung einer internen konvektiven Grenzschicht über der Insel Nauru bestätigt werden.

Es zeigte sich jedoch, dass die Qualität der Messungen nicht zufriedenstellend war. Während der Nachbereitung der Daten konnten mehrere Quellen für systematische Fehler identifiziert und zum Teil ausgeräumt werden. Es waren dies Fehler bei der Berechnung des Wasserdampf-Absorptionsquerschnittes, Fehler bei der Bestimmung des Signal-Untergrundes und Fehler, die durch ungenügende spektrale Eigenschaften der Laserpulse verursacht waren.

Aufgrund der Qualitätsprobleme, die mit dem alten DIAL-System verbunden sind, und aufgrund seines hohen Wartungs-, Energie-, und Platzbedarfes wurde ein neues Laser-System aufgebaut. Als bestes Konzept erwies sich ein Ti:Sa-Ringlaser mit Injection Seeding und Gain-switching. Dieser neue Laser arbeitet bei einer Wellenlänge um $820\,\mathrm{nm}$ und einer Repetitionsrate von $50\,\mathrm{Hz}$. Technische Besonderheiten sind die neu entwickelte Technik zur aktiven Stabilisierung, die kontinuierliche Aufzeichnung wichtiger Parameter im Einzelschuss und die Tatsache, dass außer dem Laserkristall keine zusätzlichen optische Elemente innerhalb des Laser-Resonators benötigt werden. Erreichte Leistungsdaten sind eine Pulsenergie von $15\,\mathrm{mJ}$, eine spektrale Reinheit von $99.97\,\%$ und Puls-zu-Puls Energieschwankungen von $1.6\,\%$.

Basierend auf dem neue Lasersystem wurde ein vorläufiger DIAL-Messaufbau realisiert, der im Mai/Juni 2003 bei einem Feldexperiment am Meteorologischen Observatorium Lindenberg des Deutschen Wetterdienstes ausgiebig getestet wurde. Der Laser arbeitete sehr gut und auch die Qualität der gemessenen Daten war sehr zufriedenstellend. Es gelangen ununterbrochene Messungen von bis zu $11.5\,\mathrm{h}$ Dauer.

Contents

Chapter 1

Introduction

Water vapor is one of the most important components of the climate system. It is responsible for the formation of clouds and precipitation, and for the transport of energy (in form of latent heat) and moisture within the atmosphere and across the land/atmosphere and ocean/atmosphere interfaces. The latent heat that is released upon condensation is a driver of dynamic processes, in particular in the context of severe weather events such as thunderstorms and tropical cyclones. In addition, water vapor plays a major role in radiative transfer processes as it is the most important greenhouse gas. So-called water vapor feedback is thought to significantly enhance the temperature change that is caused by anthropogenic greenhouse gases such as CO_2 and CH_4 [1]. The importance of water vapor and of the precise knowledge of its highly variable spatial and temporal distribution has been stressed in numerous publications.

Huge international collaborative projects such as GEWEX (global energy and water cycle experiment) and GVaP (global water vapor project, part of GEWEX) [2] have been set up in order to gain a better understanding of the hydrological cycle in general and of atmospheric water vapor and the related processes in particular. Among the objectives of GVaP is the construction of a high quality, long term, global data set of the 3-dimensional water vapor distribution and its variability. Another project with a similar goal, but on a more regional scale, is CM-SAF (satellite application facility on climate monitoring) [3, 4] which is hosted by the German Weather Service (DWD). Several SAFs have been set up by the EUMETSAT consortium in order to provide satellite derived data products for various types of meteorological variables for operational and research applications. Among the products to be delivered by the CM-SAF are fields of column integrated and layer precipitable water vapor.

An integral part of both GVaP and CM-SAF is the validation of the satellite products with in situ observations and ground based remote sensing data. So-called reference stations play a key role in the validation and calibration efforts. These stations are heavily instrumented observation sites such as the DWD's Meteorological Observatory at Lindenberg (MOL) and the ARM-CART central facility in Oklahoma, USA. They are equipped with state-of-the-art in situ sensors and remote sensing instruments such as advanced radiosondes, microwave radiometers, infrared sounders, and GPS receivers in order to precisely monitor the vertical water vapor distribution on a continuous basis. The quoted instruments however either fail to provide a continuous coverage in time (radiosondes) or deliver only a very poor or no vertical resolution of the water vapor distribution in the column. The latter is also true for the satellite derived water vapor products.

The only class of instruments that can provide both high temporal and vertical resolution are water vapor lidars. Therefore, the GVaP implementation plan [5] requires a reference station to operate a lidar in order to be classified "level 1". The two possible methods are Raman lidar and DIAL (differential absorption lidar, see Chapter 2). Whereas the Raman method is technically more simple, DIAL has the advantages that it provides high resolution also during daytime and

that it does not need an external calibration source. The only reference station worldwide that operates a water vapor (Raman) lidar on a routine basis is the ARM-CART central facility (see also Section 4.2). Recently, the DWD has also decided to install both a Raman and a DIAL system at its Lindenberg site. A collaboration with our group was started in order to develop a DIAL system suitable for the intended quasi operational use at Lindenberg.

However, apart from providing ground truth for satellite measurements, DIAL is a highly valuable observation tool in its own right, just as other ground based remote sensing instruments, with the added value of high spatial and temporal resolution. If reliable operation on a routine basis can be achieved, climate monitoring on a great range of temporal and spatial scales becomes possible. For example, data sets of mean diurnal cycles or of variances or other turbulence parameters can be compiled for a large number of individual height levels. This could for example be exploited for the validation and development of computer models. The limitations of ground based water vapor DIAL also have to be mentioned. The achievable range strongly depends on the specific system design and the atmospheric conditions, but generally measurements at a range below few $100\,\mathrm{m}$ and in the upper troposphere are very hard to achieve. A DIAL system also cannot operate during rain, and clouds cannot be penetrated. Measurements up to the cloud base are however possible and due to the high temporal resolution and the very narrow field of view, only small gaps between the clouds are needed for full-range measurements. Other remote sensing methods have similar or even worse limitations. Passive optical and infrared sounders often need a completely clear sky and even high cirrus clouds render the measurements useless. Routine lidar measurements in the frameworks of the German and European aerosol lidar networks [6, 7] have shown that operations are surprisingly rarely hampered by adverse weather even at a location like Hamburg.

An improved knowledge of the distribution of atmospheric water vapor resulting from lidar measurements could also be beneficial for numerical weather prediction, in particular in the fields of cloud and precipitation forecast. To investigate how advanced humidity sensors such as lidars can improve weather forecast skills, an extensive field experiment, the IHOP campaign (international H_2O project), was carried out in 2002 involving several ground based and airborne water vapor lidars. The science plan of this campaign [8] gives a good overview of the scientific basis and lists relevant publications on the topic. The application of airborne DIAL measurements to Hurricane forecasting is described in [9]. Another review of the possible role of water vapor lidars in numerical weather prediction is given in [10].

Another important area of atmospheric research that DIAL can contribute to are process studies, in particular regarding the planetary boundary layer (PBL). The most recent campaign our group has participated in was EVA-GRIPS, a project dedicated to the measurement of surface fluxes over complex terrain (see Section 5.9). Apart from studying vertical moisture fluxes, other current activities of our group are comparisons of DIAL measurements and REMO regional model results [11] and the investigation of PBL heights that are obtained from DIAL data and other lidar products using different types of algorithms [12].

It must be stressed again, that all these applications require DIAL systems of high reliability in terms of system availability and data quality. At least in terms of data quality, which mainly hinges on the laser transmitter, it was thought that the existing MPI DIAL system (see Section 2.1) would fulfill and even highly exceed the required specifications. At the beginning of the work described in the following chapters, measurements with this existing system were carried out during several field experiments. These experiments and some of the obtained results will be described in Chapter 4. It was discovered however, that the data collected at the field campaigns showed severe quality problems and that extensive post processing and revisions in the inversion algorithm were necessary before these data could be released to other campaign participants. These quality assurance procedures will be described in Chapter 3. The already known and newly discovered shortcomings of the old system led to the decision to develop a

new laser system, focusing particularly on the projected routine operation at Lindenberg. The new laser system and first atmospheric measurements will be presented in Chapter 5. First of all however, an introduction to the DIAL technique and its theoretical foundations will be given in Chapter 2, together with a brief description of the old DIAL system.

Chapter 2

Principles of Lidar and DIAL

2.1 Introduction and System Description

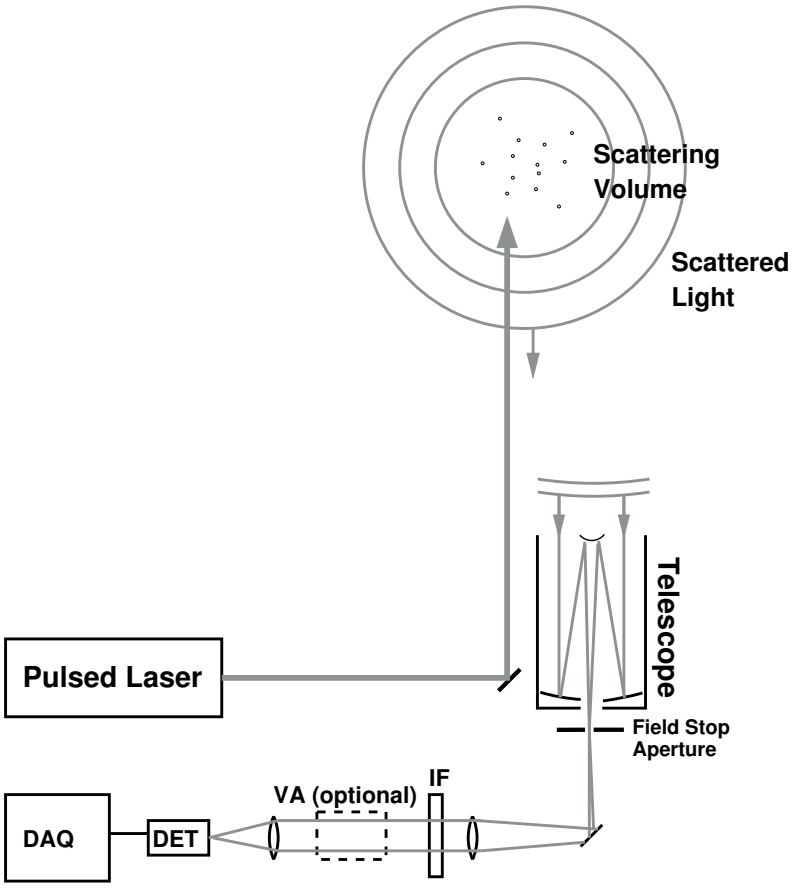

FIGURE 2.1: Schematic sketch of the lidar principle and the main parts of a lidar system. Abbreviations: IF: interference filter, VA: variable attenuator, DET: detector, DAQ: data acquisition system

The main parts of a lidar (light detection and ranging) system are sketched in Fig. 2.1. The lidar principle for atmospheric applications which is also illustrated in Fig. 2.1 works as follows: A laser repeatedly sends short, collimated pulses of light into the atmosphere. For typical systems, the length of the pulses ranges from a few to a few hundred ns, the wavelength from near infrared to near UV, the repetition rate from below 1 Hz to a few kHz, and the pulse energy from below 1 mJ to several hundred mJ. Along its way, some of the light is scattered into all directions. The light is scattered by particles which can be atoms, molecules, aerosol

particles, and cloud droplets or ice crystals. A small fraction of the light is scattered back toward the lidar system where it enters the receiving telescope. The optical axis of the telescope and the laser beam are parallel to each other and located in close proximity, sometimes the beam is sent out directly along the telescope's optical axis. The light is then focused by the telescope and passes the so-called field stop, an aperture located at the telescope's focus. This aperture limits the field of view of the telescope which mainly serves for the suppression of both background light and scattered laser light from the near range. The so-called overlap factor (see Section 2.2) which describes to what extent light from the near range is suppressed, is mainly determined by the size of the field of view. Behind the field stop, the light is recollimated and passed through an interference filter. The purpose of this optical bandpass filter is to let the wavelength of the scattered laser light pass and to block all other wavelengths in order to further reduce the background light intensity. In our alexandrite system (see below), the opportunity exists to insert an electro optical variable attenuator in the beam path. This device further attenuates the strong signal from the near range and therefore allows for increased detector sensitivity and hence increased measurement range of the system. Finally, the light is focused onto a detector where the light intensity is converted to an electrical signal which is then digitized by the data acquisition system. The round trip travel time of the light gives information about the distance of the scattering volume (see Equation 2.2), so lidar measurements are range-resolved. The round trip time also limits the maximum repetition rate of the laser emitter, it has to be chosen such that no more scattered light from the previous pulse is detectable when the next pulse is emitted. As to how information about the atmospheric composition, in particular the water vapor content can be derived from the recorded lidar signal will be explained in Section 2.2.

The principal setup outlined here is common to all lidar systems using so-called direct detection (as opposed to heterodyne detection where the received light is made to interfere with a reference light wave prior to detection), but there is a great wealth of varieties and almost no limit to the level of complexity. The laser system e.g. may emit multiple wavelengths or may have to fulfill special requirements regarding the emission spectrum. The receiving side may incorporate multiple telescopes, multiple fields of view, multiple wavelength channels, and extremely narrow-band optical filters such as etalons or atomic vapor cells. The atmospheric parameters which can be investigated with different setups are, among others, aerosol concentration and aerosol optical properties, concentration of trace gases, temperature, and wind. It is furthermore possible to install lidar systems on mobile platforms such as aircraft and also to choose an arbitrary or even variable (i.e. scanning) beam pointing direction. In the scope of this work only ground based (or in one case ship based) systems with a vertical pointing direction will be discussed.

The lidar systems used for the measurements presented in this work are a newly constructed system which will be described in Chapter 5 and the existing MPI water vapor DIAL system. DIAL stands for differential absorption lidar, a technique for measuring the concentration of atmospheric trace gases, in our case water vapor. The water vapor DIAL technique and its theoretical foundations will be described in Section 2.2. A detailed description of the existing DIAL system can be found in [13, 14]. In the following, only a brief outline of the system shall be given, with special emphasis on the modifications that have been implemented since the last publication. The laser emitter of the DIAL system is a flashlamp pumped alexandrite ring laser. As no other name or acronym for the system has been coined, the entire system will be referred to as the alexandrite system or alexandrite DIAL (system) in the following. The wavelength of the emitted laser pulses is prescribed by a cw titanium sapphire (Ti:Sa) laser, whose light is coupled ("injection seeded") into the alexandrite resonator. This Ti:Sa laser is also called seed or master laser. Its output can be switched between two wavelengths. The wavelength is switched after every shot of the alexandrite laser. In this way, the two necessary wavelengths for the DIAL technique (see Section 2.2) are generated and emitted alternatingly. Table 2.1

Pulse Energy	$> 30\,\mathrm{mJ}$
Repetition Rate	$20\,\mathrm{Hz}$
Wavelength	$720 - 730\,\mathrm{nm}$
Frequency Stability	$\pm 200\,\mathrm{MHz}$
Spectral Width	$< 40\,\mathrm{MHz}$

TABLE 2.1: Parameters of the (injection seeded) alexandrite laser.

gives an overview of the most important parameters of the laser system. The receiving side now consists of two telescopes. In addition to the original $28\,\mathrm{cm}$ telescope, a larger telescope of $40\,\mathrm{cm}$ diameter has been installed. Furthermore, the system has been transferred into a new container. This 20-foot standard container has a special certification by Germanischer Lloyd that allows ship based operations. More measures were taken in order to make the system fit for operation on board sea-going ships and in tropical environments:

- Before, the telescopes simply looked through a large opening in the container's roof. Now optical grade quartz windows have been installed for both the telescopes and the outgoing laser beam. In this way, the interior of the container is shielded from the outside environment, keeping out dust, sea spray, and rain and also making it possible to maintain a stable temperature inside the container.
- A powerful air conditioning (AC) system has been installed which is suitable for operation under tropical conditions. During operation, the AC unit, which is resistant to corrosion by sea salt, is placed outside the container.
- The optical table the system rests on has been fitted with a special, homebuilt damping system, which can also handle horizontal forces as opposed to the usual active air dampers.

These modifications were implemented by the beginning of 1999. Then the system was employed in a series of field experiments in 1999 and 2000, the first of which was the Nauru99 campaign taking place on board a ship in the tropical western Pacific. Following to that came three campaigns at the ARM-CART central facility observation site in Oklahoma, USA, the last of which took place in November and December 2000 and was called AFWEX. These campaigns will be described in more detail in Chapter 4.

2.2 The DIAL Equation

The backscatter signal power P which is received from a distance R by the lidar system is described by the lidar equation:

$$P(R) = E_o \cdot \frac{A_o \cdot c}{2 \cdot R^2} \cdot O(R) \cdot \xi \cdot \beta(R) \cdot \exp\left(-2\,\tau\,(R)\right), \tag{2.1}$$

(from [15], in modified form) where $\tau(R)$ is the optical depth between the system and R, $\beta(R)$ is the backscatter coefficient at R (both aerosol and molecular), ξ is the transmission of the emitter and receiver optics, c is the speed of light, A_o is the area of the receiving telescope, E_o is the emitted laser pulse energy, and $O(R)$ is the overlap factor. This factor describes what fraction of the received light reaches the detector due to geometrical reasons. In the usual setup, using a telescope that is focused to infinity, this factor goes from zero at $R = 0$ to unity at a certain distance and then remains constant. This is due to the fact that in the near range, the

image of the scattering volume is out of focus in the plane of the field stop. The region with $O(R) = 1 = const.$ is called region of full overlap.

Actually, P is a transient signal which is recorded over time. The distance R of the scattering volume is determined via the travel time t of the light:

$$R = \frac{1}{2} \cdot c \cdot t, \tag{2.2}$$

where the factor $\frac{1}{2}$ is due to the fact that the light has to travel two ways between the lidar system and the scattering volume. Equation 2.1 is simplified and applies only under certain conditions. The following points have to be considered:

- Equation 2.1 describes the instantaneous power received from one distance. Since the laser pulse possesses a finite length, actually power from a certain range of distances is received at the same time. If the laser pulse length Δt_{pulse} is shorter than $\frac{2 \cdot \Delta x}{c}$, where Δx is the range resolution of the data acquisition (DAQ) system, this can be neglected. Otherwise the laser pulse shape has to be considered explicitly to calculate the shape of the transient return signal, which is then the convolution of the above expression and the normalized pulse envelope.

- Only elastic, incoherent, single scattering is considered. Other scattering processes are neglected, in particular inelastic and multiple scattering. This is valid as inelastic (i.e. Raman) scattering cross sections are much smaller than elastic scattering cross sections. Multiple scattering can be neglected when the concentration of scatterers is sufficiently low and the receiving field of view is sufficiently narrow.

- It is assumed that the laser spectrum is so narrow, that the wavelength dependence of β and τ can be neglected. Furthermore, the fact is neglected that the optical depth τ can be different on the way toward and back from the scattering volume since the spectrum of the light can be broadened in the scattering process due to the thermal motion of the scatterers.

The last point, the so-called Rayleigh-Doppler effect will be briefly addressed in Section 2.3. For a more detailed discussion on the lidar equation see [15] or [16, 17, 18]. The mechanisms contributing to the optical depth τ are aerosol extinction (due to scattering and absorption), extinction caused by molecular or Rayleigh scattering and gaseous absorption:

$$\tau(R) = \tau_{ae}(R) + \tau_{Ray}(R) + \tau_{gas}(R).$$

The factors in Equation 2.1 containing β and τ can then be rewritten:

$$\beta(R) \cdot \exp\left(-2\,\tau\left(R\right)\right) = \beta_{att}(R) \cdot \exp(-2\,\tau_{gas}(R)). \tag{2.3}$$

The backscatter term and the aerosol and Rayleigh extinction terms have now been unified to an attenuated backscatter term β_{att}. There are spectral regions where any absorption by gases in the atmosphere is negligible except for water vapor absorption. For water vapor DIAL (first introduced in [19]), two laser frequencies are chosen in such a region, one of which exhibits stronger water vapor absorption than the other. Since the frequency with stronger absorption is usually located at the center of an absorption line, it is called the online frequency ν_{on}. The frequency with less absorption is called offline frequency ν_{off}. As water vapor absorption lines are very narrow, the difference between the two frequencies can be made very small. In this case, the optical properties of the atmosphere (except for water vapor absorption) can be regarded as equal: $\beta_{att,on} = \beta_{att,off}$. If the two frequencies are very close and are not emitted

simultaneously but with alternating shots, as it is the case for the systems described in this work, the same interference filter and the same detector can be used for both frequencies. For the moment we further assume that the offline frequency does not exhibit any water vapor absorption. With these simplifications we can take the expressions for the received signal for the two frequencies and for two different distances R_1 and $R_2 > R_1$ and combine them in the following way:

$$\frac{P_{off}(R_1) \cdot P_{on}(R_2)}{P_{off}(R_2) \cdot P_{on}(R_1)} = \frac{\exp\left(-2\,\tau_{H_2O}(R_2)\right)}{\exp\left(-2\,\tau_{H_2O}(R_1)\right)},$$

where τ_{H_2O} stands now for the water vapor optical depth at the online frequency. Note that it is not necessary that E_o and other factors be the same for online and offline, as long as they are range-independent. The overlap factor $O(R)$ is only range-independent above a certain distance. In the near range where $O(R)$ is not constant, the inversion would still be possible if it were the same for both wavelengths, but this can usually not be guaranteed due to slight differences in the laser beam pointing direction [20]. We can now write $\tau_{H_2O}(R_2)$ as the sum of the optical depth between the system and R_1 and the optical depth between R_1 and R_2:

$$\tau_{H_2O}(R_2) = \tau_{H_2O}(R_1) + \tau_{H_2O}(R_1, R_2).$$

According to the Lambert-Beer law we can rewrite $\tau(R_1, R_2)$ as

$$\tau_{H_2O}(R_1, R_2) = \Delta R \cdot \bar{\alpha},$$

where $\Delta R = R_2 - R_1$. So it is now possible to calculate a mean absorption coefficient $\bar{\alpha}$ for the interval between R_1 and R_2. Usually though, $\bar{\alpha}$ is presented as an absorption coefficient α which is assigned to the mean distance $\overline{R} = (R_1 + R_2)/2$:

$$\alpha(\overline{R}) = \frac{1}{2\Delta R} \cdot \ln\left(\frac{P_{off}(R_2) \cdot P_{on}(R_1)}{P_{off}(R_1) \cdot P_{on}(R_2)}\right). \tag{2.4}$$

If we drop the assumption that the offline frequency exhibits no absorption, α becomes the differential absorption coefficient $\Delta\alpha = \alpha_{on} - \alpha_{off}$.

How the differential absorption is converted to humidity is described in the following section.

2.3 Water Vapor Absorption

In water vapor DIAL the aim is to measure the number density of water molecules (which can be converted to the water vapor density or absolute humidity ρ_{H_2O}). To convert the product of the measurement, the differential absorption $\Delta\alpha$, to the number density N_{H_2O}, the differential absorption cross section $\Delta\sigma = \sigma_{on} - \sigma_{off}$ needs to be known because:

$$N_{H_2O} = \frac{\Delta\alpha}{\Delta\sigma}. \tag{2.5}$$

The dependence of the absorption cross section on the frequency is referred to as the absorption spectrum. This spectrum consists of a large number of absorption lines. Each of the lines is associated with a transition between two discrete rotational-vibrational energy levels. The energy difference between the two levels determines the frequency ν_o of the absorption line. Since the lines are not infinitely narrow, ν_o should rather be called the center frequency.

The following two broadening mechanisms determine the width and the shape of the absorption lines:

Doppler broadening: This is the broadening caused by the random thermal motion of the molecules. Purely Doppler broadened spectral lines have a Gaussian shape and their width is proportional to the square root of the absolute temperature.

Collision or pressure broadening: Since the lifetime of the upper level of a spectroscopic transition is finite, the uncertainty principle commands that also the width of the resulting absorption line be finite. The unperturbed lifetime of the upper level determines the natural line width of the transition. When a molecule undergoes a collision during the radiation process, the phase of the emitted wave train is perturbed. This shortening of the unperturbed emission time leads to an increase in line width [21]. The resulting line shape is Lorentzian.

Under atmospheric temperature and pressure conditions, collision broadening is dominant at sea level, whereas Doppler broadening becomes important in the upper troposphere and above. In general though, both mechanisms have to be considered and the resulting line shape is the so-called Voigt profile, a convolution of a Gaussian and a Lorentzian curve. A further mechanism determining the line shape is so-called Dicke narrowing. Due to the shortening of the mean free path by collisions, Doppler broadening is reduced under high pressure conditions. The maximum deviations from a classical Voigt profile are in the order of $1\,\%$ and the effect can hence be neglected [22].

The absorption cross section $\sigma(p, T, \nu, \nu_o)$ of a water molecule at a given frequency ν and for a given absorption line centered at frequency ν_o is dependent on the temperature T and the pressure p and the composition of the surrounding atmosphere. Therefore, $\Delta\sigma$ also depends on height and a knowledge of the pressure and the temperature profile is necessary for the DIAL inversion. If a suitable absorption line is chosen for the online frequency, the temperature dependence of $\Delta\sigma$ is small enough that pressure and temperature profiles calculated from a ground measurement and standard lapse rates yield a sufficient accuracy [17] (see also Fig. 3.5). If available, values from a radio sounding or a computer (forecast) model can of course be used as well.

In the calculations presented here, it is assumed that the laser spectrum of the DIAL instrument is very narrow compared to the absorption lines. This assumption is not always valid, especially if the light is scattered by molecules (Rayleigh scattering) rather than aerosol particles, because the thermal motion of the molecules induces Doppler broadening of the scattered light, hence this is called the Rayleigh-Doppler effect. An effective cross section has then to be calculated which is the integral over the product of the broadened laser spectrum and the absorption spectrum. This procedure is called Rayleigh-Doppler correction. An in-depth discussion of this can be found in [23, 16, 17].

Except for the Doppler width, all other absorption line parameters cannot be calculated accurately but need to be measured. It is possible though to extrapolate the line parameters to temperatures and pressures they were not measured at. The necessary formulas are given in the following. Instead of the frequency ν, the quantity used will be the wavenumber $\tilde{\nu} = \nu/c_o$, where c_o is the speed of light in vacuum.

This is the basic formula for calculating σ:

$$\sigma(p, T, \tilde{\nu}, \tilde{\nu}_o) = S(T, \tilde{\nu}_o) \cdot V(p, T, \tilde{\nu}, \tilde{\nu}_o) \tag{2.6}$$

where S stands for the line strength and V for the Voigt-function. S is also called line intensity or line integrated cross section, since it is equal to the integral over $\sigma(\tilde{\nu})$, as the integral over $V(\tilde{\nu})$ is equal to one by definition. The cross section at the line center is therefore proportional to the line strength and (approximately) inversely proportional to the line width. Both factors are hence of equally high importance for an accurate calculation of σ.

Voigt-Function The Voigt-function is calculated the following way:

$$V(p, T, \tilde{\nu}, \tilde{\nu}_o) = \frac{1}{\Delta\tilde{\nu}_D \cdot \sqrt{\pi}} \cdot H(\frac{\Delta\tilde{\nu}_c}{\Delta\tilde{\nu}_D}, \frac{\tilde{\nu} - \tilde{\nu}_o}{\Delta\tilde{\nu}_D}), \tag{2.7}$$

where $H(a, b)$ is the classical Voigt-Function:

$$H(a, b) = \frac{a}{\pi} \int_{-\infty}^{+\infty} \frac{\exp(-y^2)}{a^2 + (b - y)^2} \, \mathrm{d}y.$$

The expression $\Delta\tilde{\nu}_D$ stands for the Doppler-broadened line width:

$$\Delta\tilde{\nu}_D = \tilde{\nu}_o \cdot \frac{\sqrt{2 \cdot k_B}}{c \cdot \sqrt{m}} \cdot \sqrt{T}, \tag{2.8}$$

where m stands for the molecular mass. This is the half width at e^{-1}. To obtain the full width half maximum (FWHM) one has to multiply $\Delta\tilde{\nu}_D$ by $2 \cdot \sqrt{\ln(2)}$. The term $\Delta\tilde{\nu}_c$ stands for the collision-broadened line width (in this case the half width half maximum):

$$\Delta\tilde{\nu}_c = \Gamma_c(p_o, T_o) \cdot \frac{p}{p_o} \cdot \left(\frac{T_o}{T}\right)^{\eta_c}, \tag{2.9}$$

where $\Gamma_c(p_o, T_o)$ is the line width measured[1] at pressure p_o and Temperature T_o and η_c is the exponent describing the temperature dependence of the collision broadening. The pressure broadening and hence Γ_c also depends on the species of molecules it is caused by. In this context, the composition of the atmosphere can be regarded as constant except for the highly variable portion of water vapor itself. Therefore one distinguishes between the broadening caused by dry air (air broadening) and the broadening caused by water vapor (self broadening). Equation 2.9 then reads:

$$\Delta\tilde{\nu}_c = \Delta\tilde{\nu}_{c,air} + \Delta\tilde{\nu}_{c,H_2O}, \tag{2.10}$$

where both terms of the sum are calculated using the according parameters Γ_c and η_c and partial pressures. Note that Γ_c is usually about five times larger for water vapor than for dry air and hence absorption lines are broader in humid air than they would by in dry air at the same total pressure.

Line strength The line strength $S(T, \tilde{\nu}_o)$ is calculated the following way:

$$S(T, \tilde{\nu}_o) = S(T_o, \tilde{\nu}_o) \cdot \left(\frac{T_o}{T}\right)^{1.5} \cdot \exp\left(\frac{E}{k_B} \cdot \left(\frac{1}{T_o} - \frac{1}{T}\right)\right), \tag{2.11}$$

where $S(T_o, \tilde{\nu}_o)$ is the strength of the absorption line measured at T_o, E is the ground state energy of the according transition, and k_B is Boltzmann's constant. In the spectroscopic literature, usually $E'' = E/(h \cdot c_o)$ is given instead of E, where h is Planck's constant and c_o is the speed of light in vacuum. Furthermore, E'', just as $\tilde{\nu}$, are given in units of cm^{-1} instead of m^{-1}.

[1] In this context p_o and T_o do not necessarily stand for the standard conditions commonly used in spectroscopic literature, $p_o = 1\,\mathrm{atm} = 1013.25\,\mathrm{hPa}$ and $T_o = 296\,\mathrm{K}$. Parameters as Γ_c are usually given at these standard conditions. This does not necessarily mean that they were measured at these conditions, but rather that they have been transformed using the same equations as given here.

Pressure shift If an absorption cross section is measured at a non-negligible air pressure, the maximum of the absorption line is shifted to a different, usually lower wavenumber [24, 25]. To correctly calculate the cross section, the line center wavenumber $\tilde{\nu}_o$ in Equation 2.6 and Equation 2.7, which applies to very low pressures (in the following called "vacuum" line center, with the quotation marks reminding of the fact, that in a vacuum of course no absorption can take place), has to be replaced by the pressure shifted line center $\tilde{\nu}'_o$:

$$\tilde{\nu}'_o = \tilde{\nu}_o + \Delta\tilde{\nu}(p_o, T_o) \cdot \frac{p}{p_o} \cdot \left(\frac{T}{T_o}\right)^{\alpha}, \tag{2.12}$$

where $\Delta\tilde{\nu}(p_o, T_o)$ is the shift of the line center measured at pressure p_o and temperature T_o and α is the exponent of the temperature dependence of the line shift. Here pressure refers to the total pressure. A distinction between dry air and water vapor is usually not necessary since the partial water vapor pressures encountered in the atmosphere are too low to cause a significant shift [26].

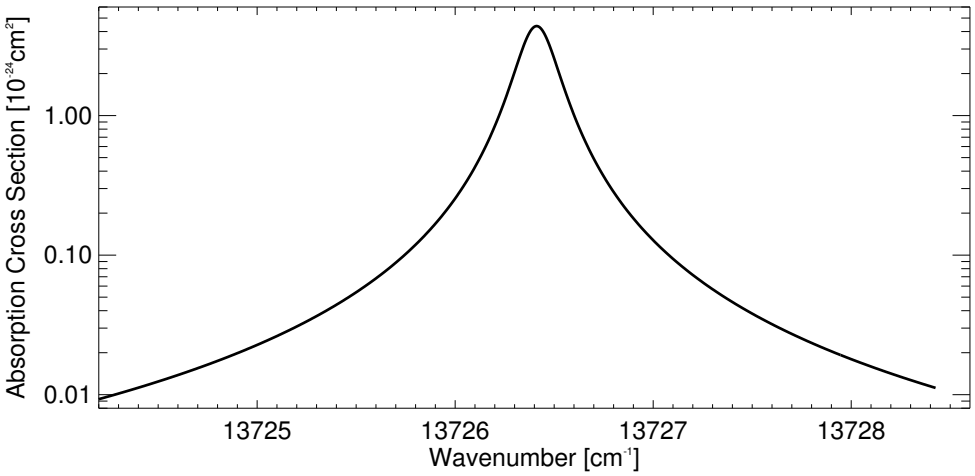

FIGURE 2.2: Profile of a single absorption line, calculated for $p = 1012\,\text{hPa}$ and $T = 29\,^{\circ}\text{C}$ and $\rho_{H_2O} = 22.6\,\text{g/m}^3$, using parameters from HITRAN (see section 3.1.1).

Total cross section So far, we have only considered the cross section of a *single* absorption line. Such a line is shown in Fig. 2.2. The profile has been calculated for $p = 1013.25\,\text{hPa}$, $T = 296\,\text{K}$, and $\rho_{H_2O} = 22.6\,\text{g/m}^3$. We can see that the absorption drops quickly away from the line center, but does not become zero. So for an accurate calculation of the cross section at a certain wavenumber $\tilde{\nu}$, the contributions of all lines, or at least of those in the vicinity of $\tilde{\nu}$, need to be summed up. The total cross section $\sigma(p, T, \tilde{\nu})$ then reads:

$$\sigma(p, T, \tilde{\nu}) = \sum_{\tilde{\nu}_o} \sigma(p, t, \tilde{\nu}, \tilde{\nu}_o). \tag{2.13}$$

A portion of the spectrum similar to Fig. 2.2 where all available lines were used for the calculation is shown in Fig. 3.3.

Chapter 3

Quality Assurance

The accuracy with which the water vapor density can be measured depends on the accuracy of the quantities going into DIAL inversion formulas Equation 2.4 and Equation 2.5. These quantities are the backscatter signal intensities $P(R)$ and the differential absorption cross section $\Delta\sigma$.

When post processing the data from the campaigns in 1999 and 2000, several factors were found which would compromise this accuracy if their influence were neglected. Regarding the absorption cross section, the sources of errors can be divided into two groups:

- Errors associated with the calculation of $\Delta\sigma$ as described in Section 2.3, due to inaccurate absorption line parameters in spectroscopic databases as well as mistakes in the calculation itself (mainly oversimplification). This point will be discussed in Section 3.1

- Errors due to deviations in the laser spectral properties from the specified values. How such deviations could be detected and partly corrected for is described in Section 3.2.

Regarding the backscatter signal levels, it was found that systematic errors were caused by errors in the determination of the signal baseline. This will be discussed in Section 3.3.

3.1 Spectroscopic Issues

Until 1999, in our group some of the steps laid out in Section 2.3 were neglected for the calculation of the differential absorption cross section $\Delta\sigma$. Since for our DIAL systems the online frequency had always been chosen at the center of an absorption line, it was thought to be sufficient to consider only that particular line and not to apply the summation as in Equation 2.13. This can be adequate when a strong absorption line is used as is the case for low water vapor densities. The effect of self broadening (Equation 2.10) was also neglected since it plays only a minor role under low humidity conditions. The Nauru99 campaign (a description of the campaign will be given in Section 4.1), which took place in a tropical environment then showed that under humid conditions, these simplifications can lead to substantial systematic errors in the retrieved humidity. Therefore the retrieval algorithm was revised, and with it the database of line parameters used for the calculation of $\Delta\sigma$. Furthermore a list with recommendations for the best online/offline pairs was compiled.

The sensitivity studies presented in the following are based on profiles of pressure, temperature, and absolute humidity which represent the mean of all radiosonde ascents conducted during the core period of Nauru99 from Jun 22 to Jul 14 1999. These mean profiles are shown in Fig. 3.1.

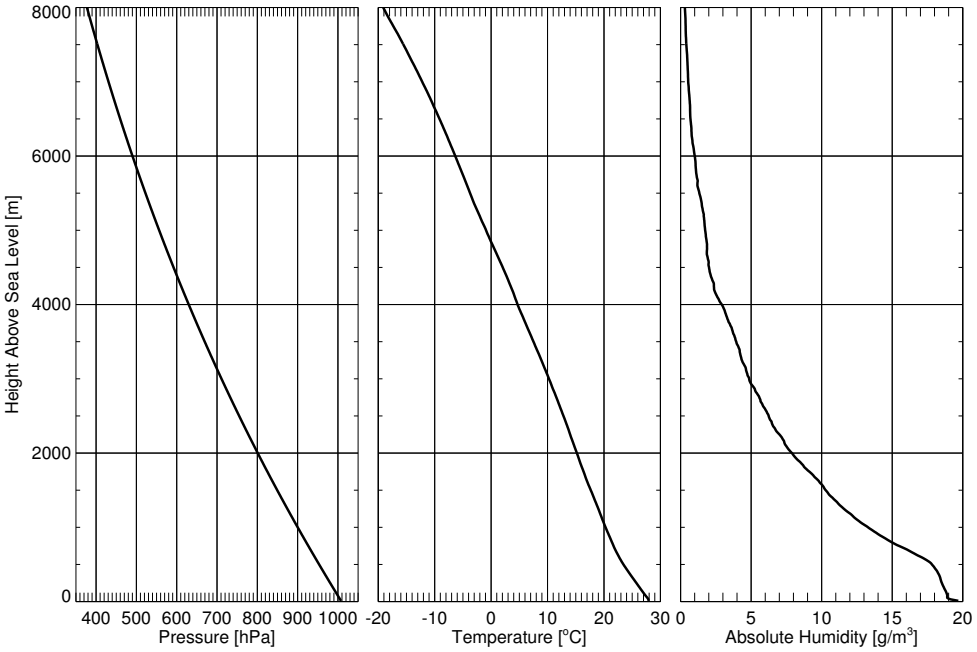

FIGURE 3.1: Mean profiles of pressure, temperature and absolute humidity for the Nauru99 campaign (from radiosonde data).

Parameter	Description
E	Ground state energy
S	Line strength
$\Gamma_{c,air}$	Air broadened line width
$\eta_{c,air}$	Exponent for temperature dependence of $\Gamma_{c,air}$
$\Delta\tilde{\nu}$	Pressure shift
α	Exponent for temperature dependence of $\Delta\tilde{\nu}$
Γ_{c,H_2O}	Self broadened line width
η_{c,H_2O}	Exponent for temperature dependence of Γ_{c,H_2O}

TABLE 3.1: Parameters needed for the calculation of the absorption cross section $\sigma(\tilde{\nu})$ for an individual absorption line.

3.1.1 Line Parameter Database

Table 3.1 list all the parameters needed for the calculation of the absorption cross section for a single absorption line, according to Section 2.3. Various sources for such parameters can be found in the literature, none of them providing all parameters necessary for the calculation of $\Delta\sigma$ and some also only providing parameters for selected lines. Furthermore, line parameter values from different sources also show substantial disagreement.

For the compilation of a database of "best values" for absorption line parameters, we have therefore first tried to assess the accuracy of the different sources and rank them accordingly. The required parameters are then taken from the most accurate available source. If a parameter is not listed in any of the sources, it is calculated from other known parameters by an empirical formula or a best guess value is taken.

The sources we have considered are the following:

HITRAN database [27]. This database tries to give a comprehensive set of absorption lines for various molecular species. Comprehensive meaning that it should be possible to reproduce the whole absorption spectrum by superposing the individual lines. For water vapor, the latest dataset has been published in 2001 [28], this incorporates the corrections to the 1996 edition described in [29]. The line parameters in this database are mainly derived from Fourier transform spectroscopy measurements (e.g. [30]) and some also from theoretical calculations. References for the source of the parameters are given for each line in HITRAN. A list of the according references is available at [31].

Grossman and Browell [26, 22]. These publications contain only few, comparatively strong lines in the $720\,\mathrm{nm}$ region. These lines were specially selected for their suitability for DIAL measurements and were carefully and individually characterized by laser spectroscopy. For some lines, these publications also give more parameters than HITRAN, in particular the pressure shift. With Ponsardin and Browell [32], a similar publication is available for the $820\,\mathrm{nm}$ region.

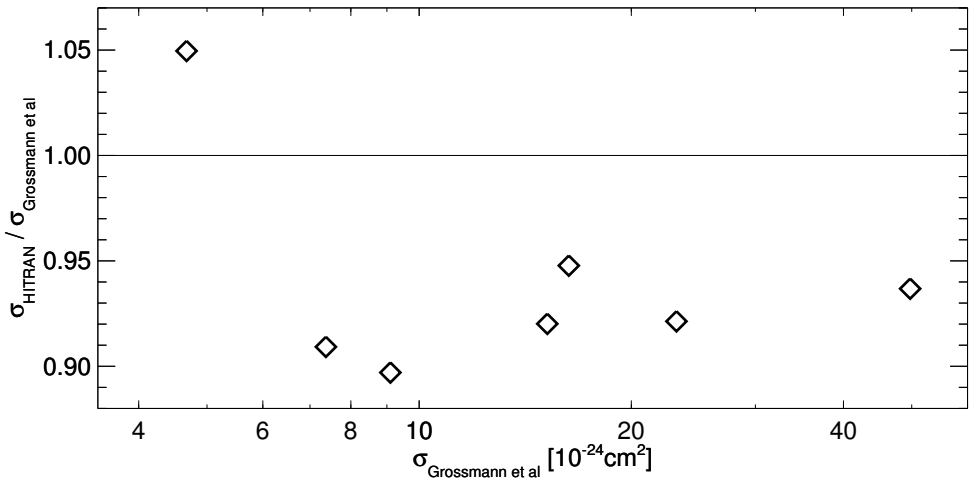

FIGURE 3.2: Comparison between absorption cross sections (at line center and standard conditions) calculated using parameters from Grossmann and Browell [26, 22] and HITRAN (2001 edition [28]).

Regarding the accuracy or reliability of the different sources, Fig. 3.2 shows a comparison of absorption cross sections derived from HITRAN and from Grossmann and Browell. The calculation was done for all lines used as online frequency for the alexandrite DIAL system (these lines are listed Table A.1), using $p = 1013.25\,\mathrm{hPa}$ and $T = 296\,\mathrm{K}$, so that parameters

η and α are of no relevance, pressure shift and self broadening were neglected. One can see that, apart from one line, σ is systematically lower by up to $10\,\%$ in HITRAN, which directly translates into higher retrieved water vapor densities (Equation 2.5). Considering the great care used for the line characterization in Grossmann and Browell [26, 22], we conclude that the values from these publications are more accurate than those from HITRAN. This hypothesis is supported by other authors' results. Belmiloud et al. [33, 34] give comparisons between their results, values from Grossman and Browell [26], Ponsardin and Browell [32], and from HITRAN. They observe integrated band intensities that are higher by $10\,\%$ for the $720\,$nm band (also called 4ν polyad) and by $15\,\%$ for the $820\,$nm Band ($3\nu + \delta$ polyad) compared to the latest HITRAN edition. Compared to [26], their observed average line strength is only higher by $2\,\%$ and higher by $3\,\%$ compared to [32]. Because of this good agreement, one should also consider to use the ESA database that originates from the work of Belmiloud et al. [33, 34], described in [34, 35, 36], instead of HITRAN in the future.

After it has been determined which lines are needed for the calculation of σ_{on} and σ_{off} (described in Section 3.1.2), the following step-by-step procedure is carried out in order to find all the needed parameters:

1. If the line is listed in [26, 22] or [32], take all the available parameters from there.

2. Take all missing parameters, if possible, from HITRAN.

3. If the line is not listed in [26, 22] or [32], use HITRAN and and take all available parameters from there. S, $\Gamma_{c,air}$, $\eta_{c,air}$, and Γ_{C,H_2O} are given in HITRAN for all lines.

4. Parameters which are still missing now are calculated or chosen the following way:

5. E: For some weak lines, E is not given in HITRAN. These are always lines which are not centered at the actual online wavelength. Therefore they are only important in the way that their wings influence the online or offline cross section. This influence is only important in regions where lines are broad, i. e. at low altitudes. As E is mainly important to calculate the line strength at low temperatures (see Equation 2.11), i. e. at high altitudes, it should be no problem to choose zero as a best guess value.

6. $\Delta\tilde{\nu}$: no values are given in HITRAN. Therefore, use the empirical formula given in [22]: $\Delta\tilde{\nu}(p_o, T_o) = 0.363 \cdot \Gamma_{c,air}(p_o, T_o) - 0.0476\,\mathrm{cm}^{-1}$. This formula applies to the $720\,$nm region. A similar formula is given in [32] for the $820\,$nm region: $\Delta\tilde{\nu}(p_o, T_o) = 0.26 \cdot \Gamma_{c,air}(p_o, T_o) - 0.036\,\mathrm{cm}^{-1}$.

7. α: is listed in none of the sources. Therefore, use the empirical formula given in [22]: $\alpha = -52\,\mathrm{cm} \cdot \Delta\tilde{\nu}(p_o, T_o) - 0.15$.

8. η_{C,H_2O}: Use the empirical formula from [26]: $\eta_{c,H_2O} = 3.24\,\mathrm{cm} \cdot \Gamma_{c,H_2O}(p_o, T_o) - 0.68$.

A special case is presented by the absorption line at $\tilde{\nu}_o = 13726.426\,\mathrm{cm}^{-1}$. This line was used extensively for the online wavelength during the Nauru99 campaign. For this line, no air broadening coefficient $\Gamma_{c,air}$ is given in [22], but only the coefficient for pure nitrogen, Γ_{c,N_2}. Since an empirical formula is given which relates Γ_{c,N_2} to $\Gamma_{c,air}$, it was decided to use this formula for deriving $\Gamma_{c,air}$ rather than taking it from HITRAN. The formula reads:

$$\Gamma_{c,air}(p_o, T_o) = 0.907 \cdot \Gamma_{c,N_2}(p_o, T_o).$$

3.1.2 Selection of Lines

The best possible way to calculate $\Delta\sigma$ would be to add up the contributions of all available absorption lines. But since $\Delta\sigma$ depends on pressure, temperature, *and* humidity (see Section 3.1.4), this summation over several thousand lines would have to be conducted anew for each retrieved data point. An alternative is to find the lines which contribute most to σ_{on} and σ_{off} and use only these for the calculation. Once the N lines for σ_{on} and the M lines for σ_{off} have been determined, the expression for $\Delta\sigma$ reads:

$$\Delta\sigma = \sigma_{on} - \sigma_{off} = \sum_{i=1}^{N} \sigma(\tilde{\nu}_{on}, \tilde{\nu}_i) - \sum_{j=1}^{M} \sigma(\tilde{\nu}_{off}, \tilde{\nu}_j). \tag{3.1}$$

Conforming with the nomenclature introduced in Section 2.3, $\sigma(\tilde{\nu}_{on}, \tilde{\nu}_i)$ denotes the cross section at the wavenumber $\tilde{\nu}_{on}$ of the absorption line centered at $\tilde{\nu}_i$. In order to find the lines to be put into Equation 3.1, the following steps are carried out:

1. For one set of atmospheric conditions a "true" $\sigma_{on,true}$ and a "true" $\sigma_{off,true}$ are calculated. This is done by adding up the contributions of all absorption lines in the entire absorption band. For the atmospheric conditions the highest pressure, temperature and humidity encountered during Nauru99 were chosen, because this is when the broadening is maximal and thus the influence of absorption lines in the vicinity to a certain wavelength is biggest. The values for p, T, and ρ_{H_2O} where $1012\,$hPa, $29.0\,^{\circ}$C and $22.6\,$g/m^3 respectively. For this calculation, which is only concerned with a relative quantification of cross sections, only line parameters from HITRAN were used. The possible difference in σ when only one line is considered compared to the whole spectrum is illustrated in Fig. 3.3.

2. The contributions of the individual lines to $\sigma_{on,true}$ and $\sigma_{off,true}$ are sorted in descending order.

3. For σ_{on} as many of the most contributing lines are included in the summation that the difference between the sum and $\sigma_{on,true}$ becomes less than $1\,\%$:

   $$\sigma_{on,true} - \sigma_{on} < 0.01 \cdot \sigma_{on,true}. \tag{3.2}$$

   This is of course arbitrary and the maximum allowed difference between $\sigma_{on,true}$ and σ_{on} could also be set to a different value. For σ_{off}, the cut-off for the summation is determined by a similar criterion:

   $$\sigma_{off,true} - \sigma_{off} < 0.01 \cdot \sigma_{on,true}. \tag{3.3}$$

4. Now N absorption lines have been selected for a sufficiently accurate calculation of σ_{on} and M lines for the calculation of σ_{off}. Some of these lines can be identical. For the reason of simplification, all unique lines are finally put into one database which is then used for the calculation of both σ_{on} and σ_{off}. This might slightly increase the time needed for the calculation but will not deteriorate its accuracy.

Sensitivity Fig 3.3 shows clearly how strong the influence of neighboring lines can be even at the center of an absorption line. This particular case represents the combination of online and offline frequency which, although not ideal (see Section 3.1.3), was used most frequently during the Nauru99 campaign. Also at the offline frequency, a substantial amount of absorption is still present, which necessitates the inclusion of yet more lines into the calculation of $\Delta\sigma$. To fulfill the conditions laid down in Equations 3.2 and 3.3, a total of six lines is needed. What

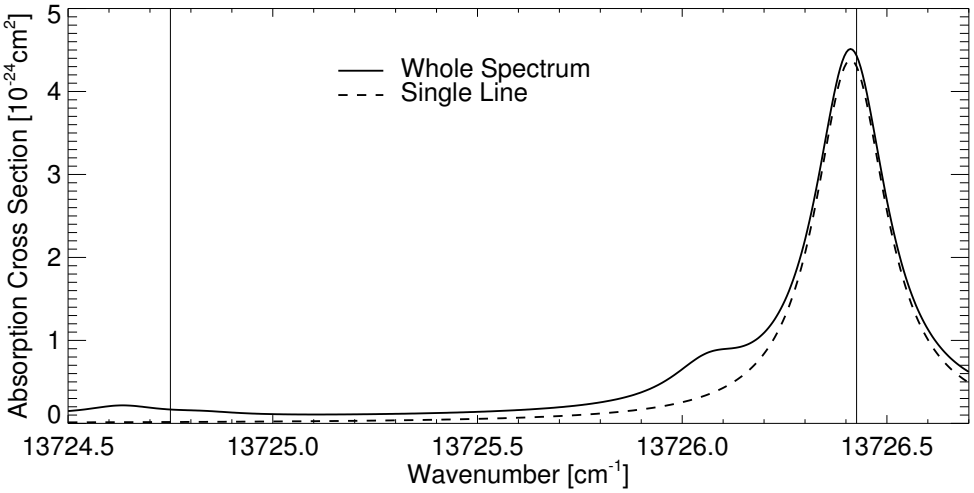

FIGURE 3.3: Water vapor absorption spectrum calculated using all available lines (solid line) and only one absorption line (dashed line). Vertical lines indicate the positions of online and offline frequency. Other parameters as in Fig. 2.2

the effect would be if only one line were used for the calculation is illustrated in Fig 3.4, which depicts the errors in the calculation of σ_{on}, σ_{off} and $\Delta\sigma$, all relative to $\Delta\sigma_{true}$. In this case, the two errors almost cancel out because of the strong offline absorption. With an offline frequency in a region of negligible absorption though (which is recommended), the resulting error would be as large as the error for σ_{on} alone. It is not possible that errors for σ_{on} and σ_{off} add up, since neglecting the influence of additional lines will always lead to an underestimation of σ for both wavelengths.

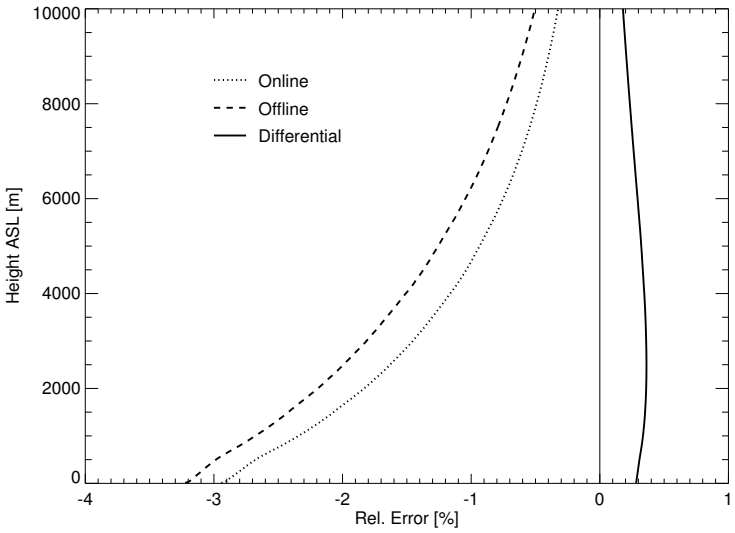

FIGURE 3.4: Error in calculation of σ_{on}, σ_{off} and $\Delta\sigma$ when only one absorption line is used, relative to the true value of $\Delta\sigma$. Height-dependent atmospheric parameters were taken from the reference profiles shown in Fig. 3.1

3.1.3 Selection of Online and Offline Frequency

Although the previous Section gives the impression that $\Delta\sigma$ can be calculated accurately enough for any combination of $\tilde{\nu}_{on}$ and $\tilde{\nu}_{off}$, this is not truly the case. In order to minimize uncertainties,

the selection of $\tilde{\nu}_{on}$ and $\tilde{\nu}_{off}$ should be guided by the following principles:

- $\tilde{\nu}_{on}$ should be at the center[1] of a well characterized absorption line, i.e. a line listed in [26, 22] for the $720\,\text{nm}$ region or in [32] for the $820\,\text{nm}$ region.
- The influence of neighboring lines on σ_{on} should be as low as possible.
- The absorption at $\tilde{\nu}_{off}$ should be as low as possible, i.e. $\tilde{\nu}_{off}$ must not lie near the center of a strong line and the influence of adjacent lines should also be as low as possible. Furthermore, σ_{off} should not strongly depend on pressure and temperature or on the laser frequency, hence $\tilde{\nu}_{off}$ should not be located on the slope of a strong line.
- The transition belonging to the online absorption line should have a ground state energy that minimizes the temperature dependence of the absorption cross section at the line center. A plot of this dependence is shown in Fig. 3.5. The optimum for E'' lies around $180\,\text{cm}^{-1}$, values between 0 and $350\,\text{cm}^{-1}$ are acceptable. Low values of E'' give the additional advantage of a cross section that increases with height more strongly than for high values of E'' (the decreasing pressure will in any case lead to a growing σ). This helps in compensating for the decreasing humidity and achieving better signal statistics at high altitudes.

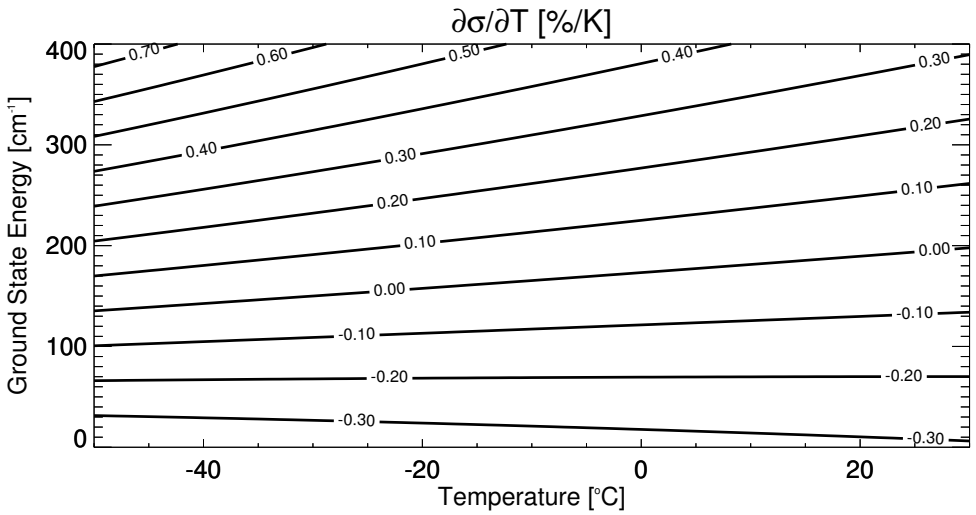

FIGURE 3.5: Influence of the ground state energy on the temperature dependence of the absorption cross section at line center. All parameters except E'' are taken from line No. 17 in Table A.2, the pressure dependence of $\partial\sigma/\partial T$ is negligible.

Regarding the offline frequency, for the alexandrite DIAL system the choice of $\tilde{\nu}_{off}$ for a given $\tilde{\nu}_{on}$ is rather restricted:

$$\tilde{\nu}_{off} = \tilde{\nu}_{on} + n \cdot \Delta\tilde{\nu}_{on/off} \text{ with } n \in [-2, -1, 1, 2] \text{ and } \Delta\tilde{\nu}_{on/off} \approx 1.67\,\text{cm}^{-1}.$$

The reason for this is that the offline frequency is provided by the same seed laser as the online frequency (for a description of injection seeding see Section 5.6.1), and the laser is switched between the two frequencies for alternating shots, for details see [14]. For some lines which are in principle well suited as online frequency, it is therefore impossible to find an offline frequency which is not situated near the center or on the slope of a strong absorption line.

[1] In principle, $\tilde{\nu}_{on}$ could be tuned to the pressure shifted line center instead of the "vacuum" line center. If this is advantageous and if yes, the pressure shift at which height should be considered will be discussed in Section 3.2.

Another thing to bear in mind is the necessity to use an interference filter that fits the selected laser frequency. These filters are manufactured for a certain central transmission wavelength and a certain bandwidth. By tilting the filter, the central wavelength can be shifted to shorter values, but this tuning range is rather restricted. We have decided to detune the filters of $1\,\mathrm{nm}$ width that we use by no more than $1\,\mathrm{nm}$.

Considering all the points mentioned in this section, lists of suitable $\tilde{\nu}_{on}/\tilde{\nu}_{off}$ combinations, absorption lines needed for the calculation of $\Delta\sigma$ (see Section 3.1.2), and best line parameters (see Subsection 3.1.1) have been compiled, both for the existing alexandrite system and for the new Ti:Sa system which operates in the $820\,\mathrm{nm}$ region. These lists can be found in Appendix A.

3.1.4 Influence of Self Broadening

Due to self broadening, water vapor absorption lines are broader in humid air than in dry air at the same total pressure (Equation 2.10). Since the integrated line strength S is not affected by pressure (Equation 2.11), an increased line width results in a lower cross section at the line center.

So the difficulty arises, that for the calculation $\Delta\sigma$ and hence for the DIAL inversion (Equation 2.5), the humidity itself needs to be known. Since this quantity is only the result of the measurement and is not known beforehand, an iterative approach has to be taken: A first guess profile is calculated assuming zero humidity. In Fig. 3.6A, we can see the result of this calculation for the atmospheric conditions shown in Fig. 3.1. In regions of high humidity, it yields an underestimation of up to $9\,\%$. This would also be the resulting error if self broadening were neglected. In a second step, $\Delta\sigma$ is then calculated again using the humidity retrieved in the first step. With this $\Delta\sigma$, the obtained absolute humidity deviates from the true value by less than $1\,\%$, as it can be seen in Fig. 3.6B. Considering this small remaining difference, another iteration can be regarded unnecessary.

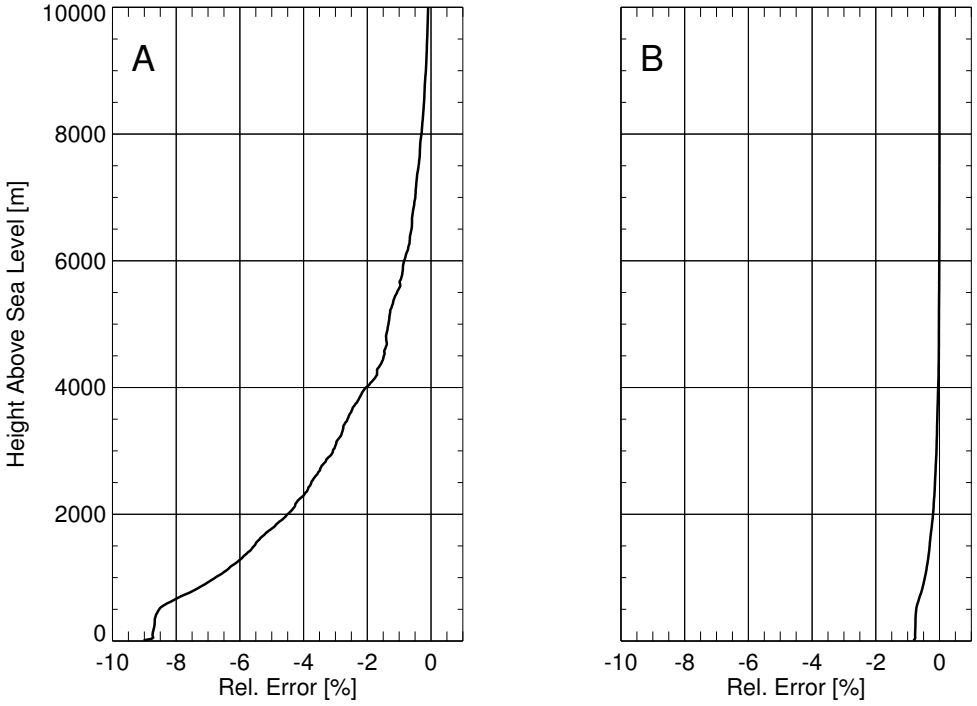

FIGURE 3.6: Relative Error in Humidity retrieval due to self broadening: After retrieval assuming zero humidity (A) and after reiterating the calculation using the humidity obtained in the first step (B)

3.1.5 Summary

This is a short summary of the points to be taken care of and the magnitude of possible errors regarding the spectroscopic database and the calculation algorithm for $\Delta\sigma$:

Source of line parameters: Taking parameters from HITRAN instead of more reliable sources can result in underestimation of $\Delta\sigma$ up to $10\,\%$. In the case of the absorption line used most frequently for the Nauru99 campaign, an overestimation of $5\,\%$ would result.

Self broadening: Neglecting its influence can result in overestimating $\Delta\sigma$ by up to $9\,\%$ in regions of high humidity.

Neighboring absorption lines: Neglecting their contribution to σ_{on} can result in an underestimation of $\Delta\sigma$ by several percent.

3.2 Laser Issues

Regarding the determination of $\Delta\sigma$, we have so far only been concerned with the absorption spectrum of water vapor, however $\Delta\sigma$ depends just as strongly on the spectrum of the emitted laser pulses. An ideal laser spectrum would have its center frequency exactly at the specified value, be very narrow compared to the absorption lines and have all light energy concentrated inside this narrow interval. The deviations of these three parameters (center frequency, spectral width, and spectral purity) from the ideal values which can be tolerated without having to apply corrections depend both on the circumstances of the measurement and on the accuracy one wishes to achieve. For a detailed discussion see [17]. In [17] a set of requirements for the spectral properties is given which should be sufficient for all possible measurement situations. The requirements are chosen such that the systematic error resulting from one parameter will stay below $3\,\%$ and the overall error below $5\,\%$ throughout the troposphere. These requirements are listed in Table 3.2, they apply for the online frequency and for the case that this frequency is situated at an absorption line center.

Parameter	Requirement
Frequency Deviation	$< 210\,$MHz
Spectral Width	$< 390\,$Mhz
Spectral Purity	$> 99.5\,\%$

TABLE 3.2: Spectral quality requirements for a water vapor DIAL laser emitter.

It has been shown that the specifications of the alexandrite laser system can be far better than the requirements listed in Table 3.2 [14]. During the Nauru99 campaign however, first indications were found that under field conditions and for prolonged operation, the necessary spectral quality could not always be maintained. An example of a measurement where a quality problem becomes apparent is shown in Fig. 3.7. This time-height plot is a composite of the small and the large telescope channel with the border between the two at $1000\,$m. The fact that the two channels do not merge very well in some cases is a different problem which is still not completely understood up to this day. The most striking feature visible in the plot is a regular vertical stripe pattern indicating oscillations in the calculated humidity. Since these oscillations are visible in both channels and can hardly be of real atmospheric origin, they are most likely caused by fluctuations in the laser spectrum.

Until Nauru99, there was little possibility to monitor the spectral properties of the alexandrite DIAL system during operation. The frequency is prescribed by the Ti:Sa master laser. This

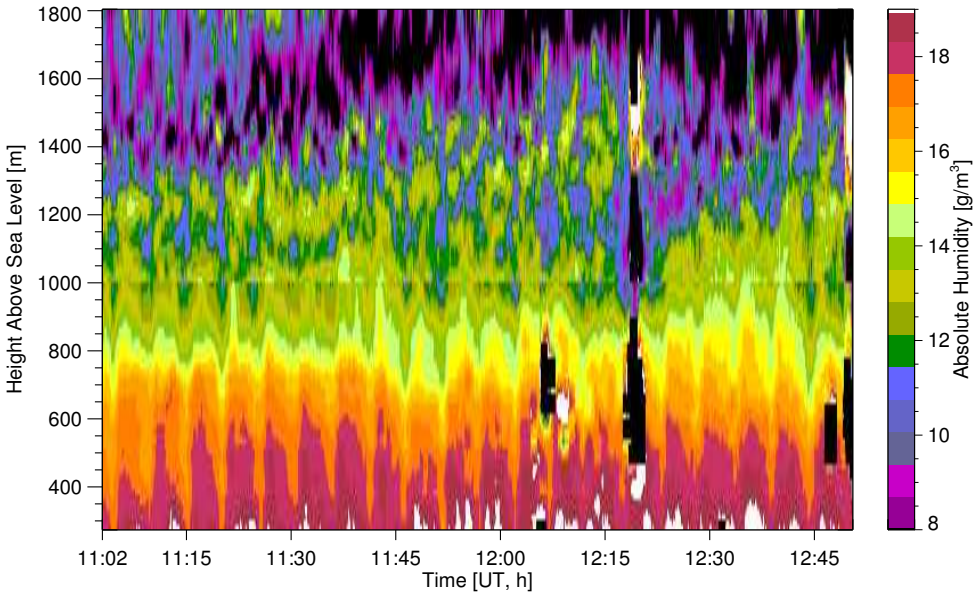

FIGURE 3.7: Time-height plot of a water vapor DIAL measurement taken on 10 Jul 1999 during the Nauru99 campaign.

laser is tuned using a Burleigh WA1500 wavemeter. Since this instrument needs about 1 s to complete a measurement, it does not produce useful readings once the online/offline switching is activated. If injection seeding is successful, the emitted pulses are of the same frequency as the master laser and show a very narrow spectral width. If, as in our case, no measures are taken to ensure single frequency operation, the alexandrite laser mostly operates on two longitudinal modes, resulting in a spectral width of about 80 MHz, corresponding to the mode spacing of the laser. If seeding is however not or only partially successful, i.e. the so-called seed efficiency is low, none or only part of the laser pulse energy is emitted within the desired narrow spectral interval. The rest shows a much wider spectrum and therefore leads to a reduction of the spectral purity of the pulse. Apart from a Fabry-Perot etalon, which provides only a qualitative visual check of the seed efficiency, no possibility existed to monitor this parameter during operation. Active control schemes had been developed which should ensure a stable master laser frequency [14] and reproducible single frequency operation of the slave laser [37], but they apparently proved not to be reliable enough for long term operation and were thus not employed during the campaigns described in this work.

3.2.1 Setup for Quality Monitoring

To obtain better information about the laser spectrum, a long path absorption cell and a photo acoustic absorption cell were installed.

The long path absorption cell is used for measuring the transmission of laser light through a certain volume of a gaseous substance [38], in our case water vapor. By using a special mirror configuration, the path length the light travels inside the cell can be made many hundred meters long. If the vapor density inside the cell is high and the air pressure low, the cell will become practically opaque if the laser is tuned to a sufficiently strong absorption line. Then, the spectral purity of the light is equal to the absorption of the cell and it can be directly determined by measuring the residual transmission [14]. This device proved to be valuable for laboratory measurements, operational field use however is more difficult and could not be achieved so far. The two main problems are:

- For a laboratory characterization of the spectral purity, the laser is usually tuned to a very

strong absorption line. It is justified to assume that the spectral purity will be even better if a weaker line is used, because then the losses due to water vapor inside the cavity are lower and the laser is ”less reluctant” to operate at such a wavelength. The lines used for atmospheric measurements are usually weaker and then the theoretical transmission of the absorption cell is still in the order of several per cent. This puts higher requirements on the accuracy of the calculation of the cell absorption as well as on the measurement of the residual transmission.

- As a reference, it is also necessary to measure the cell transmission at the offline frequency. For the field use, this results in high signal dynamics because online and offline transmission have to be measured in the same configuration. In the laboratory, the beam leaving the cell can be attenuated for the offline measurement.

The photoacoustic cell [39] is a small cylinder with windows on either end, so that a laser beam can pass through, and it has a microphone attached to the side of it. In our case, the cell is filled with pure water vapor. If a laser pulse passes the cell, a sound impulse is generated which is detected by the microphone. The amplitude of the microphone signal is proportional to the absorbed energy. This energy is in turn proportional to the density of the absorbing medium, the absorption cross section, and the laser pulse energy. For a more detailed description of this technique, especially regarding the data acquisition, see [25]. As opposed to the long path cell where transmission is measured, here absorption is measured directly. If the conditions inside the cell remain constant, both the density and the absorption spectrum stay constant. If the signal is then divided by the laser pulse energy, the resulting quantity, further on called ”photoacoustic absorption”, can serve to detect changes in the laser spectrum. If the laser is initially tuned to the maximum of an absorption line and shows no spectral impurity, any deterioration in the spectral properties, i.e. detuning and reduced spectral purity, will lead to a reduced photoacoustic absorption. The absence of air inside the cell has the effect that there is negligible pressure shift and also that the absorption lines are much more narrow than under atmospheric conditions, which leads to an increased sensitivity to laser frequency changes and also a higher signal level due to the increased absorption cross section. Since the attenuation of light inside the cell is very low due to the short path length, the cell can be placed directly in the powerful outgoing beam. This results in good signal statistics and allows absorption measurements on a shot-to-shot basis. For measuring the pulse energy, some per cent of the light intensity is deviated toward a pyroelectric sensor by a glass plate placed in the outgoing beam.

The described setup became fully operational for the AFWEX campaign, conducted in Oklahoma in December 2000 and the data presented in the following were collected during this campaign. For a more detailed description of AFWEX see Section 4.2. An example of photoacoustic absorption data is shown in Fig 3.8. The relative standard deviation of the online absorption is only $1.0\,\%$ and it is therefore possible to make quantitative assessments of the laser spectral properties on a single shot basis. In the following section, the type of laser malfunctions that were identified using photoacoustic absorption data will be presented. It will also be described when and how the effects of such problems could be corrected for or if discarding the data was necessary.

3.2.2 Results

The primary parameters regarding the laser spectrum are frequency and spectral purity. Deviations from the specified values will lead to a reduced photoacoustic absorption for both parameters. Therefore, it is not possible to determine the reason why one isolated laser shot showed reduced absorption from the photoacoustic measurement alone. A statement is possible

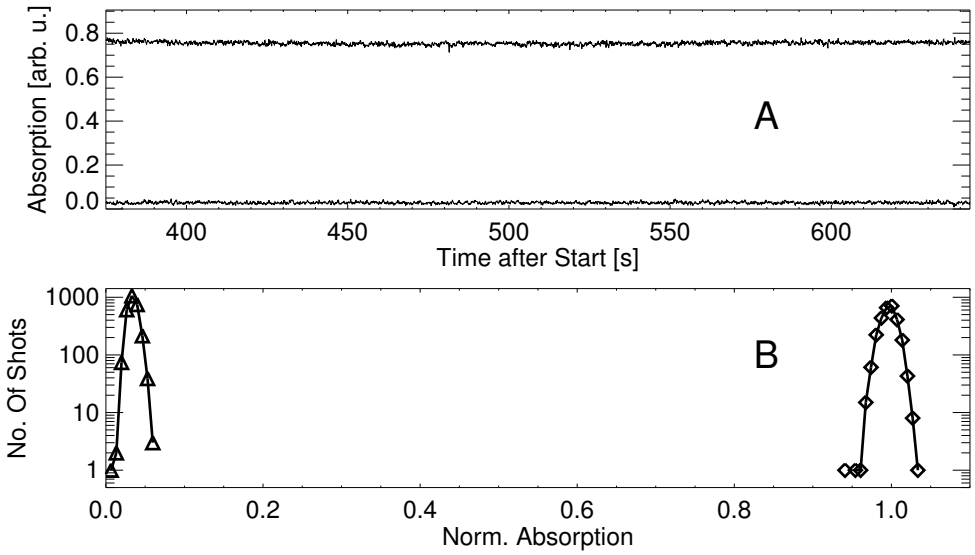

FIGURE 3.8: Time Series (A) and distribution (B) of a photoacoustic absorption measurement. Both online (upper trace in A, diamonds in B) and offline channel (lower trace in A, triangles in B) are shown.

however if a time series containing many shots is considered. Regarding the spectral purity, stable operation without active control can only be achieved if the seed efficiency is high or if it is zero. Any intermediate state will be inherently very unstable and the measured photoacoustic absorption will show a large shot-to-shot variation. Changes in the laser frequency (determined by the master laser) on the other hand will not occur in a way of large, random variations from shot to shot but rather in the way of a slow drift which can be accompanied by so-called mode-hops, i.e. a sudden change of the master frequency by one mode spacing, 180 MHz in our case. Examples for both kinds of behavior will be presented in the following.

3.2.2.1 Spectral Impurity

Fig 3.9 shows the same measurement as in Fig 3.8, this time for the entire length of the datafile. Only the online channel is shown. The time series of the absorption in Fig 3.9A shows significant variations throughout the measurement. For the first 2300 s these variations occur in a regular pattern and can be attributed to laser frequency changes (see below). The rest of the file shows a substantial number of shots with reduced absorption. To quantify the fraction of these bad shots, a threshold value for the absorption was introduced, indicated by the dotted line in Fig 3.9A. Fig 3.9B shows the fraction of shots lying below this threshold for 1 min intervals. Due to the high number of these bad shots, it was decided to use only the first 3400 s of the measurement and discard the rest. Several more measurements were found which had to be partly or entirely discarded because of a high number of shots bearing a low spectral purity. Some measurements were also found, where there is a hint that the fraction of bad shots varies in a periodic fashion, which would explain the origin of patterns like in Fig. 3.7. During the Nauru99 campaign however, when the measurement shown in Fig. 3.7 was recorded, the photoacoustic absorption setup was not implemented in the current form yet and later the phenomenon did not occur in such a pronounced way anymore.

Correcting the data affected by badly seeded laser shots was unfortunately not possible for the following reasons:

- Due to the high variation of the photoacoustic absorption because of frequency changes (see below), it was not possible to quantify the degree of spectral purity accurately enough.

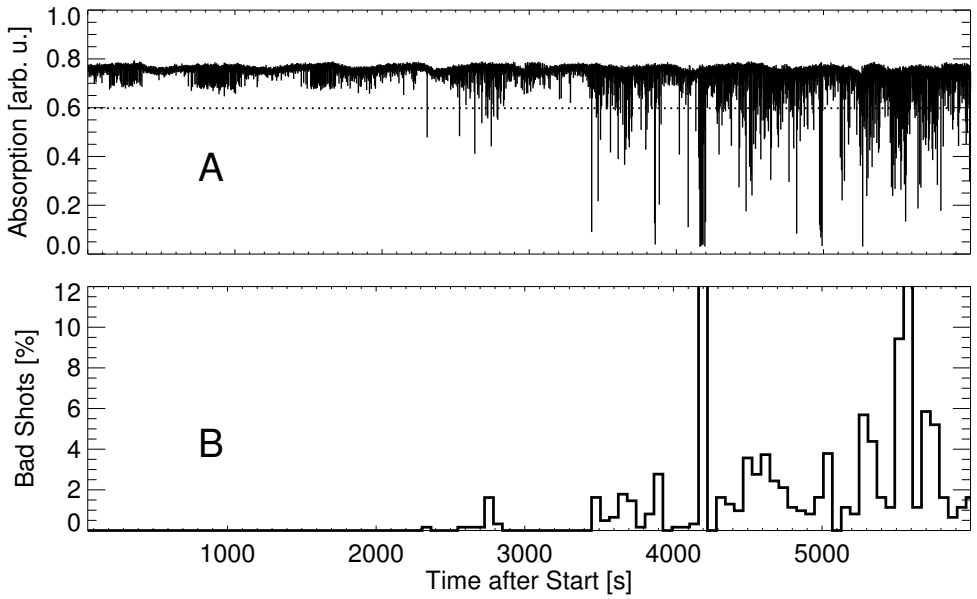

FIGURE 3.9: Photoacoustic absorption measurement revealing shots of low spectral purity. Time series (A) and fraction of bad shots per 1 min interval (B). The dotted line in A represents the value below which a shot is classified bad.

- Since the spectral purity varies strongly from shot to shot, the correction needs to be applied on a single shot basis. As the lidar data are averaged over 100 shots before they are stored, this cannot be done in post processing.
- A correction on a single shot basis is further not possible because the data streams for lidar and absorption data are not synchronized to that level.

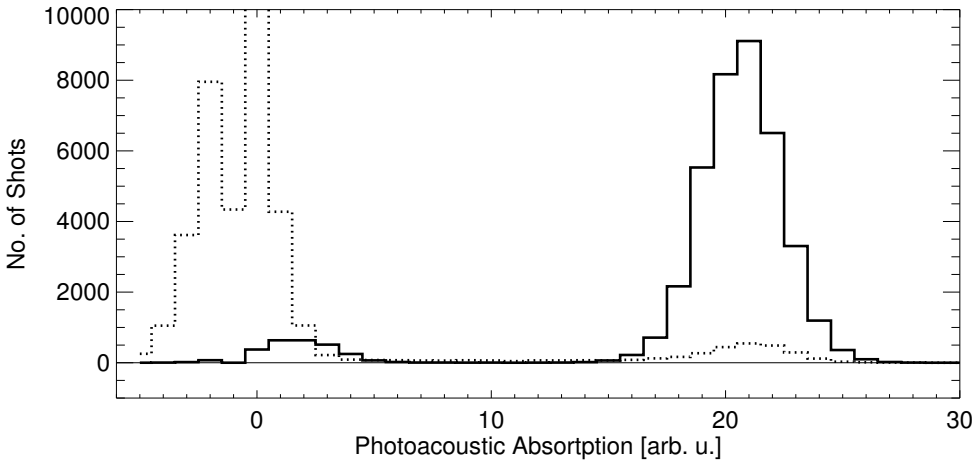

FIGURE 3.10: Distributions of the photoacoustic absorption from one measurement for the online channel (solid line) and the offline channel (dotted line). Failure of the online/offline switching led to a wrong classification of some shots.

A special case of low spectral purity is the failure of the online/offline switching and the resulting assignment of shots to the wrong channel. If a certain fraction of the recorded online shots was actually offline or vice versa, it will both lead to an underestimation of the retrieved humidity. Close to the ground, the relative error is equal to the fraction of wrongly classified shots for both cases. For online shots that were mistaken for offline, the error decreases with height (the

”wrong” light is attenuated by absorption), whereas offline shots assigned to the online channel have the same effect as reduced spectral purity: a systematic error that increases with height. Therefore, only a very small fraction of offline shots can be tolerated in the online channel ($0.5\,\%$ equivalent to a spectral purity of $99.5\,\%$). This kind of problem can also be identified with the photoacoustic measurement. Examples of such a behavior were only found when an earlier setup was used where the resolution of the photoacoustic absorption measurement was much lower than shown in Fig 3.8. Therefore a presentation of the time series would not be very instructive and only the distribution is shown in Fig. 3.10. About $9\,\%$ of the shots which were registered as offline were in fact online and about $6\,\%$ of the registered online shots were in fact offline.

3.2.2.2 Frequency Detuning

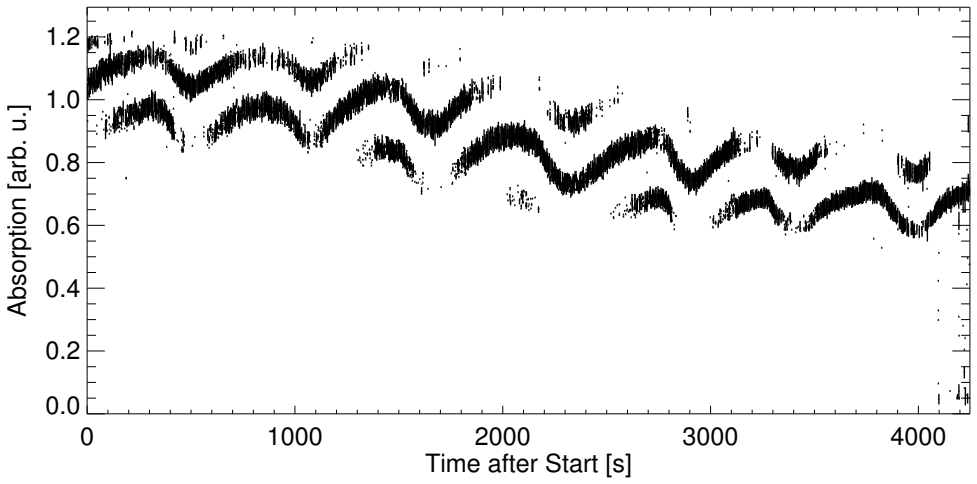

FIGURE 3.11: Time series of a photoacoustic absorption measurement revealing a laser frequency drift.

If reduced photoacoustic absorption is caused by frequency detuning of the master laser, the absorption will not vary in a chaotic fashion as in the case of a low seed efficiency. An example of a strong frequency drift is shown in Fig 3.11. In five discrete steps, the measured absorption decreases steadily during the course of the measurement. These discrete changes are caused by mode hops, jumps of the laser frequency between two longitudinal eigenmodes of the laser resonator, which in this case are separated by about $180\,$Mhz. These jumps are accompanied by a continuous, oscillatory variation which results from changes in the resonator length, probably due to temperature fluctuations. Note that the relative amplitude of the absorption changes that are associated with the modehops gets bigger as the frequency moves away from the absorption line center. In fact, if the shape of the absorption line is known, this relative amplitude $(Abs_{high} - Abs_{low})/Abs_{high}$ can be used to determine the frequency detuning even if there is no absolute calibration for the absorption level. For one particular absorption line and a certain pressure and temperature inside the photoacoustic cell, the relationship between the absorption change associated with a modehop and the laser detuning is shown in Fig. 3.12. Using this graph, the mean laser detuning can be determined, as long as modehops do occur.

In cases as shown in Fig. 3.11 which have occurred only very rarely, no attempt was made to correct the data. The more common behavior was that the mean laser frequency remained constant during one measurement as it is shown in Fig. 3.13. This graph shows two consecutive measurements. During the short break between them, the laser frequency was readjusted because the wavemeter had indicated a detuning by $360\,$MHz. The photoacoustic absorption indicates indeed that the laser was more strongly detuned during the first measurement than

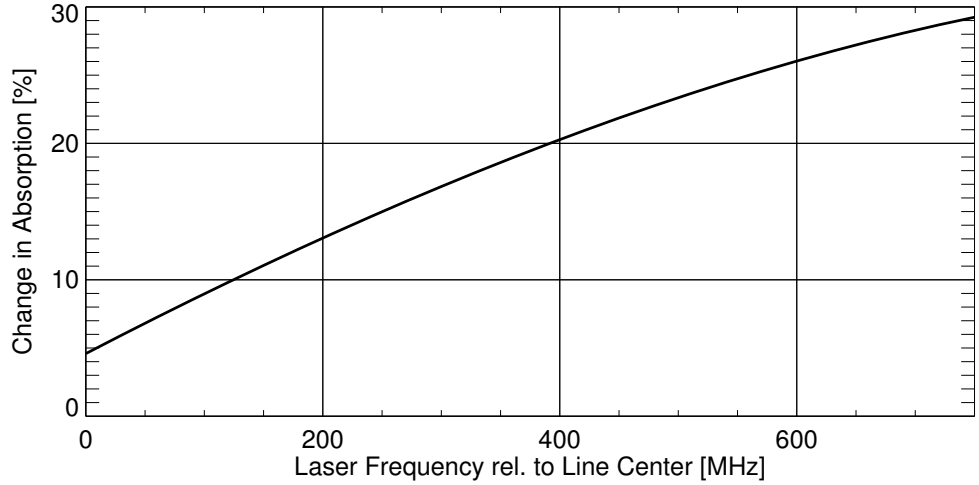

FIGURE 3.12: Relative change in photoacoustic absorption when laser frequency changes to next higher mode ($+180$ MHz). Calculated for the absorption line at $13717.1747\,\mathrm{cm}^{-1}$ and pure water vapor at 18 hPa and $25\,^{\circ}$C

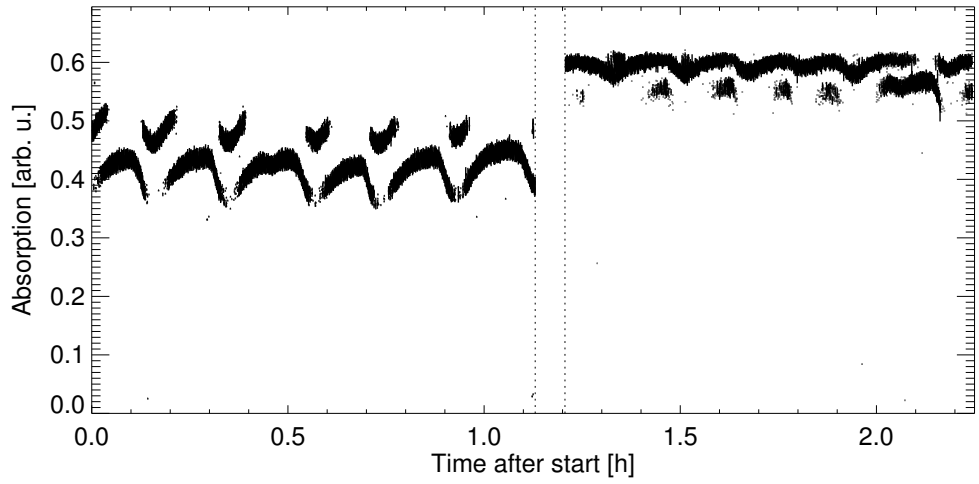

FIGURE 3.13: Time series of two consecutive photoacoustic absorption measurements, dashed lines indicate the gap between the measurements.

during the second, regarding the mean absorption level as well as the amplitude of the jumps. The evaluation of the amplitude yielded a detuning by $720\,\mathrm{MHz}$ for the first measurement and $260\,\mathrm{MHz}$ for the second. This difference of $460\,\mathrm{MHz}$ can be said to agree, within the error margin of this method, with the value obtained from the wavemeter. Even more interesting is the fact that even after readjusting the laser frequency, a considerable frequency error remains. For almost all measurements recorded, such a frequency offset could be found. The cause of this offset has to be a wrong calibration of the wavemeter. To clarify this point, a test measurement was carried out where the laser frequency was slowly scanned over an absorption line and photoacoustic absorption and wavemeter readings were recorded simultaneously. The result was, that at the absorption maximum, the wavemeter reading was indeed about $600\,\mathrm{MHz}$ lower than the literature value for the line center.

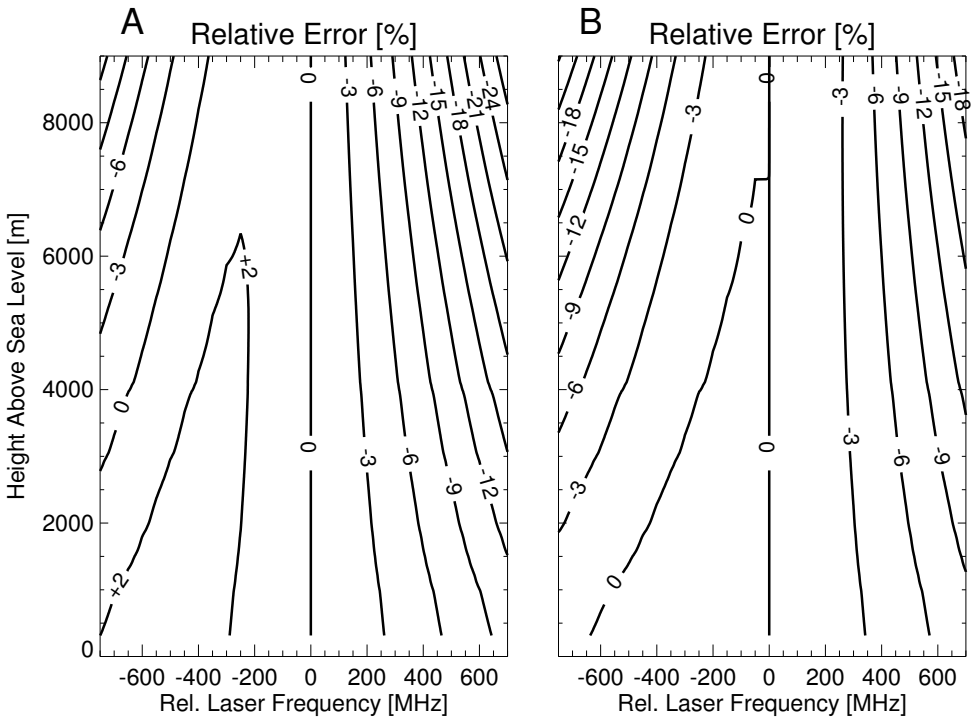

FIGURE 3.14: Systematic error resulting from laser detuning if frequency set point is at "vacuum" line center (A) and if frequency set point is $200\,\mathrm{MHz}$ below line center (B). Calculation is done for absorption line at $13717.175\,\mathrm{cm}^{-1}$ with atmospheric data from radiosonde ascent from AFWEX campaign on 12 Dec 2000, 5:30 UT.

What the systematic error resulting from (uncorrected) laser detuning would be is illustrated in Fig. 3.14A for a particular absorption line and a particular set of atmospheric conditions. If the set value for the laser frequency is the "vacuum" absorption line center, the resulting error strongly depends on the direction of the detuning because of the pressure shift. Unfortunately, this direction cannot be inferred from the photoacoustic absorption measurements, but because of the large effect that was seen, especially at low altitudes, it was concluded that the detuning was always positive. This is supported by the aforementioned calibration check of the wavemeter.

To correct for the effect of laser detuning, the online absorption cross section used for the DIAL inversion (Equation 2.5) has to be calculated at the actual laser frequency and not at the line center. The effect which this correction can have is illustrated in Fig. 3.15. This graph shows the DIAL measurements corresponding to the photoacoustic measurements shown in Fig. 3.13. After the correction no more significant jump between the two time series can be seen and the comparison to a radiosonde value is also very good.

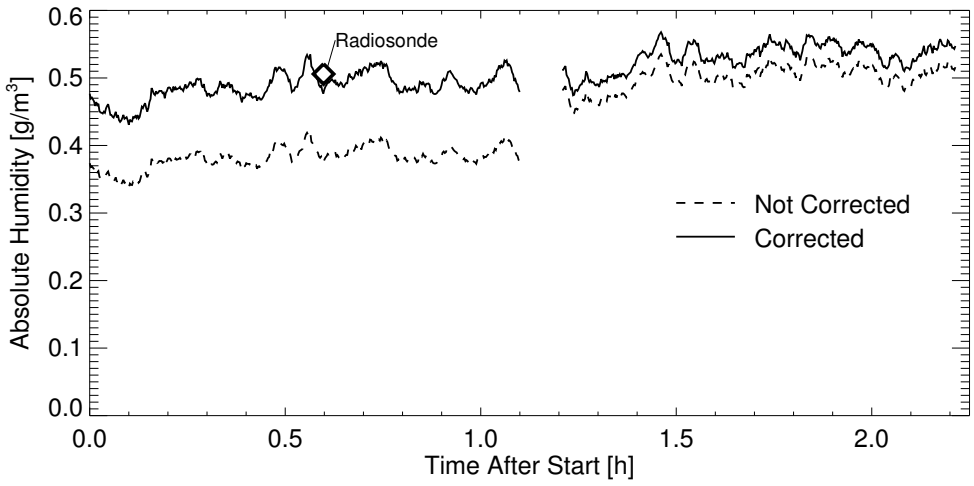

FIGURE 3.15: Mean water vapor measured by DIAL between 5000 and 7000 m above sea level. A gliding average over 2 min has been applied, start of the measurement is 5:11 UT on 12 Dec 2000. Data are plotted before and after laser detuning correction, a value from a radio sounding is shown for comparison.

In the future one should by any means try to avoid laser detuning since the method presented here for determining the actual laser frequency is only of limited accuracy and also relies on the occurrence of modehops. Therefore regular checks of the wavemeter calibration by means of an absorption line scan should be carried out, as it was already proposed in [14][2]. Obviously one cannot rely on the specified accuracy of the instrument of 81 MHz at 730 nm. A further possibility which should be considered is to decrease the sensitivity to laser detuning by choosing the frequency set point not at the "vacuum" line center, but at the pressure shifted line center, taking the pressure shift at the maximum altitude one expects to cover with the measurement. The sensitivity which would result then is shown in Fig. 3.14B where the set frequency is chosen 200 MHz below the vacuum line center, corresponding to the pressure shift found at 9000 m above sea level. One can see that only in this case the resulting error stays below 3 % for a detuning of up to ± 210 MHz, as it was stated in Table 3.2. For a maximum range of 4000 m, which is more realistic under normal, especially daylight conditions, the acceptable detuning becomes as large as ± 380 MHz if the frequency set point is chosen at the pressure shifted line center at that altitude.

3.3 Signal Acquisition Issues

The accurate determination of the backscattered light intensity $P(R)$ (in the following also called lidar signal, see also Equation 2.1) is crucial for the calculation of the differential absorption (Equation 2.4) and hence also for the retrieval of the absolute humidity (Equation 2.5). It is not possible to measure $P(R)$ directly, because the recorded signal will always be composed of the actual lidar signal and a signal baseline. The baseline itself consists of a background light contribution and an electronic offset. Furthermore, this baseline can be affected by electromagnetic interference (EMI), that is generated when the laser is fired because of the powerful and fast high voltage pulses that are involved. To measure all the various components, several types

[2] Another possibility for the reported laser detuning could be wrong literature values for the line positions. Although this seems to be quite unlikely and all authors consider the line positions given in HITRAN accurate (e.g. [35]), a calibration of the wavemeter by means of a photoacoustic absorption measurement also eliminates this potential source of error.

of signals are recorded.

The signal voltage that is recorded by the data acquisition system (DAQ) after the emission of a laser pulse shall be called $U_{lidar,sig}(R)$:

$$U_{lidar,sig}(R) = q \cdot P(R) + U_{back}(R) + U_{EMI}(R), \tag{3.4}$$

where q stands for the sensitivity (of detector and amplifier), U_{back} for the background signal and U_{EMI} for the EMI signal component. The background signal is composed of the background light component and an electronic offset:

$$U_{back}(R) = q \cdot P_{back}(R) + U_{offs}(R).$$

The background light level can be considered range independent. In our system however, the possibility exists to use a variable attenuator [40] which also imposes an attenuation on the background light. To determine the then range dependent background, the DAQ system and the variable attenuator are started a second time between two laser shots. Then the signal voltage which shall be called $U_{lidar,back}$ is recorded:

$$U_{lidar,back}(R) = U_{back}(R). \tag{3.5}$$

For simplicity, we assume that no EMI component is present in $U_{lidar,back}$. We also include the possibility that the electronic offset U_{offs} has a range dependence, but $U_{offs}(R)$ shall by definition be the same for $U_{lidar,sig}$ and $U_{lidar,back}$. Any difference in the baseline between the two signals shall then be attributed to U_{EMI}. U_{back} can vary due to changes in sky brightness, but because the time between the measurements of $U_{lidar,sig}$ and $U_{lidar,back}$ is short ($25\,\mathrm{ms}$ in our case), it can be regarded identical for the two signals, especially after averaging over many interleaved shots.

All the signals described so far are recorded in the ”lidar” operation mode of the system, i.e. in the usual mode for atmospheric measurements. Therefore the recorded voltages have been assigned the subscript $lidar$. With only the two measurements described in Equations 3.4 and 3.5 the true signal baseline $U_{back}(R) + U_{EMI}(R)$ cannot be determined since U_{EMI} is not known (if U_{EMI} is simply ignored, large systematic errors may result as it will be shown below). Therefore, dedicated measurements in ”EMI” operation mode have to be carried out. Here, the signals are recorded in the usual way, but the laser beam is blocked and not emitted into the atmosphere. The two recorded signal voltages are then:

$$U_{EMI,sig} = U_{back}(R) + U_{EMI}(R)$$

and

$$U_{EMI,back} = U_{back}(R).$$

$U_{EMI}(R)$ can now be calculated by subtracting the two signals. Before this U_{EMI} is used to calculate the signal baseline, it has to be investigated if it is the same as for the lidar measurement or if it may be different due to temporal variations.

During the campaigns in 1999 and 2000, two different types of DAQ systems were used which showed very different behavior with respect to EMI. How the EMI contributions were found and what additional treatment of the raw signals was applied in order to achieve the smallest possible systematic and statistical errors will be described in Section 3.3.1 for the old DAQ system and in Section 3.3.2 for the new one.

3.3.1 DAQ System Used until 1999

Fig 3.16 shows raw signals for online and background ($U_{lidar,sig}(R)$ and $U_{lidar,back}(R)$ according to Equations 3.4 and 3.5) from the small telescope channel recorded with the DAQ system that

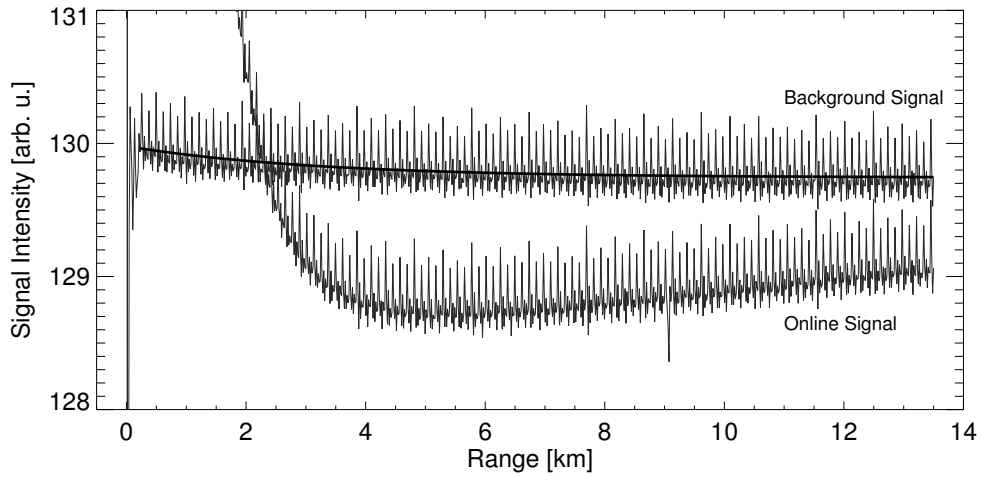

FIGURE 3.16: Raw signal (small telescope), averaged in time over entire datafile (82 min, no averaging in height). The background signal has been fitted with an exponential decay curve.

was used until 1999. The signals have been averaged in time over an entire datafile (82 min) and no averaging in height has been applied. With the statistical noise reduced by the long averaging, two features become apparent:

- Both online and background signal have a regular pattern imprinted on them. This signal contribution is caused by the crosstalk between analog and digital signal lines inside the DAQ system. Because of its distinctive shape, this signal component will in the following be called "comb". Furthermore, the mean background signal level is not constant but shows a slight decay although no variable attenuator was used. These signal components can be attributed to the electronic offset U_{offs}, which can be, and is in this case, height dependent.

- The mean online signal level drops very quickly *below* the background signal level. It is hence obvious that the signal baseline is heavily influenced by EMI and U_{EMI} cannot be ignored. It is probably a coincidence that the EMI-induced offset is negative in this case, but for this particular channel (online, small telescope) the lidar signal decreases so fast, that without any bias the online and the background signal should be identical in the far range. Therefore a positive offset would become apparent as well.

Since the EMI component that was derived from the dedicated EMI measurements proved to be quite stable in time, it could be concluded that it is also a good representation for the EMI component contained in the lidar measurements. In Fig. 3.17A the signal from the online and the background channel from an EMI measurement are shown, again temporally averaged over the whole datafile (100 s). The difference between online and background (Fig. 3.17B) gives the EMI contribution $U_{EMI}(R)$ for the online channel. In order to eliminate additional noise which would be added to the signal when such an EMI curve is subtracted, it was replaced by a smooth third order polynomial fit curve. The same procedure was carried out for the offline channel as well where, somewhat surprisingly, U_{EMI} generally turned out to be slightly different from the online channel.

The range dependent component $U_{offs}(R)$ of the background signal, composed by the "comb" and the decay, which apparently can be quite well approximated by an exponential decay as indicated by the fit curve in Fig. 3.16, does not require a correction if the background subtraction is done point-by-point. This procedure however will add much random noise to the signal. If one assumes that the comb component is constant in time, one can take a different

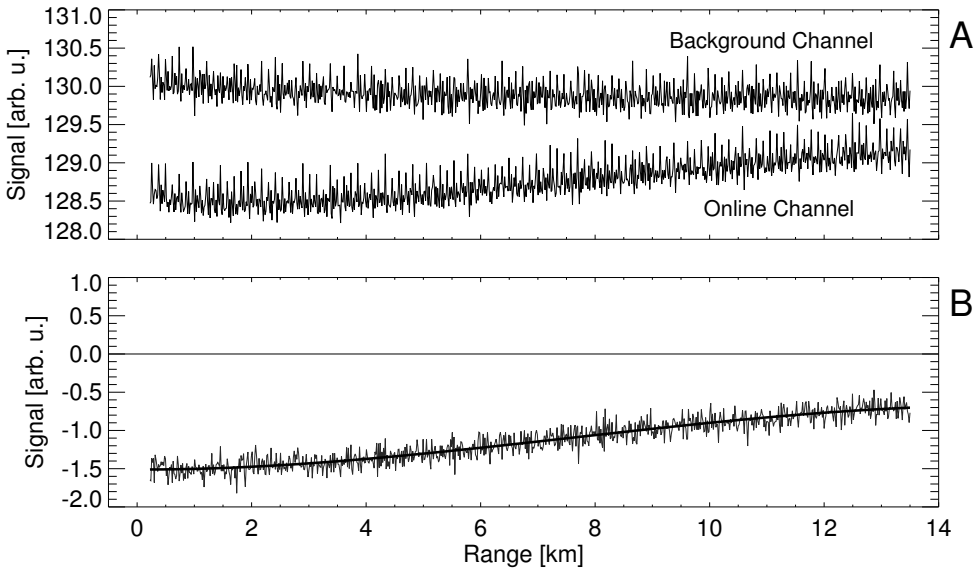

FIGURE 3.17: EMI measurement. Time averaged signal from online and background channel (A). Difference between the two signals and 3rd order polynomial fit (B).

approach in order to minimize the additional noise. By averaging the background over an entire datafile and subtracting a fitted exponential decay, a representation of the comb containing very little noise is generated. This "mean comb" is then subtracted from each individual signal record. After the comb has been removed in this way (which can be verified by calculating the autocorrelation function which will reveal remaining comb-related periodicity even if it is buried in noise), it is possible to replace the noisy background records by smooth, individually fitted exponential decay curves, similar to Fig. 3.16, just that a single background record contains more noise.

The final effect which the described corrections have on the retrieved humidity is shown in Fig 3.18. A mean profile (10 min average, small telescope) from the same datafile as presented in Fig 3.16 has been calculated with and without applying the corrections to the raw signal described above. The systematic difference between the two profiles (Fig 3.18C) which rapidly grows with height (as the raw signal level decreases) is caused by the EMI-induced offset of the signal baseline. The systematic error grows above the acceptable $3\,\%$-level already at a height of 420 m. Below 350 m, the data cannot be used due to the incomplete overlap between laser beam and telescope field of view. If a correction were not possible, practically the entire profile would be rendered useless due to an offset of no more than $0.04\,\%$ of the full signal range of the DAQ system[3]. The amount of EMI induced offset which is still tolerable is hard to quantify, but it is safe to say that the effect will only be negligible if the offset level is significantly smaller than the random noise level at the temporal and spatial averaging chosen for the DIAL inversion. Fig. 3.17A shows that in the case presented here, the offset becomes significantly larger than the random noise already at a resolution of 100 s in time and 15 m in height. For the profiles in Fig. 3.18A, averaging over 600 s and up to 300 m has been applied, yielding an even much lower level of random noise.

The effect which is caused by the replacement of the height-resolved background by a smooth curve becomes evident in Fig 3.18B. The statistical error (calculated from the variance of the 10 s-resolution time series at each height) is reduced. This effect also increases height since the contribution of the background noise becomes more important the smaller the

[3]The unit of the signal intensity in Fig. 3.16 and 3.17 is actually one least significant bit (LSB) of the AD converter. Since this ADC has a resolution of 12 bit, the full signal range goes from 0 to 4095.

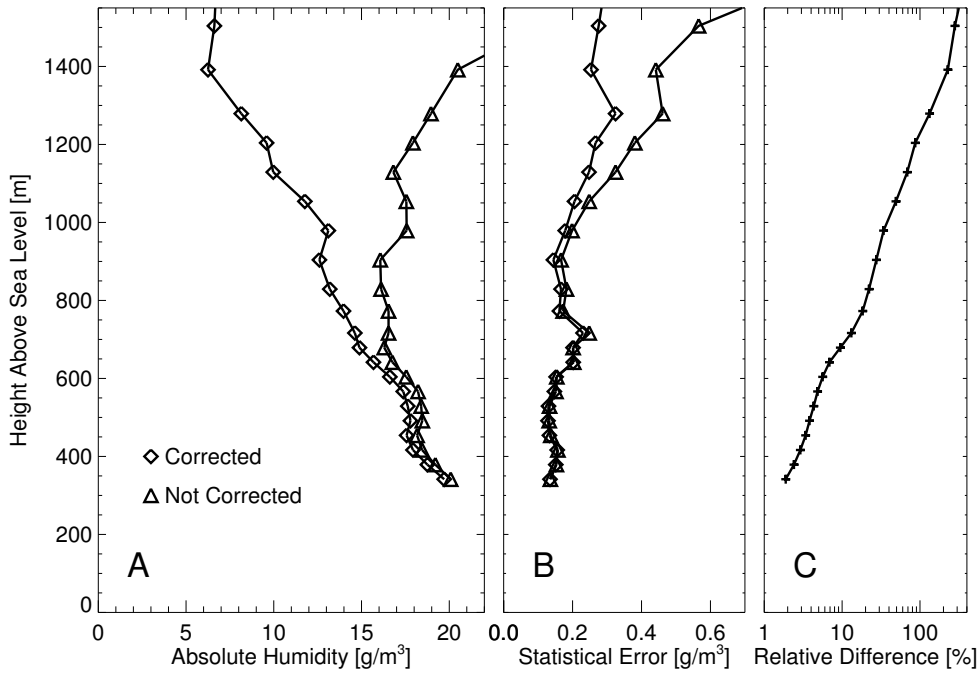

FIGURE 3.18: Absolute humidity profile measured during Nauru99 campaign (small telescope, 10 min average, start 23 Jun 1999, 13:28 UT), with and without the corrections related to signal processing (A), statistical error of the retrieved values (B) and relative difference between the two humidity profiles (C).

lidar signal gets.

A similar behavior with respect to the different signal components, although less pronounced, was also found for the large telescope channel and therefore the same correction procedures were applied, except for the cases where the variable attenuator was used. In these cases, only the EMI correction could be applied but not the described treatment of the background signal.

3.3.2 DAQ System Used from 2000 on

A new, homebuilt DAQ system based on 14-bit AD-converters was used for the field campaigns in 2000. The data presented in this section were collected during the AFWEX campaign. Furthermore, the variable attenuator was used routinely for the large telescope channel. This time, no noticeable comb pattern on the signals could be found and no significant EMI contribution was present in the small telescope channel. For the large telescope channel however, the EMI measurements revealed a significant positive offset which appeared to be height-independent. An example is shown in Fig. 3.19. An explanation for this behavior is probably that the EMI signal U_{EMI} decays on a millisecond timescale so that it appears to be constant within the $102.4\,\mu$s during which the backscatter signal is recorded, but has significantly decreased when the background is measured 25 ms after each laser shot. It also became apparent that the offset levels found in the EMI measurements were strongly related to the detector and preamplifier configuration. In some test measurements the variable attenuator was not used. The preamplifier was then operated at a much lower gain and the EMI-induced offset became significantly lower. The offset vanished completely when a new type of detector with integrated preamplifier (Licel APD) was used. Because of the missing experience and the low signal levels obtained from this detector, it was not used routinely yet.

As opposed to the old DAQ system, the EMI-induced offset appeared to be quite variable and EMI measurements were also not carried out very regularly. Therefore a method was developed to extract the signal offset directly from the lidar data. Since the offset is height independent,

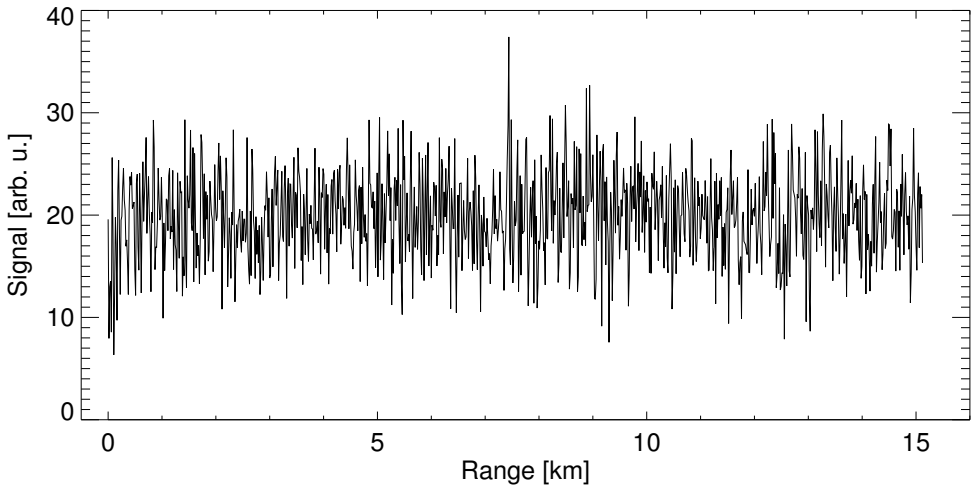

FIGURE 3.19: EMI measurement with the new DAQ system (similar to Fig. 3.17 B)

the easiest would be to take the signal level that remains at the far end of the measurement range after background subtraction as the offset. This however is only possible if there is no more detectable backscatter signal at this altitude. Due to the use of the variable attenuator and other factors (nighttime measurements, reduced signal dynamics due to low aerosol load in the near range), light was indeed still detected even in the online channel up to the maximum range of the DAQ system of 15.4 km, so this simple method could only be applied in the presence of clouds. At very high altitudes though, both water vapor absorption and aerosol backscatter were found to be negligible. The only relevant mechanism determining the shape of the backscatter profile is then the elastic molecular or Rayleigh scattering. If, as it was the case due to regular radiosonde ascents, the pressure and temperature profiles are also known, it is possible to calculate the Rayleigh backscatter and extinction coefficients and hence also the expected shape of the measured backscatter profile.

Fig. 3.20A shows a measured backscatter profile in the $\ln(PR^2)$ representation (logarithm of the range corrected backscatter signal). The data were averaged over the entire datafile (128 min) with no averaging in height. The peculiar shape of the measured profile in the lower range is caused by the variable attenuator. Above about 10 km the transmission of the attenuator does not change anymore. Since only the shape of the profile is of interest (and not the absolute signal level), one has the freedom to multiply the calculated theoretical Rayleigh profile with a constant factor which translates into a constant offset in the $\ln(PR^2)$ representation. The best possible match which can be achieved when U_{EMI} is neglected is shown in Fig. 3.20A. This is done by minimizing the sum of the squared differences in a certain height range (least square method), here between 12 and 15 km. The result is, that the profiles do not agree very well since their slopes are rather different. The agreement can be greatly improved if an additional offset is added to the backscatter signal (to the raw signal, not to the $\ln(PR^2)$) which is varied as well for optimizing the match between the two profiles. The offset which yields the best agreement is then taken to correct the raw signal before the DIAL inversion. Fig. 3.20B. shows the result of this offset correction, now the measured and the calculated profile show very good agreement.

The offset values to the raw signal which were found by this method range up to $0.2\,\%$ of the full signal range of the DAQ system. Apart from the better agreement with the calculated Rayleigh profiles, there are some more points which prove the validity of this method:

- The order of magnitude of the signal offset found agrees well with the level seen in the EMI measurements.
- The method also works for the online channel. The obtained offset levels are similar but

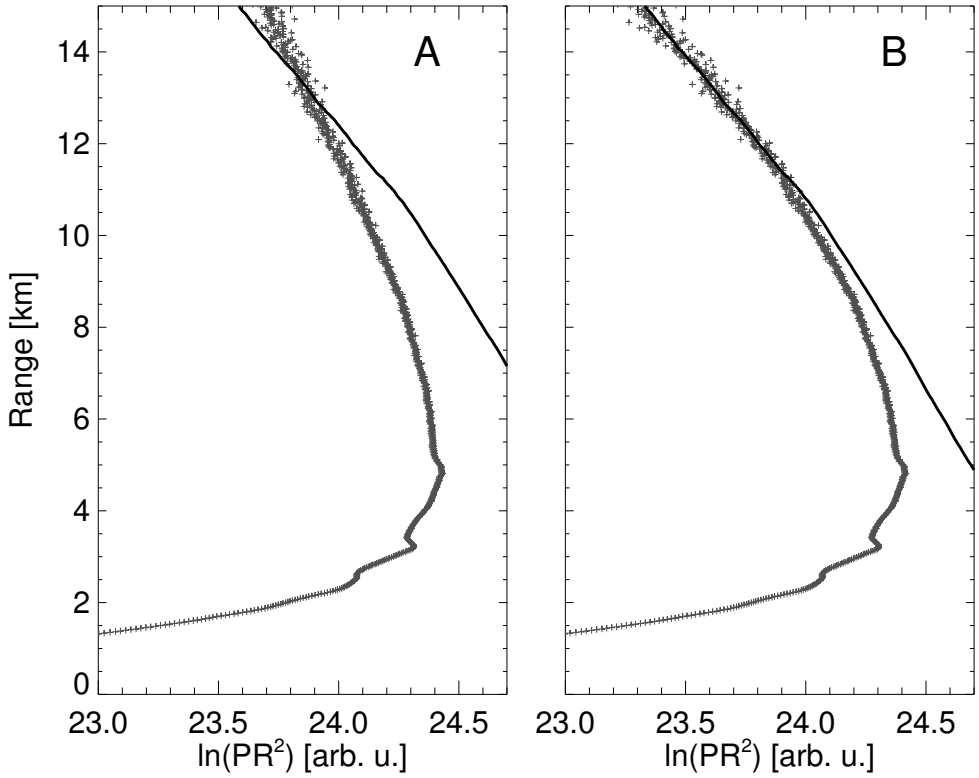

FIGURE 3.20: Attempt to bring measured $\ln(PR^2)$ (offline, crosses) into agreement with calculated Rayleigh profile (solid line), without (A) and with offset correction (B), for details see text.

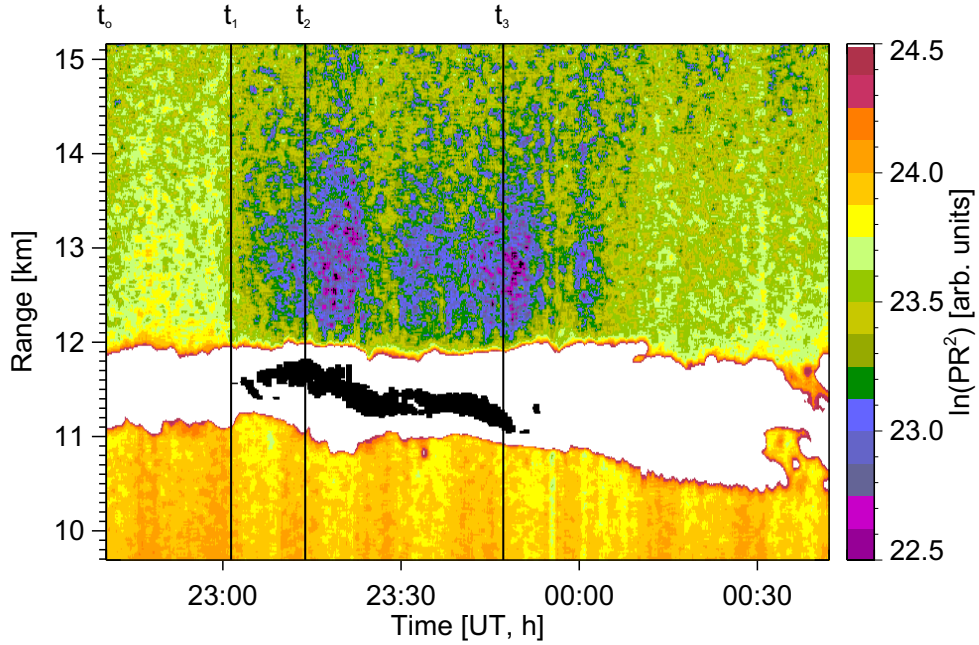

FIGURE 3.21: Time-height plot of $\ln(PR^2)$ containing a cirrus cloud of variable thickness, used to check the validity of the described Rayleigh method for offset correction (see Fig. 3.22). Start of the measurement was on 6 Dec 2000.

slightly different from the offline channel which also agrees well with the EMI measurement results.

- In the case of one measurement, periods both of thin and of thick cirrus were found within the same datafile, as it is shown in Fig. 3.21. The signal from above the thin cirrus clouds was still strong enough to apply the Rayleigh fitting method (period between t_o and t_1 in Fig. 3.21). The offset obtained in this way is very close to the raw signal level found above the thick cirrus (between t_2 and t_3 in Fig. 3.21), as it is illustrated in Fig. 3.22.

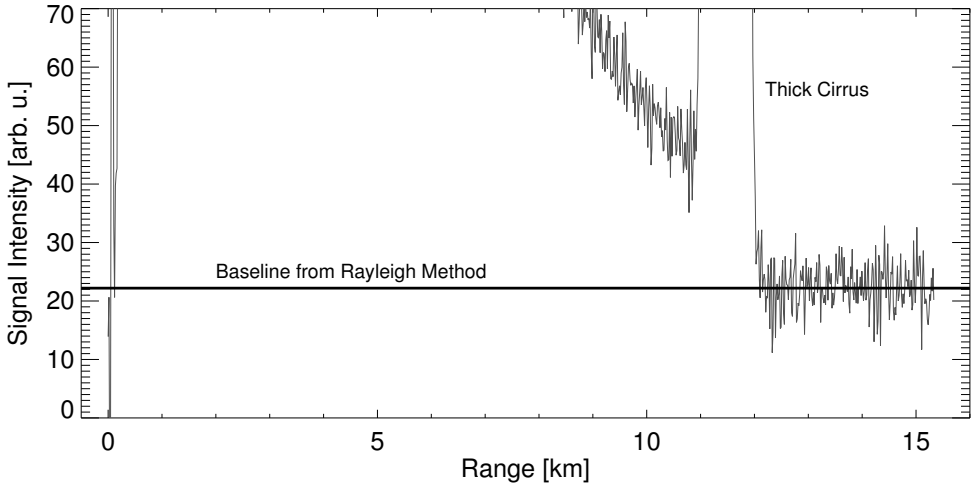

FIGURE 3.22: Raw signal level that is found behind a thick cirrus cloud (between t_2 and t_3 in Fig. 3.21) compared to the signal offset calculated above thin cirrus (between t_o and t_1 in Fig. 3.21) by means of the Rayleigh method.

Fig. 3.23 shows the effect of the described offset correction on the retrieved absolute humidity. This time, the effect is less obvious at first, since the positive offset causes the retrieved humidity to become negative at a certain height. This could also be caused by random errors. A variance analysis however shows, that the relative random error is far below $100\,\%$ above and below the zero-crossing point and that the bias has to be systematic. The bias is effectively removed when the offset correction is applied to the raw signal. The relative difference between uncorrected and corrected signal is shown in Fig. 3.23B. Again the systematic error due to the offset in the signal baseline is below $3\,\%$ only for very few data points (below $2500\,$m), whereas the relative random error (after correction, not shown) stays below $5\,\%$ up to $6000\,$m and below $10\,\%$ up to $7000\,$m.

3.4 Discussion

Apart from the aspects connected to the spectroscopic database and the proper calculation of the differential absorption cross section (Section 3.1), all sources of systematic error in this section result from a bad performance of the lidar system, the laser emitter in particular (Section 3.2). Since we did not anticipate such problems and had no appropriate means of monitoring the system performance or failed to interpret the available information correctly, almost all the results presented here were only found in the course of the data post processing. This had the consequence that large amounts of data had to be discarded. Fortunately, some of the problems found could be corrected for, but especially in the case where the laser operating frequency was detuned far from the absorption line center, the uncertainty of results obtained in such a way will always be higher compared to when the laser operates within the specified limits.

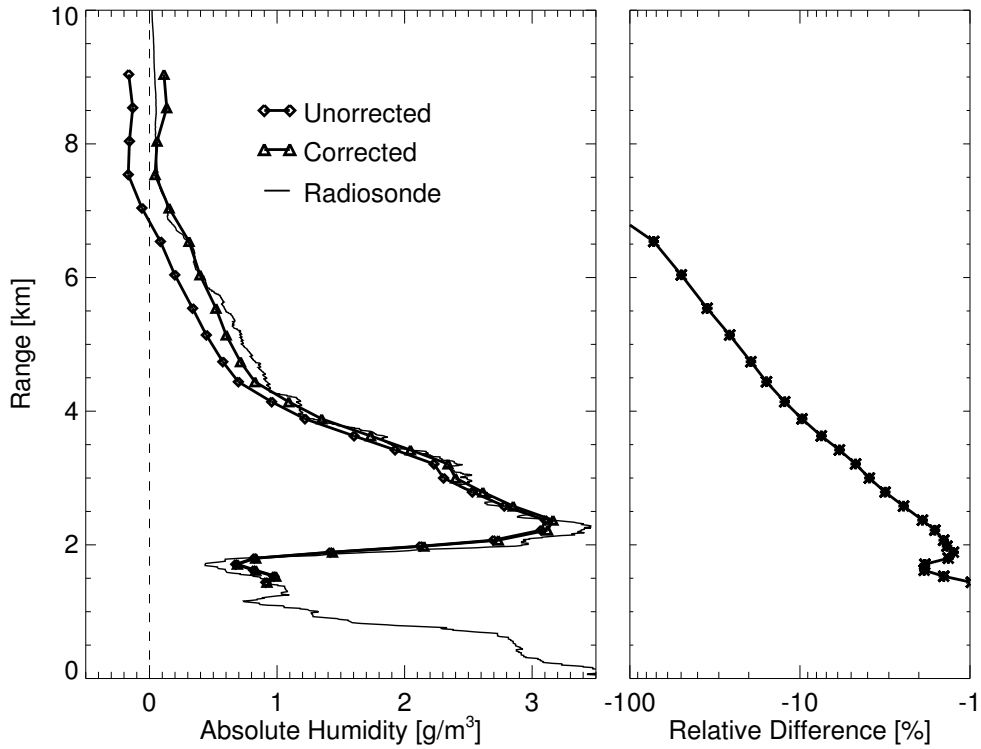

FIGURE 3.23: Absolute humidity profile measured during the AFWEX campaign (large telescope, 15 min average, start 7 Dec 2000, 2:30 UT), with and without offset correction (A). A radiosonde profile is shown for comparison (launch at 2:26 UT). Plot B shows the relative difference between the corrected and uncorrected DIAL profile.

We believe however that we have now identified many (potential) reasons for the problems described. These reasons and the measures for their elimination are the following:

- An additional heating system now maintains a constant temperature inside the container even at very low outside temperatures. This will avoid problems caused by large temperature fluctuations in the container as they occurred during the AFWEX campaign, e.g. the drift of the laser wavelength as shown in Fig. 3.11.

- The calibration of the wavemeter will be checked regularly by means of the described photoacoustic absorption line scan. This will prevent the laser from operating at the wrong frequency due to wrong wavemeter readings. With such a scan it can also be checked if the laser frequency remains constant once online/offline switching is activated, when the wavemeter cannot be used anymore.

- Some modifications were applied to the optical setup to improve the stability of the coupling between master and slave laser. Badly seeded shots as shown in Fig 3.9 are probably due either to a low seed intensity being coupled into the slave resonator or the seed and the slave laser beam going out of alignment. Both can be caused by mechanical drifts.

- The cooling system of the alexandrite laser has also been modified. The temperature of the water which cools the flashlamps and heats the laser crystal is now kept constant within 0.3 K whereas before cyclic variations on the order of 3 K occurred. These variations were presumably the cause of the distortions shown in Fig. 3.7. This effect however probably only started to play a role when the laser was already operating at the edge of stability and was then caused by the temperature variations to drift in and out of this stable region.

- The detector setup which consisted of discrete photo diode, preamplifier and high voltage supply modules will be replaced by integrated packages which appear to be much less susceptible to electromagnetic interference. It should also be attempted to locate the source of the strong electromagnetic fields and then shield it better. A very likely source is the pump chamber of the alexandrite laser with its open lying, unshielded high voltage cables and arc lamps.

Furthermore, the gathered data will in the future be frequently checked during operation in order to identify problems as soon as they arise and not only after the end of a campaign. It has become evident however, that the alexandrite laser is intrinsically not suitable for reliable long term operation. Reasons will be discussed in Chapter 5 where the development of a new laser system will be described.

What has also been demonstrated in the previous section is that the accurate determination of small signal levels is of paramount importance and that this accuracy can especially be compromised by errors in the measured signal baseline. The required accuracy is particularly high for ground based systems. In addition to the geometrical $1/R^2$ dependence, the signal dynamics is further enhanced by the aerosol and water vapor concentrations that usually also decrease with height.

Chapter 4

Selected Results from Field Campaigns

In the following, some results from the field campaigns in 1999 and 2000 will be presented. The data were all recorded with the alexandrite DIAL system and subjected, where applicable, to the control and correction procedures described in Chapter 3. The campaigns cannot be covered in full within the scope of this work, but many results have already been published elsewhere or will be published in the future. References will be given in the appropriate sections. It also must be stressed that the campaigns were a collaborative effort and practically all members of our group at the time participated in the preparation and the carrying out of the campaigns and in the post processing of the data (with the author himself often only to a lesser extent).

4.1 Nauru99

4.1.1 Introduction

The Atmospheric Radiation Measurement Program (ARM) [41,42] seeks to monitor the climate in various areas of the world, one of them being the tropical western Pacific (TWP). A special emphasis is put on radiative transfer processes. For this purpose several so-called Atmospheric Radiation and Cloud Stations (ARCS) have been set up on locations along the equator. The second station which was established in 1999 is the ARCS-2 station located on Nauru island ($0.52°$S, $166.92°$E) [43]. This island is approximately circular in shape with a diameter of about 5 km. Apart from a narrow, few hundred meters wide rim along the coast, it mainly consists of a plateau with a maximum elevation of 65 m where phosphate has been mined and hence very little vegetation exists. A map showing the outline of the island and the position of the ARCS-2 station can be found in Fig. 4.8.

The Nauru99 intensive field campaign took place in June and July 1999 [44, 45]. It involved the ARCS-2 station which had been augmented with additional instruments, the NOAA research ship Ronald H. Brown (or Ron Brown), the Japanese research ship Mirai, and a Cessna 404 aircraft from Flinders University, Adelaide, Australia.

The campaign consisted of three parts (all times referring to the location of the Ron Brown):

- A so-called large triangle period from 23 Jun, 5:00 UT until 30 Jun, 7:00 UT. During this period the Ron Brown was stationed next to a TAO (Tropical Atmosphere Ocean project [46]) observation buoy at $2°$S, $165°$E and the Mirai next to a buoy at $0°$S, $165°$E. The two ships and the island hence formed a triangle with sides approximately 200 km in length, while the aircraft conducted flights along this triangle. The objective of this configuration was to characterize as well as possible the marine climate in an area that corresponds to the size of a grid box of a global climate model, as the gathered data were to be used for a single column model. It was however not stated in what way exactly. A further objective was the intercomparison of ship and buoy measurements.

- A small triangle period where the two ships moved in closer on the island such that their distance was reduced to roughly 50 km. The main purpose of this period was to carry out dual-Doppler studies of precipitation events in the vicinity of Nauru island using the two ships' C-band weather radars. This period lasted from 1 Jul, 8:30 UT until 4 Jul, 0:00 UT. As no precipitation occurred, it was decided to interrupt this configuration for a ship-to-ship intercomparison. So the ships moved close to each other and lay alongside from 3 Jul, 0:00 UT until 3 Jul 5:30 UT.

- Both ships conducted ship-island intercomparisons where the ships took up various positions close to Nauru island. The Mirai did this before the start of the large triangle period, the Ron Brown at the end of the campaign. The ship arrived at the island on 4 Jul, 1:30 UT and conducted measurements in its vicinity until 14 Jul. Another important goal was the investigation of the so-called island effect, i.e. the question whether the measurements taken at the ARCS-2 station are representative for the marine environment or if they are biased by the influence of the island.

The MPI water vapor DIAL system was installed on the Ronald H. Brown. To our knowledge this was the first time that a water vapor DIAL system was operated on board a ship. Apart from contributing to the mission objectives just mentioned, the demonstration of the feasibility of ship based water vapor DIAL measurements was of special interest for us. The measures that were taken to make the system fit for operation under tropical conditions and on board a ship have been described in Section 2.1.

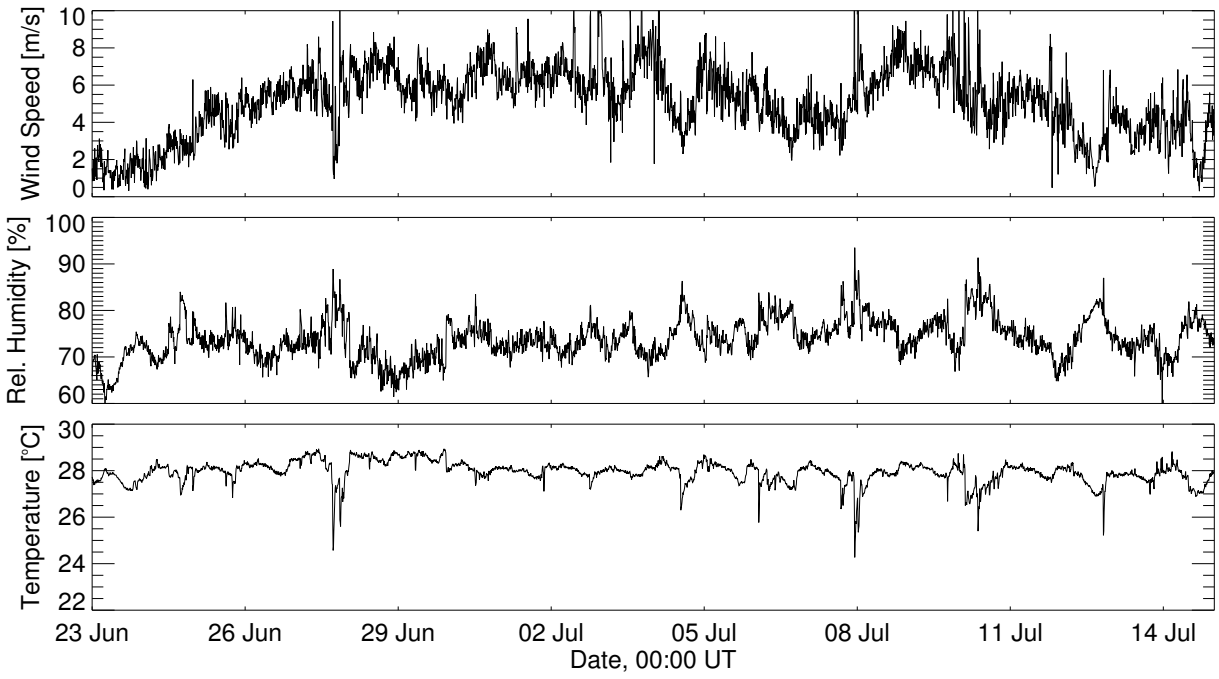

FIGURE 4.1: Temperature, relative humidity and wind speed during the Nauru99 campaign, measured on board the Ron Brown by the ship's own sensors, 15 min averages.

The weather conditions during the campaign were quite stable as it took place during a period of suppressed convection in the Julian-Madden oscillation. Hence very few rain showers occurred and the cloud cover consisted mainly of broken, shallow fair-weather cumulus clouds of varying fraction (see e.g. Fig. 4.2 and Fig. 4.3). Cirrus was frequently present although its base often lay above 13500 m so that it could not be detected by the DIAL system. Time series of temperature, relative humidity, and wind speed are shown in Fig. 4.1. Relative humidity and

temperature varied only in a narrow range, the few sudden drops in measured temperature are associated with rain showers. Also the winds were quite low which facilitated the ship based DIAL operations. For the core period between 23 Jun and 14 Jul there is no indication that the system performance was impaired by too heavy ship motions. Another impression of the atmospheric state during the campaign can be gained from the mean radiosonde profiles shown in Fig. 3.1.

4.1.2 Collection and Processing of a Large Dataset

During the large and the small triangle period it was attempted to keep the system operating around the clock in order to provide a dataset with as few gaps as possible for the projected modeling efforts.

Apart from the regular breaks every 90 to 120 min which were used to back up the data, check the alignment of the system, and conduct the described EMI measurements (see Section 3.3), the dataset shows some more gaps due to technical problems such as power failures and maintenance operations like flashlamp replacements. Some of the data also had to be discarded due to the aforementioned bad laser performance (see e.g. Fig. 3.7). Nevertheless, several days worth of data without major interruptions could be collected. A first period goes from 23 Jun, 00:00 UT until 28 Jun, 00:00 UT and a second period from 1 Jul, 22:00 UT until 4 Jul, 00:00 UT. Many more hours of data were collected on the other days, but then mainly during daytime.

Hence a quite unprecedented amount of data had to be processed. The primary desired product were mean profiles averaged over 5 to 15 min. The automatic generation of profiles for fixed, predetermined time intervals was not practicable due to the irregular breaks and, what is more important, the frequent occurrence of broken low clouds. Only one record (1 record = 10 s) containing a cloud would render an entire profile useless. So an automatic procedure was developed to detect cloud free periods in the measurements and fit profiles into these periods in a way that as much as possible of the 'healthy' data could be used. The procedure works as follows:

- All files are first processed at 10 s temporal resolution, i.e. without averaging in time.
- Each 10 s profile is checked for clouds. A profile is assumed cloud free when all retrieved water vapor values between 800 and 2500 m for the large telescope and between 300 and 1000 m for the small telescope are within a realistic range. The occurrence of clouds quite reliably leads to unrealistically low or high or even undefined humidity values being retrieved. Our DAQ system possesses the unique feature not only to record the sum of the single shot signal values but also the sum of the squared values. The "raw standard deviation" which can be calculated from this parameter can serve as another indicator for clouds, especially at cloud edges where the retrieved humidity values lie within a realistic range but are nevertheless biased due to the high signal dynamics.
- If a cloud free period is at least 31 records long, a mean profile is calculated for this period. When the period is longer than 101 records, it is divided up for the calculation of several profiles. The number of profiles is chosen such that the averaging period for the resulting profiles comes as close as possible to 51 records (the quoted numbers are entirely arbitrary).
- The profiles are calculated in a way that first the raw signal is averaged and then the DIAL inversion is carried out. At the same time a profile of the statistical error is calculated from the standard deviation of the 10 s resolution data. The same height resolution grid is used for the entire campaign.

- Finally the profiles are manually checked for plausibility and parts at the upper and the lower end where the error is too large due to a too small signal or due to incomplete overlap are discarded.

- For visualization in a time-height plot, the profiles are interpolated to a regular grid in time and height. Points which lie more than a certain amount of time outside an interval where a profile was calculated are masked out (5 min for the figures presented here). This method of obtaining and visualizing continuous fields in the presence of irregular breaks and broken clouds will further on be called ”profile interpolation method”.

For two particular days, when the system performance was good and near continuous operation was achieved, different representations of the obtained dataset of mean profiles shall be presented. The first day is 23 Jun, a practically cloud-free day and the second day is 25 Jun where more low clouds and also some middle high clouds were found.

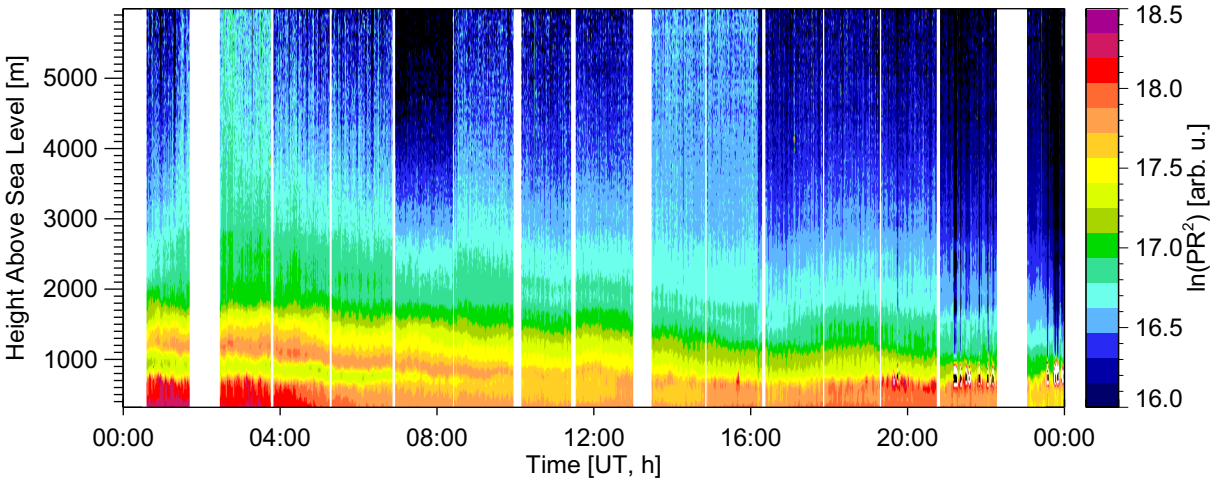

FIGURE 4.2: Time-height plot of $\ln\left(PR^2\right)$ for 23 Jun 1999, small telescope channel, offline

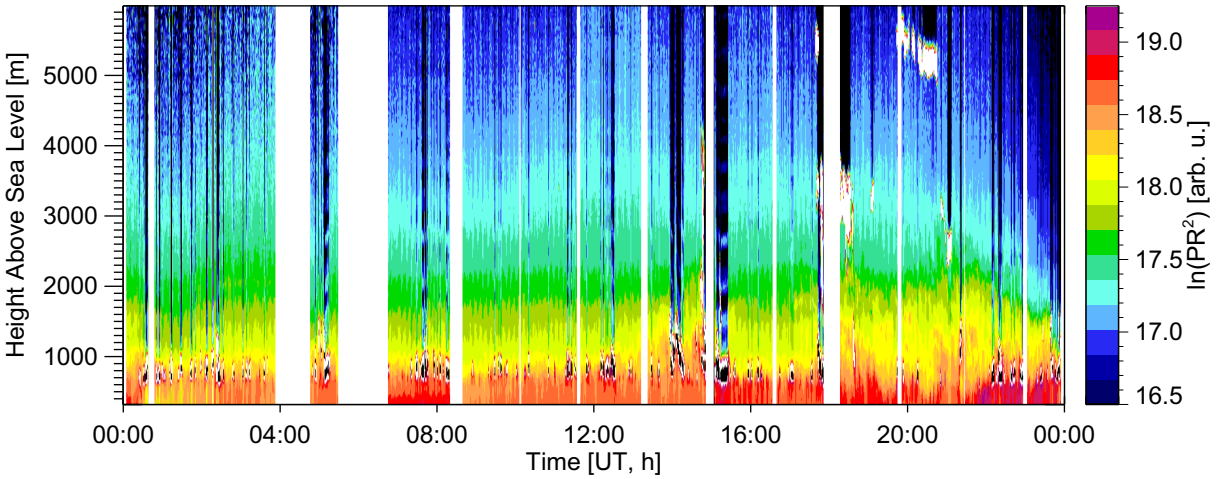

FIGURE 4.3: Time-height plot of $\ln\left(PR^2\right)$ for 25 Jun 1999, small telescope channel, offline

The distribution of clouds, aerosol layers, and the times of operation can be inferred from the time-height plots of the logarithm of the range corrected lidar signal ($\ln\left(PR^2\right)$, offline), shown in Fig. 4.2 and 4.3. Whereas low clouds occur only during the last four hours on 23 Jun,

they can be found throughout the day on 25 Jun. It is interesting to note that no diurnal cycle is visible in the plots (local noon is at around 1:00 UT), neither regarding boundary layer height nor cloud cover. This is due to the fact that the measurements were made at sea, far away from land.

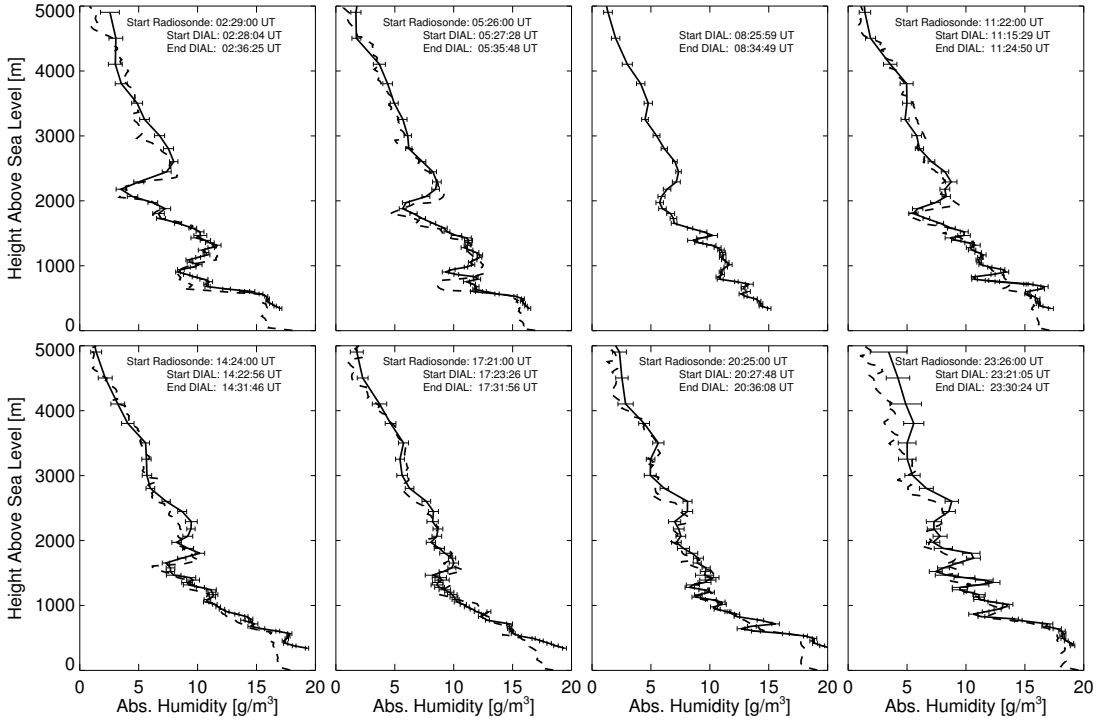

FIGURE 4.4: Profiles of absolute humidity from DIAL measurements (solid line) and radiosondes (dashed line) for all radiosondes launched from the Ron Brown on 23 Jun 1999. The humidity sensor of the sonde launched at 8:30 UT failed.

As frequent balloon soundings were conducted during the campaign, the opportunity exists to compare the automatically generated lidar profiles to radiosonde data. A radiosonde was launched every 3 hours starting at 2:30 UT. Fig. 4.4 and Fig 4.5 show DIAL and radiosonde profiles of absolute humidity for the eight launch times per day. For the DIAL, the profile was chosen whose start of the averaging interval lies closest to the time of the balloon launch. Only profiles were selected that lie no more than 30 min away from the time of the launch. For the radiosonde ascent on 23 Jun, 8:30 UT the humidity sensor failed, so no radiosonde data is shown for this time.

The result of this intercomparison is that the agreement is mostly very good and even at a range of 5000 m the DIAL still produces useful results in some cases. Problems still exist in the near range and in the region around the top of the boundary layer, where the DIAL profiles sometimes show an S-shaped ”hook”. This is probably due to rapid signal changes in these regions which the detector is not able to follow due to a too long response time. The question as to what extent a too slow detector can introduce systematic errors to the calculated humidity is a point which should be investigated more deeply in the future. A faster detector response and a higher sampling rate of the DAQ system may be needed, in particular if the measurement range is to be extended to lower altitudes by using a wider field of view. Apparently the artifacts in regions of steep backscatter gradients are not caused by the Rayleigh-Doppler effect. Attempts to apply the Rayleigh-Doppler correction in the inversion process did not yield an improvement. The increased statistical error which can sometimes be observed is probably due to an increased daylight background, especially in the case of the 7th profile on 25 Jun (start 20:21 UT) which was recorded underneath an altocumulus cloud at about 5500 m.

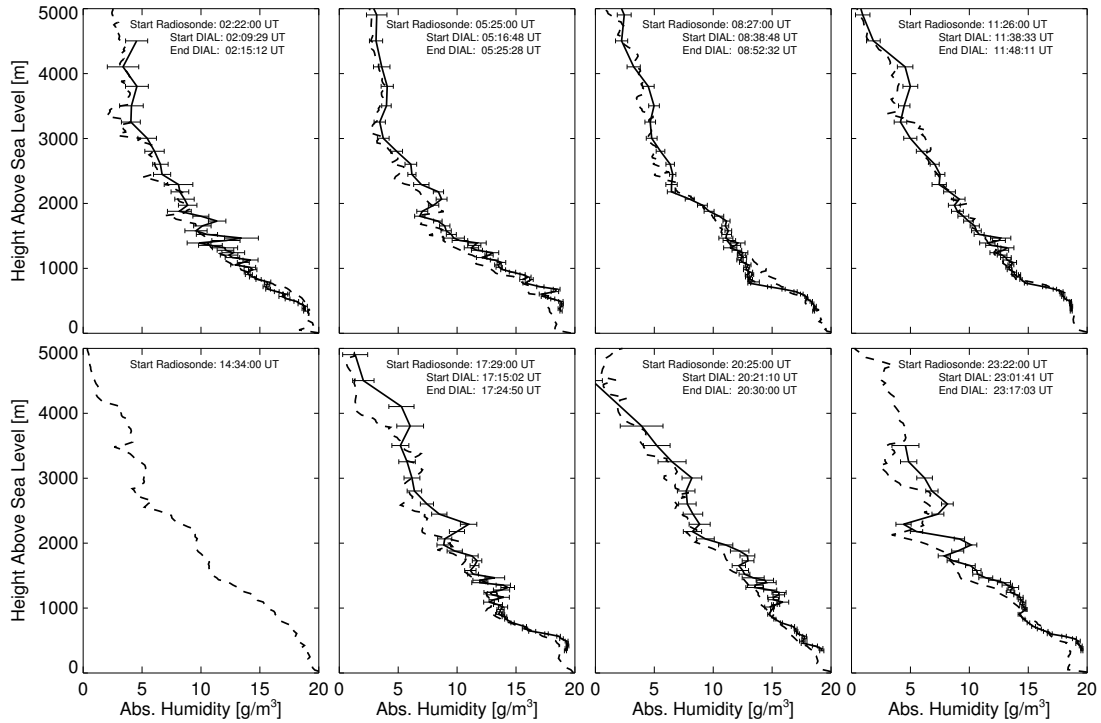

FIGURE 4.5: Profiles of absolute humidity from DIAL measurements (solid line) and radiosondes (dashed line) for all radiosondes launched from the Ron Brown on 25 Jun 1999. For the launch at 14:34 UT no DIAL profile could be calculated.

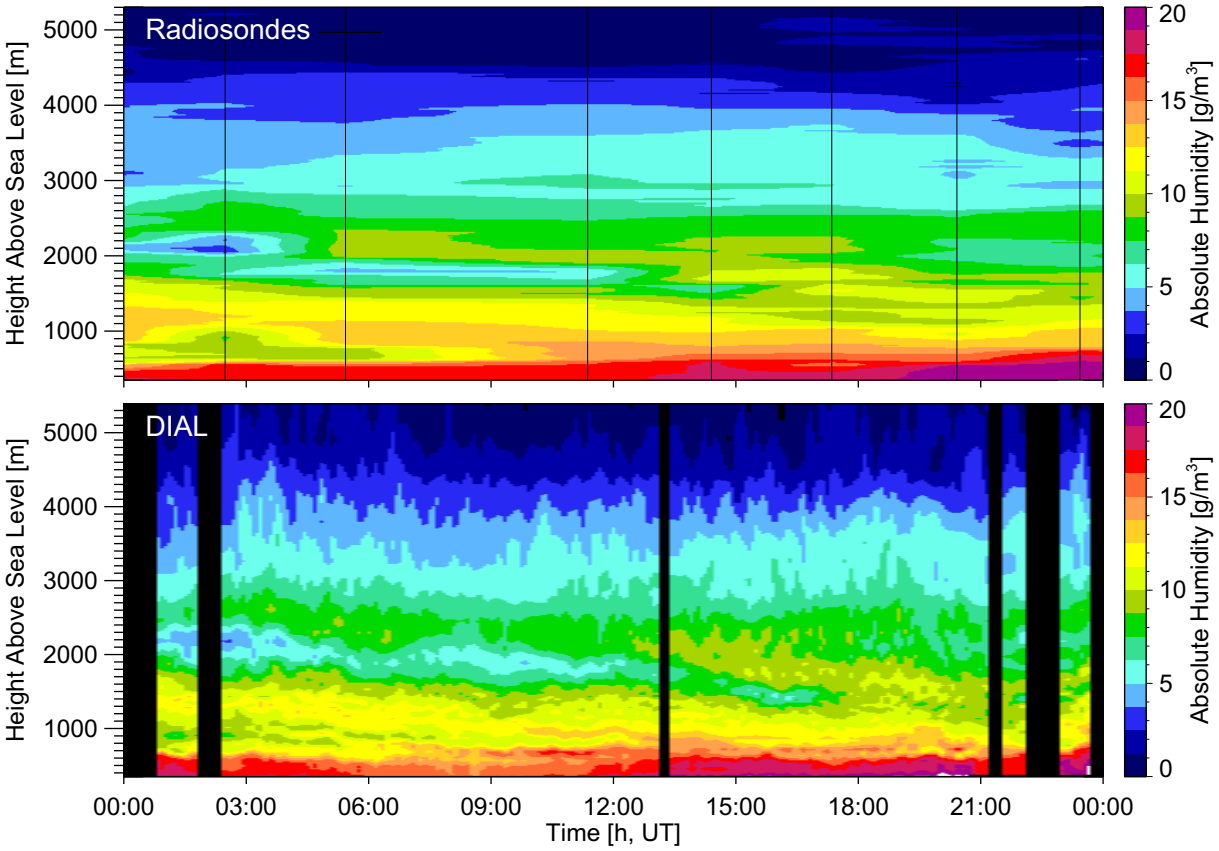

FIGURE 4.6: Interpolated fields of absolute humidity from radiosonde (upper panel) and from DIAL measurements for 23 Jun 1999, measured on board the Ron Brown. Vertical lines in the upper panel indicate radiosonde launch times.

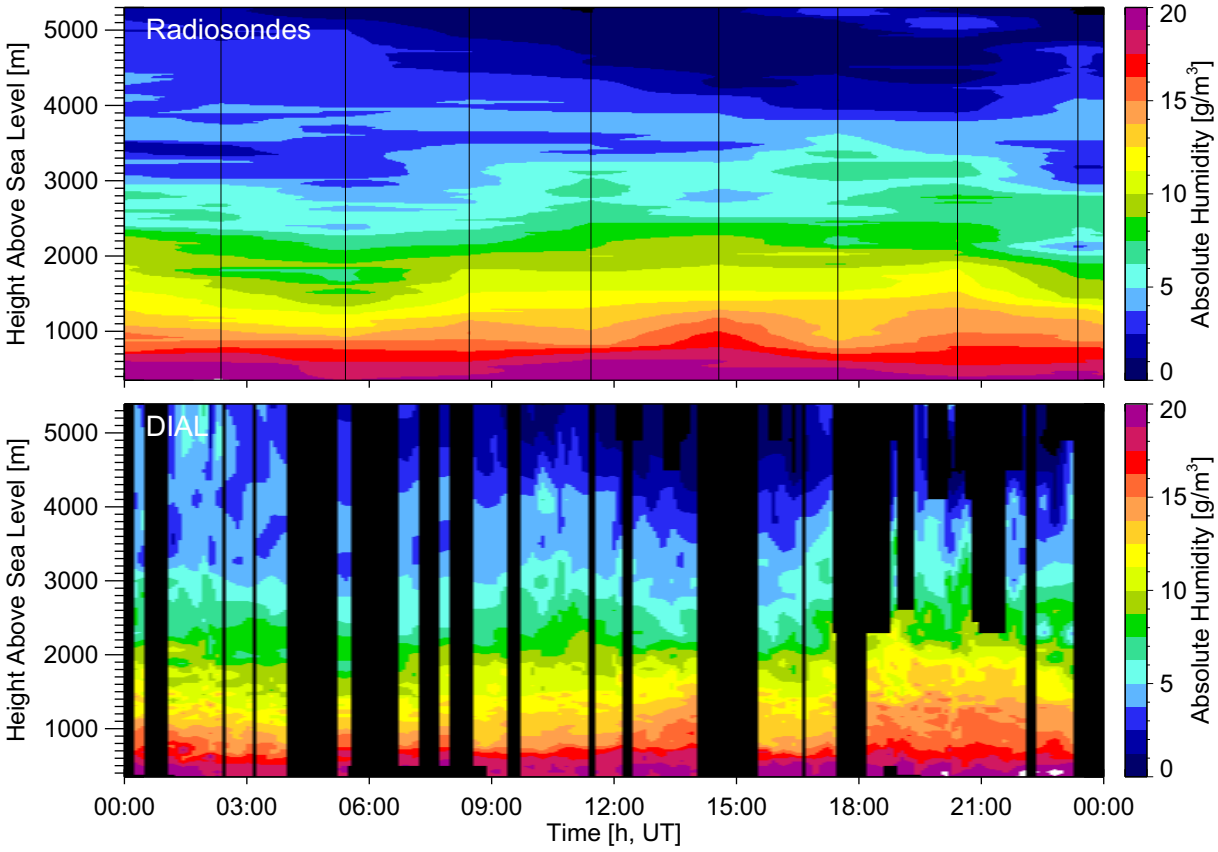

FIGURE 4.7: Interpolated fields of absolute humidity from radiosonde (upper panel) and from DIAL measurements for 25 Jun 1999, measured on board the Ron Brown. Vertical lines in the upper panel indicate radiosonde launch times.

Fig 4.6 and Fig 4.7 finally show time-height plots of absolute humidity generated by the profile interpolation method described above. For comparison, plots are shown that are obtained from the interpolation of radiosonde profiles. The first point to be noted is that the profile interpolation method provides a good way at least for the visualization of DIAL data over longer periods of time and in the presence of irregular gaps due to breaks in operation or due to the presence of broken clouds. The regular fields generated by this method may possibly also serve other purposes, such as the comparison with model results. The way such fields are generated has of course to be kept in mind and it needs to be carefully assessed as to which extent periods containing clouds can be just neglected without introducing a bias to the data. In a convective boundary layer, the humidity below cumulus clouds will certainly be different from the humidity in cloud free parts. If the cumuli are however shallow and the fractional cloud cover is not too high, it should be valid to assume that above such clouds, in the free troposphere, there is no systematic difference in humidity between cloudy and cloud free parts. The second point that is illustrated in Fig. 4.6 and Fig. 4.7 is the fact that the DIAL which delivers continuous data (in this case at a mean resolution of about 8 min) reveals much more detail in the temporal evolution of the water vapor distribution than radiosondes, even if the sondes are launched at an unusually high frequency of eight times per day. At normal observation stations, radiosondes are launched only two times per day.

4.1.3 Island Effect

As stated already in Section 4.1.1, one objective of the campaign was to investigate if the atmospheric parameters measured at the ARCS-2 site are really representative for the open ocean or if the data are biased due to the influence of the island. To investigate the influence of the island on the local atmosphere (the so-called island effect), the ship circled around the island several times at low speed, keeping a distance of about 1.6 km from the shore. This distance was assumed to be small enough to detect an island effect when the ship was passing the downwind or leeward side of the island, i.e. when the air arriving over the ship had to pass over the island first, whereas the atmosphere at the upwind or windward side was assumed to be unaffected by the island. To investigate whether a possible disturbance was caused by the distortion of the flow by the island's orography or if it was due to the heating of the island's surface during the day and the resulting formation of an internal boundary layer, the circumnavigation was started before dawn on 13 Jul at 17:00 UT (corresponding to 14 Jul, 5:00 local). The formation of a thermal boundary layer is likely, due to the lack of vegetation on the island and the resulting large sensible heat flux, whereas the orographic effect was expected to be small due to the island's small size and low elevation.

Each round trip took about two hours and 10 trips were completed altogether so that the last trip was finished on 14 Jul, 14:30 UT. The ship track (reconstructed from GPS data) for one such round trip is presented in Fig. 4.8. The coastline of the island and the position of the ARCS-2 site are also shown. In order to be able to correlate the ship's position with the wind direction, an azimuth angle ϕ_{ship} was introduced which is the angle between North and a line connecting the ship and a fixed point at the center of the island. An azimuth angle ϕ_{wind} (wind direction plus $180°$) was introduced likewise, both angles are illustrated in Fig. 4.8. When $\phi_{ship} = \phi_{wind}$, the ship is located downwind from the island.

In order to get a first overview of the atmospheric structure above the ship during the circumnavigations, a time-height plot of $\partial/\partial R \ln(PR^2)$, the derivative of the logarithm of the range-corrected backscatter signal (from the offline channel) was compiled. This representation is particularly suited to visualize the boundaries of aerosol layers. The plots for the first five round trips are shown in Fig. 4.9, together with graphs of ϕ_{ship} and ϕ_{wind}. The most prominent feature is the top of the boundary layer, represented by the (sometimes broken) dark band

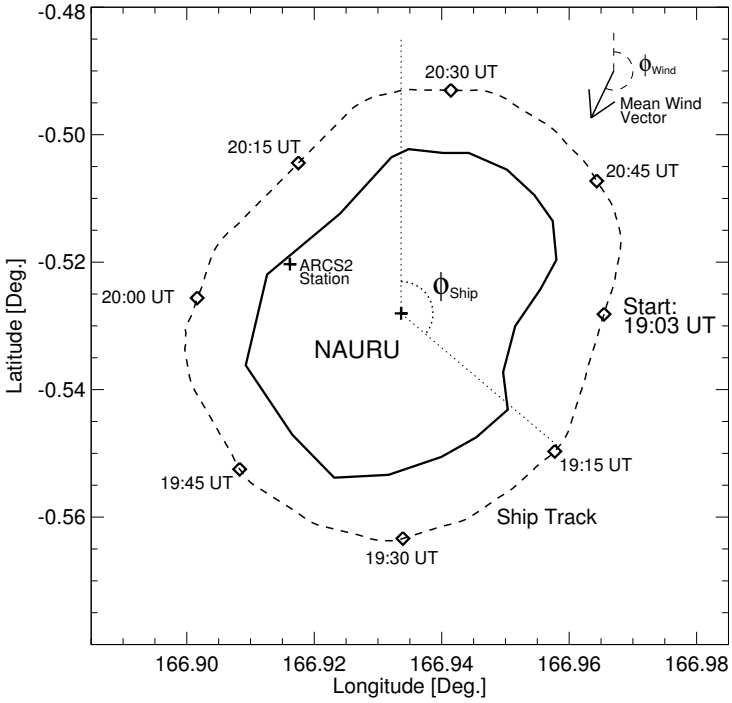

FIGURE 4.8: Ship track for one trip around Nauru island on 13 July 1999. The wind vector shown was calculated from data from the ship's own sensors and averaged for the duration of the round trip.

at around $750\,\mathrm{m}$. Sometimes, small cumulus clouds occur at this height. During the first two round trips (upper part of Fig. 4.9), the time around sunrise at 18:55 UT, no correlation between the ship's position and the lidar signal can be inferred. After 21:00 UT on the other hand a clear change in the structure of the boundary layer can be detected each time the ship passes the downwind side (or "wake") of the island at around 21:30 UT, 23:30 UT, and 1:55 UT. It can also be observed that the effect increases with time, i.e. with the progressive heating of the island's surface. The structure is similar in all three cases: the top of the boundary layer is lowered at the edges of the wake and increased at the center, and an increased level of turbulence is visible inside the wake. In Fig. 4.10 the raw $\ln(PR^2)$ is shown for two passes of the island wake. In this representation it becomes obvious that the disturbance of the boundary layer by the island effect even gives rise to cumulus cloud formation, thin clouds at first that still can be penetrated by the laser beam and later thicker, opaque clouds. This is very likely due to the lifting of moist boundary layer air above the condensation level.

These findings, i.e. the formation of an internal boundary layer over the island due to heat-driven convection and the initiation of cloud formation, were confirmed by the measurements of the scanning HRDL-lidar system on board the Ronald H. Brown and by satellite imagery. The HRDL-lidar conducted continuous elevation angle or RHI scans with the beam pointing perpendicular to the ship track and was thus able to map the aerosol distribution directly over the island [47]. The development of the boundary layer and the wake could be visualized in an impressive way. The evaluation of visible satellite images showed that the island is on many days of the year the starting point for the formation of a cloud street extending up to several hundred kilometers downwind from the island [48].

The phenomenon of cloud formation already presents a potential severe disturbance to the measurements at the ARCS-2 site which is unfortunately located at the western shore of the island, i.e. on the leeward side, since so close to the equator the prevailing wind direction is east. A point of special interest for the DIAL is to investigate what influence the island effect has on the water vapor distribution. Unfortunately the quality of the retrieved water vapor data from

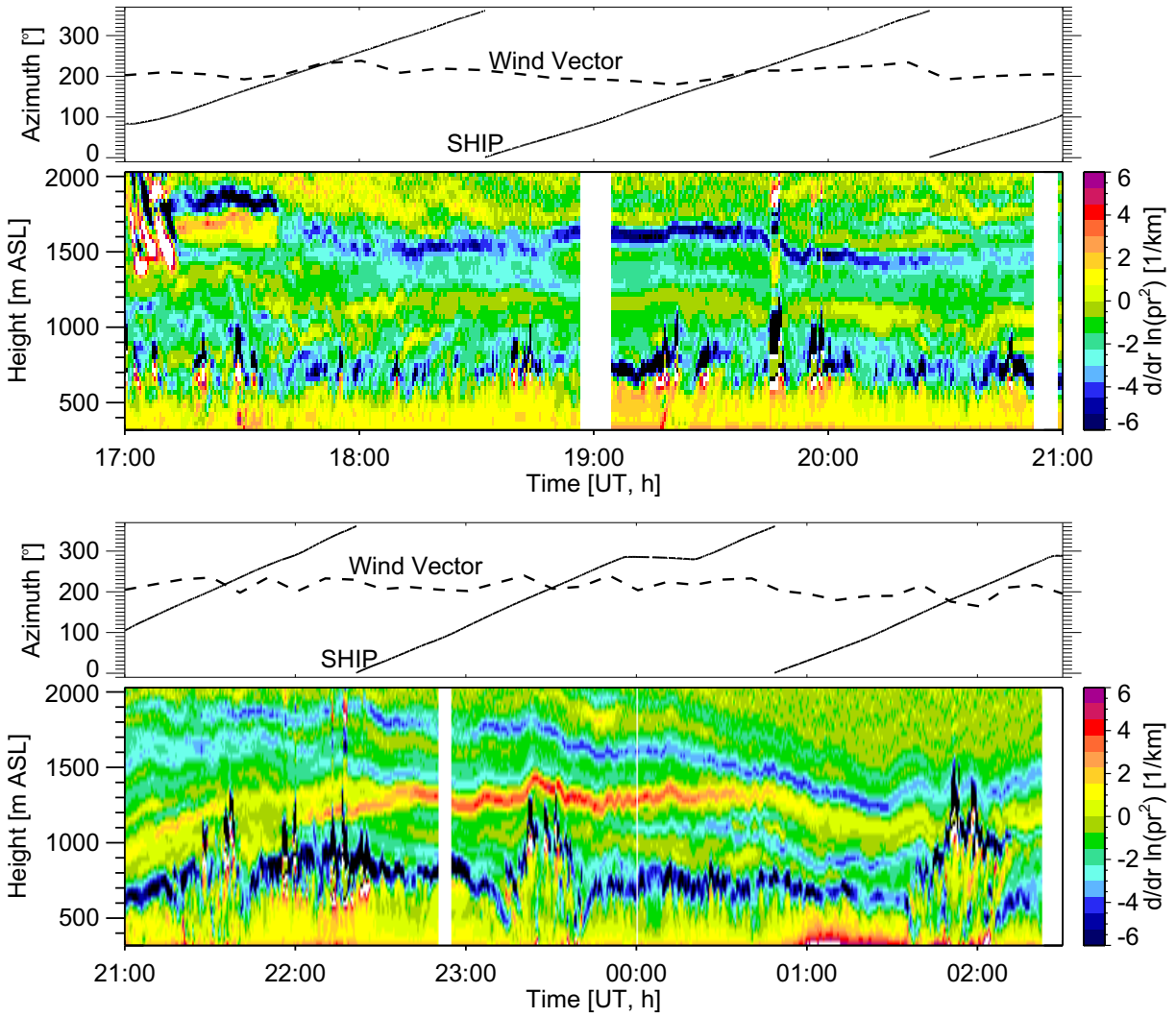

FIGURE 4.9: Time-height plots of $\frac{\partial}{\partial R} \ln(PR^2)$ (offline channel) for the first five circumnavigations of Nauru island starting on 13 Jul, together with plots of the azimuth angles ϕ_{ship} and ϕ_{wind}. For explanations see text and Fig. 4.8.

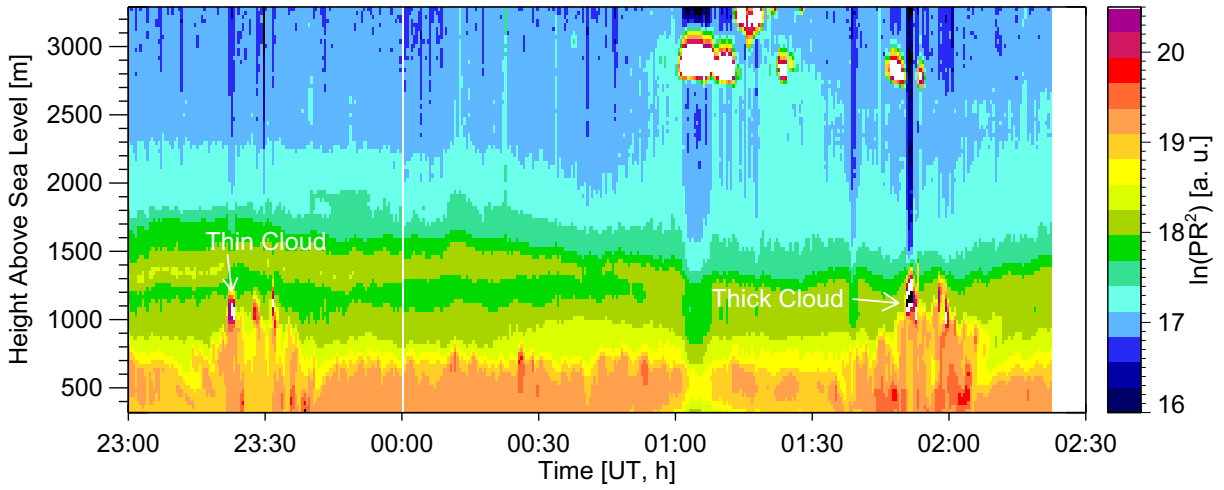

FIGURE 4.10: Time-height plots of $\ln(PR^2)$ (offline channel) for part of the circumnavigations of Nauru island. Each time the ship passes the leeward side of the island, clouds are detected (for a plot of the ship's position over time see Fig. 4.8).

the circumnavigations is not very good due to bad laser performance. Other, so far unknown reasons had the effect that after 14 Jul, 1:00 UT the quality deteriorated even further, resulting in unrealistically high retrieved humidity values and large statistical errors. So the only time the retrieved humidity data lend themselves to a closer investigation of a well formed island plume is at around 23:30 UT. A time-height plot of the absolute humidity from the small telescope channel for this particular passage of the island wake is shown in Fig. 4.11. The same overall

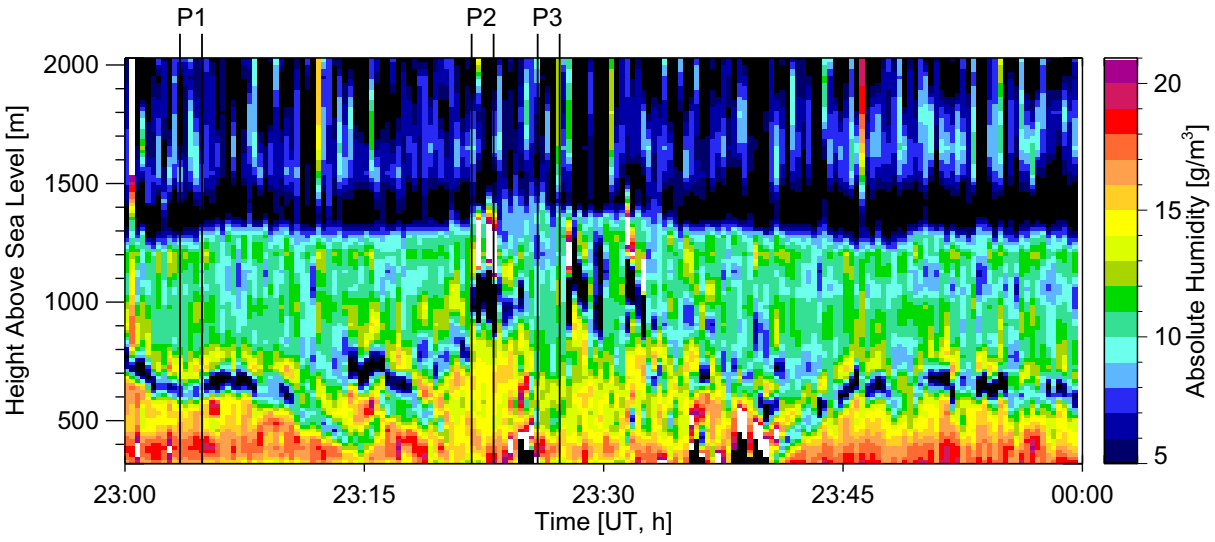

FIGURE 4.11: Time-height plot of the retrieved absolute humidity for part of the circumnavigations of Nauru island (small telescope channel, for a plot of the ship's position over time see Fig. 4.8). The vertical lines indicate time intervals where mean profiles have been calculated (see. Fig. 4.12).

structure as in the backscatter signal can be found. Unfortunately the plot apparently contains some artifacts such as the exaggerated dip in humidity at the top of the boundary layer and invalid values due to signal overload at clouds and in the near range. Some qualitative statements are however possible: the fact that moist air is transported to higher altitudes resulting in cloud formation is confirmed. Between the regions of cloud formation on the other hand, drier air is transported downward. To illustrate this further, three time intervals have been selected for the calculation of mean profiles, these $130\,$s intervals are indicated in Fig. 4.11 and the profiles of mean absolute humidity and humidity fluctuation (the standard deviation of the $10\,$s time series) are shown in Fig 4.12. The first profile represents the unperturbed marine atmosphere. The standard deviation indicates that the top of the boundary layer is located at $650\,$m. The true humidity around the boundary layer top is obscured by the aforementioned artifact. If one assumes that the concentrations inside and above the boundary layer are constant, one would obtain a humidity value of about $16\,$g/m^3 below $650\,$m and $11\,$g/m^3 above. The second profile is located inside a column of moist air inside the island plume, it can only be calculated up to the bottom of the overlying cumulus cloud. It shows that here air with a humidity between 14 and $15\,$g/m^3 is found up to an altitudes of $850\,$m. A profile of the raw $\ln\,(PR^2)$ (not shown) indicates that the cloud base is located at about $1000\,$m, so in fact the transport of moist air should even extend to this altitude. The third profile finally is also located inside the island plume, but in a region of dry air. The boundary between humid and moist air is now pushed down to $450\,$m and the humidity above this level is as low as that found above the boundary layer over the open ocean. This would also result in a reduction of the precipitable water vapor column content of $1\,$mm inside the dry region compared to the open ocean. At a column content of $46\,$mm derived from the radiosonde ascent from the Ron Brown on 13 Jul, 23:30 UT, this corresponds to a reduction of $2\,\%$. It may be possible that this change in the water vapor column content has an

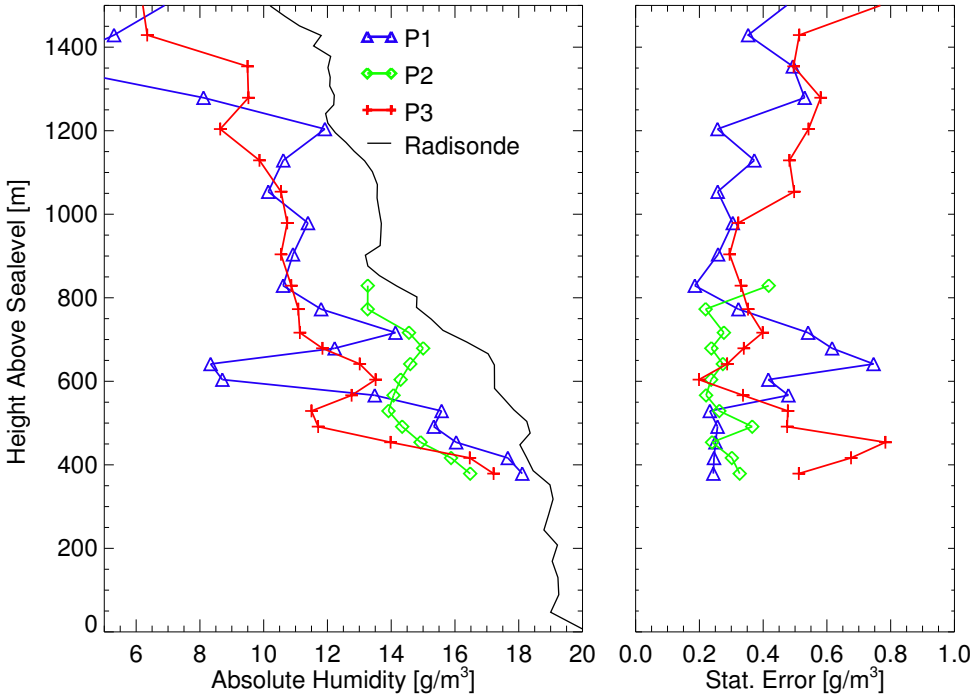

FIGURE 4.12: Mean profiles of absolute humidity and the according statistical error, recorded during the circumnavigations of Nauru island. Profile P1 was recorded over the open ocean, P2 and P3 were recorded inside the island's wake. The times for which the profiles were calculated are indicated in Fig. 4.11, the radiosonde was launched from the Ron Brown at 23:30 UT.

influence on the local radiation budget, but surely not as high as the clouds forming as a result of the island effect. It has indeed been shown that the downwelling shortwave radiation measured at the ARCS-2 site is significantly lower than that measured at the center of the island or off the island's coast on the windward side [49].

4.2 ARM-SGP Campaigns

The ARM program also runs a so-called Cloud and Radiation Testbed (CART) located in the United States' Southern Great Plains (SGP), with various measurement sites in northern Oklahoma and southern Kansas. At the heart of this is the central facility in northern Oklahoma (36.61°N, 97.49°W), a heavily instrumented meteorological observation site [50]. This site played host to three field experiments which all had the purpose of characterizing the water vapor distribution, using different instruments and comparing the results obtained with the different methods. Among the methods were active remote sensing (i.e. lidar, both DIAL and Raman method), passive remote sensing (microwave radiometry, Fourier transform spectroscopy), and in situ measurements (ground based, with balloons, and with aircraft). The first campaign took place in September and October 1999 [51] and had no special name, the second in September and October 2000 and was called WVIOP (water vapor intensive observation period), [52] and the third in November and December 2000 and was called AFWEX (ARM-FIRE water vapor experiment) [53]. Regarding water vapor lidars, the number of participating instruments increased steadily from one campaign to the next. In the first campaign, the MPI alexandrite system and the permanently installed CART Raman lidar (CARL) [54] took part. For WVIOP the NASA-Goddard scanning Raman lidar (SRL) [55] was added and for AFWEX also the NASA LASE (laser remote sensing experiment) system [56], an airborne DIAL system.

An important issue for the campaigns that was already hotly debated during Nauru99 was

a potential (dry) bias in routine radiosonde measurements, not only at high altitudes where the standard RS80 sondes are known to have problems due to the low temperatures ([57] and references therein), but also regarding the integrated column precipitable water vapor (PWV), which is mainly determined by the lower tropospheric humidity [58]. The bias was inferred from comparisons with microwave radiometers. It was discussed if the measured radiosonde humidity profiles should be scaled such that the PWV fits the value obtained by microwave radiometry or if the use of novel RS90 sondes would bring an improvement. Raman lidar can only address the question as to how a systematic error is distributed with height, but cannot help to quantify the absolute value as the measurement itself needs a calibration source. As the radiosonde bias is estimated to be in the order of maximum $10\,\%$, no attempt was made to make a judgment based on the alexandrite DIAL data since the uncertainty remaining with all potential sources of systematic error described in Chapter 3 cannot be regarded as sufficiently small.

Another point was that comparisons with DIAL measurements revealed inconsistencies in the calibration of the CARL instrument. This lidar uses two different modes of operation (daytime mode and nighttime mode) as well as two different receiving channels (near range with a wide field of view and far range with a narrow FOV), but apparently only one calibration value is used, the PWV measured by a microwave radiometer. At first a jump in the humidity time series measured by CARL could be observed that occurred at the time when the system was switched from daytime to nighttime mode. A description and a discussion of this phenomenon can be found in [59] and [60]. The latter publication gives a more detailed description of the calibration procedure and states that the jump in the humidity time series is not only seen in comparison to DIAL, but also to microwave radiometer measurements. Later on, it was also discovered that the humidity measured by CARL not only shows inconsistencies in time but also in height and that a jump in the profile is found at the point where near range and far range channel are merged [61]. In [59] and [60] there is also a comparison of the two systems with respect to statistical error and measurement range both for nighttime and daytime operation. The finding was that the DIAL system achieves lower errors and a greater range than the Raman system during daytime, whereas the Raman system performs better than the DIAL during nighttime. It has to be stressed that for the CARL system already a great effort has been made to enable daytime measurements. Less advanced Raman systems are usually not capable of daytime operation at all.

For the AFWEX campaign, one main focus was put on characterizing the upper tropospheric humidity. This is usually very difficult for ground based DIAL due to the high signal dynamics, especially in the online channel. Usually, much of the water vapor is concentrated in the lower troposphere and the upper troposphere is much drier. The accurate measurement of low water vapor concentrations commands the use of a strong absorption line, but then most of the online radiation is already absorbed in the humid lower troposphere. In addition to that, the aerosol backscatter also usually decreases with height and during daytime the small signals received from the upper troposphere are buried in the daylight background. During the AFWEX campaign however, atmospheric conditions were encountered that were favorable for high reaching DIAL measurements. A mean profile measured under such conditions is shown in Fig. 4.13. Only data from the large telescope channel are shown. The data were averaged over $15\,$min and the height resolution ranges from $60\,$m below an altitude of $1300\,$m asl to $1000\,$m above an altitude of $4000\,$m asl. The elevation of the measurement site is $311\,$m asl. Both humidity and aerosol load in the near range were comparatively low. A tentative calculation using the small telescope channel yields the result that the scattering ratio $\beta_{aerosol}/\beta_{Rayleigh}$ was in the order of one in the near range, decreasing about linearly to zero at $6\,$km. A further increase of the measurement range was brought about by the fact that the measurement was recorded at nighttime (local time is UT minus 5 hours) and that the variable attenuator was used. The fact that the

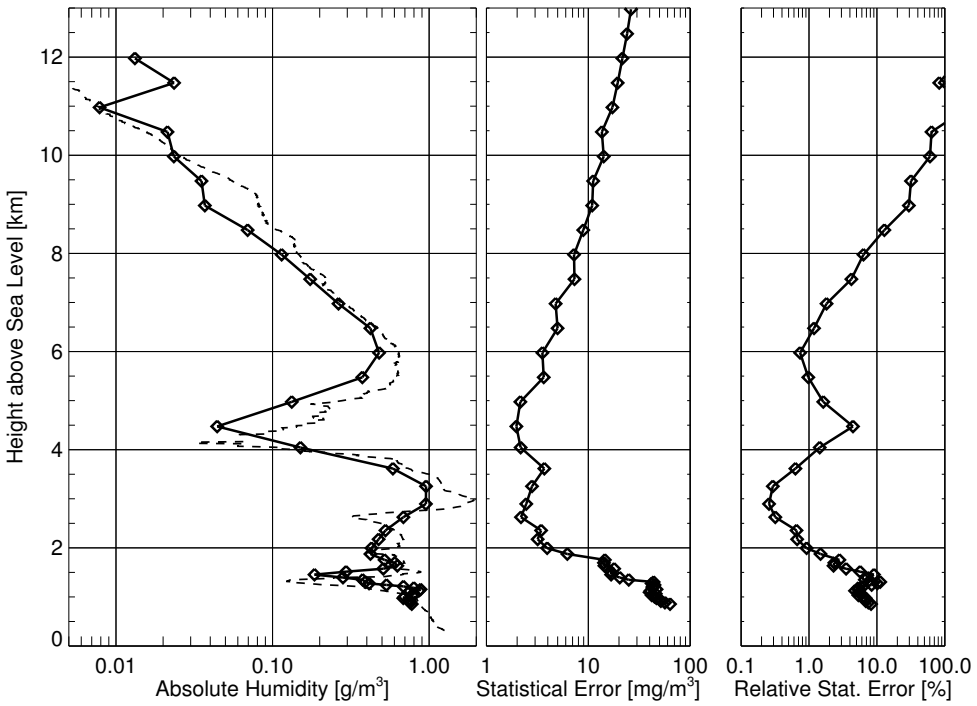

FIGURE 4.13: Mean profile of absolute humidity and the according statistical error measured during the AFWEX campaign. Averaging period is 15 min, start on 12 Dec 2000, 6:24 UT. Also shown is a radiosonde profile (dashed line), the launch was is at 5:30 UT.

DIAL profile measurement shows good agreement with the radiosonde up to a height of 11 km may be a coincidence, but that the relative statistical error stays below 10 % up to a height of 8 km even at these very dry conditions is quite remarkable.

Chapter 5

New Laser System

5.1 Motivation

As laid out in Chapter 1, water vapor DIAL can make valuable contributions to meteorological research regarding long-term observations on a routine basis as well as process studies in the framework of intensive field experiments. The primary prerequisite for this are DIAL systems of high reliability in terms of system availability and measurement accuracy. The results presented in Section 3.2 indicate that our old alexandrite laser based DIAL system does not fulfill these requirements. Even with the measures to improve performance outlined in Section 3.4, there are several reasons why a better alternative should be found:

- The laser is inherently hard to control because the flashlamps deposit a large amount of heat in the laser rod. A rather optimistic estimate for the minimum absorbed pump energy is $25\,\mathrm{J}$ [13]. Small relative fluctuations in pump pulse energy lead thus to large fluctuations in the rod refractive index which depends on temperature. Reasons for the high pump energy are the large pump volume and losses caused by many resonator internal optical elements (at least 22 transmission surfaces plus 4 mirrors).
- The numerous optical surfaces also make the system prone to optical damage.
- The mechanical stability is low because the resonator is very long ($2.5\,\mathrm{m}$).
- The level of maintenance needed is high. This is also one reason why bad laser performance could go unnoticed even during the AFWEX campaign where the necessary monitoring equipment was already in place, since normal operation already takes up so much manpower that it is hard to pay additional attention to unexpected effects.
- The laser electronics are badly engineered by the manufacturing company. The consequences are low reliability, long downtimes and also the EMI problems described in Section 3.3 are partly caused by this. Many components also seem to reach their age limit.
- The system is heavy and consumes lots of space and energy. This is not a real problem for long term operation, although low energy consumption is of course desirable as well, but a more compact system would facilitate the use in field campaigns, especially in remote areas or on board smaller ships.

The expectation that a newly developed laser transmitter would yield substantial improvements compared to the alexandrite system was built on the great progress that has been made in the fields of laser, computer, and signal processing technology over the last years.

5.2 Requirements

Some of the specifications for a DIAL emitter for tropospheric water vapor profiling are listed in Table 3.2. These requirements are mandatory, some freedom exists though for the choice of wavelength, pulse energy, and average power.

Wavelength region Numerous water vapor absorption bands exist in the visible and infrared spectral region. For wavelengths longer than about 1050 nm, the sensitivity of available detectors is very low and since also the Rayleigh scattering cross section decreases as λ^{-4}, measurements in regions of low aerosol content (mainly above the boundary layer) will be very difficult at such wavelengths. The remaining possibilities are the absorption bands around 940 nm, 820 nm and 720 nm. DIAL operation has been demonstrated in all of these spectral regions and none of them offers really decisive advantages for ground based measurements. Therefore, the choice of wavelength can mainly be guided by the availability of suitable laser sources.

Power / Pulse Energy The emitted average power is a primary factor determining the statistical error or signal to noise ratio (SNR) of the received lidar signal, which directly translates to the statistical error of the retrieved humidity. To find out as to what extent the laser pulse energy plays a role for the SNR, let us look at the following considerations: Let N_{laser} be the number of laser photons received from a certain range interval and N_{back} the number of photons from background light. N_{laser} is not measured directly but needs to be calculated as the difference of the total number of photons received and the number of background photons: $N_{laser} = N_{total} - N_{back}$. If the measurement is "shot noise limited", i.e. there are no other sources of noise present which contribute to the overall statistical error, we obtain the following expression for SNR, according to Poisson statistics and the error propagation law:

$$SNR = \frac{N_{laser}}{\sqrt{N_{laser} + 2 \cdot N_{back}}}.$$

We see that the maximum possible SNR is achieved in the presence of no background light: $SNR_{max} = \sqrt{N_{laser}}$. In this case it is of no importance if a certain number of photons is gathered from one pulse of high energy or from many pulses of low energy, and hence only the average laser power is of relevance. To assess the influence of background light, we compare SNR to SNR_{max}:

$$\frac{SNR}{SNR_{max}} = \sqrt{\frac{N_{laser}}{N_{laser} + 2 \cdot N_{back}}} = \sqrt{\frac{\frac{N_{laser}}{N_{back}}}{\frac{N_{laser}}{N_{back}} + 2}}.$$

We have now expressed the dependence of SNR/SNR_{max} on the ratio of N_{laser} and N_{back}. A plot of this function is shown in Fig. 5.1. Since SNR is already referenced to SNR_{max}, this graph directly gives the behavior of the SNR which is achieved for a given averaging time at constant average power and variable pulse energy, which is proportional to N_{laser}. It can be seen that the SNR decreases rapidly once the received light intensity drops below the background intensity. Apart from being proportional to the laser pulse energy, N_{laser} strongly decreases with range. Hence the background light is the ultimate[1] factor which limits the achievable measurement range of a DIAL system and a certain minimum pulse energy is required to achieve a sufficient range.

[1] "Ultimate " meaning that this applies only to the shot noise limited case. In real systems the noise level from other sources (e.g detector and amplifier noise), can be higher than the shot noise of the background light and therefore be the limiting factor for the maximum range. This can especially be the case for nighttime operation. For a comprehensive overview of noise sources and achievable resolution in water vapor DIAL see e.g. [62, 63].

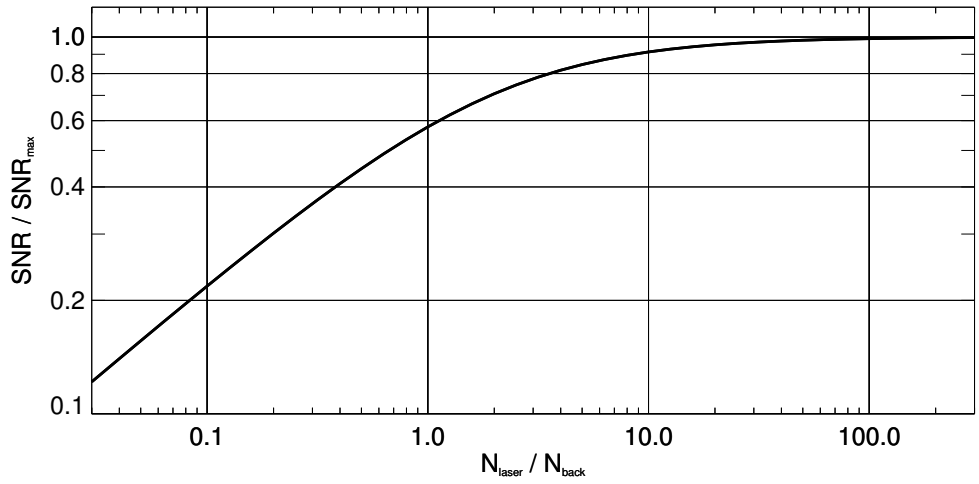

FIGURE 5.1: Reduction of SNR depending on the ratio of signal to background photons, relative to SNR without background (maximum SNR)

Of course both N_{laser} and N_{back} depend on numerous other factors. For N_{laser} this is mainly the strength of the aerosol backscatter and extinction (the term $\beta(R) \cdot \exp\left(-2\,\tau\,(R)\right)$ in Equation 2.1) and for N_{back} these are the bandwidth of the interference filter, the field of view of the telescope, and the sky brightness. However, the ratio of N_{laser} and N_{back} is not influenced by the size of the telescope, the transmission of the receiver optics, and the detector efficiency. The sky brightness depends mainly on the elevation angle of the sun, the cloud cover, and, especially in the near infrared, on the aerosol content. Because of these numerous factors, it is difficult to give a hard figure for the sky brightness. Calculations with the SBDART radiative transfer model [64] suggest that under cloud free conditions the spectral radiance I_ν should only rarely exceed the level of $0.025\,\mathrm{W\,nm^{-1}\,sr^{-1}\,m^{-2}}$ at $\lambda = 820\,\mathrm{nm}$ and a viewing zenith angle of $0°$. The major part of the background light results from solar radiation scattered by aerosol particles and the aerosol load assumed in the default configuration of the SBDART model appears to be quite high (for an aerosol-free atmosphere the obtained radiance is lower by a factor of 7.5). Whereas a high aerosol load was assumed for the calculation of the background light intensity, for a calculation of the intensity of the backscattered laser light an aerosol-free atmosphere was assumed. With a telescope field of view of $1\,\mathrm{mrad}$ (full angle) and a filter bandwidth of $1\,\mathrm{nm}$ one obtains the result that at a laser pulse energy of $6\,\mathrm{mJ}$ the level of the backscattered laser light drops below the background level at a range of $3000\,\mathrm{m}$. So even with a rather high background intensity that results from a high aerosol load, measurements are still possible in aerosol-free regions at a pulse energy of $6\,\mathrm{mJ}$, which is therefore considered to be sufficient. This situation (high aerosol load on one hand and the objective of taking measurements in aerosol-free regions on the other hand) is indeed often encountered, that is when the aerosol is confined to the boundary layer (for an extensive statistical analysis of aerosol distributions over Europe see [7]). In this case however the measurement range is more likely limited by the high signal dynamics caused by the strong decrease of the backscatter coefficient at the boundary layer top rather than by the background light. If however the range is to be extended far above the boundary layer, the backscatter signal from the near range needs to be suppressed by a smaller field of view which in turn also reduces the background intensity. So even then, there is not really a strong need for higher pulse energies.

For a calculation of the necessary average power or the necessary integration time at a given output power, the lidar signal return was modeled for two height levels. The instrument and atmospheric parameters used for this calculation are listed in Table 5.1. The background light intensity was set to zero. Using the formulas for the relative random error in the calculated

Parameter	1st height level	2nd height level
Laser pulse energy	6 mJ	
Laser repetition rate (per channel)	10 Hz	
Laser wavelength	820 nm	
Transmission of optics	30 %	
APD quantum efficiency	80 %	
APD excess noise factor	2	
APD gain	100	
NEP amplifier noise	$1.4 \cdot 10^{-13}$ W Hz$^{-0.5}$	
Telescope diameter	0.28 m	0.4 m
Aerosol lidar ratio	50 sr	
Aerosol backscatter coefficient	$8.0 \cdot 10^{-7}$ m^{-1} sr^{-1}	0
Height above ground	600 m	3000 m
Height resolution	60 m	300 m
Water vapor optical depth in range cell (one way)	0.05	
Water vapor optical depth between ground and height level (one way)	0	1

TABLE 5.1: Parameters used for a model calculation of the DIAL signal statistics. Abbreviations: APD: avalanche photo diode, NEP: noise equivalent power.

absolute humidity from [65], we get the following results: To obtain a random error of 5 %, an averaging time of 0.6 s for the first height level and of 43 s for the second height level is needed. This lies well below the maximum tolerable integration times needed for meteorological applications. So if the assumed detection performance can really be achieved, a total output power in the 120 mW range is already sufficient.

5.3 Possible Laser Sources

In the following, design considerations for a new DIAL laser emitter will be presented, focusing on achieving high reliability and low maintenance at sufficient output power and pulse energy and, if possible, also on compactness and low energy consumption.

5.3.1 Overall Laser System

The requirements for a water vapor DIAL laser transmitter are very demanding as high pulse energies are to be combined with stringent spectral properties (see Table 3.2). A suitable laser system is still not commercially available, so for a homebuilt system at least as many key components as possible should originate from commercial suppliers and be of high technical maturity and proven reliability. Furthermore, proof of principle should have been given by other authors before for a possible concept, in order not to have to break too much new technical ground and to be able to focus on enabling operational use. For maximum stability, the following points shall be part of the overall design concept:

- Frequency control should be accomplished by the injection seeding method: a single frequency cw laser (”master laser” or ”seed laser”) is tuned to and stabilized at the desired wavelength. The light from this laser is coupled into the resonator of the pulsed slave laser. Under certain conditions the slave laser will then acquire the same spectral properties as the master laser and emit single frequency laser pulses. The advantages of this

concept are that frequency control of a cw laser is much easier than for a pulsed laser and also that less or even no optical elements for frequency selection are needed inside the cavity of the pulsed slave laser. This results in a more simple (and compact) setup, higher output power due to lower intra cavity losses, and reduced danger of optical damage.

- The system should be of high passive stability and additionally the most crucial parameters should be actively controlled and monitored. Possible elements for increased passive stability are:
  - A compact and rigid setup
  - Active temperature control of the system environment
  - Isolation from floor vibrations
  - Shielding of the system from dust and other contaminants
- For higher simplicity and easier control, online and offline frequency should not be provided by one master laser which is rapidly switched between the two frequencies but rather by two separate lasers whose outputs are alternatingly coupled into the slave laser.

5.3.2 Master Lasers

The task of the cw master laser is to prescribe the frequency for the slave laser. In terms of stability and absolute accuracy this frequency has to follow the requirements listed in Table 3.2. The tuning range has to extend over all frequencies which are intended for use as online and offline frequency. The radiation from a master laser has to meet some further requirements in order to ensure successful injection seeding of the slave laser:

- The output power has to be sufficiently high. Available publications indicate that for a slave laser of the projected type $1\,\mathrm{mW}$ of seed power is sufficient [66, 67]. Considering the losses caused by optical elements between master and slave laser, the fact that the laser might have to be operated below the maximum power, and also that higher seed power leads to an improved slave laser performance (see Section 5.6), a suitable master laser should at least provide $20\,\mathrm{mW}$ of maximum output power.
- The laser has to operate in single frequency mode which results in a spectral width of no more than few MHz.
- The short term frequency stability has to be significantly better than the $210\,\mathrm{MHz}$ listed in Table 3.2, otherwise it will be difficult to match the cavity length of the slave resonator to the seed frequency. The maximum tolerable amount for such fluctuations depends on the acceptance range in which seeding is still successful. Long term drifts on the other hand can be compensated by a suitable active stabilization scheme.
- Beam profile and pointing stability have to be such that efficient and stable coupling of the beam into a single mode optical fiber is possible. Transporting the seed light via fiber from the master to the slave laser yields a higher modularity of the system and makes a more compact setup possible. Additionally, at the exit of a single mode fiber, beam profile and pointing stability are excellent. This ensures that a high and stable degree of overlap of the seed beam with the fundamental transverse cavity mode, the so-called TEM00 mode, of the slave laser can be achieved, another prerequisite for successful injection seeding.

In certain wavelength regions, all these requirements are met by a special type of diode lasers, so-called external cavity diode lasers (ECDL). Compared to other possible laser types (dye, Ti:Sapphire, OPO etc.) they consume far less power, are far less expensive, more compact, and also offer highly reduced complexity which results in easier operation and higher reliability. Considering these advantages, it is highly desirable to make use of such lasers and the availability of them becomes a primary factor when choosing the wavelength range of the laser system. At present, sufficiently powerful ECDLs only seem to be available for the 820 nm and the 940 nm region, but not for the 720 nm region.

5.3.3 Slave Laser

The task of the slave laser is to "accept" the frequency prescribed by the master laser and emit pulses of sufficient energy and spectral purity. The spectral purity mainly depends on the success of the injection seeding process. The measure of this success, the seed efficiency, can be defined as the ratio of the energy emitted inside the desired spectral interval and the total energy.

The spectral width of the pulses is also mostly determined by the slave laser. In true single frequency operation, the minimum spectral width of the pulse is given by the so-called Fourier limit which results from the Fourier transform of the pulse envelope [68]. For a Fourier limited Gaussian pulse, the pulse length Δt and the spectral width $\Delta\nu$ (both FWHM) are related as: $\Delta t \cdot \Delta\nu = 0.441$. So-called chirp can lead to a broadening of the spectrum above the Fourier limit. Even so, for typical pulse lengths of at least 10 ns for which the Fourier limit is 44 MHz, the spectral width of a single frequency slave laser will very likely always remain below the maximum allowed value of 390 MHz.

We have decided to set up a laser pumped titanium sapphire (Ti:Sa) laser, operating at around 820 nm. This laser and its virtues will be described in detail in Section 5.5. Possible other concepts and the reasons why they were ruled out are the following:

Dye lasers are complex, possess a low spectral purity, and show various other drawbacks, e.g. the laser material is toxic and flammable.

Directly flashlamp pumped lasers: The disadvantages of an alexandrite based system have been described in Section 5.1. The same principle limitations apply to titanium sapphire based systems. Due to the limited market and the small number of manufacturers, the development level and the technical maturity of such systems has to be considered very low.

Diode lasers offer far too low pulse energies. Peak powers are at best in the Watt range. At a pulse length of 200 ns, which is the tolerable maximum in order to achieve a sufficient range resolution, a peak power of 1 W corresponds to a pulse energy of $0.2\,\mu$J.

Directly diode pumped lasers are attractive due to the low power consumption and long lifetime of laser diodes. Since laser diodes should be continuously operated for maximum efficiency[2], the obtainable pulse energy is determined by the upper state lifetime of the

[2]There are pulsed, so-called quasi-cw or qcw laser diodes. Typical qcw 1 cm single stripe emitters offer peak powers of up to 100 W compared to up to 50 W for cw emitters of the same dimensions [69,70,71,72]. This increase in peak power by a factor of only two is accompanied by severe drawbacks. The average power is reduced due to maximum duty cycles of only 2 to $20\,\%$, costs are higher, and the lifetime is significantly shorter (at maximum pulse length and duty cycle the specified minimum lifetime for the qcw model in [69] is only 417 h compared to 10000 h for the cw model). Apart from one exception (Thales Diva, see Section 5.5.1.3), diode *pumped* lasers based on qcw diodes appear not to be commercially available at all to our knowledge.

For an operational ground based system cost efficiency and lifetime are primary concerns, whereas for airborne systems the higher compactness of qcw diode pumped lasers can be an important advantage [73].

laser material. The probably most promising materials for water vapor DIAL applications are Cr:LiSAF and Cr:LiSGaF [74], whose upper state lifetimes ($67\,\mu$s or $88\,\mu$s respectively) are still rather short and laser diodes of the required wavelength and power are available only at a very high price. This is also a quite novel concept which would result in a high development effort of uncertain outcome. A different alternative are diode pumped Nd:YAG lasers. Apart from its principal laser transition at 1064 nm, Nd:YAG also offers (much weaker) transitions at 1112 nm and 1123 nm. The tuning range at each of these wavelengths is about 1 nm and a few water vapor absorption lines can thus be covered. A DIAL system based on this technology was developed in our own group [75]. The goal for this system however was to combine water vapor and wind measurements, using heterodyne detection, in one system. For water vapor measurements alone, the system is far from optimal due to the long wavelength (see Section 5.3.2), the low pulse energy, and the restricted choice of absorption lines. Furthermore, a high pump power is necessary, resulting from the weakness of the laser transition, and sufficiently powerful single frequency diode lasers for injection seeding are not available either. Therefore the advantages of laser diode technology, namely compactness, simplicity, and high energy efficiency, do not apply to the full extent for this system.

Optical parametric oscillators (OPOs) put much higher requirements on the pump laser. Its spectral properties have to be as good as the desired output properties and the beam profile needs to be single transverse mode. This concept is only favorable if operation far away from the gain peak of Ti:Sapphire at 800 nm is needed, e.g. at 940 nm where very strong absorption lines can be found for measurements at very low humidities, e.g. in the tropopause region [73].

5.3.4 Pump Source for the Slave Laser

For the projected Ti:Sa slave laser a pulsed pump laser which emits in the blue-green spectral region is needed. If exotic concepts such as copper vapor lasers are ruled out, the only remaining alternatives are Q-switched, frequency doubled, neodymium (Nd) or ytterbium (Yb) based lasers with an emission wavelength around 520 nm. Both flashlamp (apparently always with Nd:YAG as laser material) and diode pumped versions are available.

As stated in the previous paragraph, the maximum achievable pulse energy for (continuously) diode pumped lasers is limited by the upper state lifetime of the laser material. In the Nd family, Nd:YLF offers the longest lifetime of $525\,\mu$s [76]. Commercially available diode pumped lasers based on this material therefore usually achieve their highest pulse energies at a repetition rate of 1 kHz. The maximum average output power is reached at 3 kHz and it is about 20 to $40\,\%$ higher than at 1 kHz [77, 78, 79, 80]. So for a given minimum pulse energy, the pump laser would yield a comparatively high average power which results in good signal statistics but also in a technically more demanding system and in high costs.

As opposed to the diode pumped models which have entered the market quite recently, flashlamp pumped Nd:YAG lasers have undergone several decades of development and are today produced in series by numerous companies. The technical maturity of this laser type is therefore very high and compactness and efficiency are almost equal to diode pumped systems. The main advantage of this laser is that standard models offer far higher pulse energies at a far lower cost. The usual repetition rates lie between 10 Hz and 50 Hz. The disadvantage of flashlamp pumped Nd:YAG lasers are lower pointing and energy stability, a less well defined beam profile, and a higher level of maintenance. The flashlamps typically need to be replaced after $3 \cdot 10^7$ shots which amounts to 417 h of operation at a repetition rate of 20 Hz or 167 h at 50 Hz. Producers of diode pumped lasers typically claim a lifetime of 5000 h for the pump diodes. For well-engineered lasers though, a flashlamp change is quick and easy and considering the high

price of a new set of pump diodes, the running costs[3] are probably not higher than for diode pumped systems.

Since neither of the two alternatives offers absolutely clear advantages over the other, the decision about the final solution for the pump source was kept open at the beginning of the project and different approaches were tested. This will be described in Section 5.5.1.3.

5.4 Master Laser

Following the considerations in Section 5.3.2 two different models of external cavity diode lasers were tested.

The first model (Toptica DL100), an external cavity laser in Littrow configuration. It yields a high output power, but it proved to be unstable with respect to wavelength and beam pointing direction. Furthermore, the tuning behavior turned out to be rather unpredictable and therefore setting the output frequency to certain value was cumbersome.

The second diode laser is a TEC500 model, manufactured by Sacher Laser. This laser has a grating resonator in Littman configuration, illustrated in Fig. 5.2. In this configuration, as opposed to the Littrow configuration, the beam is not coupled out via a moving element and hence its position remains fixed when the wavelength is changed by tilting the tuning mirror. The fact that some light leaves the resonator unused ("loss beam" in Fig. 5.2) leads to an output power which is reduced by about a factor of two compared to the Littrow configuration. The TEC500 laser was fitted with fiber coupling optics by the company Schäfter&Kirchhoff. These optics include a Faraday isolator for the suppression of back reflections which lead to unstable operation, an anamorphic element for circularization of the elliptic beam profile (this improves the fiber coupling efficiency), and a beam splitter with a second fiber port where a small portion of the radiation is coupled out for frequency control purposes (see Section 5.4.2). Both the tuning behavior and the stability of this laser proved to be far better than for the DL100 model. Therefore only the properties of the TEC500 and not of the DL100 laser shall be discussed further. It is planned to use eventually two TEC500 lasers for both the online and the offline channel. Meanwhile, the TEC500 laser is used for the online channel and the DL100 for the offline channel where the requirements are less stringent.

5.4.1 Tuning Behavior

The main parameter on which the output frequency of the TEC500 laser depends is the angle of the tuning mirror. For coarse adjustment, this angle is set manually by a fine-pitch screw which can be accessed without opening the housing of the laser head. The fine tuning is accomplished by a piezo element. The voltage applied to this piezo can be set manually at the laser supply unit or remotely via an analog input channel. The drive current of the laser diode also influences the laser frequency. This can also be controlled manually or remotely. Since the temperature also has an influence on the output frequency, it is actively controlled via a Peltier element on which the laser resonator is mounted.

Fig. 5.3 shows how the laser frequency depends on piezo voltage and diode current. The voltage was varied across the full possible range, the current in a range that yields a sufficient output power. This so-called modemap shows a regular pattern which is governed by characteristic modehops (sudden changes in the laser frequency).

[3] For the 50 Hz flashlamp pumped Nd:YAG laser, which was finally employed as pump source, the flashlamp costs are about 3 EUR per hour. For the 20 Hz model of the same laser type, the costs are 1.2 EUR per hour. The electric power consumed is about 1 kW, so electricity costs are negligible compared to flashlamp costs. An external supply of cooling water is not needed.

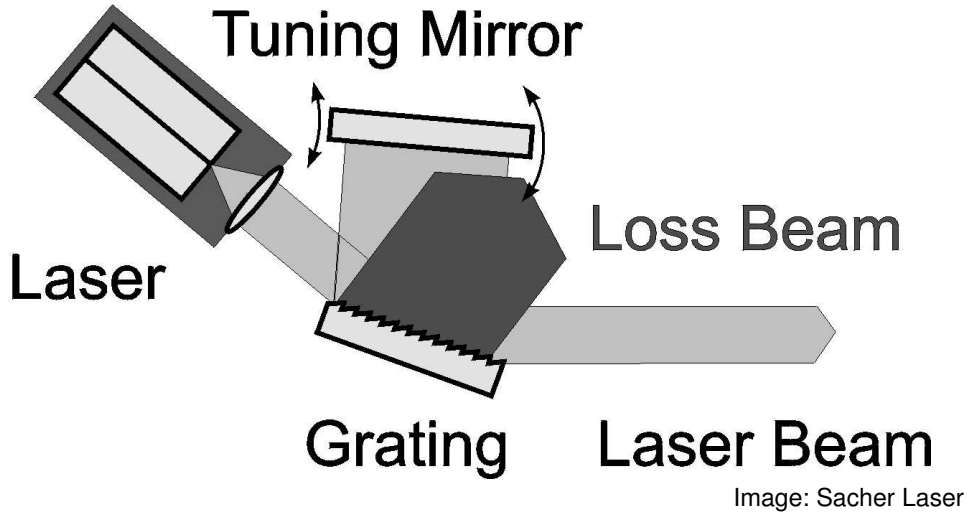

FIGURE 5.2: Schematic setup of the TEC500 master laser: external cavity diode laser in Littman configuration.

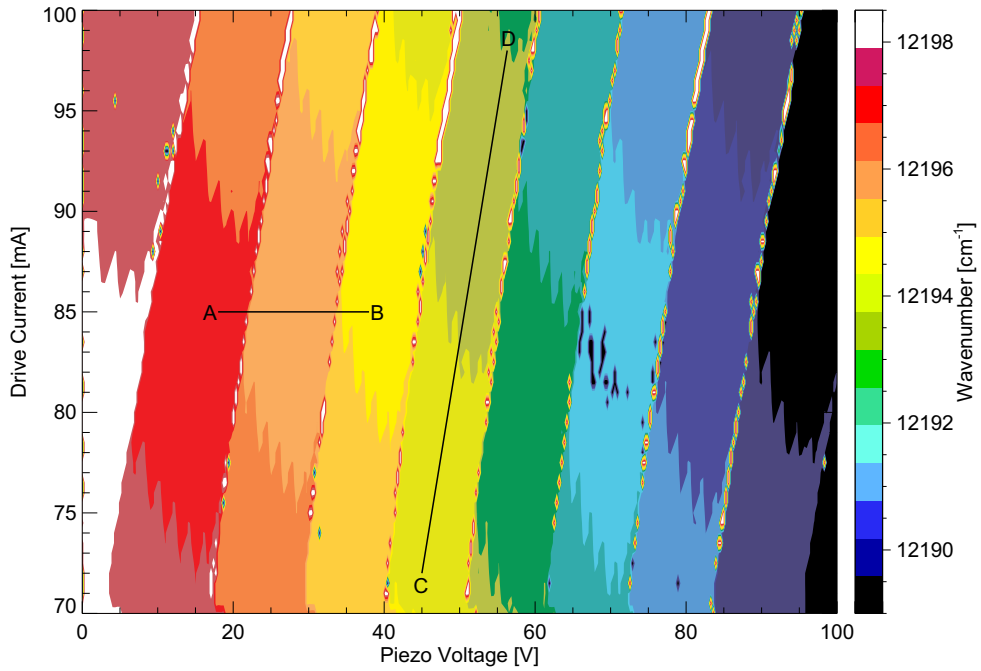

FIGURE 5.3: "Modemap" of the TEC500 master laser: dependence of the laser frequency on the drive current and on the voltage applied to the grating piezo.

To better illustrate the tuning characteristics, Fig. 5.4 shows the behavior of the frequency when the laser is tuned along two different lines in the voltage-current diagram. In Fig. 5.4A, the piezo voltage is varied at a constant current, corresponding to line A-B in Fig. 5.3. The two characteristic mode spacings become apparent. The small mode spacing of about $3\,\mathrm{GHz}$ corresponds to the optical length (or free spectral range) of the entire resonator and the large mode spacing of about $28\,\mathrm{GHz}$ corresponds to the length of the laser diode. Between modehops, the frequency varies at about $-1.8\,\mathrm{GHz/V}$. For modehop free tuning over a wider range, piezo voltage and diode current need to be varied simultaneously along a line which runs parallel to the regions of large modehops. The result of such a measurement is shown in Fig. 5.4B where voltage and current are varied along the line C-D in Fig. 5.3. In this way, modehop free tuning over $30\,\mathrm{GHz}$ is achieved at a rate of $-2.7\,\mathrm{GHz/V}$.

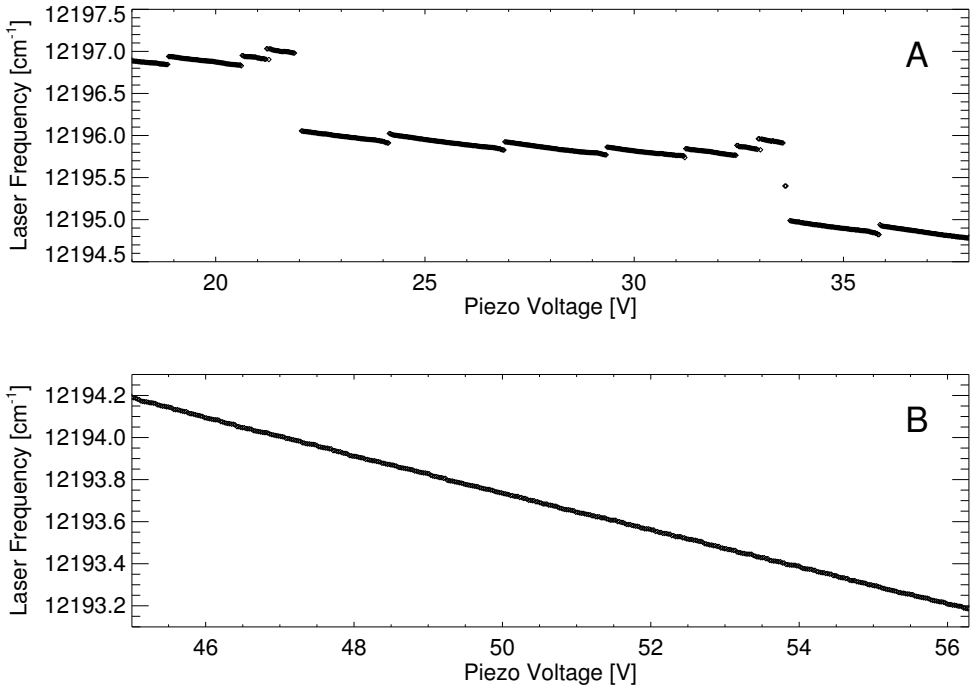

FIGURE 5.4: Tuning behavior of the TEC500 laser. A: piezo voltage is varied at constant drive current (line A-B in Fig. 5.3). B: piezo voltage and drive current are varied at the same time (line C-D in Fig. 5.3).

The frequency range which is covered by remote controlled tuning is $9.5\,\mathrm{cm}^{-1}$ or $0.64\,\mathrm{nm}$. The coarse tuning range of the TEC500 laser goes from 812 to $835\,\mathrm{nm}$ which covers all the absorption lines published in [32] which lie between 813 and $821\,\mathrm{nm}$. With these lines, whose strengths range from 2 to $50 \cdot 10^{-24}\,\mathrm{cm}$, all except the very driest meteorological conditions can be covered. The absorption lines which have so far been selected for use with the newly constructed DIAL system, and for which suitable interference filters have been purchased, are listed in Table A.3. They include the strongest and the weakest available line.

5.4.2 Stability and Accuracy

5.4.2.1 Output Power

As long as modehops do not occur, the output power of a diode laser is inherently very stable. Of more concern is the coupling efficiency into the optical fiber which proved to be very unstable for the Toptica DL100 system. For the TEC500 system, no significant decrease in coupling efficiency could be observed since the system was shipped in December 2001.

5.4.2.2 Accuracy

The device for measuring the frequency of the master laser is an Angstrom WS/7 wavelength meter, manufactured by High Finesse. This Fizeau interferometer based instrument has an optical fiber input and the data is read out via a PCI card which needs to be plugged into a PC running Windows. Stand-alone operation of the instrument is not possible. The laser frequency values which are calculated and displayed by the instrument software can however be accessed by other applications running on the same PC and can also be passed on to other computers via the RS232 interface. The resolution of the wavelength meter is 0.01 pm and the accuracy is specified as 0.07 pm corresponding to 4.5 and 31 MHz respectively at 820 nm.

The instrument needs to be calibrated at regular intervals with a laser of known frequency. Usually a frequency-stabilized helium-neon (HeNe) laser is employed for this purpose. The findings in Section 3.2 however indicate that the best would be to use the water vapor absorption lines themselves as frequency standard. Due to the small line strengths it is technically very demanding to lock the cw master laser directly to the used absorption line[4]. Hence a procedure was developed that is similar to the absorption line scan method for verifying the calibration of the Burleigh WA1500 wavemeter. This method was presented in Section 3.2.2.2. Again, the frequency of the master laser is scanned across an absorption line and the frequency measured by the wavelength meter and the output signal of a photoacoustic absorption cell are recorded simultaneously. Not the output from the master laser itself is sent through the cell, but the pulses from the injection seeded slave laser (see Section 5.6). The result of such a measurement is depicted in Fig. 5.5 where the laser frequency was scanned over the absorption line at $12190.7435\,\mathrm{cm}^{-1}$. The difference of the wavemeter reading at the line center and the literature

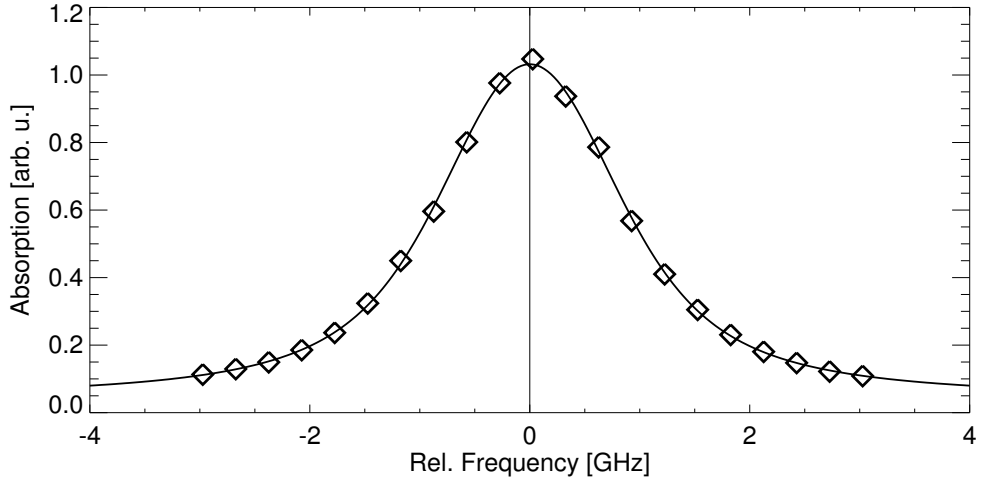

FIGURE 5.5: Photoacoustic absorption measurement (diamonds) for calibration of the WS7 wavelength meter. The center of the absorption profile was determined by fitting a Voigt curve (solid line) to the measured values.

value can then be used to correct the wavemeter readings.

For frequent re-calibrations[5] the scan procedure is somewhat cumbersome. Therefore we use a stabilized HeNe laser (TOPAG LHN-303) whose long term frequency stability is specified to be better than $\pm 2 \cdot 10^{-8}$, or ± 9 MHz. By repeatedly carrying out the described absorption

[4]If a way of locking the seed laser directly to the used absorption line could be found, this would at the same time render the wavelength meter obsolete and only an instrument of much lower accuracy would be needed in order to identify the right absorption line.

[5]The manufacturer specifies that re-calibration of the instrument is needed every one to two months. Or own findings indicate, that a re-calibration every three days is advisable.

line scan using different calibration constants, the best value of the HeNe laser frequency was evaluated to be 473.612704 THz. If this value is used for the calibration routine in the wavemeter software, the difference between the wavemeter reading and the literature value was only 11 MHz at the center of the water vapor absorption line.

5.4.2.3 Frequency Stability

Passive Stability Since the seed laser wavelength is to be actively controlled, only the following considerations are relevant for the passive frequency stability:

- For the active frequency control of the *seed* laser, the frequency is periodically measured by means of the wavemeter and then readjusted accordingly. The maximum frequency drift occurring within such a control cycle must not exceed the allowed range of ± 210 MHz. Usually, the online frequency is measured every 0.5 s. Sometimes though, the online master laser stabilization loop is halted and the wavemeter is used to measure the offline frequency, which causes interruptions of up to 12 s.

- To ensure successful injection seeding, the length of the *slave* resonator needs to be matched to the seed wavelength. Using a special control scheme (see Section 5.6), the slave cavity length is readjusted for every shot of the according wavelength, i.e. with a laser repetition rate of 20 Hz, the readjustment for the online channel is repeated every 0.1 s. Measurements which are presented in Section 5.6.3 show that seeding is successful if the seed frequency and the slave cavity frequency differ by no more than 20 MHz.

Hence the requirements resulting from these two points are a frequency stability of at least ± 210 MHz on a timescale of 12 s in order to keep the output frequency within the specified limit and ± 20 MHz for 0.1 s in order to ensure successful injection seeding. To improve the passive stability of the TEC500 laser, it has been housed in a thermally isolated box. The temperature inside this box is stabilized to at least $\pm 0.1\,^{\circ}$C by means of a thermoelectric air-to-air cooling module (Supercool AA-020) and a Peltier control module (Toptica DTC 100).

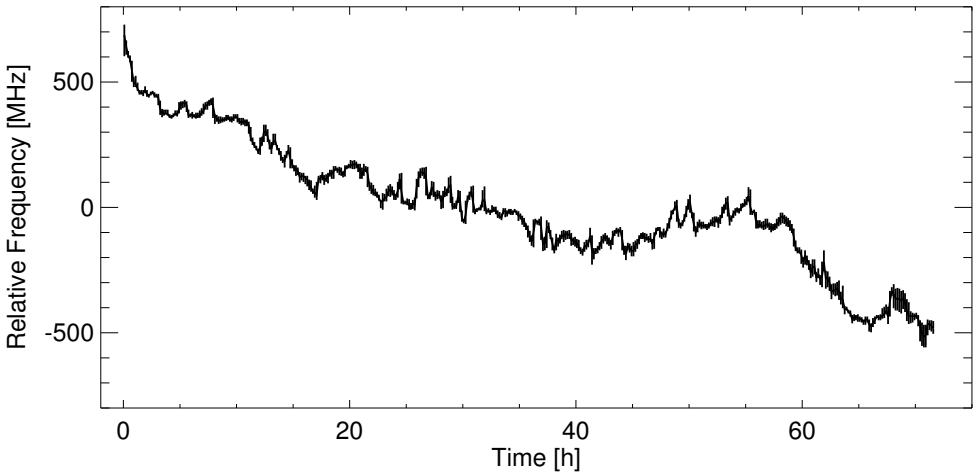

FIGURE 5.6: Long term measurement of the passive frequency stability of the TEC500 seed laser. The sampling period was 2 s.

A recording of the frequency of the non-stabilized TEC500 laser over several days is shown in Fig. 5.6. It can be seen that the longterm drift is rather small. Only during the first hour of the measurement when the laser was still warming up and after 68 h when the laser was apparently getting into an unstable region of operation, do significant drifts or fluctuations occur. If these

parts are excluded from the analysis, the shortest period where the frequency drifted over more than of 210 MHz was 1.75 h and the largest change taking place within 12 s was 36 MHz. Hence the requirement for the "mid-term" stability of ± 210 MHz is certainly fulfilled. Since the data were recorded only every 2 s, it is hard to infer from this measurement if the short term stability is sufficient. This parameter is primarily important in the context of bringing the slave resonator into resonance with the seed frequency in order to achieve injection seeded operation. Whether the stability both of the seed frequency and of the mechanical setup are sufficient for this purpose will therefore be discussed in the according Section 5.6.

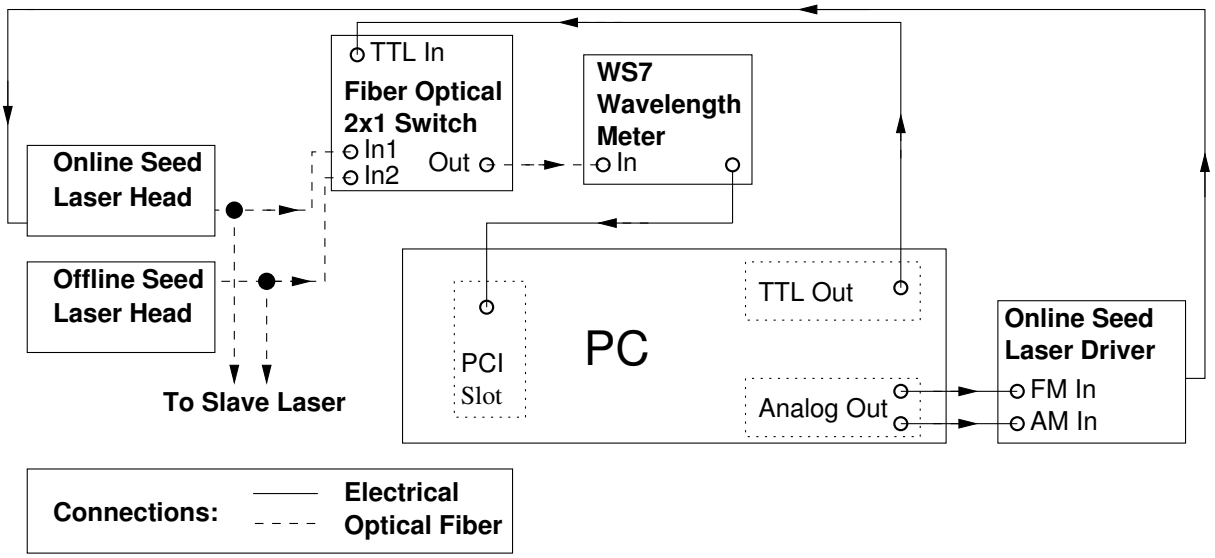

FIGURE 5.7: Schematic sketch of the hardware setup of the seed laser frequency stabilization. Abbreviations: FM: frequency modulation, AM: amplitude modulation

Active Stabilization The setup for the active stabilization of the online frequency is sketched in Fig. 5.7. Regarding the *offline* seed laser, the setup described here only serves to monitor its frequency at regular intervals. The active control of the offline frequency is part of the slave laser stabilization mechanism, which will be described in Section 5.6.2.

At the center of the setup is a personal computer incorporating the PCI interface card of the wavelength meter, an analog-digital multi-IO card (National Instruments PCI-MIO 16E1), and an additional analog output card (Adlink PCI-6208V). The control software running on the PC is implemented in LabView. From each seed laser, about one per cent of the light intensity is tapped from the output by a fiber optic beam splitter and routed to a 2x1 fiber optic switch (Sercalo 2x1). This switch is operated by a TTL signal sent out from the PC and it selects the wavelength that is routed to the wavelength meter. Most of the time, the online seed laser is selected. Its laser frequency is measured and compared to the set value. The control signal sent to the laser driving electronics is calculated by a PI-algorithm. Every two minutes the stabilization loop is halted and the offline wavelength is measured for two seconds. The resulting gaps of up to 12 s mentioned above are due to the fact that the wavelength meter needs some time to adjust itself to the different light intensity levels of the two wavelengths.

Since the same PC is also responsible for the stabilization of the slave laser cavity (see Section 5.6.2), which requires a large amount of computing power, the seed wavelength control loop is gone through only once every 0.5 s although up to 50 measurements per second can be taken by the wavelength meter. For monitoring purposes, the values of the measured frequencies and the control signal are stored on hard disk.

In Section 5.4.1 it has been shown that the frequency of the TEC500 laser depends both on the applied tuning piezo voltage and on the diode current. The according inputs have been named ”FM in” and ”AM in” respectively in Fig. 5.7, since the piezo voltage acts primarily on the laser frequency and diode current on the output power. In order to evaluate in which way these two parameters have to be varied to achieve the best frequency stability, the nature of the frequency drifts which the control loop has to compensate was investigated. Therefore, modemaps similar to that shown in Fig. 5.3 were recorded at different times after the laser had been switched on. The result is shown in Fig 5.8 where a section of the modemap is

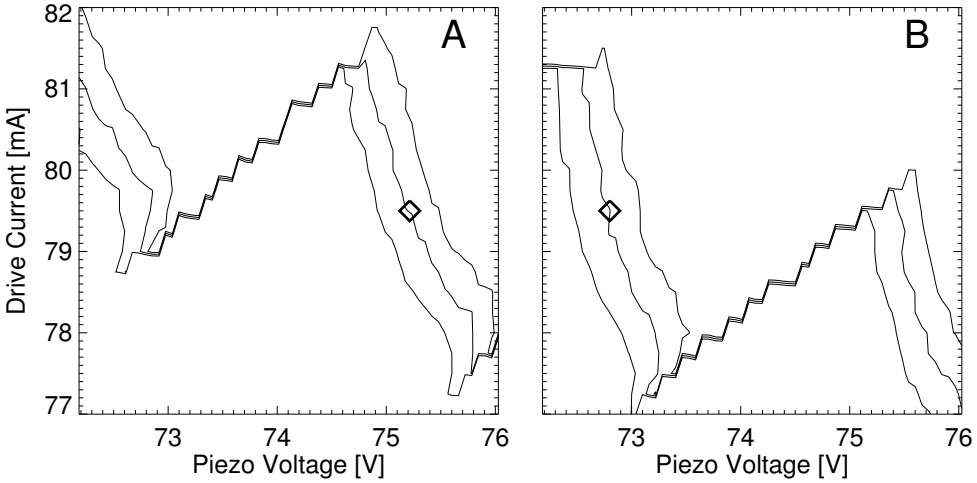

FIGURE 5.8: Section of the modemap of the TEC500 laser recorded immediately after switching on the laser (A) and 34 min later (B). Shown are isolines for 3 different frequencies 300 MHz apart and a possible set point (square).

plotted in an isoline representation. It can be seen that the pattern shifts along a line of constant current which indicates that the frequency drift is caused by a varying tuning mirror angle, probably due to creep of the piezo element. Therefore, only the piezo voltage is varied for the frequency stabilization and the drive current is kept constant. Time series of the stabilized laser frequency and the according control signal are shown in Fig. 5.9. Other measurements exist, where the frequency could be stabilized over more than 60 h, but in the case here the final soft and hardware setup was used, in which the control loops for seed and slave laser were run in parallel and the offline frequency was regularly monitored as well. The maximum deviation from the set frequency, the absorption line center at $12190.774\,\mathrm{cm}^{-1}$, was 57 MHz and the RMS (root mean square) deviation was 9 Mhz. The range which is spanned by the control signal corresponds to a frequency change of 530 Mhz (see Section 5.4.1) and the pronounced dips are probably due to sudden changes in the room temperature due to the starting air conditioning.

The conclusion which can be drawn from the investigations of both passive and active stability is that the passive stability, even with the additional thermal stabilization of the seed laser, is not sufficient for continuous operation over many hours and that active control is definitely needed. The frequency stability achieved with the active control loop however greatly exceeds the required level.

5.5 Slave Laser

Following the considerations in Section 5.3.3, it was decided to set up an injection seeded Ti:Sa laser. The laser will be a gain-switched ring laser. Gain switching occurs if the pump laser pulse is much shorter than the lifetime of the upper laser level. This results in the emission

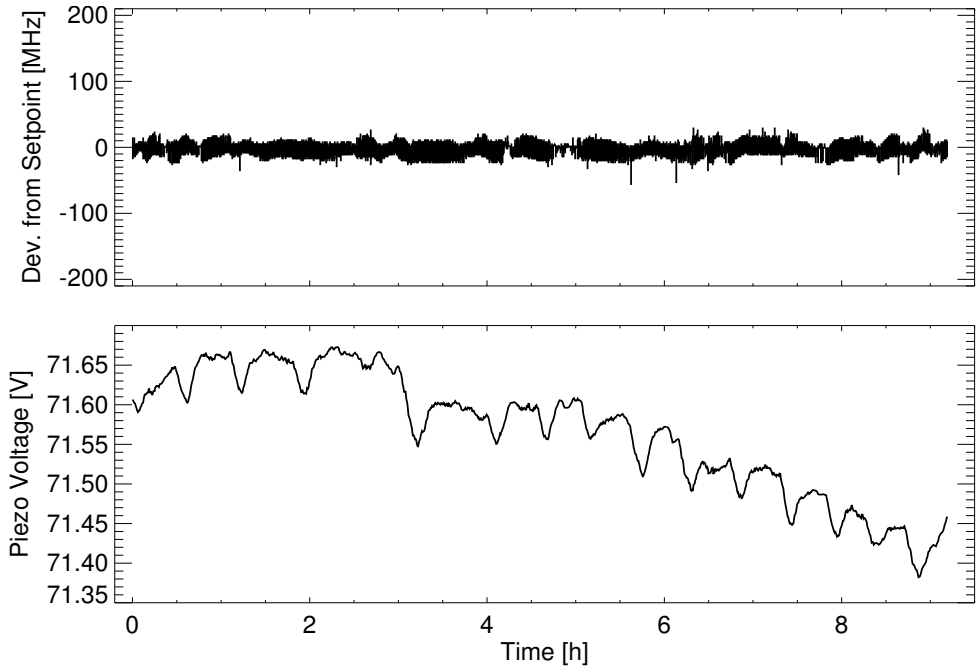

FIGURE 5.9: Laser frequency and control signal for the stabilized TEC500 laser. The frequency set point was $12190.744\,\mathrm{cm}^{-1}$.

of one short giant pulse, similar to q-switched operation. The advantage of gain switching is that no optical elements inside the cavity are needed, which reduces complexity and losses. An additional drawback of a q-switch is that it prevents the buildup of a high seed light intensity inside the cavity. A ring laser is needed to achieve traveling wave operation, since a standing wave leaves regions of undepleted gain (a phenomenon called spatial hole-burning), which favors the lasing of parasitic modes and makes single frequency operation very difficult. A second prerequisite to prevent the formation of standing waves is unidirectional operation. This shall not be achieved by using an optical diode inside the cavity but the direction of lasing shall also be prescribed by the seed light. Therefore the combination of injection seeding, ring resonator, and gain-switching eliminates the need for any intra cavity optical elements except the laser crystal itself. Also necessary for successful injection seeding are a polarized laser output and TEM00-mode operation. Polarization is achieved by a Brewster-angled laser crystal and TEM00 operation is ensured by matching the radius of the pumped volume to the radius of the TEM00 mode (this method is also called gain aperturing).

An important point is that in free running, unseeded mode, the slave laser will emit pulses in both directions. The pulses emitted in the backward direction are directed toward the seed laser, which has therefore to be protected by optical isolators. On the other hand, the energy ratio of the pulses emitted in forward and in backward direction is a good indicator for the seed efficiency defined in Section 5.3.3. If one assumes that the unseeded portion of the laser energy is emitted equally in the forward and the backward direction and the seeded part only in the forward direction, the seed efficiency η_{seed} can directly be calculated as:

$$\eta_{seed} = \frac{E_{for} - E_{back}}{E_{for}} = 1 - \frac{E_{back}}{E_{for}}, \tag{5.1}$$

where E_{for} and E_{back} are the laser pulse energies emitted in the forward and backward direction. The latter will further on also be called ”backpulse energy”. If the assumption is completely valid and if one can further assume that the spectral purity of the seeded portion is $100\,\%$, η_{seed} is at the same time an expression for the spectral purity of the laser pulses.

5.5.1 Setup

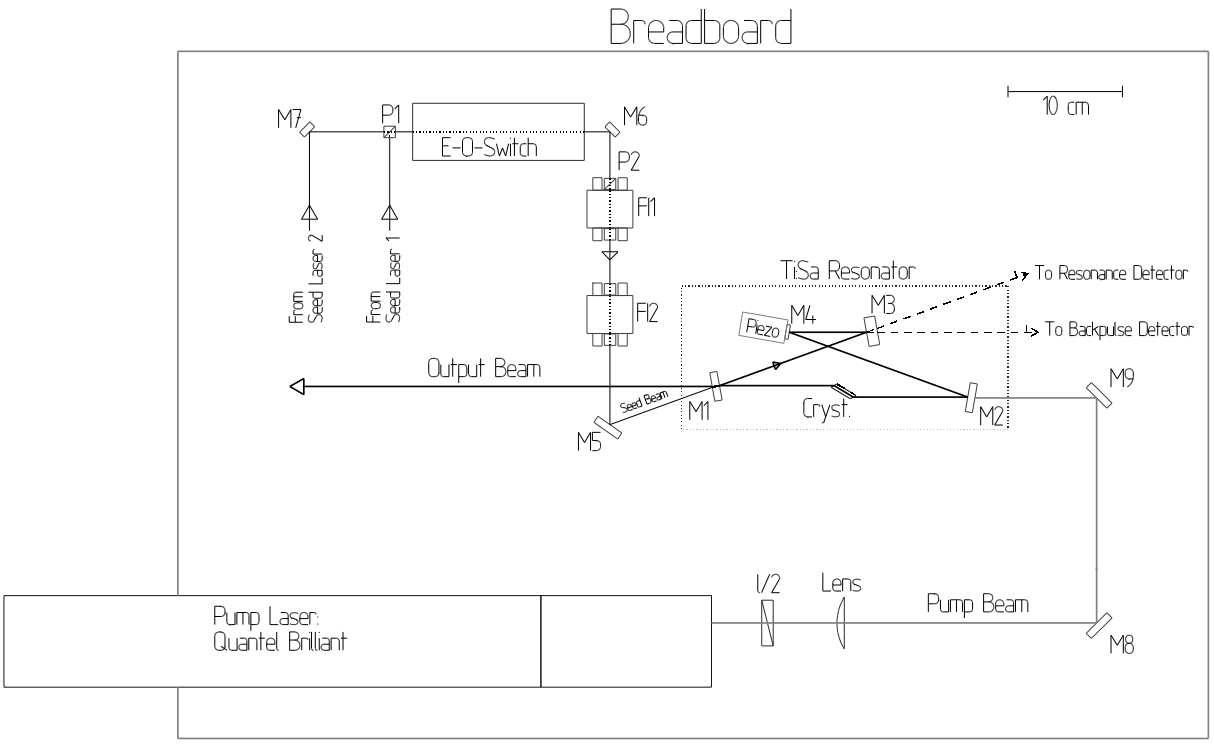

FIGURE 5.10: Layout of the slave laser breadboard, drawing is to scale. Abbreviations: M: mirror, FI: Faraday isolator, l/2: half wave plate, P: polarizer.

A schematic drawing of the slave laser is shown in Fig. 5.10. The drawing is to scale and the entire setup fits on a breadboard measuring $60 \times 90\,\mathrm{cm}^2$. Only the head of the pump laser sticks out and it is supported by an aluminum plate bolted to the breadboard. Initially, the system was mounted on a $50\,\mathrm{mm}$ thick breadboard which proved not to be mechanically stable enough. Therefore the current breadboard is a $110\,\mathrm{mm}$ thick model manufactured by Melles Griot. For a further increase in stability, the height of all beams was reduced from 100 to $63\,\mathrm{mm}$. The different components will be described in detail in the following sections.

5.5.1.1 Seed Beam

The seed light from both master lasers is delivered to the slave system by single mode, polarization maintaining optical fibers. The end of each fiber is fitted with a collimator with adjustable focus (Schäfter&Kirchhoff 60FC-4-A6,1-02). The focal length of $6.2\,\mathrm{mm}$ of the collimators is chosen in a way that inside the slave resonator a focus at the same location and of the same size as the resonator eigenmode can be generated. Thus, no additional mode matching optics are required. The two beams, whose polarizations are perpendicular to each other, are combined at the polarizer P1. Seed laser No. 1 is the online seeder and its light is coupled out from the fiber in vertical polarization. The collinear beams then pass through an electro-optical modulator (Linos LM0202). If a voltage of about $290\,\mathrm{V}$ is applied to this modulator, the polarization of both beams is rotated by $90°$. If no voltage is applied, the polarizations remain unchanged. After the modulator the two collinear beams pass the polarizer P2 which is part of the Faraday isolator FI1. The single beam which has vertical or s-polarization at P2 will pass it whereas the other beam is reflected out of the beam path. In this way, the switching between the two seed lasers which is needed for dual wavelength operation is achieved. Fig. 5.11 shows a plot of the

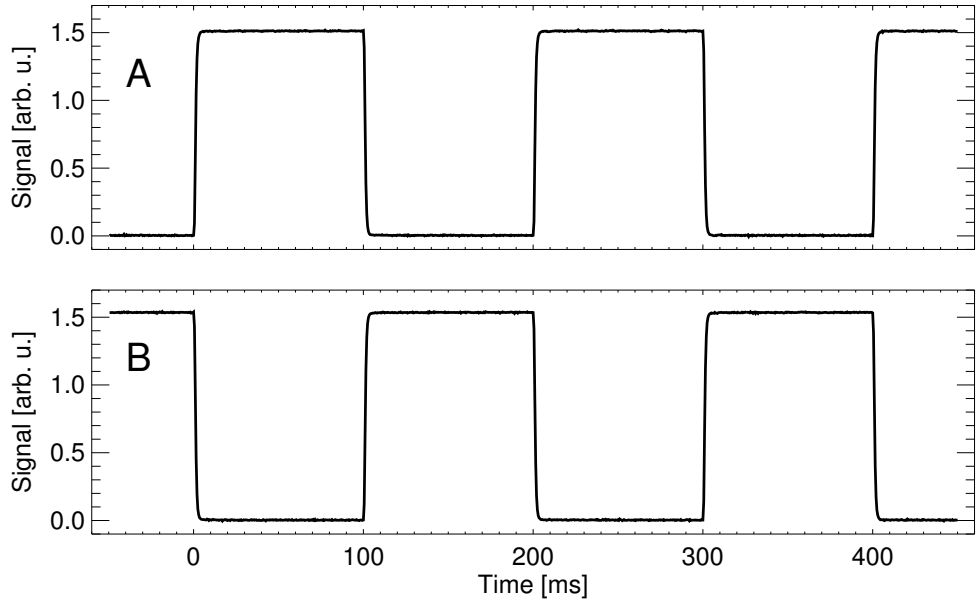

FIGURE 5.11: Wavelength switching by means of an electro-optical modulator. Shown are the measured seed light intensities incident on the slave laser cavity for online (A) and offline (B). The other of the two master lasers was blocked for each measurement.

power of each of the two master lasers measured behind P2. For this measurement, the other of the two lasers was blocked and switching was done at a rate of 5 Hz, adapted to the pump laser which was used initially (Thales Diva, see below). The achieved extinction ratios are 1:410 and 1:500 for online and offline master laser respectively. The switching rise time for the current setup is 1.6 ms. This is sufficiently short for the projected final switching rate of 25 Hz but can be shortened to the sub-μs level by employing a different high voltage driver.

Before being coupled into the slave laser resonator through the output coupling (OC) mirror M1, the seed beam passes two Faraday isolators. Their purpose is to shield the seed lasers and the optics in the beam path from the powerful laser pulses which are emitted from the Ti:Sa laser in this direction in case injection seeding fails. The specified suppression for each of the isolators (Linos FR820) is 40 dB. Each isolator rotates the polarization of the passing seed beam by $45°$, hence after FI2 the seed beam has the required horizontal or p-polarization. The suppression of the isolators can be optimized by rotating the entrance polarizer about the optical axis. This optimization is not done using the back-reflected seed beam, as it is usual, but in a way that the pulses from the unseeded slave laser are attenuated as much as possible. This is important since the suppression is wavelength-dependent and the wavelength of the unseeded slave laser is different from the seed wavelength. It turned out, that the standard thin film polarizers of the Faraday isolators could not withstand the high pulse energy emitted from the slave laser. FI2 was therefore retrofitted with calcite polarizing prisms (Thorlabs GL5-B).

5.5.1.2 Resonator

The ring resonator is made up by the mirrors M1 through M4. The laser pulses are coupled out and the seed beam is coupled in through the partially reflective output coupling mirror M1. The reflectivity of this mirror is $73\,\%$ and its backside is anti-reflection (AR) coated at 820 nm. All other mirrors are highly reflective (HR) at 820 nm. The pump beam is coupled in through mirror M2 which is on both sides coated for high transmission at the pump wavelength of 532 nm. Mirror M4 is mounted on a piezo element (Piezomechanik HPSt 150/14-10/12 VS22) for active control of the cavity length. The maximum expansion of the piezo stack is specified as $10\,\mu$m

at an applied voltage of $150\,\mathrm{V}$. The light which leaks through mirror M3 is directed toward detectors used for control and monitoring purposes (see Section 5.6). The angle of incidence for all mirrors is $10°$. In the initial setup, both M1 and M2 where concave mirrors with a radius of curvature of $2\,\mathrm{m}$. The optical cavity length l' (geometrical length times refractive index) of the resonator is about $600\,\mathrm{mm}$. The free spectral range (FSR) and hence the longitudinal mode spacing which for a ring resonator is defined as

$$\mathrm{FSR}=\frac{c_o}{l'} \tag{5.2}$$

is then about $500\,\mathrm{MHz}$.

The laser crystal (Saint-Gobain) is cylindrical with a diameter of $5\,\mathrm{mm}$ and a length of $19.5\,\mathrm{mm}$. The end faces are cut at Brewster's angle. Thus, p-polarized light incident at the proper angle experiences very low reflection losses. This holds for the laser light circulating inside the cavity as well as for the pump light. The doping level of the Ti:Sa crystal is specified as 0.1 weight-% Ti-ions. For the length of the crystal, this results in a pump light absorption of approximately $97\,\%$. The crystal is mounted in a copper block. To optimize the heat transport from the crystal to the mount, the gap between the two is kept as small as possible and filled with a thermal grease of high thermal conductivity (Electrolube HTCP). Currently no further cooling measures are implemented. For future operation at higher average power, it is planned to fit the crystal holder with a passive heat sink.

The cavity layout was designed according to published examples [81, 82]. The lengths were chosen as short as possible but long enough to prevent the beam from being blocked by optical mounts. After a preliminary design was fixed, the stability of the cavity and the radius of the fundamental mode where investigated by means of the ABCD-matrix formalism [83]. The mode radius inside the crystal was adapted to the maximum allowed pump energy density of $4\,\mathrm{J/cm^2}$ [84, 85]. At a maximum projected pump energy of $20\,\mathrm{mJ}$, the suitable radius is $0.4\,\mathrm{mm}$. The adaption of this radius was done by varying the radius of curvature (ROC) of the two concave resonator mirrors M1 and M2. The mode radius obtained for a ROC of $2\,\mathrm{m}$ is plotted in Fig. 5.12 . The beam shows a slight astigmatism, meaning different radii in the tangential

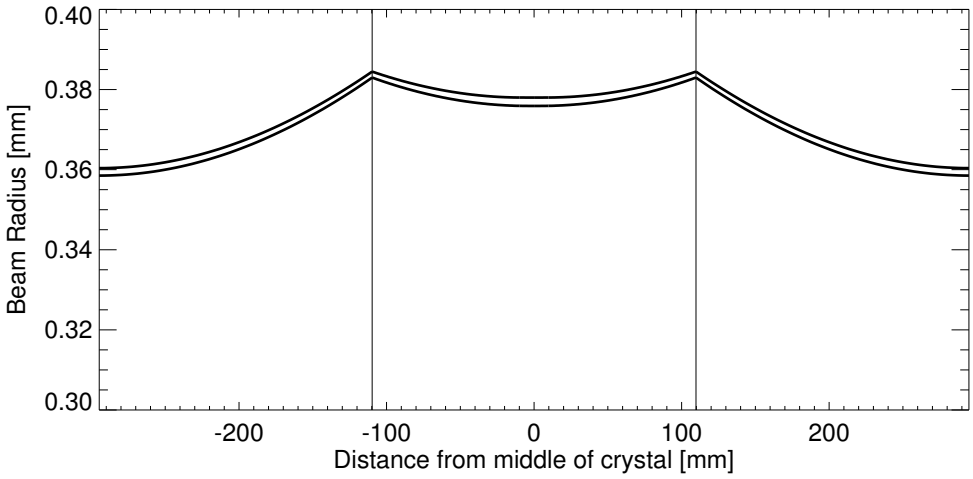

FIGURE 5.12: Radius of the fundamental cavity mode in the sagittal plane (upper curve) and tangential plane (lower curve) if M1 and M2 are concave mirrors with an ROC of $2\,\mathrm{m}$. The vertical lines indicate the positions of M1 and M2.

(horizontal) and the sagittal (vertical) plane. This astigmatism is caused by the Brewster angled laser crystal and is only partly compensated by the spherical cavity mirrors. The calculated radius inside the crystal is with $0.38\,\mathrm{mm}$ very close to the desired value.

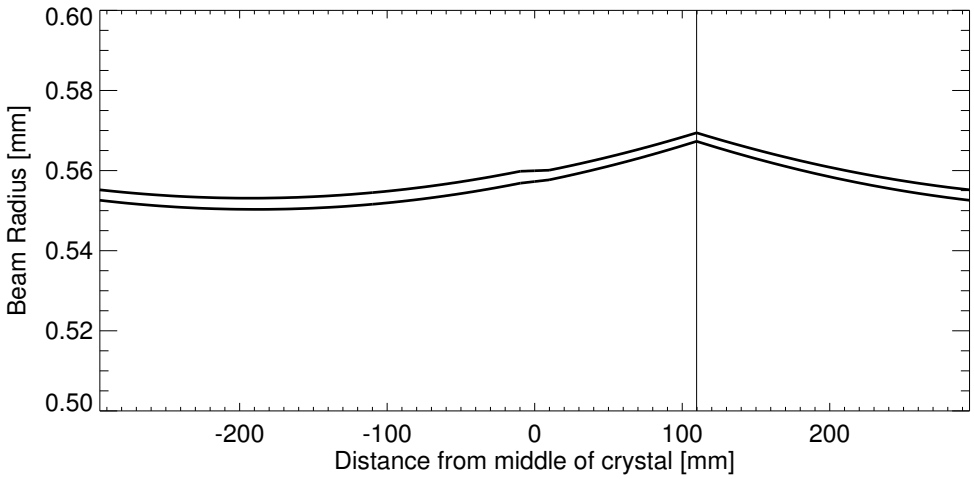

FIGURE 5.13: Radius of the fundamental cavity mode in the sagittal plane (upper curve) and tangential plane (lower curve) if all cavity mirrors are flat, except for M1 with a ROC of $5\,\mathrm{m}$. The vertical line indicates the position of M1.

In the final setup however, a pump laser is used which can produce pulse energies of up to $85\,\mathrm{mJ}$ (see Section 5.5.1.3). It was therefore investigated to which extent the pump energy can be increased by increasing the beam diameter inside the laser crystal. A possible solution consists of increasing the ROC of M1 and M2. If one of the two mirrors is replaced by a flat mirror and the other one by a mirror of $5\,\mathrm{m}$ ROC, a mode radius as shown in Fig 5.13 is obtained. Now the beam radius inside the crystal is $0.56\,\mathrm{mm}$, making pump energies of up to $39\,\mathrm{mJ}$ possible.

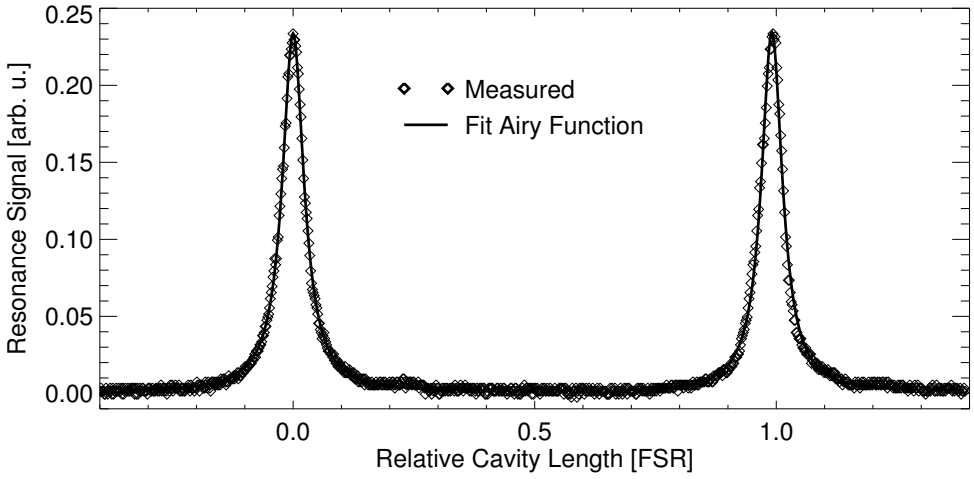

FIGURE 5.14: Seed laser intensity circulating inside the slave cavity as a function of cavity length. The intensity was measured behind cavity mirror M4, the length was was varied by applying a linear voltage ramp to the piezo element. The finesse deduced by fitting an airy function to each of the two peaks was 18.4 and 18.9 respectively.

The alignment of the cavity and the seed beam is achieved by optimizing the cavity finesse. The finesse can be determined by modulating the cavity length (using the piezo element on which the mirror M4 is mounted) and measuring the seed light intensity leaking through mirror M3. The result of such a measurement is shown in Fig. 5.14. Since the length was varied over more than one FSR, two resonance peaks can be seen (see also Section 5.6.1). A high finesse is indicated by high and narrow peaks. If seed beam and cavity are misaligned with respect to

each other, several (low) peaks can be observed for one FSR. If such secondary peaks are still present after the best possible geometrical alignment, this indicates that the seed beam and the cavity mode are not well matched, either with respect to polarization or to position and size of the beam waist. The philosophy behind this approach is that the finesse provides an objective criterion to achieve the optimum alignment both of the ring resonator itself and of the seed beam with respect to the resonator. This alignment should therefore not be changed anymore once the pump laser is activated but rather the alignment of the pump beam should be used for optimizing the output power. This is only valid if thermal effects induced by the pump light do not lead to a lateral shift of the seed beam. Such an effect could so far not be observed.

The finesse of an optical resonator depends on the reflectivity of the mirrors and on intra cavity losses. The finesse values inferred by fitting an Airy function to each of the two resonance peaks shown in Fig. 5.14 are 18.4 and 18.9 respectively. For a lossless ring cavity with an OC mirror of $73\,\%$ reflectivity, the theory laid out in [86] yields a finesse of 19.9. Then, for the lower of the two measured values a round trip loss of $2.6\,\%$ is calculated[6]. This loss is significantly lower than the transmissivity of the OC mirror and should have therefore only very little negative impact on the achievable output power. For the Ti:Sa crystal used initially (TOPAG) however, a round trip loss of $10\,\%$ was determined and the achieved output power was hence significantly lower than for the new crystal.

5.5.1.3 Pump Laser

As discussed in Section 5.3.4, neither diode nor flashlamp pumped lasers offer clearly superior advantages as pump sources. Therefore both alternatives were tested.

For the first setup, a diode pumped laser (Thales Diva) was used. This laser offers a pulse energy of 20 mJ at a repetition rate of 10 Hz. The experiments with this laser were successful and 7 mJ of single frequency output were obtained from the injection seeded Ti:Sa laser. Although the repetition rate and hence the average power generated with the Diva laser as pump source is too low for high resolution atmospheric measurements, the practicability of using a diode pumped laser could be demonstrated. As it turned out that the output power of the Diva laser is unstable and sensitive to room temperature fluctuations (probably due to a design fault), this line of development was not pursued further and results obtained with this laser shall not be discussed in more detail. The construction of a sufficiently powerful transmitter based on a diode pumped laser would be possible with a pump source offering the same pulse energy at a higher repetition rate. As mentioned in Section 5.3.4, diode pumped lasers offering 20 mJ at a repetition rate of 1 kHz are now commercially available, although at a very high price. By reducing the beam radius inside the Ti:Sa crystal and the transmission of the output coupling mirror, it is possible to achieve a good pumping efficiency also at lower pulse energies. If the generated pulse energy is then still high enough to achieve a sufficient signal to background ratio, a less powerful and hence less costly pump laser could be employed.

The second pump source that was tested was a flashlamp pumped, frequency doubled Nd:YAG laser (Quantel Brilliant). It operates at a repetition rate of 20 Hz and emits pulse energies of up to 85 mJ at 532 nm. The primary concern with this laser was the transverse intensity distribution of the beam (also called beam profile). Close to the exit aperture, the laser beam shows a so-called flat top profile and a diameter of about 5 mm. In order to investigate how the beam could be focused down to the right diameter of 0.8 mm, measurements with a CCD camera were carried out. For these measurements, an $f = 75$ cm lens was placed in front of the exit aperture and the beam profile was recorded at various distances behind the lens. At each

[6] An even better method for determining the round trip loss would be to measure the light intensity reflected off the OC mirror. In resonance, this intensity dips the more at higher intra cavity losses. For the case presented here, a decrease in intensity by $29\,\%$ should be observed. For a lossless cavity there would be no decrease.

position an effective beam diameter was calculated. For this, the area was determined where the light intensity is above $13.5\,\%$ of the maximum intensity. The effective diameter is then the diameter of a circle with the same area. The dependence of effective radius on distance from the lens is shown in Fig. 5.15. No measurement at the very focus was taken, but it is obvious that there the beam diameter is much too small. Since focusing with a lens of longer focal length is not possible due to a lack of space on the breadboard, the laser crystal has to be placed outside (in this case in front of) the focus. Then, the beam converges inside the crystal which will lead to a reduced degree of overlap with the laser beam and hence a reduced efficiency, but at the same time it will lead to a more pronounced gain aperturing effect which prevents higher order transverse modes from lasing. To obtain a non-converging beam inside the crystal, an attempt was made to generate a focus of the right diameter close enough to the laser head by using two lenses in a Galilei telescope configuration (a positive lens followed by a negative lens of shorter focal length). It showed that this is possible in principle, but the lateral position of this focus proved to be very unstable. This is due to the magnification of the pointing instability by such a setup.

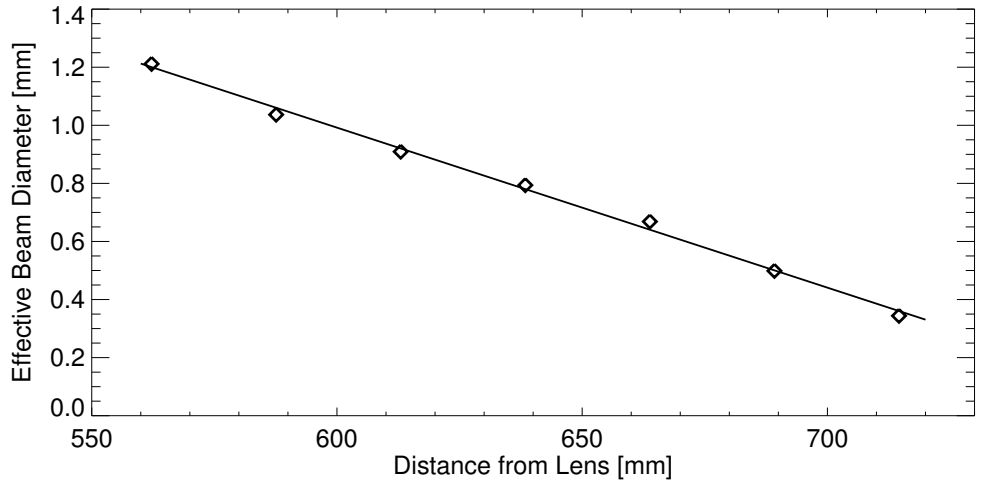

FIGURE 5.15: Effective beam diameter of the Brilliant pump laser measured behind a $f = 75\,\text{cm}$ lens together with a linear fit.

Another problem with placing the laser crystal outside the focus of the multimode pump beam is that there the intensity distribution is not well defined. In order to asses if this distribution is suitable, it was compared to an ideal Gaussian profile. An intensity map of the beam profile at the position where the beam diameter is closest to the desired value of $0.8\,\text{mm}$ is shown in Fig. 5.16, together with a vertical and a horizontal cross section through the point of maximum intensity. At first sight the profile looks rather inhomogeneous and deformed. It even appears that there is a so-called hot spot, a region of enhanced intensity, which may lead to optical damage of the laser crystal. However, a quantitative assessment yields the following:

- The ratio of maximum and average intensity inside the effective radius is 2.4 and only slightly higher (i.e. worse) than for a Gaussian profile where it is 2.32. The fraction of the total energy inside the effective radius is $85\,\%$ and only slightly less than for the ideal case with $86.5\,\%$.

- The correlation coefficient with an ideal Gaussian profile is 0.97. For this calculation, an ideal profile was taken which has the same effective radius and whose center lies at the centroid of the measured profile.

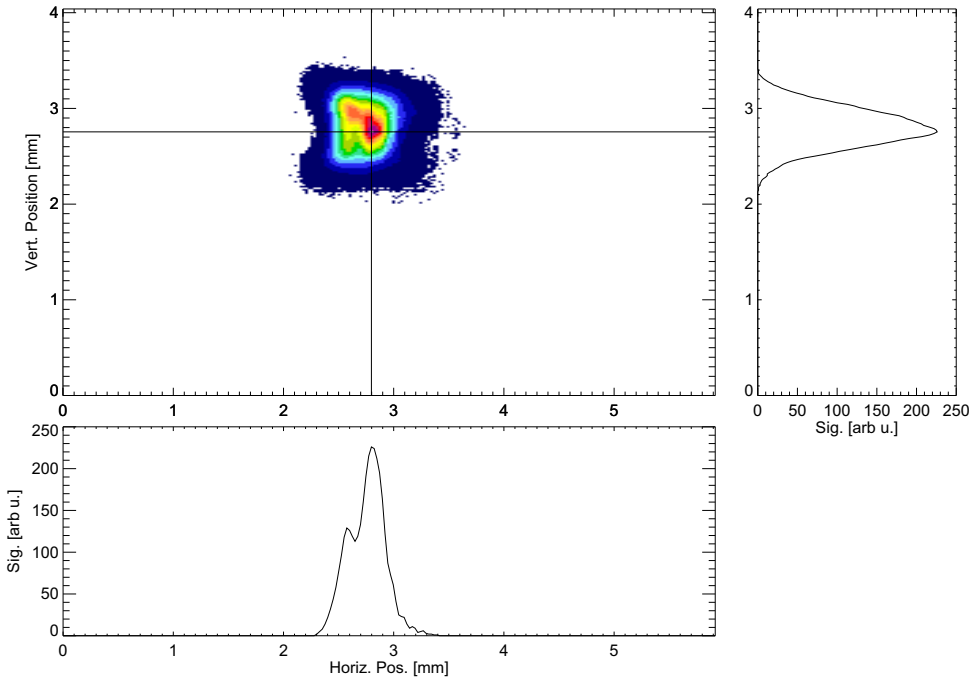

FIGURE 5.16: Intensity distribution of the focused Brilliant pump laser measured $63.8\,\text{cm}$ behind an $f = 75\,\text{cm}$ lens together with horizontal and vertical cross sections through the point of maximum intensity.

The first point disproves the presence of a real hot spot and the second point shows that the deformation of the profile is actually not very severe. Therefore, the intensity distribution should be well suited for pumping the Ti:Sa laser.

5.6 Injection Seeding

5.6.1 Principle

In unseeded or free running mode, the emission spectrum of the slave laser is very broad, an example is shown in Fig. 5.28. This is because the laser is emitting on many longitudinal modes of the cavity, all with different eigenfrequencies. In the amplification process, the light intensity of these modes is built up from spontaneous emission, which has a fairly constant level over a wide spectral range. In injection seeding, light whose frequency and spatial intensity distribution is matched with one of the cavity modes is coupled into the cavity. Thus, this particular mode is given a ”head start”, meaning that its intensity is built up from a much higher initial level. Since the amplification is proportional to the initial intensity, this mode will then also receive much more of the stored energy than other modes. In the ideal case, this mode will draw so much energy that not enough is left for any other mode to start lasing and the laser will operate ”single frequency”, resulting in a very narrow output spectrum.

Injection seeding can only be successful if there is one cavity mode whose eigenfrequency is the same as the seed frequency. If this condition is met, one says that the slave cavity is in resonance with the seed laser. The crucial parameter for the resonance condition is the phase shift $\Delta\varphi$ between seed light which is ”freshly” coupled into the cavity and the light which has completed one round trip. For a ring resonator, this phase shift reads:

$$\Delta\varphi = 2\,\pi \cdot \left(\frac{l'}{\lambda_o} - m \right), \tag{5.3}$$

where l' is again the optical length of the cavity, λ_o is the vacuum wavelength of the seed light, and m is a positive integer which can be chosen arbitrarily, usually such that $0 \leq \Delta\varphi < 2\,\pi$ or $-\pi \leq \Delta\varphi < \pi$. Resonance is given if $\Delta\varphi = 0$.

It also depends on $\Delta\varphi$ how much of the seed light can be coupled into the cavity and how high the intensity of the light circulating inside the cavity is. This intensity is highest for $\Delta\varphi = 0$ and lowest for $\Delta\varphi = \pi$. By measuring this circulating intensity (further on also called resonance signal), as it is shown in Fig. 5.14, $\Delta\varphi$ can be determined. Changing the cavity length by one λ (in our case $\lambda \approx 820\,\text{nm}$) is equivalent to changing $\Delta\varphi$ by $2\,\pi$, according to Equation 5.3. In the following, a change in cavity length by one λ is also, somewhat incorrectly, referred to as a change by one FSR, since it has the same effect as keeping the cavity length constant and changing the seed frequency by one FSR. In order to maintain the resonance condition, $\Delta\varphi$ has to be kept close to zero which means that the cavity length has to be kept constant within a small fraction of the wavelength. This can generally only be achieved by an active control loop. How big the allowed range for $\Delta\varphi$ is will be shown in Section 5.6.3. Actively maintaining a constant $\Delta\varphi$ by influencing the slave cavity length is also called "locking the slave cavity to the seed laser".

5.6.2 Setup

Several methods have been described for locking an optical cavity to a cw laser or vice versa[7]. Some of these schemes such as the dither-lock [87] and the Hänsch-Couillaud method [88], were originally intended for the use with cw lasers only. Since the detector which measures the resonance signal will always also receive the powerful laser pulse, the applicability of such methods for injection seeding of pulsed lasers is limited. A method specially devised for injection seeding is the ramp-and-fire technique [89]. Here, the length of the slave resonator is quickly ramped and the pump laser is fired when a resonance is detected. Since the time window in which the pump laser can be fired is small, the cavity length has to be ramped over at least one FSR in a very short time ($\approx 30\,\mu$s). This results in high mechanical stress for the piezo element. A modification of this method is the ramp-hold-and-fire technique [90] where the time of the laser shot is fixed and the cavity is held in resonance until the shot. Again the ramping has to be done very quickly. Another drawback of the so far described methods is that they only lock the "cold" cavity. If the refractive index of the laser material changes too much due to the heating by the pump pulse, the resonance condition may actually not be fulfilled anymore at the time of the shot.

Other methods do not make use of the resonance signal but try to optimize a parameter which is an indicator for the seed efficiency, e.g. the pulse buildup time [91] or the spectral purity [73]. The disadvantage here is that drifts are only recognized when the seed efficiency already shows a significant degradation. Therefore this method is only well suited for high repetition rate systems since there it is easier to tolerate a certain number of "bad" laser pulses and the reaction times to drifts are also faster.

An additional problem for DIAL operation is to lock the cavity to two different wavelengths for alternating shots. With most of the techniques mentioned, it will not be possible to lock the slave cavity to a different (arbitrary) wavelength in the time between two laser shots because of the limited capture range and bandwidth of the stabilization loop. Most DIAL emitters described in literature work around this problem by either not using injection seeding at all (e.g. the French LEANDRE II system [92]), trying to achieve seeding without cavity resonance (the first and also currently used version of our alexandrite system [93], and probably also the NASA

[7] Locking a laser to a cavity means that for maintaining a constant $\Delta\varphi$ (see Equation 5.3) not the cavity length but the laser frequency is actively influenced. In this case, changing $\Delta\varphi$ by $2\,\pi$ corresponds to changing the laser frequency by one cavity FSR (see Equation 5.2).

LASE system [94]), or using seeding only for the online wavelength [95]. The only method mentioned above which provides for a straight forward solution of the problem is ramp-and-fire which was implemented in a modified form in the single frequency setup of our alexandrite system [37].

Because of the various drawbacks and technical difficulties associated with the known methods, we have invented an active control method which has not been reported before to our knowledge and that provides a solution for all these problems. The new method is a modification of the ramp-and-fire technique. The cavity length is also actively modulated over at least one FSR in order to meet the resonance condition at the time of the laser shot. As opposed to ramp-and-fire however, it is not the time when the pump laser is fired which is varied, but the cavity modulation. The mechanical stress for the piezo element is also much lower because this modulation is achieved by applying a comparatively slow sinusoidal voltage to the piezo element on which one cavity mirror is mounted. The amplitude of the voltage is chosen such that the modulation covers slightly more than one cavity FSR. This ensures that a resonance will always occur at some point, regardless of the actual relation between cavity phase (see Equation 5.3) and voltage. The voltage has double the frequency of and a constant phase relation with the pump laser pulse train.

The time (or delay) at which a resonance occurs with respect to the pump pulse is controlled by a DC offset which is added to the modulation voltage. In Fig. 5.17 the principle of this method is illustrated by means of a model calculation. In this model, the response of the piezo element to the applied voltage is linear, the resonator finesse is 18.4, and no drift of the cavity length is present. Hence a resonance always occurs when the voltage acquires a certain fixed value. In a real system the voltage at which the resonances appear will change due to drifts in

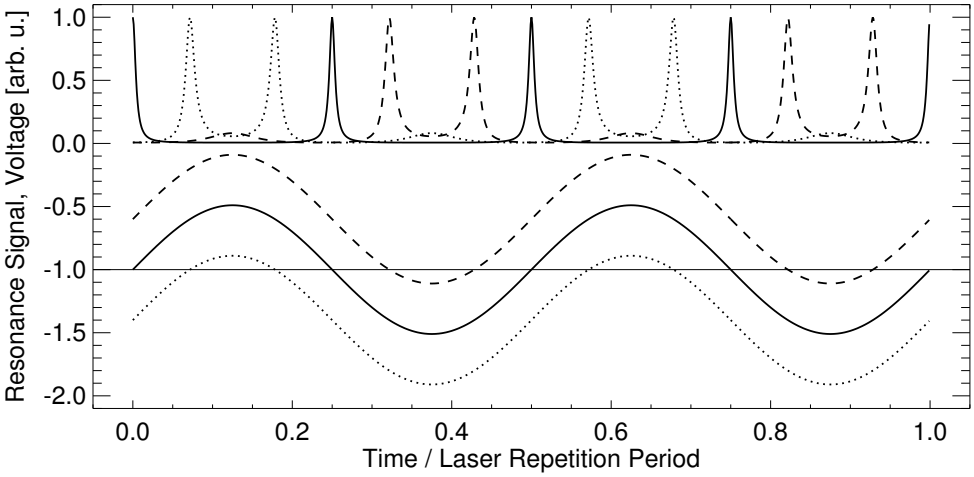

FIGURE 5.17: Modeled resonance patterns (upper curves) in response to modulation voltages with three different offsets.

the cavity length. The task of the control loop is to adjust the offset of the modulation voltage such that the delay of the resonance peaks remains constant. The position of the actual peak of interest close to or, if the described heating effects play no role, exactly at the time of the laser shot can however not be determined due to the blinding of the detector by the laser shot itself which cannot be separated from the resonance signal. Therefore the peak occurring one modulation period after the peak of interest is taken as the reference. For a constant modulation frequency, which is easy to maintain, the delay between this peak and the peak of interest will always remain fixed, regardless of variations in the modulation amplitude and the piezo response. Since piezo actuators show a hysteresis whose shape can possibly change with age, temperature, and also with the applied offset voltage, such variations in the response function

can indeed not be ruled out. Therefore it is necessary to modulate the cavity length at the double rather than the same frequency as the pump laser repetition rate.

With this control scheme it is now possible to maintain an arbitrary resonance peak delay and hence an arbitrary $\Delta\varphi$ at the time of the laser shot. By measuring the laser pulse energy emitted in the backward direction, it can be determined for which peak delay the highest seed efficiency is achieved. Thus, the possible influence of the heating of the laser crystal by the pump pulse can be quantified and eliminated.

Regarding the problem of dual wavelength operation, it would be possible to split the control loop into two independent loops for each wavelength, each keeping track of a separate offset voltage. After the occurrence of the relevant resonance peak and before the next laser shot, the offset would then have to be switched in a very short time, resulting again in very high acceleration values for the piezo element if the difference between the two voltages is high. Since however the offline wavelength only has to be situated in a region of sufficiently low absorption, which is at least several GHz wide for all online frequencies which are intended for use with the new system (see Appendix A.2), it is possible to choose an offline frequency whose difference to the online frequency is an integer multiple of the FSR of the slave resonator (about $500\,\mathrm{MHz}$ in our case). Thus, the offline frequency can be locked to the slave cavity which is in turn locked to the online frequency. Now the stabilization system consists as well of two separate control loops which are activated alternatingly for online and offline shots, but the offset voltage does not need to be changed for the offline wavelength. In this way, absolute stabilization is also provided for the offline frequency as long as neither of the two loops lose lock because one of the control signals reaches the limit of the allowed range or because of any other event which requires that lock be newly established.

The hardware elements involved in the stabilization loop are sketched in Fig. 5.18. The core of the setup is the same standard personal computer which is also used for controlling the seed wavelength (see Section 5.4.2). The routines for stabilizing master and slave laser are run in parallel and are implemented in LabView. The routine for stabilizing the slave cavity length works in the following way: When a trigger impulse from the pump laser is received, the time series of the resonance signal is digitized for a time sufficiently long to capture the desired delay of the reference peak. For diagnostic purposes the signal from the backpulse detector is digitized in parallel. Both signals are first passed through a $10\,\mathrm{kHz}$ low-pass filter. For the resonance signal, this is to ensure that the accuracy of the determination of the peak delay is not deteriorated by high frequency ripple and for the backpulse signal the intention is to make the fall time of the signal long enough to be able to digitize it with the AD-converter sampling rate of $250\,\mathrm{kHz}$. After that, the delay of the reference peak is determined and compared to the set value. The difference between actual and set delay is used to calculate the value of the new offset voltage. The algorithm for this is described in Appendix B. If the resonance signal originated from the offline seeder (recognized via a digital input channel that is connected to the on-offline switch), not the offset of the modulation voltage is changed, but the voltage sent to the frequency modulation input of the offline diode laser driver. The wavelength is switched $0.5\,\mathrm{ms}$ after each laser shot. It is not done earlier after the shot in order to avoid that switching occurs while lidar data are still recorded, thus avoiding EMI problems. The control software comprises some more elements which serve the following purposes:

- Find the ”right” maximum: The trace of the resonance signal always contains more than one maximum. Therefore, only a certain interval of time around the set delay is searched for maxima. Then, one also has to be able to distinguish true resonance maxima from secondary maxima caused by imperfect alignment or by noise. This is done by calculating a threshold value using the entire time series which always contains at least one true resonance peak.

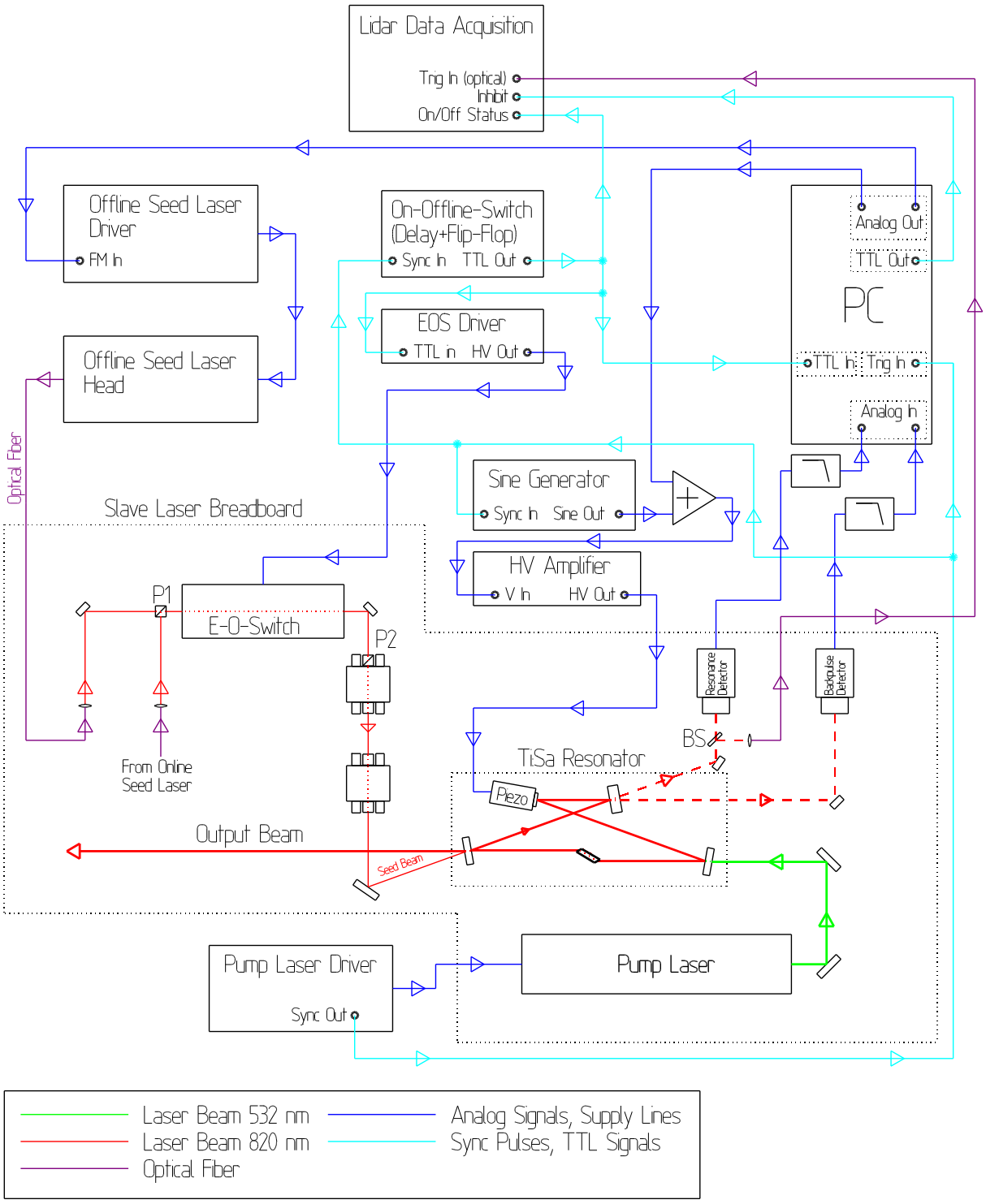

FIGURE 5.18: Schematic diagram of the hardware setup for slave laser stabilization and wavelength switching. Abbreviations: Trig: trigger, Sync: synchronization, FM: frequency modulation, V: voltage, HV: high voltage, EOS: electro-optical switch, P: polarizer, BS: beam splitter, PC: personal computer. For details see text, for a complete and annotated drawing of the optical setup see Fig. 5.10.

- Set a control signal back to the middle of the allowed working range once the limit of that range has been reached. Both for online and offline channel, the range is big enough to vary the controlled parameter over several FSR of the slave cavity. If such an event really occurs, the new lock point for the offline frequency can differ from its initial value. This is not very critical, since the allowed range in which the offline frequency can vary is at least $10\,\mathrm{GHz}$ wide (see Appendix A.2), but nevertheless the offline frequency is monitored at regular intervals.

- Decide whether lock is established and the seed efficiency is sufficiently high (by evaluating the backpulse energy). This status signal is sent to the lidar data acquisition system in order to block the recording of data if the laser pulses are not of sufficient quality. If too many badly seeded shots occur in a row, the pump laser is switched off automatically in order to avoid damage of optical elements.

- The height of the resonance peaks is also evaluated. If this height shows a too strong reduction, it means that either the alignment of the slave cavity has deteriorated or the seed laser is not operating single frequency anymore. In both cases an alert is generated and the recording of data is interrupted.

- Save all relevant parameters for each shot to hard disk. These are:

  - The position of the resonance peak
  - The amplitude of the resonance peak
  - The backpulse energy
  - The control signal
  - Both in hardware and in software, two more analog input channels are reserved for a future recording of the pulse energy and the signal from a photoacoustic cell on a single shot basis.

5.6.3 Results

The parameter that is controlled by the slave laser stabilization loop is the position or delay of a resonance peak. How this delay can be converted to the cavity phase shift at the time of the laser shot is explained in Appendix B. It shall now be shown how stable this phase shift can be kept on one hand and what stability is actually needed for successful injection seeding on the other hand.

What stability can be achieved is shown in Fig. 5.19 where under active stabilization the phase shift for each shot was recorded for more than $8\,\mathrm{h}$. In the next paragraph it will be shown that the plotted range is at the same time the allowed range. For 8 shots out of 301822 a phase shift outside the allowed range is observed. For the shots around $5.5\,\mathrm{h}$ these disturbances were probably caused by vibrations of the optical table because somebody had been working on it. The width of the distribution is much smaller than the allowed range. The standard deviation for all points is $0.0064\,\pi$, which is equivalent to $9\,\%$ of the allowed range. For the offline channel (not shown), the number of shots outside the allowed range is 83 and the standard deviation is $0.0094\,\pi$.

In order to determine the size of the allowed range for the cavity phase shift for successful injection seeding, a measurement was carried out where the seed efficiency as a function of the phase shift was measured. This measurement was repeated for different seed light intensities, where the seed light was attenuated by the electro optic modulator usually used for on/offline switching. The seed efficiency was determined by measuring the ratio of the pulse energies

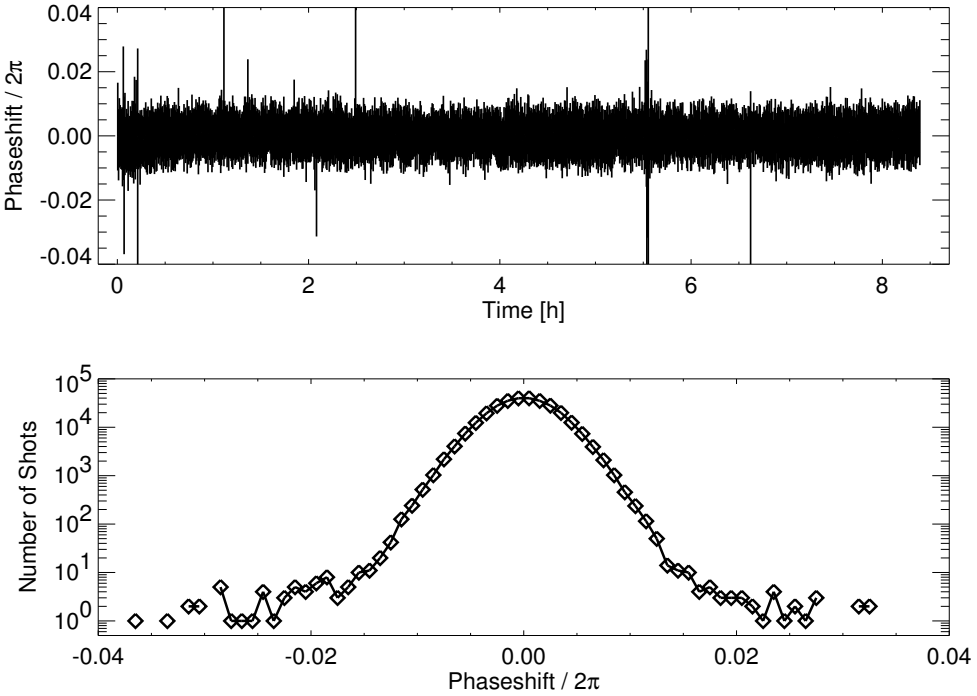

FIGURE 5.19: Time series and distribution of the phase shift of the slave cavity for the online channel. 8 out of 301822 points lie outside the plotted range.

emitted in the forward and in the backward direction (see Equation 5.1). For this measurement, the pump energy was $35.5\,$mJ resulting in an output energy of $12.3\,$mJ. The forward and backward pulse energies were measured with photo diodes. Since the backpulse detector would be overloaded for unseeded operation at such a high pump energy, the measurement was calibrated by measuring the backpulse energy at a lower pump energy where the output energy in unseeded mode was $2.5\,$mJ. The result is shown in Fig. 5.20. Even though for good seeding the backpulse energy is very small and the error associated with its measurements is quite large, a very regular behavior can be observed. A smaller phase shift as well as a higher seed intensity lead to a higher seed efficiency. As saturation could not be observed, it is somewhat arbitrary to decide when the seed efficiency is high enough. If the seed efficiency is really the same as the spectral purity, a value of $99.5\,\%$, equivalent to a backward to forward energy ratio of 0.005 would be sufficient, according to Table 3.2. In order to allow for possible errors in this measurement and also for the possibility that the spectral purity is lower than the seed efficiency, a value of 0.001 was chosen for the maximum ratio. For the highest seed intensity, which can always be achieved, this results in an allowed range for the cavity phase shift of $\pm 0.08\,\pi$. Since one FSR corresponds to a phase shift of $2\,\pi$, the maximum allowed phase shift corresponds to $\pm 20\,$MHz. The stability (standard deviation) that was actually observed for the online channel is $\pm 1.6\,$MHz, including both fluctuations of the seed laser frequency and of the slave cavity length due to vibrations. For the maximum seed intensity, the mean seed efficiency inside the range of the achieved stability is $99.97\,\%$.

In Fig. 5.21 the ratio of the backward and forward pulse energies is shown for the same measurement as in Fig. 5.19. This shows that the stability of the phase shift that was shown in Fig. 5.19 does indeed lead to the desired stability of the seed efficiency. Here, 7 out of 301200 points lie outside the plotted range (this time series is slightly shorter since the pump laser had been switched off before the measurement was stopped) and the mean value of the ratio is 0.00016. One has again to bear in mind the large uncertainty of this value, but it indicates, that the seed efficiency that can be routinely achieved is significantly higher than the demanded

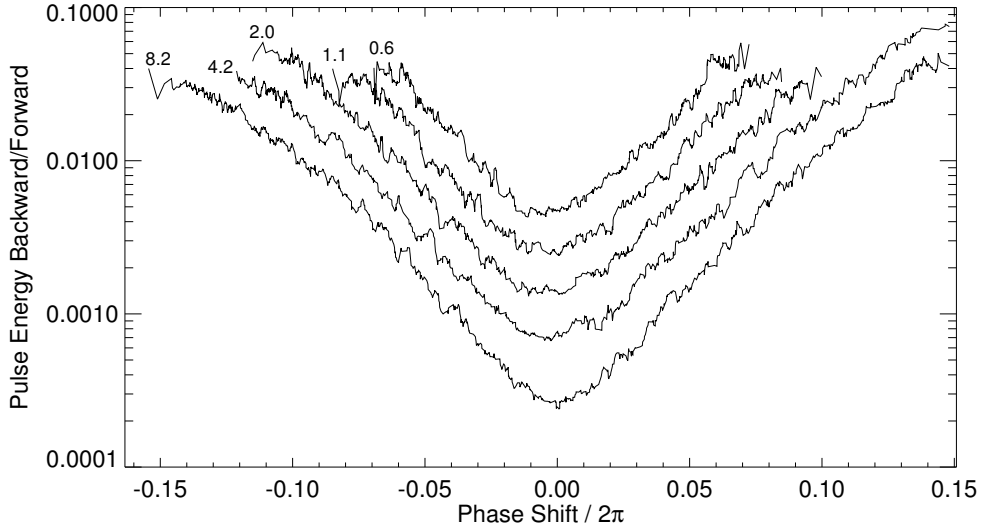

FIGURE 5.20: Ratio of the pulse energy in forward and backward direction as a function of cavity phase shift measured at different seed laser powers. The numbers at the curves denote the seed power incident on the OC mirror in mW. A running mean over 9 points has been applied.

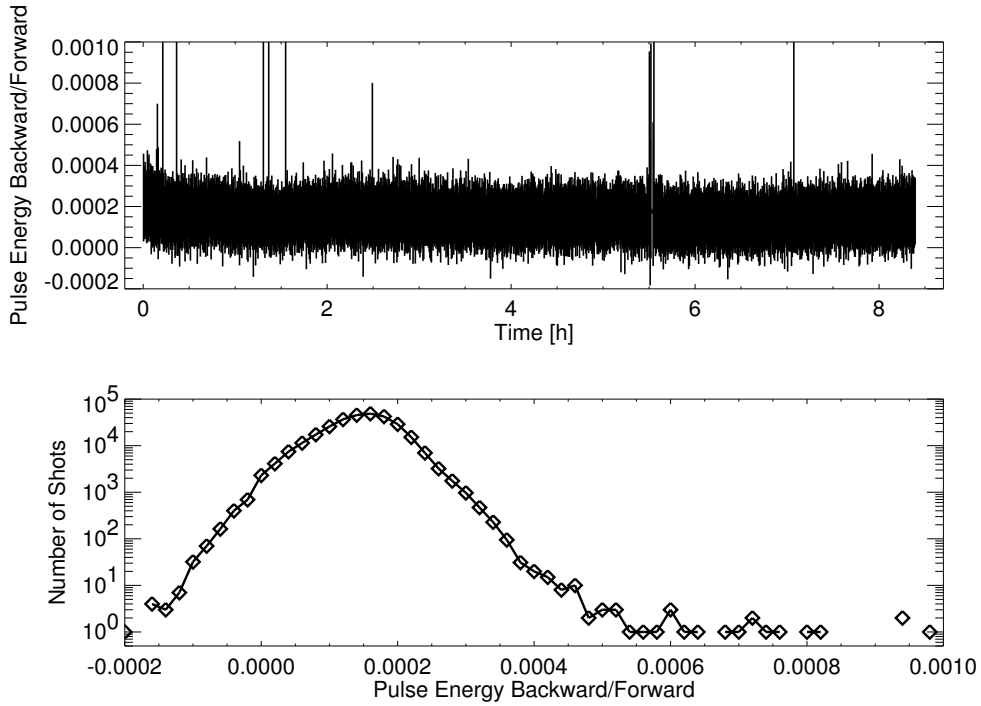

FIGURE 5.21: Time series and distribution of the ratio of the pulse energy in forward and backward direction for the same measurement as shown Fig 5.19. 7 out of 301200 points lie outside the plotted range.

$99.9\,\%$. This will be confirmed by a direct measurement of the spectral purity presented in Section 5.7.3. For the offline channel (not shown), the mean ratio was $5 \cdot 10^{-5}$. The reason why this is significantly lower than for the online channel can be the seed intensity which was $30\,\%$ higher than for the online channel.

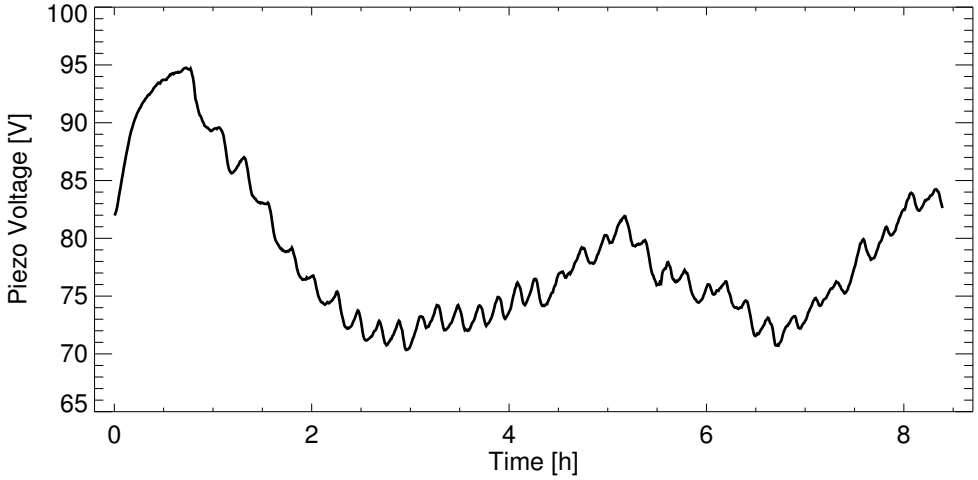

FIGURE 5.22: Time series of the control signal for the slave resonator length for the same measurement as shown Fig 5.19.

The control signal for locking the slave laser cavity to the online wavelength is shown in Fig. 5.22. The voltage that is needed to change the resonator length by one FSR is about $12\,\mathrm{V}$, hence without stabilization the length would have varied by about $2\,\mathrm{FSR}$ during the time shown. So on one hand, the variation is so large, that active control is definitely needed but on the other hand it is so small that the possible range of the control signal from 0 to $150\,\mathrm{V}$ ensures continuous lock without the need to re-establish it for very long times.

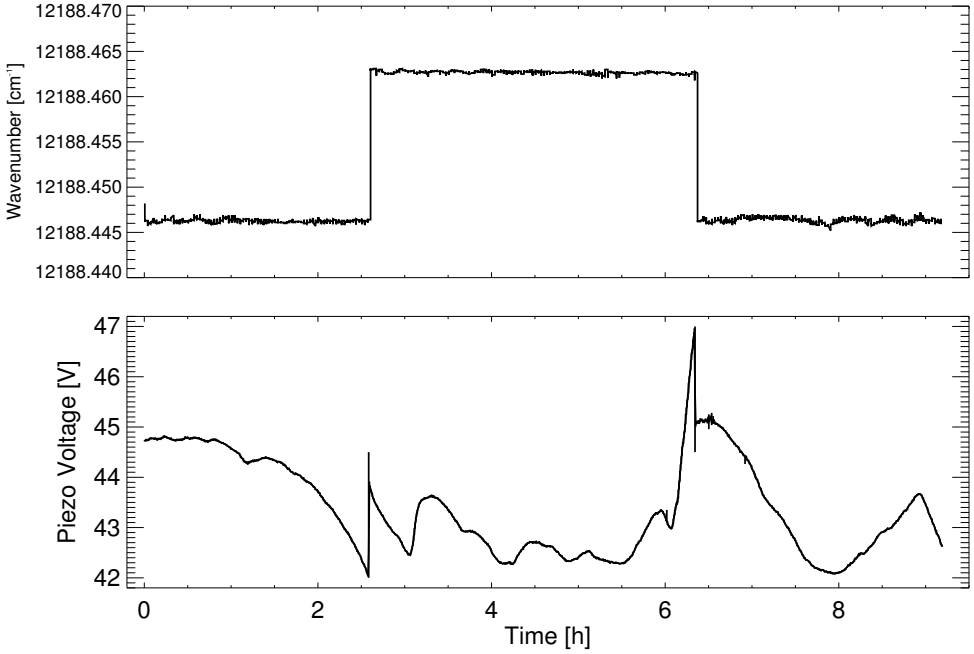

FIGURE 5.23: Time series of the offline frequency and the according control signal, same measurement as Fig 5.9.

Injection seeding for the offline wavelength is achieved by locking the corresponding seed

laser to the slave cavity. Thus, the frequency of this laser is also stabilized and it differs from the online frequency by a multiple of the FSR of the slave cavity. The control signal is in this case sent to the tuning piezo of the offline seeder. It is calculated from the delay of the resonance peak using a PI (proportional-integral) algorithm. At $2\,$min intervals, the offline frequency is monitored. A time series of this frequency and the according control signal is shown in Fig. 5.23, it is taken from the same measurement as the one shown in Fig. 5.9 where the stability of the online frequency was demonstrated. It can bee seen that the offline frequency is also very stable. Twice however, the control signal reached the limit of the allowed range from 42 to $47\,$V and was set back to the middle of the range. This was then accompanied by a jump in the frequency of one FSR of the slave resonator. This measurement also provides a method of measuring the size of the FSR. It is given by the difference of the two occurring mean frequencies $\nu_{off,high}$ and $\nu_{off,low}$. With $\tilde{\nu}_{off,low} = 12188.4463\,\mathrm{cm}^{-1}$ and $\tilde{\nu}_{off,high} = 12188.4627\,\mathrm{cm}^{-1}$ we obtain an FSR of $492\,$MHz. The record of the resonance peak position shows, that when the jumps in the control signal occurred, the position lay outside the allowed range only for one shot each.

5.7 Laser System Performance

The results regarding frequency control of the master laser have already been presented in Section 5.4, the results regarding active stabilization of the slave cavity and injection seeding in Section 5.6.3. In this section, a further characterization of the output parameters of the injection seeded and, where appropriate, of the unseeded Ti:Sa laser shall be given.

5.7.1 Output Power and Temporal Characteristics

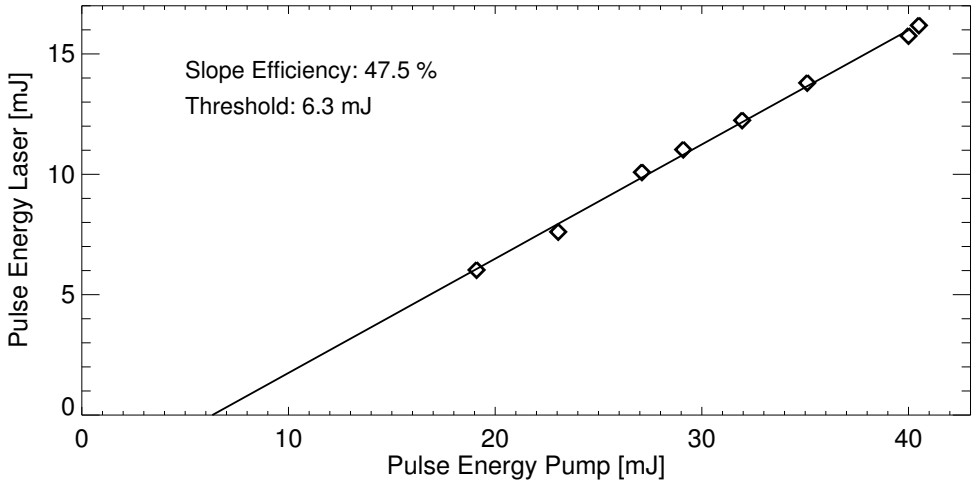

FIGURE 5.24: Output energy of the injection seeded Ti:Sa laser (diamonds). Slope efficiency and threshold were determined by means of a linear fit (straight line)

Fig. 5.24 shows a graph of the mean output energy of the seeded Ti:Sa laser dependent on the pump energy. The mean output power of the pump and of the slave laser were measured with an Ophir 3A-P-Cal thermopile head. The observed slope efficiency was $47.5\,\%$ at a threshold energy of $6.3\,$mJ. The maximum achieved output energy was $16.2\,$mJ. The laser was operated at this energy for many hours, but then the laser crystal was damaged for unknown reasons. Therefore further operation was continued at a pump power of $35\,$mJ, yielding $12.5\,$mJ of output power. All other measurements presented in the following were taken at this energy level. This

is not the highest possible output energy. The pump laser which is used in the final setup shows a smoother beam profile which first leads to a higher pump efficiency and possibly also to an increased damage threshold (see Section 5.8). The output power in unseeded mode was not characterized in detail for the final resonator configuration since it is difficult to dump the beam that is emitted in the backward direction at such high energy levels. Earlier measurements showed, that both threshold energy and output power are about the same in unseeded mode, only that half the energy is emitted in the backward direction, and hence the energy emitted in the forward direction is only half as high as in seeded mode.

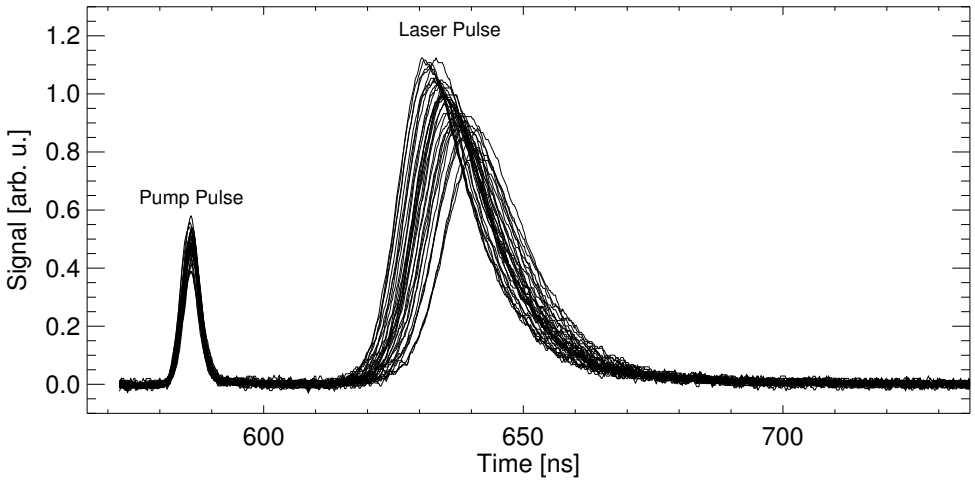

FIGURE 5.25: Traces of 35 output pulses, the time is given relative to the q-switch trigger signal from the pump laser.

Fig. 5.25 shows the traces of 35 output pulses measured with a high speed photo detector (bandwidth 220 MHz) and recorded with a digital sampling oscilloscope. Some residual pump light was falling on the detector as well. The analysis shows that the timing jitter of the pump pulse relative to the q-switch trigger signal is negligible. Using the centroids of the pump and of the output pulse, pulse buildup times in the range from 49.9 to 58.9 ns were determined, with the mean value being 53.9 ns and the standard deviation 2.5 ns. The measured width of the laser pulses (FWHM) ranges from 16.0 ns to 18.6 ns, here the mean value is 17.1 ns.

Fig. 5.25 shows already that the output energy of the Ti:Sa laser shows some variations. For a better characterization of these fluctuations, the pulse energy was recorded on a single shot basis for more than 8 h. This was done in parallel with the measurements presented in Fig. 5.19 and Fig. 5.21. Fig. 5.26 shows the time series and the distribution function of the measured online pulse energies. The offline pulse energies behave practically identical and could not be told apart from the online in this kind of representation. An average over 300 Shots has been applied to the time series in order to visualize long term drifts. These drifts stay within $\pm 4\,\%$ of the overall mean. Both longterm and short term fluctuations are represented in the distribution function. The relative width of the distribution (standard deviation) is $6.7\,\%$.

5.7.2 Beam Profile

The beam profile of the seeded Ti:Sa laser was recorded using a CCD camera. The measurement was taken 113 cm from the OC mirror which is, according to Fig. 5.13, 145 cm away from the beam waist. The intensity map together with vertical and horizontal cross sections is shown in Fig. 5.27. Using the indicated $1/e^2$ Gauss fit diameters and assuming a beam waist diameter of 1.1 mm for both horizontal and vertical direction, the following formula can be used to obtain

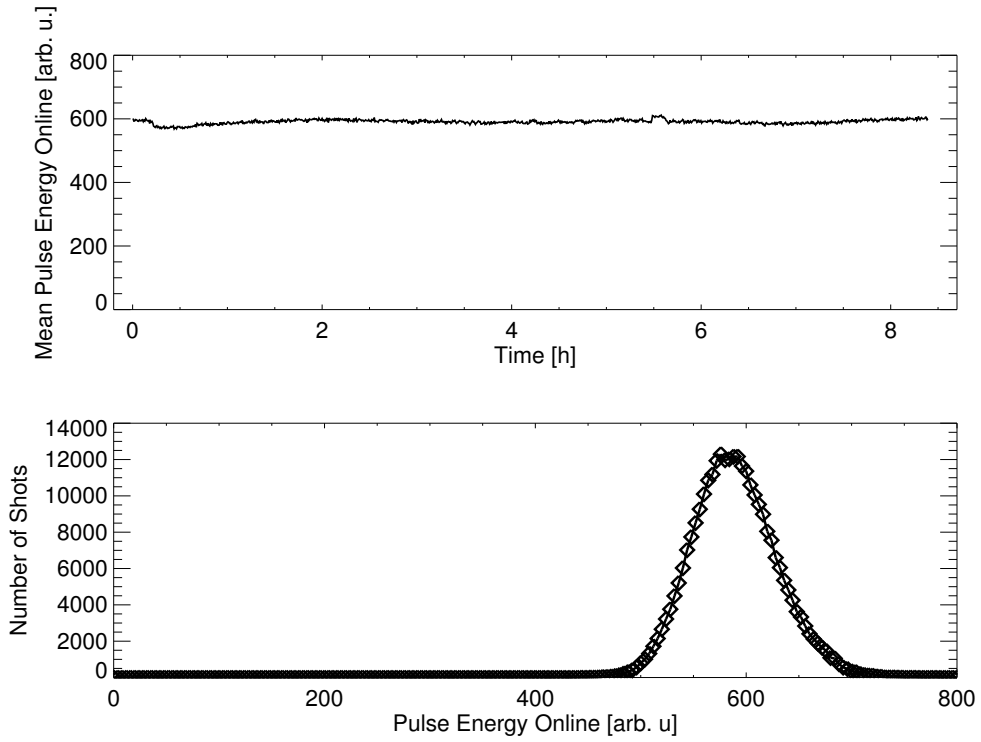

FIGURE 5.26: Pulse energy of the Ti:Sa laser recorded over more than 8 hours. For the time series an average over 300 shots has been applied.

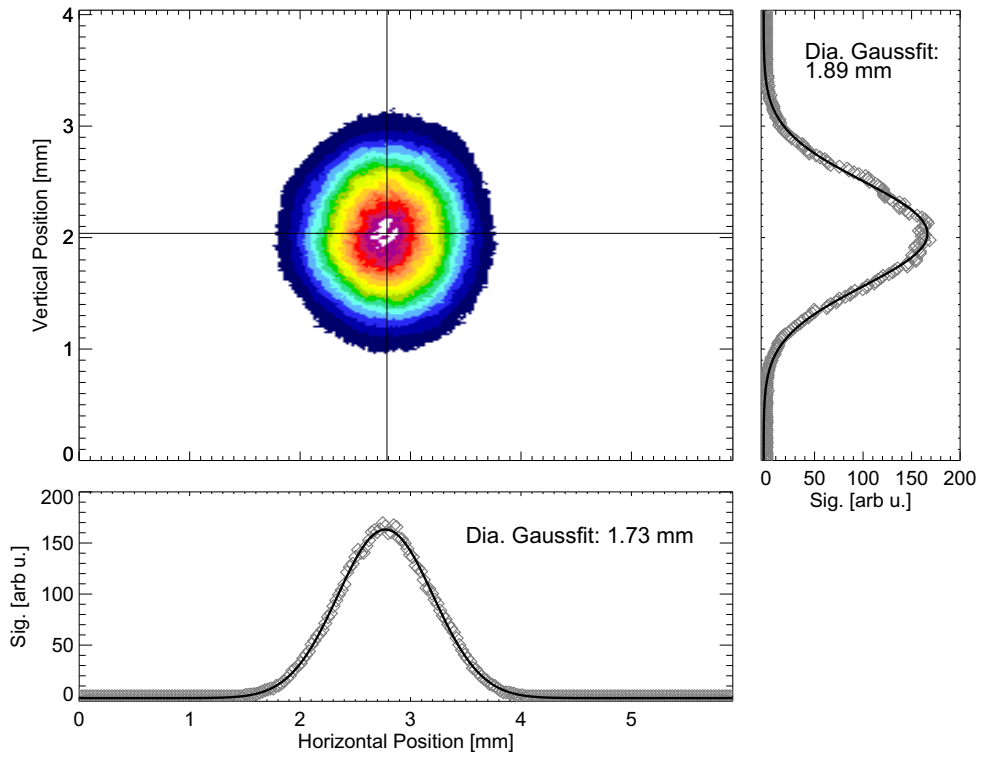

FIGURE 5.27: Intensity map of the injection seeded Ti:Sa laser together with cross sections through the centroid (diamonds) and Gaussian fit curves (solid line). The profile was recorded 113 cm behind the OC mirror.

an estimate for the M^2 value [96]:

$$w(z) = w_o \cdot \sqrt{1 + \left(\frac{4\, M^2\, \lambda\, z}{\pi\, w_o^2} \right)^2},$$

where z is the distance from the beam waist, w_o is the beam diameter at the waist, and w is the diameter at position z. The result is $M^2 = 1.0$ for the horizontal direction and $M^2 = 1.1$ for the vertical direction. Although this is not a very accurate way of determining M^2, it is nevertheless safe to say that the beam quality is very good and very close to a diffraction limited TEM00 beam. The resulting far-field diffraction angle (full angle) is then 0.95 mrad for the horizontal and 1.1 mrad for the vertical direction.

5.7.3 Spectral Properties

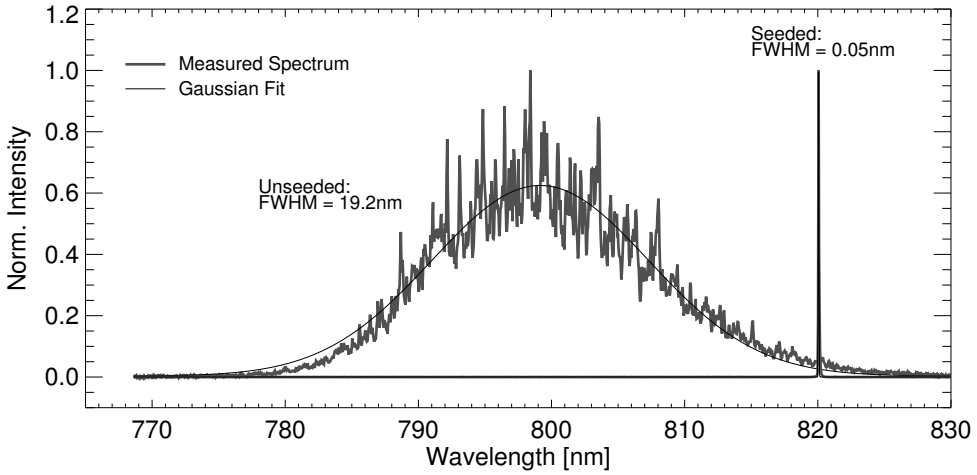

FIGURE 5.28: Output spectrum of the Ti:Sa laser in seeded and unseeded mode, measured with Ocean Optics HR2000 grating spectrometer. The width determined for seeded operation is equal to the instrumental resolution.

Measured with Spectrometer A first investigation of the slave laser spectrum was carried out using a fiber coupled grating spectrometer (Ocean Optics HR2000), offering a spectral resolution of 0.05 nm. Fig. 5.28 shows spectra measured for seeded and unseeded operation. Both spectra were averaged over 100 laser pulses. As expected considering the wide fluorescence spectrum of the laser material, the free running output spectrum shows a very large width. The shown Gaussian fit yields a FWHM of 19.2 nm. The strong modulation of the spectrum is somewhat surprising as it does not show in other publications. This may be due to the fact that the used spectrometer has an exceptionally high resolution compared to the 1.0 nm or more found for other common spectrometer types. It is interesting to note that the maximum of the unseeded spectrum at 799 nm lies rather far away from the projected operating wavelength around 820 nm. This could lead to the conclusion that injection seeded operation is not possible without additional measures to narrow and to force the free running output toward the 820 nm, e.g. by placing a birefringent filter or a prism inside the slave cavity. It has however been shown already in Section 5.6.3 that successful injection seeding is indeed possible without such measures, if the seed power is sufficiently high and good phase and mode matching between the seed laser and the slave cavity is provided.

The spectrum recorded for seeded operation on the other hand shows a width of only 0.05 nm which is equivalent to the instrumental resolution. It will be shown below that the actual width of the spectrum is less than 100 MHz or 0.0002 nm.

Measured with Wavelength Meter The WS7 wavelength meter (see Section 5.4.2) is also capable of performing measurements with pulsed laser sources. Therefore it can be used to characterize the center frequency of the Ti:Sa laser pulses and can also to give an upper limit for the spectral width of the pulses. First the seed laser was coupled into the wavelength

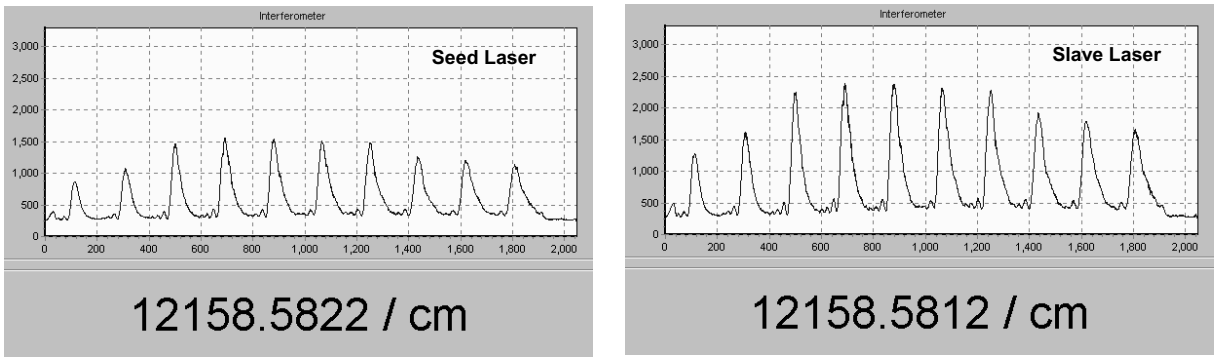

FIGURE 5.29: Screen shots of the WS7 wavelength meter display. Shown are the interferograms from the Fizeau interferometer with the highest resolution together with the measured wavenumbers for seed and injection seeded slave laser.

meter, then shortly afterward the injection seeded slave laser. Screen shots with the interferograms and measured wavenumbers are shown in Fig. 5.29. The displayed absolute value of the wavenumber is not correct since the calibration data was missing on the computer where the images were generated, but this has only negligible influence on the difference between the two values. For this measurement, the seed laser was not actively stabilized. The two measurements yield a difference of $30\,\mathrm{MHz}$ between seed and slave laser, so considering the specified accuracy of the wavelength meter, no significant indication of frequency pulling can be found and the wavelength of the slave laser pulses is practically identical with the seed wavelength.

Since the raw interferogram data are made accessible by the wavelength meter software, it is also possible to use it for an assessment of the spectral width of the laser pulses. For the following analysis it is assumed, that the line width of the seed laser is much smaller than the spectral resolution of the wavelength meter which is about $500\,\mathrm{MHz}$. Thus, the interferogram recorded with the seed laser is essentially equal to the instrument function. To investigate if the slave laser shows a spectral width that is large enough to influence the shape of the interferogram, part of the interferograms of the slave and the seed laser were subtracted. Before that, the signal was normalized and shifted in a way that the location of the peak is the same for both interferograms. The result is shown in Fig. 5.30. No systematic difference is visible in the shape of the two interferograms. To investigate what minimum spectral broadening can be detected by this method, synthetic interferograms were generated by convolving the seed laser interferogram with a calculated Gaussian laser spectrum. The frequency scale for this spectrum is obtained by dividing the number of pixels between two maxima in the interferogram by the FSR of the interferometer ($4\,\mathrm{GHz}$). Subtracting the normalized seed laser interferogram from a synthetically broadened interferogram yields a characteristic double peak which is particularly pronounced at the location of the steep flank of the interference peak. Fig. 5.31 shows the difference in this particular region. One can see that a spectral line width of $100\,\mathrm{MHz}$ should already produce a pronounced signature and we can therefore conclude that the spectral width of the Ti:Sa pulses lies below this value.

Measured with Multipass Absorption Cell The long path or multipass absorption cell has been introduced in Section 3.2.1. As stated there, it provides a mean of quantifying the spectral purity of the injection seeded laser pulses. The optical setup used for coupling the light

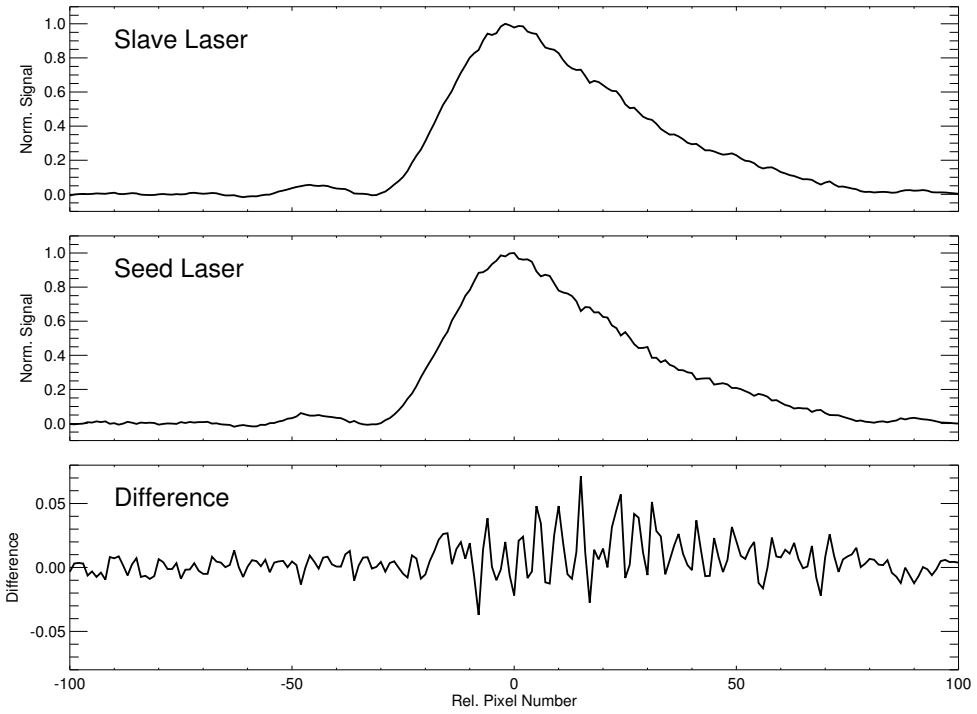

FIGURE 5.30: Part of the interferogram from slave and seed laser and the difference of the two signals. The signals have been normalized and the x-axes shifted such that the location of the peak is the same for both signals.

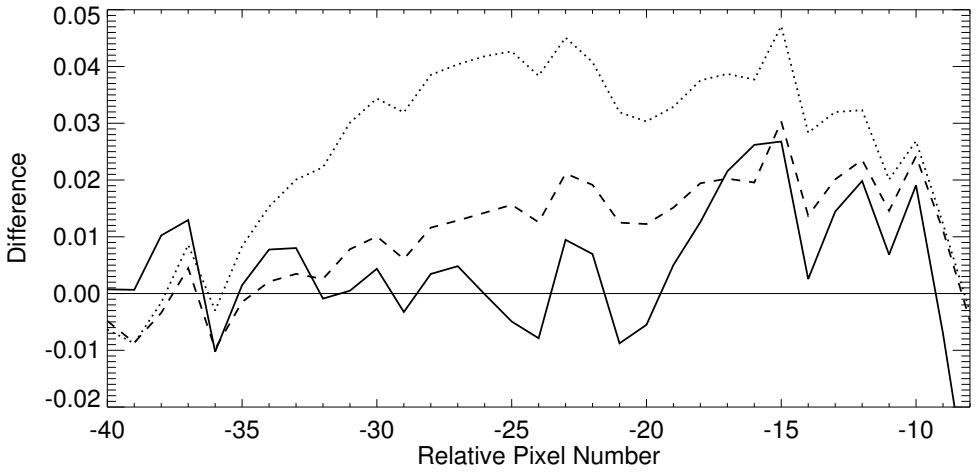

FIGURE 5.31: Difference between slave laser and seed laser interferogram (same as in Fig. 5.30, solid line) and differences between synthetically broadened interferograms and the seed laser interferogram. The laser line widths (FWHM) for calculating the broadened interferograms were 100 MHz (dashed) and 200 MHz (dotted)

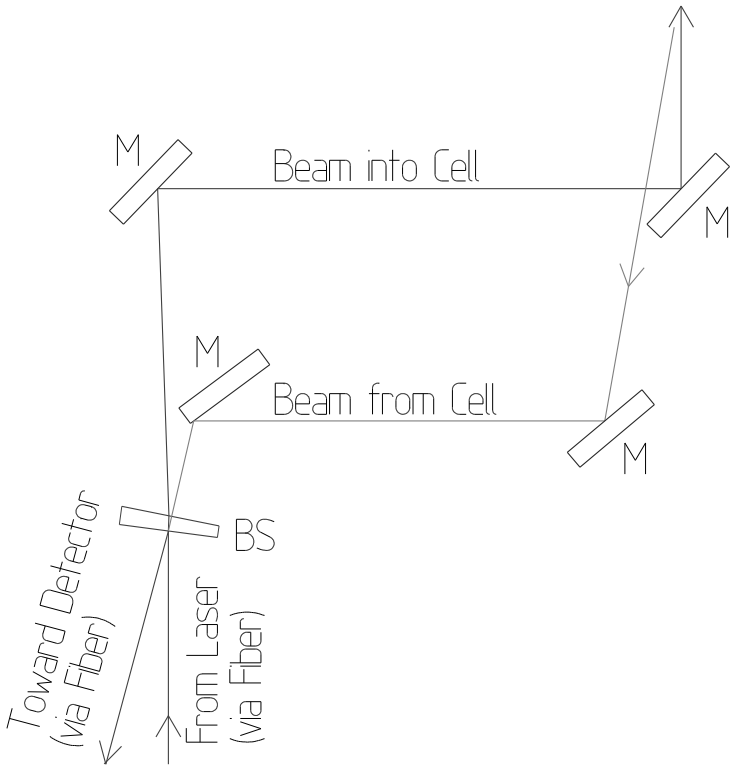

FIGURE 5.32: Optical setup for coupling laser light in and out of multipass absorption cell.

in and out of the absorption cell is sketched in Fig. 5.32. It is mounted on a small breadboard which is directly bolted to the absorption cell. The light is transported from the laser to the cell and from the cell to the detector by means of optical fibers. This allows the setup to be aligned with a visible laser. Furthermore, the cell which is quite bulky does not need to be installed on the same optical table as the laser. The light intensities going into and coming out of the cell are measured with the same detector (Femto HCA-S photoreceiver with $1\,\mathrm{MHz}$ bandwidth), the ingoing and outgoing pulses can be separated by their travel times. The difference of the travel times also gives a measure of the absorption path length. A small fraction of the ingoing light is reflected toward the detector by the beam splitter, an uncoated glass wedge. The small angle of incidence is chosen in order to make the reflectivity of the beam splitter polarization in-sensitive. The beam coming out of the cell which is not collinear with the ingoing beam, is steered through the back of the beam splitter by two mirrors such that it eventually also reaches the end of the fiber which leads to the detector. The light intensities of the two beams reaching the detector can be varied by changing the coupling efficiency into the fiber by tilting the beam splitter or one of the steering mirrors.

For the measurement the cell was filled with $22\,\mathrm{hPa}$ of pure water vapor at a temperature of $26\,^{\circ}\mathrm{C}$ and the absorption path length was $650\,\mathrm{m}$. The theoretical transmission of the cell around the strong absorption line at $12195.191\,\mathrm{cm}^{-1}$ was calculated using line parameters from the ESA-WV database [35, 36]. At the line maximum, the theoretical transmission of the cell is only $1.3 \cdot 10^{-10}$. Hence a wide frequency range around the line center is available where the theoretical transmission is significantly lower than $0.5\,\%$ and the spectral purity can thus be quantified to the needed accuracy without strict requirements for the stability of the laser frequency.

In order to quantitatively measure the transmission through the absorption cell, a wavelength scan was conducted starting at $12195.591\,\mathrm{cm}^{-1}$ where the calculated absorption is only $3\,\%$. At this wavelength the measurement was calibrated as the transmission of the optics was not known. Then the laser frequency was changed in discrete steps toward the absorption line

center. Whenever the light intensity coming out of the cell became too small due to increasing absorption, the ratio of ingoing and outgoing light intensity going to the detector was readjusted. In order to maintain the calibration, measurements at the same wavelength both with the old and the new intensity ratio were taken. The measured wavelength dependent transmission is

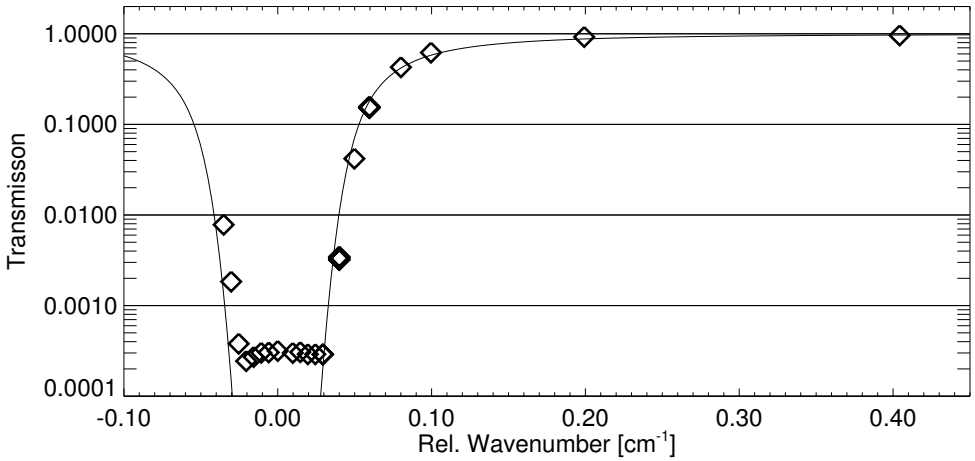

FIGURE 5.33: Measured (Diamonds) and calculated (line) transmission through multipass absorption cell. The wavenumber is given relative to the absorption line center at $12195.191\,\mathrm{cm}^{-1}$.

shown in Fig. 5.33 together with the theoretically calculated absorption. It is clearly visible that the measured transmission remains fairly constant in a certain range around the line center. Averaging over these points we obtain a value of $0.03\,\%$ for the residual transmission and hence a spectral purity of $99.97\,\%$. This agrees remarkably well with the value for the seed efficiency obtained from the backward to forward pulse energy ratio (see. Fig. 5.20). So it can be stated that the spectral purity of the laser pulses by far exceeds the demanded value and that the ratio for the pulse energies emitted in the backward and in the forward direction does provide a good way to measure this spectral purity.

5.8 Construction of a DIAL System

To demonstrate the new laser's suitability for water vapor DIAL measurements, a preliminary lidar system was constructed by fitting the laser with a receiving unit and a data acquisition system. For this, the system was transferred into a standard 20 foot container. Laser and receiving telescope rest on an optical table of the size of $1.8 \times 1.2\,\mathrm{m}^2$. All necessary equipment fits on or underneath the table and in an additional $19''$ electronics rack. Although the setup is not optimized for compactness, it fills only a small fraction of the container's interior. The telescope is mounted horizontally onto two sliding rails. Rigidly connected to this movable setup are a steerable dielectric mirror (diameter $50\,\mathrm{mm}$) for the laser beam and a fixed gold coated mirror ($45 \times 32\,\mathrm{cm}^2$) for the backscattered light. Both mirrors are mounted at a 45° angle such that the laser beam is deflected to the vertical direction and the light backscattered from the zenith is deflected toward the horizontally mounted telescope. Through an opening in the container wall, the telescope unit can be moved forward such that the deflection mirrors stick out of the container and have an unobstructed view to the sky. Just in front of the telescope, a plastic plate is mounted which only leaves openings for the telescope diameter and the laser beam. This plate moves up to the container wall when the telescope unit is slid out, thus minimizing the exchange of air between the container and the outside environment. A summary of the principal components and parameters of the DIAL system is given in Table 5.2.

beam expander	$6.25\times$
nominal beam divergence	0.18 mrad
telescope	Celestron C11, Schmidt-Cassegrain, $f/10$, diameter 28 cm
field of view (full angle)	1.1 mrad
interference filter	Barr Associates, bandwidth 1 nm FWHM
detector	Licel APD, integrated preamplifier
voltage "post amplifier"	Femto DHPVA-S, gain $20-40$ db, bandwidth 5 or 7 MHz

TABLE 5.2: Most important parameters and components of the new Ti:Sa DIAL system

The first atmospheric measurements were collected at Falkenberg (see Section 5.9) during April 2003 when the laser was operated in the configuration described above, i.e. with the 20 Hz pump laser. After this first test which already yielded good results, the pump laser was replaced by a 50 Hz Brilliant model. The 20 Hz model had a so-called GRM resonator (output coupling mirror with a Gaussian reflectivity profile), yielding a beam with low divergence and good focusability (i.e. low M^2 value), but inhomogeneous intensity profile (see Fig. 5.16). The new 50 Hz model on the other hand has a multimode beam profile with higher divergence and M^2 value, but also a more homogeneous intensity distribution and improved energy and pointing stability. Now focusing with an $f = 25$ cm lens yields the required beam diameter directly at the focus. Fig. 5.34 shows the measured beam profile. The smoother profile apparently results

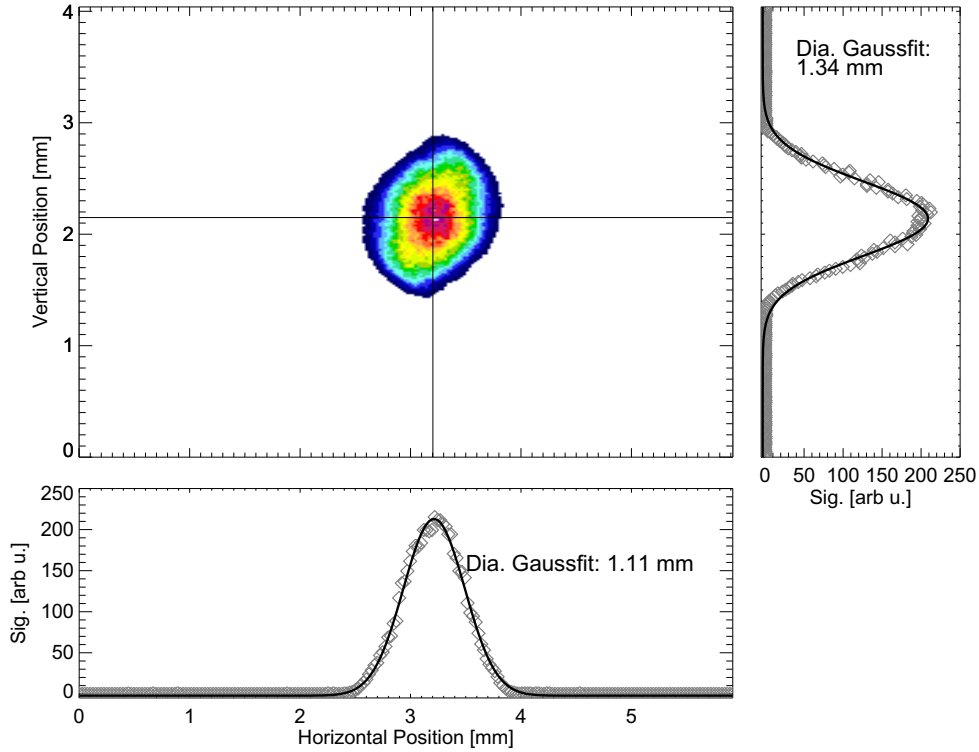

FIGURE 5.34: Beam profile of the 50 Hz Brilliant laser, measured at the focus of an $f = 25$ cm lens. Also shown are cross sections through the centroid together with Gaussian fit curves. The effective diameter as defined in Section 5.5.1.3 is 1.17 mm.

in better efficiency, so the output energy for seeded operation was 15 mJ at a pump energy of 35 mJ. The pulse energy fluctuations (long and short term) are now reduced to $\pm 1.7\,\%$ (standard deviation) compared to $6.7\,\%$ with the 20 Hz model. The ellipticity of the beam profile apparently does not cause problems. One can expect that the smooth profile also leads to

an increased damage threshold so that even significantly higher pump and output energies may be possible (the pump laser's maximum output energy is 65 mJ).

5.9 First Atmospheric Measurements

The first measurements with the newly assembled DIAL system in its final configuration were conducted at the Falkenberg site for boundary layer investigations ($52.17°$N, $14.12°$E, 75 m asl) which is part of the Meteorological Observatory Lindenberg (MOL) of the German Weather Service (Deutscher Wetterdienst, DWD). The main facility of MOL is located approximately 5 km to the north of the Falkenberg site. Radiosondes are launched from this main facility. The experiment lasted from 20 May until 14 Jun 2003. It took place at the same time as one field campaign of the EVA-GRIPS (regional evaporation at grid/pixel scale) project [97]. One goal of EVA-GRIPS was to measure turbulent fluxes, in particular evaporation, over complex terrain. Therefore a variety of measurements was carried out, among them surface based in situ flux measurements using the eddy correlation method, airborne in-situ turbulence measurements with the so-called HELIPOD, an instrument platform suspended from a helicopter, and remote sensing measurements with the MPI alexandrite DIAL system and the MPIWTR90 (a radar-rass system for profiling wind and temperature). The purpose of the latter two was to measure profiles of absolute humidity and vertical wind in (nearly) the same volume for the calculation of profiles of the vertical water vapor flux. This wealth of different measurements together with the radiosondes launched routinely at MOL gave a good opportunity to characterize the performance of the new Ti:Sa DIAL system

The weather conditions during the experiment were very favorable for lidar operations. High pressure conditions with sunny weather prevailed almost throughout the campaign. Rare thunderstorms occurred only from 5 Jun onward. Shallow fair weather cumulus clouds often started to form from late morning on, but their base was mostly located above 2000 m. The availability of the system during the experiment was very satisfactory, continuous operation over more than eight hours could often be achieved. The only limiting factor regarding uninterrupted operation turned out to be the offline seed laser which sometimes unpredictably ceased to operate single frequency with the effect that injection seeding could not be achieved anymore and the laser system was automatically switched off. This laser is anyway to be replaced by a Sacher TEC500 model which is already used for the online frequency and which did not cause any kind of problems during the campaign.

In the following, examples of the typical products that can be generated by the system shall be presented. It should be mentioned, that apart from absolute humidity, the system also provides the information of a single wavelength backscatter lidar, i.e. cloud base heights and qualitative aerosol distributions. To illustrate this, a time height-plot of $\ln(PR^2)$ for 4 Jun is shown. A textbook-like PBL structure development can be observed [98]. At first a residual layer is present, i.e. the remains of the convective boundary layer (CBL) from the previous day, extending up to about 3500 m. Several stably stratified aerosol layers can be observed within this layer. Then, at about 8:30 UT the formation of convective cells becomes visible and the newly-formed CBL eventually rises to the same height as the residual layer. At the top of these aerosol layers, the backscatter signal drops sharply (by a factor of more than five). From about 11:00 UT onward, cumulus clouds start to develop, at 16:00 UT cloud formation ceases, as the convection apparently dies down. Some cirrus clouds are also observed. This also shows that in the case of thin clouds, especially cirrus, not only the cloud bases but also the cloud tops can be observed, which in this case extend up to 13 km, the height of the tropopause (determined as the temperature inversion in the profile of the radio sounding at 07:45 UT).

For the water vapor products shown in the following, the height resolution used for the DIAL

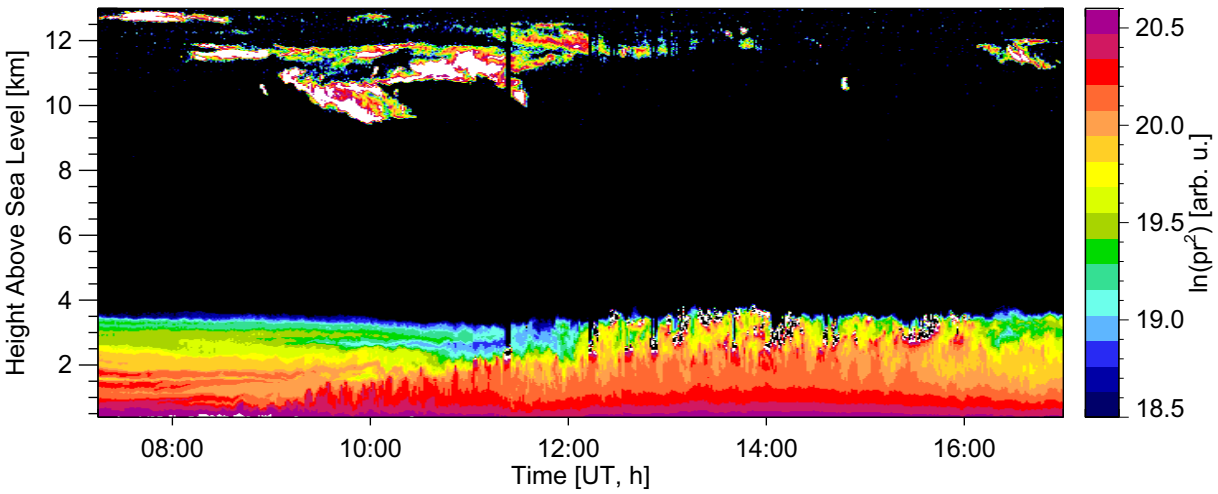

FIGURE 5.35: Time-height plot of $\ln\left(PR^2\right)$ (offline), measured at Falkenberg on 4 Jun 2003, averaged over 1 min.

inversion is 90 m up to 975 m asl, 180 m between 975 and 1875 m asl, and 300 m above. The online frequency for all measurements was $12193.247\,\mathrm{cm}^{-1}$ and the offline frequency around $12193.9\,\mathrm{cm}^{-1}$.

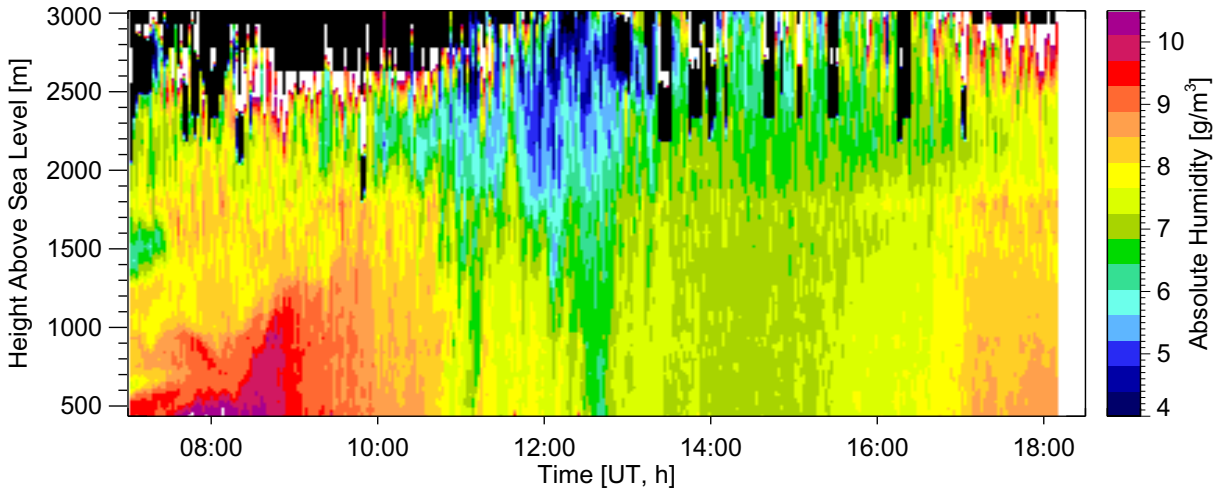

FIGURE 5.36: Time-height plot of the absolute humidity measured at Falkenberg on 3 Jun 2003 with the new Ti:Sa DIAL system, averaged over 2 min.

Time-Height Cross Section This kind of representation is very useful to gain a first overview of the temporal development of the vertical water vapor distribution. The longest uninterrupted measurement that was achieved (and was not ended due to technical problems) was collected on 3 Jun and lasted for 11 h 7 min. It is shown in Fig. 5.36. The most striking meteorological features are first the rise of the CBL starting at about 8:30 UT and the resulting dilution of the water vapor in the CBL due to entrainment of overlying dry air. Then, several changes in humidity can be observed, probably due to advection of different air masses, especially the decrease at 12:30 UT (starting earlier at higher altitudes). A more technical aspect is that at the beginning of the measurement unrealistic or undefined humidity values are obtained above 2400 m. This is not caused by clouds, but by a too low online signal. It can be seen that, because of reduced absorption, the range becomes bigger when the overall humidity decreases, e.g. at

12:30 UT. For an automatic inversion algorithm, criteria need to be found to determine at which altitude systematic errors become too large. Indicators for this can be the statistical error and the absolute signal level. An increase of the dynamic range of the detector and the DAQ system is of course also desirable. The first step will be the addition of a second receiving channel optimized for the far range with a larger telescope and a smaller field of view.

Mean Profiles Mean profiles of absolute humidity, averaged over periods of 5 to 15 min will probably be the primary product for a DIAL system operated as part of a meteorological observation site, as the DWD plans to do in the context of the GVaP reference station and in the context of CM-SAF for the validation of satellite products. For the EVA-Grips campaign, a large set of radiosonde profiles is available. In an automatic procedure, mean DIAL humidity profiles averaged over 10 min were calculated for each radiosonde ascent that lay within or close to the operating times of the DIAL system. The profiles were calculated such that the start of the averaging period is equal to the time of the sonde launch. If a DIAL measurement started too late or ended too early, a profile was calculated with the start as close as possible to the sonde launch, but not more than 30 min away. This time, no attempt was made to choose cloud-free periods, as cloud bases were usually rather high. An overall number of 54 profiles could be calculated in this way.

In the following, two sets of 8 profiles each will be shown, the first set with profiles showing very good agreement between DIAL and radiosonde (Fig 5.37), the second set with profiles showing significant deviations (Fig. 5.37). The statistical error indicated by the error bars is

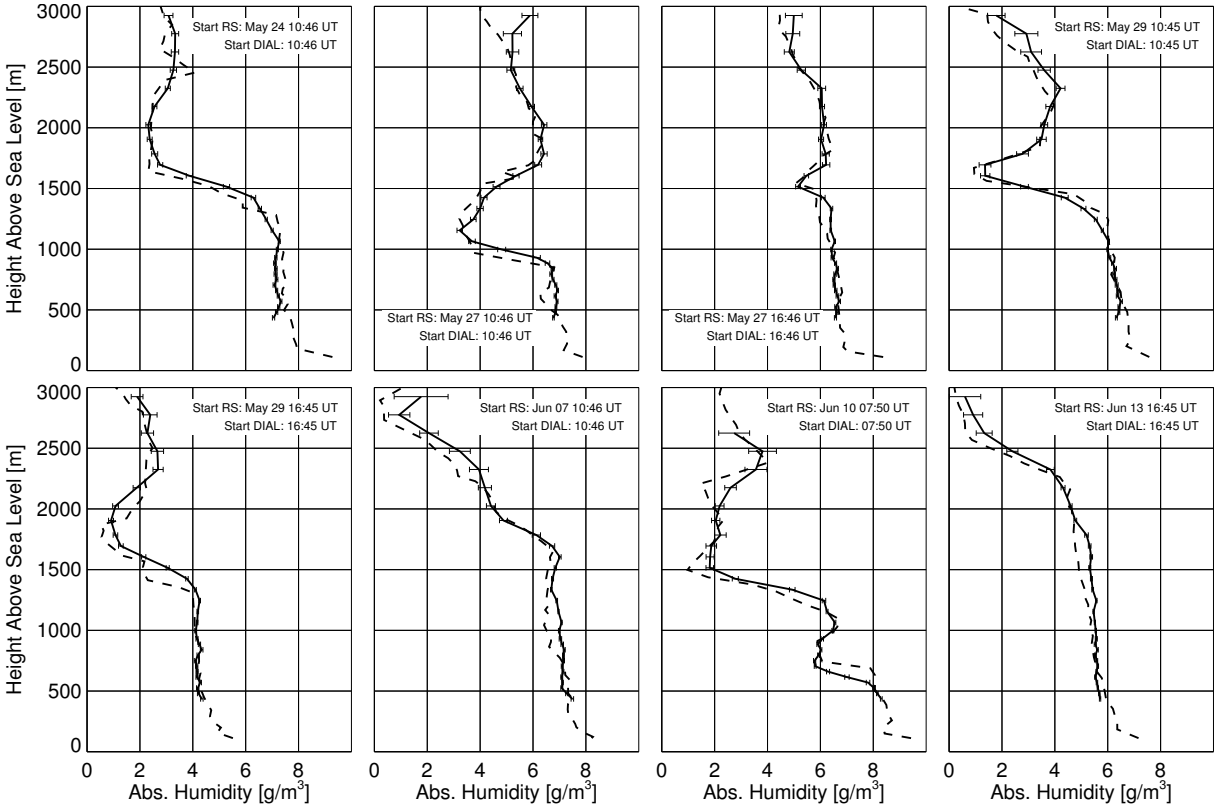

FIGURE 5.37: Profiles of absolute humidity measured at Falkenberg by DIAL (solid line) and radiosondes (dashed line). Error bars indicate the statistical error of the DIAL measurement. For more details see text.

calculated from the variance of the 10 s-resolution time series. The relative statistical error for the 10 min profiles stays below 1 % up to 1000 m for practically all profiles, for many even up to

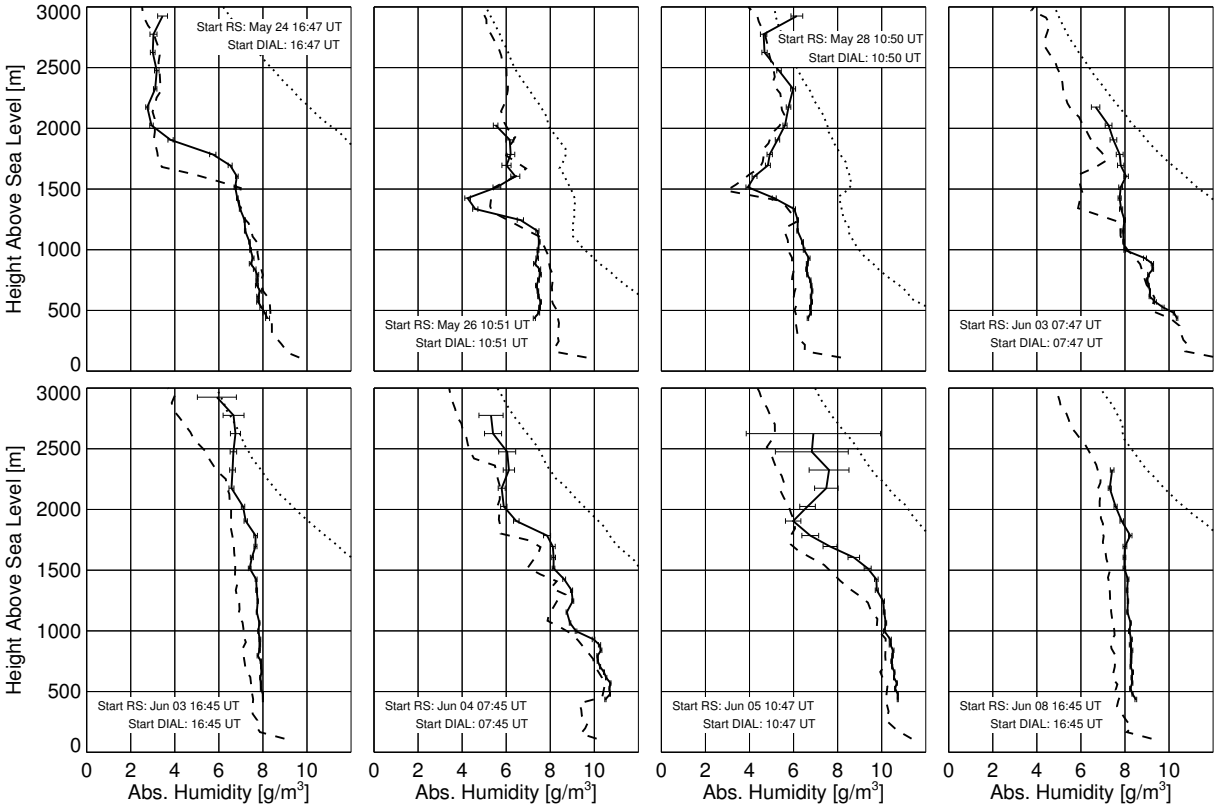

FIGURE 5.38: Profiles of absolute humidity measured at Falkenberg by DIAL (solid line) and radiosondes (dashed line). Error bars indicate the statistical error of the DIAL measurement. Also shown is the saturation humidity (calculated from radiosonde data, dotted line). For more details see text.

1500 m and more. A more detailed discussion of statistical errors will follow in the next paragraph. Regarding the systematic differences between DIAL and radiosondes, the differences observed in Fig. 5.38 do not give an indication of any problems regarding the performance of the laser system. Such problems like detuning and low spectral purity will always lead to an underestimation of the absolute humidity. The fact that the absolute values differ in the near range, i.e. inside the boundary layer and also that the heights are different at which borders of layers are located can most likely be attributed to the fact that the two instruments sampled different volumes, especially as the radiosonde launch site was located 5 km away from the DIAL. This is particularly obvious for the profiles in the last column of Fig. 5.38: both profiles had to be cut at the upper end because of an overlying cumulus cloud (the presence of clouds was inferred form the lidar backscatter signal). The humidity measured by the radiosonde however never comes close to the saturation level.

The first three profiles in the bottom row in Fig. 5.38 show the phenomenon already mentioned in the context of Fig. 5.36 (the first of the three profiles is from that period): above a certain height, in particular above the PBL, large statistical and also systematic errors can be found. This is caused by the fact that the online signal becomes too small. This first results in a low signal-to-noise ratio and also makes the calculated humidity very sensitive to a bias in the determined background level, which can never be entirely avoided. As opposed to the cases described in Section 3.3 however, here this systematic bias only starts to play a significant role when the signal level is already close to the detection limit and any attempt to correct the signal offset does not lead to a significant extension of the useful measurement range. In other words, the systematic error is not larger than the random error.

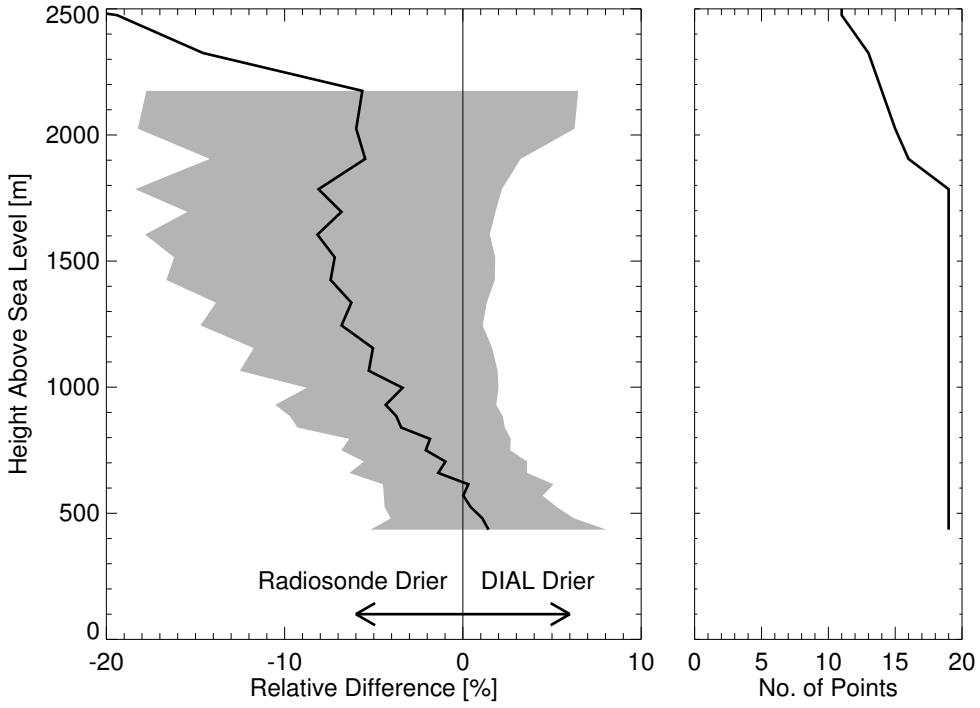

FIGURE 5.39: Mean relative difference between radiosonde and DIAL humidity profiles measured during EVA-GRIPS (left panel). The gray area indicates the standard deviation of the differences. Some profiles had to be cut at the upper end due to overlying clouds. The number of valid points for each height level is indicated in the right panel.

For a quantitative assessment of the differences between DIAL and radiosondes, those profiles were selected where the first significant drop in humidity occurs at 1800 m asl or above. This was to eliminate the difference that arises when boundaries of humidity layers are lo-

cated at different altitudes for the two instruments. The condition was fulfilled for 19 profiles. Fig. 5.39 shows a profile of the mean relative difference between radiosondes and DIAL together with the standard deviation of the differences. It can be seen that the mean difference starts from near zero at the bottom end of the DIAL height range and then steadily increases to around $-7\,\%$ at $1500\,\mathrm{m}$ asl. Above $2200\,\mathrm{m}$ asl the difference increases sharply due to the systematic error in the determination of the lidar signal level. So apart from the first $200\,\mathrm{m}$, the DIAL consistently yields higher humidity values than the radiosondes. The fact that the mean difference even shows a slight decrease above $1500\,\mathrm{m}$ asl indicates that this is not caused by the systematic errors in the DIAL data just mentioned. The standard deviation of the relative differences increases from $5\,\%$ at the bottom end of the profile to $12\,\%$ at $2200\,\mathrm{m}$ asl.

Time Series / Spectra Due to the high temporal resolution, the possibility exists to study turbulent processes using water vapor DIAL. An example where convection induced turbulent structures in the water vapor field can be observed is shown in Fig. 5.40. Much longer uninterrupted measurements are available, but it proved difficult to find cloud-free parts with stationary conditions. On 4 Jun e.g. (see Fig. 5.35), the conditions remained stationary throughout the afternoon, from the time the CBL had fully developed until convection ceased, but during that time, boundary layer clouds did occur. Even for the selected period on 10 Jun, stationary condi-

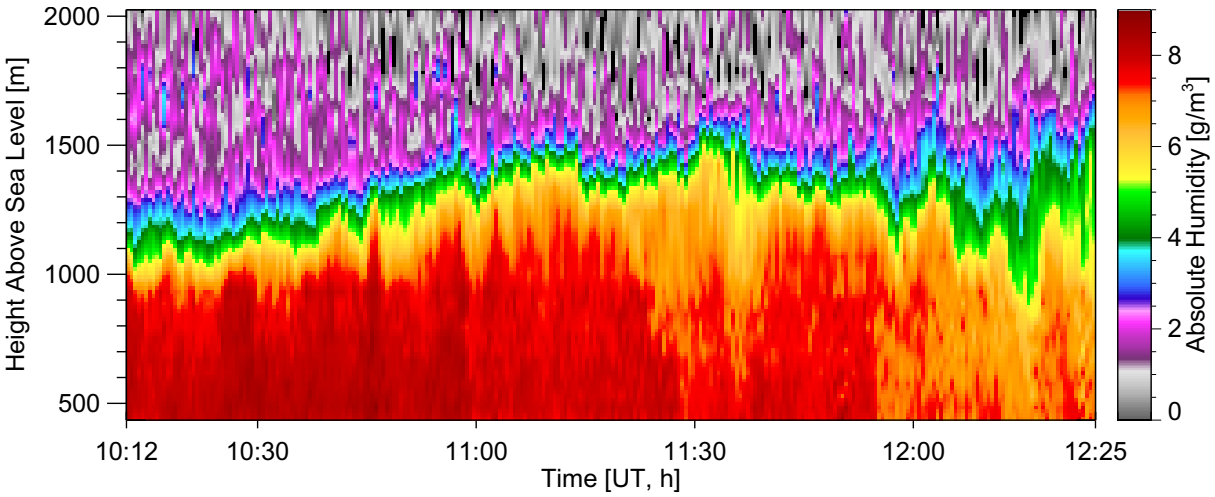

FIGURE 5.40: Time height plot of absolute humidity for 10 Jun 2002, averaged over $30\,\mathrm{s}$.

tions are not really given and progressive drying can be observed. This is particularly obvious from the time series for a single height shown in Fig. 5.41. Apart from the overall trend however, strong turbulent fluctuations can be observed in the time series. Together with information about the vertical wind, time series like this can be used for calculating the latent heat flux. Vertical wind profiles can be measured by a radar-Rass system [99, 100] or a Doppler wind lidar system [75]. The variance spectrum of this time series is shown in Fig. 5.42 in a double logarithmic representation. Variance spectrum meaning here that the integral over the spectrum shall be equal to the variance of the time series. Therefore no windowing and no trend correction was applied. A straight line showing an $f^{-5/3}$ slope is shown for comparison. One part of the spectrum appears to follow this $f^{-5/3}$ dependence quite well, which is expected for turbulence spectra in the so-called inertial subrange. This is the frequency range where kinetic energy is neither produced nor dissipated, but passed down from larger to smaller eddies.

Apart from studying turbulent processes, variance spectra are also useful to separate true atmospheric fluctuations in a time series from fluctuations that are caused by system noise, i.e. by statistical measurement errors [99]. Even if the prerequisites for a classical Kolmogorov-type

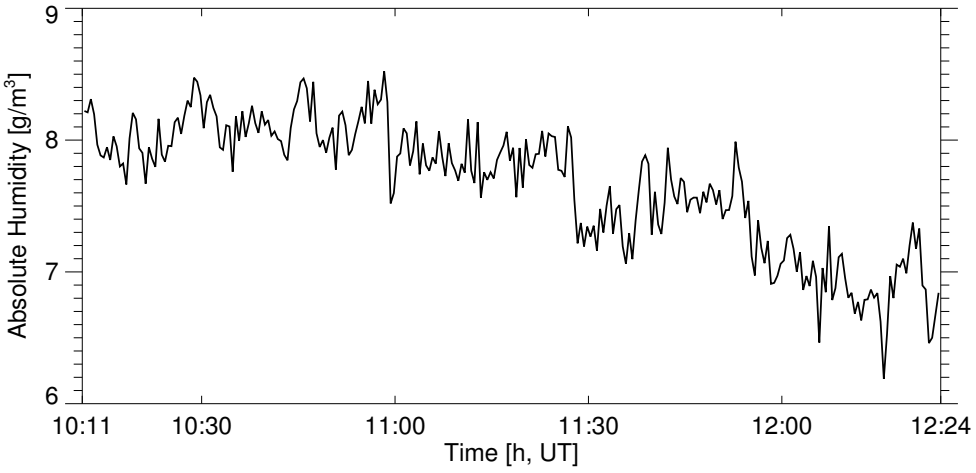

FIGURE 5.41: Time series of the absolute humidity for 10 Jun 2003 at 660 m asl, averaged over 30 s.

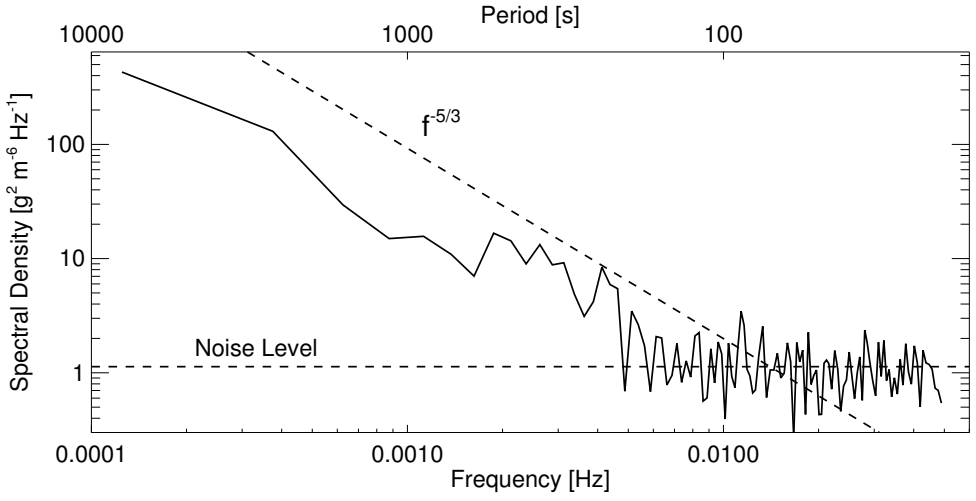

FIGURE 5.42: Variance spectrum of the time series shown in Fig. 5.41. For the calculation of the spectrum, no averaging was applied to the time series.

turbulence spectrum should not be met, the spectral atmospheric variance should always show a decrease toward the high frequency end, at least on the time scales and at the height levels investigated here, i.e. with the highest resolved frequency being 0.05 Hz and the lowest height about 300 m above ground. As the system noise should show a white spectrum, the variance level at the high frequency end of the spectrum gives an estimate of the upper limit of this noise level. The procedure of using the variance spectrum to extract the system noise level is illustrated in Fig. 5.42. The noise level indicated in Fig. 5.42 was calculated as the average over the spectral variance above 0.0375 Hz. Integrating the noise level over the entire frequency range yields a variance of $0.057\,\mathrm{g}^2/\mathrm{m}^6$. This means that the statistical measurement error (at 10 s resolution) is $0.24\,\mathrm{g/m}^3$. After the system noise level has been determined, the atmospheric variance component can be calculated as the total variance minus the system noise. In the case presented here, it amounts to $0.22\,\mathrm{g}^2/\mathrm{m}^6$. If this spectral analysis is applied to all height levels of the water vapor field, profiles of the atmospheric as well as of the system noise variance can be obtained. Such profiles are shown in Fig. 5.43. The atmospheric variance shows a slight increase with height at

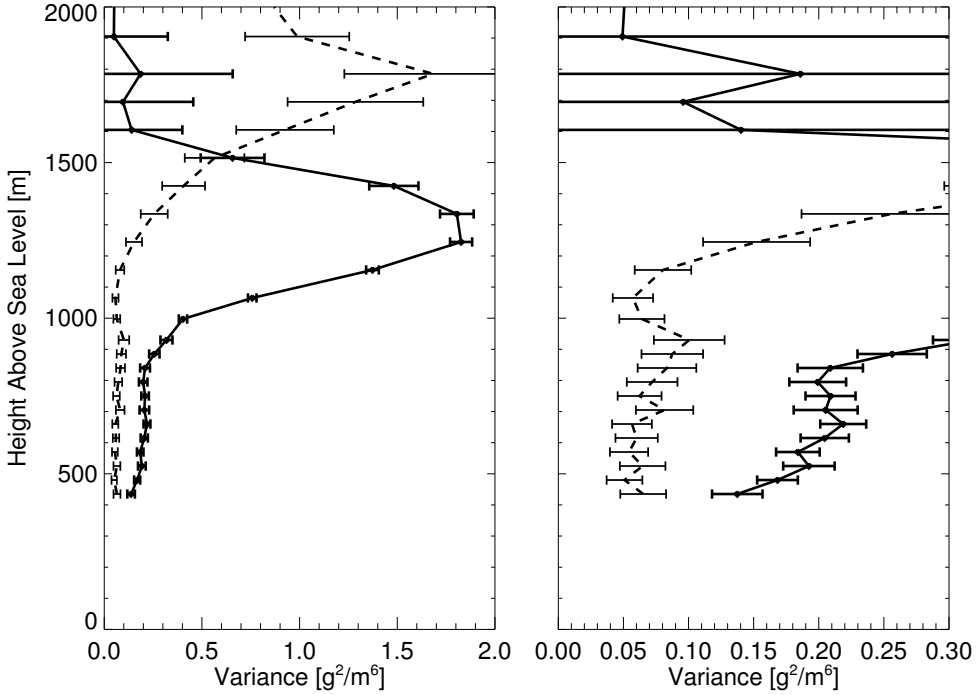

FIGURE 5.43: Humidity variance profiles calculated by applying the spectral method presented in Fig. 5.42 to each height level. Shown are the system noise component (dashed line) and the atmospheric component (solid line). The right panel shows the same data as the left panel with a reduced x-axis range in order to better illustrate the behavior in the lower range. The error bars indicate the statistical errors of the variances, calculated using the formulas from [101].

the bottom of the profile and then a very pronounced maximum in the region of the entrainment zone, where the time series cut through moist boundary layer air and through dry air from the free troposphere. The system noise profile shows a general increase with height which is due to the decreasing signal level. A decrease of the system noise is observed at the points were the height resolution is lowered, i.e. at 975 m and at 1875 m. Fig. 5.43 illustrates that profiles of the humidity fluctuations are particularly useful for the determination of the CBL height and for locating the entrainment zone [12]. Other possible applications are comparisons to computer model results and the calculation of higher order statistical moments [101] .

Chapter 6

Summary and Outlook

6.1 Summary

The beginning of the work described in the previous chapters was marked by the participation in a series of field campaigns where the existing MPI alexandrite DIAL system was employed for water vapor measurements. Extensive post-processing of the data was necessary in order to bring the accuracy of the calculated absolute humidity to an acceptable level. The problems that had to be dealt with can be divided into fundamental issues which are relevant for DIAL systems in general and issues connected to the particular laser transmitter that was used.

The first of the fundamental issues is the accuracy of the calculated differential absorption cross section $\Delta\sigma$ that is required to convert the measured differential absorption to absolute humidity. This accuracy can be impaired if:

- Inaccurate absorption line parameters are used. We believe that the parameters listed in HITRAN [27, 28] show substantial systematic errors and that the parameters which are published in Grossmann and Browell [26,22] and Ponsardin and Browell [32] are of much higher accuracy.
- The calculation of $\Delta\sigma$ is over-simplified, meaning that the effect of self-broadening and the contribution of neighboring lines to the online and offline absorption cross sections is neglected.
- The offline wavelength is chosen in a region where the absorption is not negligible and strongly dependent on the wavelength as e.g. on the slope of a strong absorption line.

These findings have led to the revision of the DIAL inversion algorithm and the compilation of a list of what we believe are the best values for the absorption line parameters required for the DIAL inversion. Furthermore, it has been evaluated what the best possible online/offline combinations are and what absorption lines need to be included in the calculation of $\Delta\sigma$.

The second fundamental issue is the accuracy of the measurement of the backscattered light intensity. It was found that this accuracy can be compromised by errors in the determination of the signal baseline. These errors are due to electromagnetic interference (EMI) that is generated when the laser is fired. It has been shown how this EMI manifests itself for two different data acquisition systems and how its influence can be corrected. Due to the inherently high signal dynamics in ground based DIAL, the errors caused even by small EMI-induced signal offsets can exceed the acceptable level already at a very small range. It also has to be emphasized that the accuracy levels which are sought are beyond the ones guaranteed by the manufacturers of data acquisition equipment. Otherwise, the measurement range would be very limited for ground based systems. Measurements with downward-looking airborne systems are much easier in this respect.

A data quality issue connected to the specific system is the bad performance of the laser transmitter with respect to the spectral properties. By using a photoacoustic absorption cell, it was discovered that very often the laser shots showed a high degree of spectral impurity or that the laser frequency was detuned from the set value. In the case of spectral impurity, no correction was possible and the data had to be discarded. For the detuning, a procedure was developed to infer the true operating frequency of the laser transmitter by evaluating the change in photoacoustic absorption that is associated with a mode hop of the Ti:Sa master laser. By using this true frequency when calculating the absorption cross section, the effect of laser detuning could be corrected for.

After the data collected during the field campaigns in 1999 and 2000 had been subjected to the various correction and control procedures, an acceptable level of data quality could be reached. Some examples of these data were presented, among them the first ship based water vapor DIAL measurements conducted during the Nauru99 campaign. At the same time, this was probably the first demonstration of ground based water vapor DIAL measurements under tropical conditions. During this campaign, a rather large dataset was collected, so procedures for automated processing and visualization of such large amounts of data were developed. Apart from the possibility of conducting measurements in a truly marine environment, another novel aspect of ship based operation was the possibility of using the ship as a mobile platform. Circumnavigating Nauru island, it was thus possible to detect that the island causes a major disturbance to the marine boundary layer. This potentially results in a bias in the measurements taken at the ARCS-2 (atmospheric radiation and cloud station) which is unfortunately located on the western shore, i.e. on the downwind side of the island.

The detected unsatisfactory performance of the alexandrite DIAL system together with its inherent limitations regarding technical reliability led to the decision to develop a new laser system. A more reliable laser transmitter is particularly needed for the projected installation of a water vapor DIAL system at the Lindenberg observation site of the German Weather Service. The best concept for a new laser was identified to be an injection seeded, gain switched Ti:Sapphire ring laser, operating in the $820\,\mathrm{nm}$ wavelength region. Aspects of the laser principle and of the chosen implementation which provide for a greatly improved stability are the following:

- Injection seeding is provided by two ECDLs (external cavity diode lasers). These are more compact, less complex and less expensive, and yield a more stable performance than other possible sources. The use of separate lasers for the online and offline wavelengths facilitates the monitoring and the stabilization of the two wavelengths.

- No optical elements are needed inside the Ti:Sa slave laser cavity except the laser crystal itself. This reduces losses and hence increases the output power, reduces the risk of optical damage, and allows for a compact setup.

- The seed efficiency and hence the spectral purity can be very easily monitored on a single shot basis by means of the laser pulse energy emitted in the backward direction.

- As the Ti:Sa laser is laser pumped, a high conversion efficiency is achieved and the heat load of the laser crystal is therefore greatly reduced. This results in a more controlled behavior. As a pump laser, q-switched, frequency-doubled Nd:YAG or lasers based on similar materials such as Nd:YLF or Yb:YAG can be used. These lasers are of high technical maturity and consume comparatively little space and energy.

- The master lasers and the slave laser are actively stabilized and the critical parameters are continuously monitored.

In the final setup, using the 50 Hz Quantel Brilliant laser as pump source, an output energy of 15 mJ could be achieved. This is well above the specified minimum of 6 mJ. The average power is in the same order as for other existing DIAL systems. The spectral properties of the output pulses are well withing the required specifications. Continuous operation over more than 11 h could be achieved. The only limiting factor for achieving longer times of operation on a truly routine basis proved to be the master laser for the offline wavelength, which will shortly be replaced by a better model that was already successfully used for the online wavelength.

The results of the first atmospheric measurements conducted near Lindenberg in April, May, and June 2003 proved to be very satisfactory, although only a preliminary, non-optimized receiving setup was used. No indications of shortcomings in the laser system performance could be found so far.

6.2 Outlook

Although nothing hints at data quality problems due to unsatisfactory laser performance, the data collected during the EVA-GRIPS campaign will be examined more thoroughly. In addition to radiosonde data, the Ti:Sa DIAL measurements will be compared to in-situ tower and HELIPOD measurements and especially to measurements taken with the alexandrite DIAL system. An in-depth analysis of the raw lidar signals as well as of the recorded laser parameters will be conducted too.

An intensive, long term test over several months at Lindenberg is planned for summer 2004. Before this, a second telescope channel optimized for far-range measurements will be added to the receiver setup. It could also be explored as to which extent the output power can be increased without damaging the laser crystal or deteriorating the laser performance. Furthermore, it will be investigated to which extent the experimental electronic and optical setup should be reengineered. Regarding the electronics, a migration to a more stable and more network-friendly platform than Windows98 will be considered, i.e. Linux together with the currently used input/output hardware or with a DSP-based architecture. The optical setup can be transferred from the breadboard to a "made-to-measure" aluminum case, now that the geometry is fixed. It should however first be scrutinized if this really yields an increase in mechanical and especially in thermal stability. On one hand, aluminum has a large thermal expansion coefficient and on the other hand, the breadboard which is currently used is of very high quality and it already incorporates sophisticated measures for thermal drift reduction and damping of high-frequency vibrations.

The laser system presented here also offers a good basis for the construction of a high-power DIAL transmitter as proposed in [62, 63] . High average power Ti:Sa systems both at low and at high repetition rates are well established in the field of ultrashort pulse generation [102,103,104]. Whether high power output at wavelengths around 940 nm can be achieved with a Ti:Sa system is not certain, but for ground based applications the 820 nm region is at least as suitable.

A high repetition rate system could be based on a high power diode pumped laser. One model which has recently entered the marked provides an output pulse energy of 18 mJ at a repetition rate of 5 kHz [105]. If a similar conversion efficiency as presented here can be achieved, almost 40 W of average output power would be reached. Providing proper thermal management (see below), the Ti:Sa laser could consist of a single oscillator not unlike the one described in this work. One problem of diode pumped lasers is the long pulse length of typically more than 100 ns. It has to be verified if gain-switched operation as presented here is still possible then.

A low repetition rate system could consist of the laser described in this work together with one or more multipass amplifier stages. The amplifier would be pumped by a high power

flashlamp-pumped laser which can provide pulse energies up to $600\,\mathrm{mJ}$ at a repetition rate of $50\,\mathrm{Hz}$ [106]. Assuming again the same conversion efficiency, the resulting output power would be almost $13\,\mathrm{W}$. The output power can be scaled up further by employing more than one pump laser, either by pumping a laser crystal from both ends or by setting up a multistage amplifier chain.

The biggest problem at very high pump power levels will probably be the thermal lens and the thermal birefringence induced in the laser crystal. These thermal effects can be greatly reduced or even completely eliminated if the laser crystal is cooled to low temperatures, as its thermal conductivity increases with decreasing temperature [107]. It is probably not necessary to go to cryogenic temperatures, but $-80^{\circ}\mathrm{C}$, which can be achieved with conventional chillers, may well be sufficient. It would then be required to house the crystal or the entire laser system in a vacuum for thermal insulation and in order to prevent condensation.

These brief considerations illustrate already, that such a DIAL system would be technically rather demanding and complex, but this is the price one has to pay for very high output powers. It has been shown however, that a far lower output power is well sufficient for measuring vertical humidity profiles. So for operational systems, a moderately powered laser is clearly the way forward, due to the greatly reduced technical complexity and the lower risk of optical damage. The system developed within the scope of this work presents a significant step toward such truly operational systems. If in the future the development effort will not be focused only on airborne, spaceborne, or ultra-high power systems and the work on ground based water vapor DIAL systems with moderate output power will be continued, this technique can be brought to a level of technical maturity that equals other passive and active remote sensing systems like Fourier transform spectrometers and radar wind profilers.

Due to the high spatial and temporal resolution and the continuous coverage, which other in-situ and remote sensing water vapor profiling instruments cannot provide, water vapor DIAL can make a great impact on meteorological research. As already laid out in Chapter 1, some important applications of operational water vapor DIAL systems are:

Ground truth: Satellites can provide global coverage, but reference stations are needed on the ground for validation and calibration of the measurements.

Climate monitoring: Long-term DIAL measurements yield high-resolution time series of the absolute humidity for many individual height levels. The knowledge about the variability of water vapor that is gained in this way is particularly useful for testing and developing atmospheric computer models.

Process studies: Reliable and compact instruments are not only needed for long-term observations, but also for the investigation of atmospheric processes in the framework of intensive field campaigns.

Appendix A

Absorption Lines and Parameters

A.1 Alexandrite Laser

In Table A.1, the possible online and offline frequencies to be used with the alexandrite DIAL system are given. The interference filter wavelengths are the ones currently available to us, the use of other online frequencies is of course possible with different filters. Table A.2 lists the necessary absorption line parameters which are needed for the calculation of $\Delta\sigma$ for the various online/offline combinations. For details see Section 3.1.

$\nu_{on}/\mathrm{cm}^{-1}$	$\lambda_{Filter}/\mathrm{nm}$	$S/10^{-24}\,\mathrm{cm}$	$\nu_{off}/\mathrm{cm}^{-1}$	$\Delta\nu_{on/off}/1.67\,\mathrm{cm}^{-1}$	Lines
13650.0270	733.0	3.04	13646.69	-2	1,2
13655.8170	733.0	2.20	13652.48	-2	4
			13654.15	-1	3,4
			13657.49	+1	4,5
13665.8201	733.0	4.80	13664.15	-1	6-9
13717.1750	729.2	7.25	13715.51	-1	10-12
			13720.52	+2	11-13
13718.5762	729.2	14.96	13720.25	+1	12
			13715.24	-2	12
			13721.92	+2	12
13726.4259	729.2	1.36	13723.09	-2	12,14,17-19
			13724.76	-1	12,15-19
13728.1798	729.2	4.50	13724.84	-2	16,19

TABLE A.1: Suitable online/offline combinations for the alexandrite based DIAL system. The best possible offline is quoted first. Here, $\Delta\nu_{on/off}$ stands for the difference between online and offline frequency, the last column lists the absorption lines required for the DIAL inversion (absorption lines and parameters are listed in Table A.2).

No.	ν_o	E''	S	$\Gamma_{c,air}$	$\eta_{c,air}$	$\Delta\nu$	α	Γ_{c,H_2O}	η_{c,H_2O}
1	13646.4103h	1006.1h	0.178h	0.0758h	0.68h	-0.0201c	0.89c	0.328h	0.38c
2	13650.0270g	42.4g	3.040g	0.1037g	0.68h	-0.0139g	0.57c	0.450g	0.78c
3	13654.6363h	0.0b	0.195h	0.0964h	0.68h	-0.0126c	0.51c	0.454h	0.79c
4	13655.8170g	212.2g	2.203g	0.0922g	0.75h	-0.0122g	0.48c	0.486h	0.89c
5	13659.8743g	586.2g	8.595g	0.0737g	0.43g	-0.0278g	1.30c	0.394g	0.54g
6	13662.5022g	552.9g	6.890g	0.0833g	0.74g	-0.0178g	0.78c	0.457g	0.66g
7	13663.2901g	136.2g	1.571g	0.0919g	0.66h	-0.0145g	0.60c	0.445g	0.76c
8	13663.9698h	136.8h	0.073h	0.0919h	0.68h	-0.0142c	0.59c	0.466h	0.83c
9	13665.8201g	134.9g	4.803g	0.0908g	0.77g	-0.0105g	0.40c	0.450g	0.79g
10	13712.9172g	325.3g	21.262g	0.0935g	0.69g	-0.0186g	0.82c	0.504g	0.85g
11	13717.1747g	275.5g	7.246g	0.0967g	0.71g	-0.0159g	0.68c	0.454g	0.79c
12	13718.5762g	300.4g	14.955g	0.0928g	0.74g	-0.0145g	0.60c	0.479g	0.77g
13	13720.4326h	0.0b	0.092h	0.0964h	0.68h	-0.0126c	0.51c	0.454h	0.79c
14	13722.3839h	382.5h	0.534h	0.0843h	0.62h	-0.0170c	0.73c	0.438h	0.74c
15	13724.6435h	0.0b	0.043h	0.0964h	0.68h	-0.0126c	0.51c	0.454h	0.79c
16	13724.8383h	0.0b	0.013h	0.0964h	0.68h	-0.0126c	0.51c	0.454h	0.79c
17	13726.0764h	0.0b	0.150h	0.0964h	0.68h	-0.0126c	0.51c	0.454h	0.79c
18	13726.4259g	142.3g	1.362g	0.0897g	0.76h	-0.0150c	0.63c	0.454g	0.78g
19	13728.1798g	136.8g	4.496g	0.0912g	0.62g	-0.0094g	0.34c	0.500g	0.91g

TABLE A.2: Absorption line parameters needed for the calculation of $\Delta\sigma$ for various online/offline pairs (see Table A.1). Units of the parameters: ν_o, E'', $\Gamma_{c,air}$, $\Delta\nu$ and Γ_{c,H_2O}: cm^{-1}, S: 10^{-24} cm, other parameters are dimensionless. The letter behind each parameter indicates the origin: g: Grossmann and Browell [26, 22], h: HITRAN 2001 edition, c: calculated from other parameters, b: best guess.

A.2 Ti:Sa Laser

In the following, online and offline frequencies and absorption line parameters for the new Ti:Sa DIAL system are given, similar to the previous section. With the new system, the offline frequency can be chosen arbitrarily. Fig. A.1 through Fig. A.6 show calculated spectra in the vicinity of each of the six selected absorption lines. Again, more lines are available if other interference filters are used. The offline region is indicated in each figure. It is chosen such that it is as close as possible to the online frequency and such that the absorption stays below $1\,\%$ of the online absorption (Fig. A.1, A.3, and A.5), or, if there is no region of negligible absorption available close enough to the line center, such that the absorption does not vary by more than 1 % of the online absorption (Fig. A.2, A.4, and A.6). With decreasing pressure (i.e. decreasing line width), the permitted offline frequency range always stays at the same location and even becomes wider. In all cases, the offline region is at least $10\,\mathrm{GHz}$ wide. For the lines at $12190.744\,\mathrm{cm}^{-1}$ (Fig. A.1), $12202.027\,\mathrm{cm}^{-1}$ (Fig. A.3), and $12226.101\,\mathrm{cm}^{-1}$ (Fig. A.5), the offline region can be extended to wavenumbers further away from the line center, but care should be taken that the separation between online and offline frequency does not become too large. The spectra were calculated using line parameters from the ESA-WV database and conditions that yield the maximum expected line broadening: $p = 1020\,\mathrm{mbar}$, $T = 30\,^{\circ}\mathrm{C}$ and $RH = 100\,\%$. These conditions were also used to evaluate which lines need to be included for the DIAL inversion as described in Section 3.1.2.

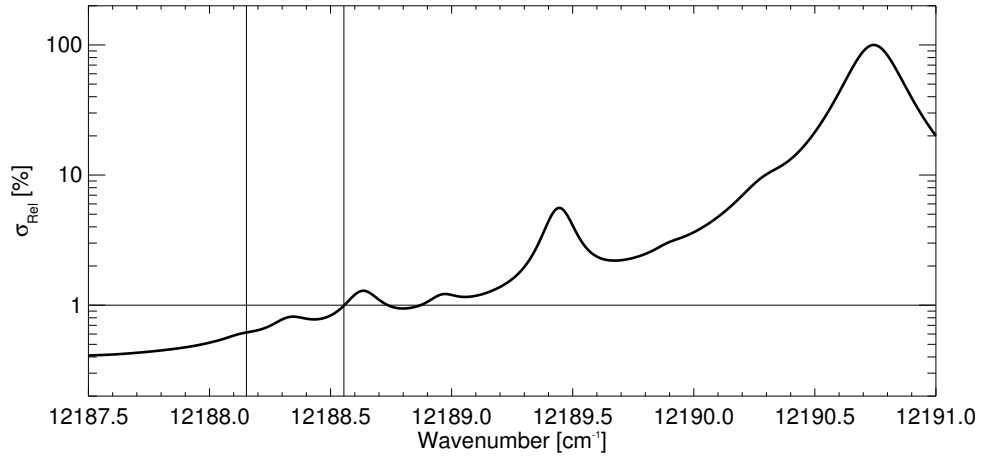

FIGURE A.1: Absorption spectrum of water vapor in the vicinity of the $12190.744\,\mathrm{cm}^{-1}$ absorption line. Vertical lines indicate the offline region.

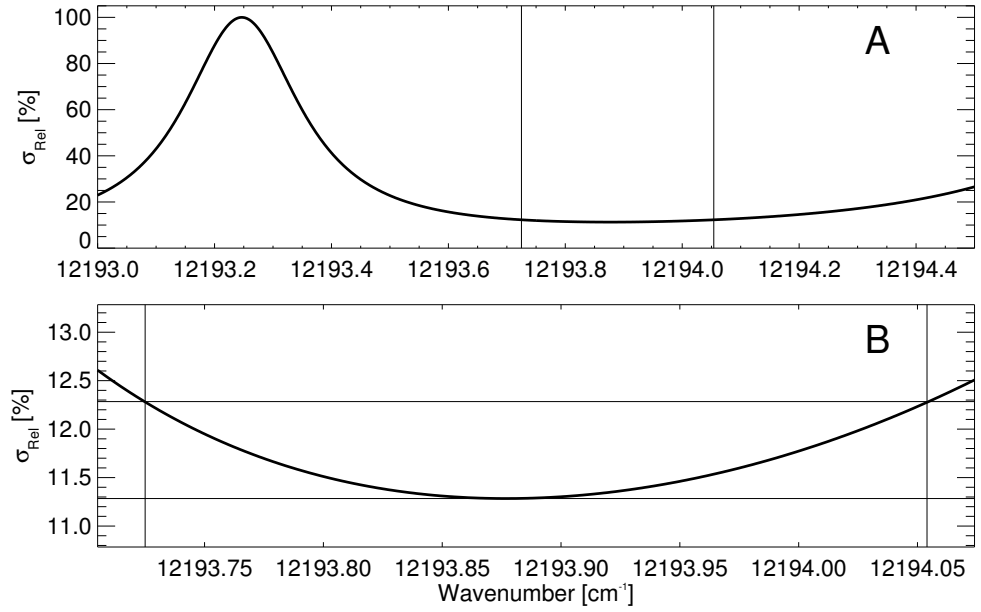

FIGURE A.2: Absorption spectrum of water vapor in the vicinity of the $12193.247\,\mathrm{cm}^{-1}$ absorption line. Vertical lines indicate the offline region. Plot A shows the whole spectrum, plot B a magnification of the offline region.

$\nu_{on}/\mathrm{cm}^{-1}$	$\lambda_{Filter}/\mathrm{nm}$	$S/10^{-24}\,\mathrm{cm}$	$\nu_{off,min}/\mathrm{cm}^{-1}$	$\nu_{off,max}/\mathrm{cm}^{-1}$	Lines
12190.7435	820.3	10.90	12188.153	12188.555	1-3,5
12193.2465	820.3	4.50	12193.725	12194.054	2-5
12202.0284	820.3	30.99	12200.330	12200.733	6
12223.0047	818.2	15.8	12220.770	12221.172	7-9,11
12226.1012	818.2	49.8	12227.309	12227.709	11
12229.5324	818.2	1.95	12228.362	12228.952	7-15

TABLE A.3: Suitable online frequencies for the Ti:Sa DIAL system, the minimum and maximum offline frequency and the absorption lines needed for the DIAL inversion (absorption lines and parameters are listed in Table A.4).

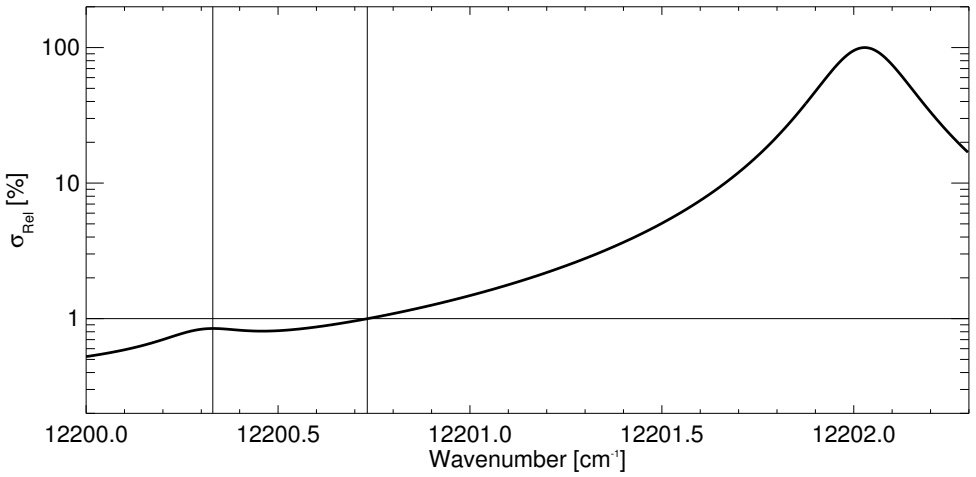

FIGURE A.3: Absorption spectrum of water vapor in the vicinity of the $12202.027\,\mathrm{cm}^{-1}$ absorption line. Vertical lines indicate the offline region.

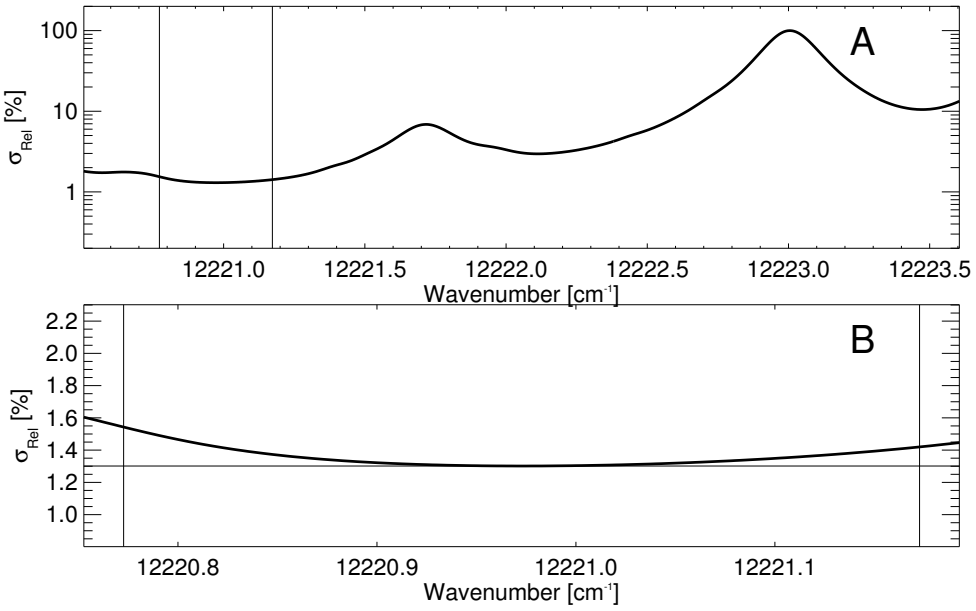

FIGURE A.4: Absorption spectrum of water vapor in the vicinity of the $12223.005\,\mathrm{cm}^{-1}$ absorption line. Vertical lines indicate the offline region. Plot A shows the whole spectrum, plot B a magnification of the offline region.

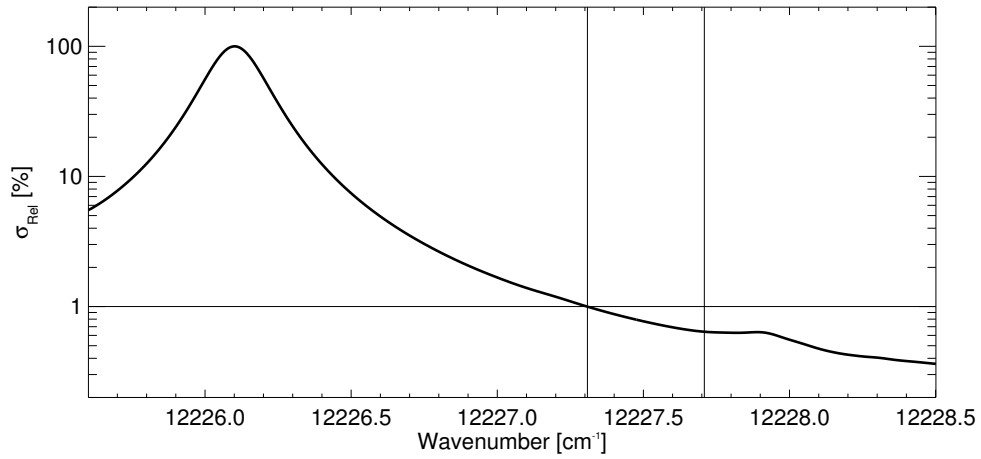

FIGURE A.5: Absorption spectrum of water vapor in the vicinity of the $12226.101\,\mathrm{cm}^{-1}$ absorption line. Vertical lines indicate the offline region.

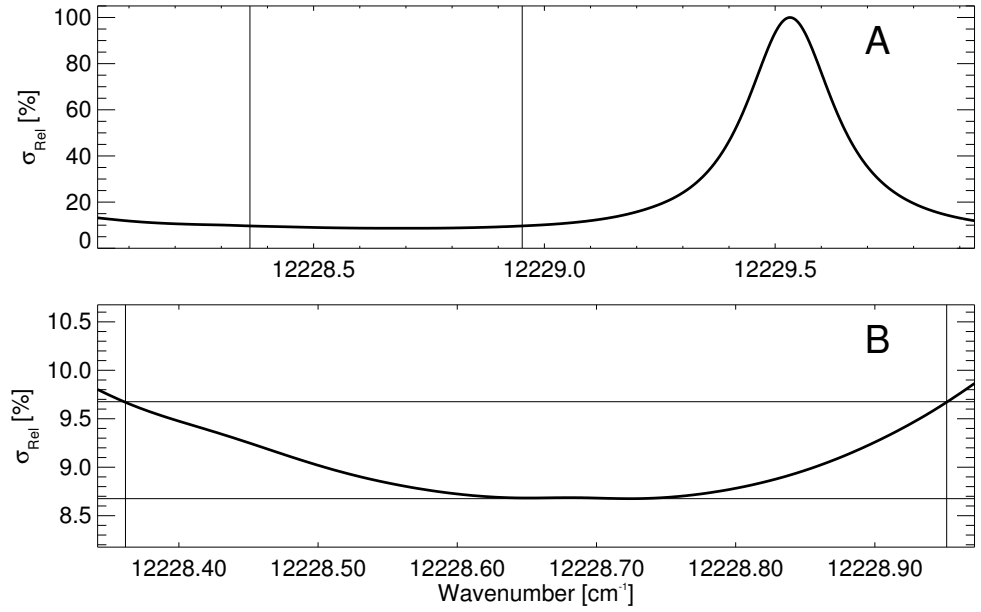

FIGURE A.6: Absorption spectrum of water vapor in the vicinity of the $12229.532\,\mathrm{cm}^{-1}$ absorption line. Vertical lines indicate the offline region. Plot A shows the whole spectrum, plot B a magnification of the offline region.

No.	ν_o	E''	S	$\Gamma_{c,air}$	$\eta_{c,air}$	$\Delta\nu$	α	Γ_{c,H_2O}	η_{c,H_2O}
1	12188.3364e	399.5e	0.016e	0.0787e	0.68e	-0.0155c	0.66c	0.405e	0.63c
2	12190.7435p	37.1p	10.900p	0.0957p	0.68e	-0.0093p	0.33c	0.534e	1.05c
3	12191.7840p	23.8p	5.400p	0.0941p	0.68e	-0.0021p	0.00c	0.561e	1.14c
4	12193.2465p	224.8p	4.500p	0.0976p	0.68e	-0.0114p	0.44c	0.521e	1.01c
5	12195.1906e	23.8e	42.700e	0.1028e	0.68e	-0.0093c	0.33c	0.528e	1.03c
6	12202.0284p	42.4p	30.990p	0.1006p	0.68e	-0.0130p	0.53c	0.528e	1.03c
7	12218.8296p	134.9p	21.850p	0.0920p	0.68e	-0.0145p	0.60c	0.489e	0.90c
8	12223.0047p	142.3p	15.800p	0.0885p	0.68e	-0.0130p	0.53c	0.477e	0.87c
9	12223.8401p	136.2p	8.080p	0.0966e	0.68e	-0.0109c	0.42c	0.497e	0.93c
10	12224.6670e	95.2e	14.300e	0.1010e	0.68e	-0.0097c	0.36c	0.519e	1.00c
11	12226.1012p	136.8p	49.800p	0.0934p	0.68e	-0.0098p	0.36c	0.487e	0.90c
12	12229.5324p	325.4p	1.950p	0.0919p	0.68e	-0.0101p	0.38c	0.502e	0.95c
13	12230.9256e	447.3e	0.664e	0.0898e	0.68e	-0.0127c	0.51c	0.462e	0.82c
14	12236.5480e	224.8e	43.300e	0.0854e	0.68e	-0.0138c	0.57c	0.439e	0.74c
15	12244.7187p	173.4p	38.100p	0.0870p	0.68e	-0.0134c	0.55c	0.533e	1.05c

TABLE A.4: Absorption line parameters needed for the calculation of $\Delta\sigma$ for various online/offline pairs (see Table A.3). Units of the parameters: ν_o, E'', $\Gamma_{c,air}$, $\Delta\nu$ and Γ_{c,H_2O}: cm^{-1}, S: 10^{-24} cm, other parameters are dimensionless. The letter behind each parameter indicates the origin: p: Ponsardin and Browell [32], e: ESA-WV database, c: calculated from other parameters.

Appendix B

Slave Laser Stabilization

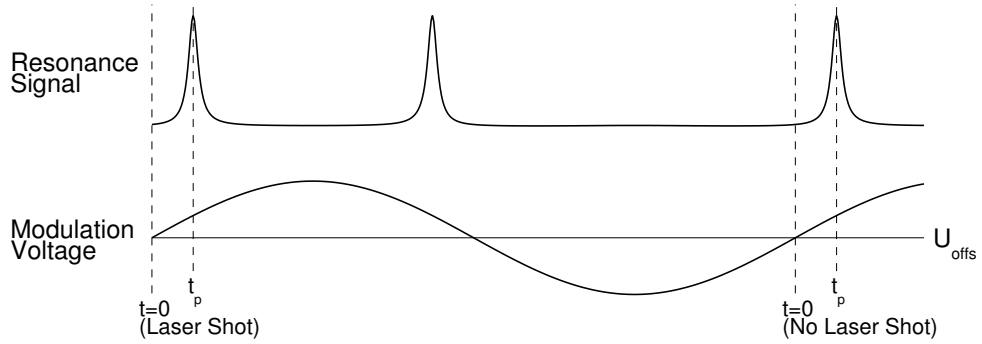

FIGURE B.1: Illustration of the slave cavity stabilization scheme.

Relation between peak delay and cavity phase shift Fig. B.1 illustrates the principle of the slave laser stabilization: A sinusoidal modulation voltage is applied to the piezo element which one of the cavity mirrors is mounted on. The piezo motion results in a varying cavity phase shift (see Equation 5.3). Whenever the cavity phase shift becomes zero, a peak is detected in the resonance signal. The expression for the modulation voltage U_{mod} reads:

$$U_{mod}(t) = U_o \cdot \sin(\omega_{mod} \cdot t) + U_{offs}\,,$$

where U_o is the amplitude of the sinusoidal voltage, ω_{mod} is the angular frequency, and U_{offs} is the DC offset voltage. The sine voltage shall be in phase with the pump laser pulse train such that the laser is fired at $t = 0$. The frequency of the sinusoidal voltage is actually twice the laser repetition rate, so the laser is fired only every second period. When the sine voltage has completed one period after the laser shot, we can set, as indicated in Fig. B.1, $t = 0$ again. As the position t_p of the peak in the vicinity of the laser shot cannot be measured due to the blinding of the detector, the peak occurring one period later is taken as a reference instead. If the frequency of the sine voltage remains constant and neither the piezo response nor the shape of the voltage undergo any *fast* changes, the two peaks marked in Fig. B.1 will always be separated by exactly one period or, in other words, the two indicated t_p will be the same.

For the following calculation we assume a linear piezo response. The time dependent phase shift which is induced by the modulation then reads:

$$\Delta\varphi(t) = 2\pi \cdot \frac{U_{mod}(t)}{U_{FSR}} + \Delta\varphi_o, \tag{B.1}$$

where U_{FSR} is the voltage difference which is needed to change the cavity length by one FSR and $\Delta\varphi_o$ is the phase shift that applies for $U_{mod} = 0$. If a resonance peak is found at $t = t_p$,

then $\Delta\varphi(t_p) = 0$. Using Equation B.1, we obtain for $t = t_p$:

$$\Delta\varphi_o = -\frac{2\pi}{U_{FSR}} \left(U_o \cdot \sin(\omega_{mod} \cdot t_p) + U_{offs}\right). \tag{B.2}$$

Using Equations B.1 and B.2 we obtain for the cavity phase shift at $t = 0$:

$$\Delta\varphi(0) = -2\pi \cdot \frac{U_o}{U_{FSR}} \cdot \sin(\omega_{mod} \cdot t_p).$$

If U_o is chosen such that exactly one FSR is covered by the modulation, i.e. $U_o = \frac{1}{2}U_{FSR}$ and if t_p is small compared to the modulation period $T_{mod} = \frac{2\pi}{\omega_{mod}}$, we finally get:

$$\Delta\varphi(0) \approx -2\pi^2 \cdot \frac{t_p}{T_{mod}} \tag{B.3}$$

This expression was used to convert the measured peak positions to the phase shifts that are presented in Section 5.6.3.

Stabilization Algorithm The Equations in the former paragraph now provide the means of calculating the change in the offset voltage that is needed to push a resonance peak from its actual position t_a back to the set position t_s. The value for t_s is chosen such that the laser pulse energy emitted in the backward direction is minimal. Due to a possible transient change in the optical cavity length caused by the heating of the laser crystal by the pump pulse, the set position of the reference peak yielding the highest seed efficiency is not necessarily at $t = 0$. If $U_{offs,a}$ is the offset voltage associated with t_a and $U_{offs,s}$ the voltage associated with t_s, we obtain, using Equation B.2:

$$U_o \cdot \sin(\omega_{mod} \cdot t_s) + U_{offs,s} = U_o \cdot \sin(\omega_{mod} \cdot t_a) + U_{offs,a}.$$

Rearranging this equation we get:

$$\Delta U_{offs} = U_{offs,s} - U_{offs,a} = U_o \cdot \left(\sin(\omega_{mod} \cdot t_a) - \sin(\omega_{mod} \cdot t_s)\right),$$

where ΔU_{offs} is the voltage that needs to be added to the actual offset voltage $U_{offs,a}$. For $t_a, t_s \ll T_{mod}$ the expression can again be simplified to:

$$\Delta U_{offs} = 2\pi \cdot U_o \cdot \frac{t_a - t_s}{T_{mod}}.$$

It is interesting to note, that for the stabilization algorithm no knowledge of U_{FSR} is required.

Acknowledgments

I wish to thank the following persons:

- My supervisor Jens Bösenberg for giving me the opportunity to work on this highly interesting, broad and exciting topic. He has given a lot of freedom, has been open to discussions and has given me many valuable suggestions and ideas. He also was the driving force for achieving impossible things like getting the new DIAL system ready in time for the first field experiment in April 2003.

- Prof. Hartmut Graßl, the second reviewer of my thesis and the other members of the thesis committee: Prof. Ernst Heumann, Christian Hübscher, and Gerhard Peters.

- Holger Linné, the wizard of computers, DSPs, FPGAs, CPLDs, TCOs and ADCs. He provided the data acquisition systems for the alexandrite and the new Ti:Sa DIAL system and also the system for recording the spectroscopic data for the quality assurance purposes described in Section 3.1. Many thanks also for his patient help with all computer related issues and for rescuing my system after I had messed it up time and time again (”What have you done again?”).

- All other current and past members of our group who have given me help and support and provided the good climate without which the completion of the work described here would not have been possible. Special thanks go to the people who participated in the various field experiments together with me, I will keep a special memory of the good atmosphere and teamwork. Extra special thanks to Björn Brügmann for the good fun we had when putting together the new DIAL system (code word ”Teleskopschiene”). The people I’m talking about are, apart from those mentioned already (in alphabetical order): Barbara Hennemuth, Annika Jahnke, Friedhelm Jansen, Andrea Lammert, Stefan Lehmann, Volker Matthias, Monika Pfeiffer, Margrit Scheller, Tom Wilkerson.

- The people from the mechanics workshop for their precise and speedy work in manufacturing needed parts. Special thanks also for the excellent work and the great cooperation at prepearing field campaigns, setting up and dismantling instruments, and especially for getting the blue container ready for the accommodation of the new DIAL system.

- Martin Dreyer for his introduction to SBDART.

- Nikolai Zhavoronkov of Max-Born-Institute, Berlin, for sacrificing one day of his time for me, when he showed me round his laboratory and gave me very helpful suggestions regarding high power Ti:Sa lasers.

- Aengus Mac Sweeney for proof-reading my thesis and Henk Schulz for mailing me the corrections.

- Alice for supporting and enduring me so bravely and for making a great effort to be patient with me, as I took a little bit longer for my thesis... again....

Bibliography

[1] B. J. Soden, R. T. Wetherald, G. L. Stenchikov, and A. Robock. Global cooling after the eruption of Mount Pinatubo: A test of climate feedback by water vapor. *Science*, 296:727–730, 2002.

[2] Science Plan (Final Draft) For the WCRP/GEWEX Global Water Vapor Project (GVap). `http://www.cira.colostate.edu/Climate/GVaP/gvap_sci_plan.pdf`, 1998.

[3] EUMETSAT. Satellite Application Facility on Climate Monitoring - Science Plan. `http://www.dwd.de/en/FundE/Klima/KLIS/int/CM-SAF/publications/documentations/sci.pdf`, 2001.

[4] H. Woick, S. Dewitte, A. Feijt, A. Gratzki, P. Hechler, R. Hollmann, K. G. Karlsson, V. Laine, P. Lowe, H. Nitsche, M. Werscheck, and G. Wollenweber. The satellite application facility on climate monitoring. *Advances in Space Research*, 30:2405–2410, 2002.

[5] Implementation Plan (Final Draft) For the WCRP/GEWEX Global Water Vapor Project (GVap). `http://www.cira.colostate.edu/Climate/GVaP/gvap_impl_plan.pdf`, 1998.

[6] J. Bösenberg, M. Alpers, D. Althausen, A. Ansmann, C. Böckmann, R. Eixmann, A. Franke, V. Freudenthaler, H. Giehl, H. Jäger, S. Kreipl, H. Linné, V. Matthias, I. Mattis, D. Müller, J. Sarközi, L. Schneidenbach, J. Schneider, T. Trickl, E. Vorobieva, U. Wandinger, and M. Wiegner. The German Aerosol Lidar Network: Methodology, Data, Analysis. MPI-Report 317, Max-Planck-Institut für Meteorologie, Hamburg, 2001.

[7] J. Bösenberg and V. Matthias et al. EARLINET: A European Aerosol Research Lidar Network to Establish an Aerosol Climatology. MPI-Report 348, Max-Planck-Institut für Meteorologie, Hamburg, 2003.

[8] D. Parsons, T. Weckwerth, and M. Hardesty. Scientific Overview Document For International H_2O Project (IHOP_2002). `http://www.atd.ucar.edu/dir_off/projects/2002/IHOPdocs/sod_IHOPv2.1.pdf`, 2001.

[9] R. Kamineni, T. N. Krishnamurti, R. A. Ferrare, S. Ismail, and E. V. Browell. Impact of high resolution water vapor cross-sectional data on hurricane forecasting. *Geophysical Research Letters*, 30:art. no.–1234, 2003.

[10] E. Gérard and J. Pailleux. Role of Water Vapor in Numerical Weather Prediction Models. In A. Dabas, C. Loth, and J. Pelon, editors, *Advances in Laser Remote Sensing*, pages 285–288. Edition Ecole Polytechnique, Palaiseau, 2001.

[11] B. Hennemuth, D. Jakob, and D. Rechid. Validation of atmospheric boundary layer structure in REMO. `http://www.cosis.net/abstracts/EAE03/08302/EAE03-J-08302.pdf`, 2003.

[12] A. Lammert. *Untersuchung der turbulenten Grenzschicht mittels Laserfernerkundung*. PhD thesis, Universität Hamburg, 2003.

[13] V. Wulfmeyer. *DIAL-Messungen von vertikalen Wasserdampfverteilungen. Ein Lasersystem für Wasserdampf- und Temperaturmessungen in der Troposphäre*. PhD thesis, Universität Hamburg, 1995.

[14] V. Wulfmeyer. Ground–based differential absorption lidar for water vapor and temperature profiling: Development and specifications of a high-performance laser transmitter. *Applied Optics*, 37:3804–3824, 1998.

[15] R. M. Measures. *Laser remote sensing*. John Wiley & Sons, New York, 1984.

[16] J. Bösenberg. Remote sensing of the troposphere using differential absorption lidar. MPI-Report 236, Max-Planck-Institut für Meteorologie, Hamburg, 1997.

[17] J. Bösenberg. Ground-based differential absorption lidar for water vapor and temperature profiling: methodology. *Applied Optics*, 37:3845 – 3860, 1998.

[18] V. Matthias. *Vertikalmessungen der Aerosolextinktion und des Ozons mit einem UV-Raman-Lidar*. PhD thesis, Universität Hamburg, 2000.

[19] R. D. Schotland. Some observations of the vertical profile of water vapor by means of a ground based optical radar. In *Proceedings of* 4^{th} *Symposium on Remote Sensing of the Environment*, pages 273–283, University of Michigan, 1966. Ann Arbor, Mich., Environmental Research Inst. of Michigan.

[20] V. Wulfmeyer and J. Bösenberg. Ground–based differential absorption lidar for water vapor profiling: Assessment of accuracy, resolution, and meteorological applications. *Applied Optics*, 37:3825–3845, 1998.

[21] M. Garbuny. *Optical Physics*. Academic Press, New York, 1965.

[22] B. Grossmann and E. V. Browell. Water–vapor line broadening and shifting by air, nitrogen, oxygen, and argon in the 720–nm wavelength region. *Journal of Molecular Spectroscopy*, 138:562–595, 1989.

[23] A. Ansmann. Errors in Ground-Based Water-Vapor DIAL-Measurements due to Doppler-Broadened Rayleigh Backscattering. *Applied Optics*, 24:3476–3480, 1985.

[24] R. S. Eng, P. L. Kelley, A. Mooradian, A. R. Calawa, and T. C. Harman. Tunable Laser Measurements of Water Vapor Transitions in the Vicinity of 5 μm. *Chemical Physics Letters*, 19:524–528, 1973.

[25] J. Bösenberg. Measurements of the pressure shift of water vapor absorption lines by simultaneous photoacoustic spectroscopy. *Applied Optics*, 24:3531–3534, 1985.

[26] B. Grossmann and E. V. Browell. Spectroscopy of water vapor in the 720 nm wavelength region: line strengths, self-induced pressure broadenings and shifts, and temperature dependence of linewidths and shifts. *Journal of Molecular Spectroscopy*, 136:264–294, 1989.

[27] L. S. Rothman, C. P. Rinsland, A. Goldman, S. T. Massie, D. P. Edwards, J. M. Flaud, A. Perrin, C. Camy-Peyret, V. Dana, J. Y. Mandin, J. Schroeder, A. McCann, R. R. Gamache, R. B. Wattson, K. Yoshino, K. V. Chance, K. W. Jucks, L. R. Brown, V. Nemtchinov, and P. Varanasi. The HITRAN molecular spectroscopic database and HAWKS (HITRAN Atmospheric Workstation): 1996 edition. *Journal of Quantitative Spectroscopy and Radiative Transfer*, 60:665–710, 1998.

[28] The HITRAN Database. `http://www.hitran.com`.

[29] L. P. Giver, C. Chackerian, and P. Varanasi. Visible and near-infrared $H_2{}^{16}O$ line intensity corrections for HITRAN-96. *Journal of Quantitative Spectroscopy and Radiative Transfer*, 66:101–105, 2000.

[30] J.-Y. Mandin, J.-P. Chevillard, C. Camy-Peyret, J.-M. Flaud, and J. W. Brault. The high-resolution spectrum of water vapor between 13 200 and 16 500 cm^{-1}. *Journal of Molecular Spectroscopy*, 116:167–190, 1986.

[31] References and Sources for HITRAN. `ftp://cfa-ftp.harvard.edu/pub/HITRAN/Global_Data/ref-table2003.pdf`, 2003.

[32] P. L. Ponsardin and E. V. Browell. Measurements of $H_2{}^{16}O$ linestrenghs and air-induced broadenings and shifts in the 815-nm spectral region. *Journal of Molecular Spectroscopy*, 185:58–70, 1997.

[33] D. Belmiloud, R. Schermaul, K. M. Smith, N. F. Zobov, J. W. Brault, R. C. M. Learner, D. A. Newnham, and J. Tennyson. New studies of the visible and near-infrared absorption by water vapour and some problems with the HITRAN database. *Geophysical Research Letters*, 27:3703–3706, 2000.

[34] R. Schermaul, R. C. M. Learner, D. A. Newnham, R. G. Williams, J. Ballard, N. F. Zobov, D. Belmiloud, and J. Tennyson. The water vapor spectrum in the region 8600-15 000 cm^{-1}: Experimental and theoretical studies for a new spectral line database. I. Laboratory measurements. *Journal of Molecular Spectroscopy*, 208:32–42, 2001.

[35] R. Schermaul, R. C. M. Learner, D. A. Newnham, J. Ballard, N. F. Zobov, D. Belmiloud, and J. Tennyson. The water vapor spectrum in the region 8800-15 000 cm^{-1}: Experimental and theoretical studies for a new spectral line database. II. Linelist construction. *Journal of Molecular Spectroscopy*, 208:43–50, 2001.

[36] European Space Agency. Measurement of H_2O Absorption Cross-Sections for Exploitation of GOME data. `http://www.badc.rl.ac.uk/data/esa-wv/`.

[37] V. Wulfmeyer and J. Bösenberg. Single-mode operation of an injection-seeded alexandrite ring laser for application in water-vapor and temperature differential absorption lidar. *Optics Letters*, 21:1150–1152, 1996.

[38] J. Altmann, R. Baumgart, and C. Weitkamp. Two-mirror multipass absorption cell. *Applied Optics*, 20:995, 1981.

[39] A. Rosencwaig. *Photoacoustics and Photoacoustic Spectroscopy*. Robert E. Krieger Publishing Company, Malabar, 1990.

[40] S. Lehmann, V. Wulfmeyer, and J. Bösenberg. Time-dependent attenuation for dynamic range reduction of lidar signals. *Applied Optics*, 36:3469–3474, 1997.

[41] G. M. Stokes and S. E. Schwartz. The atmospheric radiation measurement (arm) program: Programmatic background and design of the cloud and radiation test bed. *Bulletin of the American Meteorological Society*, 75:1201–1221, 1994.

[42] Atmospheric Radiation Measurement (ARM) Program. Home Page. `http://www.arm.gov`.

[43] Atmospheric Radiation Measurement (ARM) Program. TWP Nauru Site. `http://www.arm.gov/docs/sites/twp/nauru.html`.

[44] Atmospheric Radiation Measurement (ARM) Program. Nauru99 Science and Operations WWW Site. `http://www.arm.gov/docs/iops/1999/twp1999nauru/nauru99.html`.

[45] Atmospheric Radiation Measurement (ARM) Program. Science and Operations Plan (Draft) Nauru99. `http://www.gim.bnl.gov/cruises/mirai/n99mr/mirai_log/n99miraibnl/N99OpsPlan.pdf`, 1999.

[46] NOAA Pacific Marine Environmental Laboratory. Tropical Atmosphere Ocean project. `http://www.pmel.noaa.gov/tao/`, 2003.

[47] V. Wulfmeyer, M. Randall, C. Walther, R. K. Newsom, W. A. Brewer, and R. M. Hardesty. High-Performance 2-μm Doppler Lidar and its Shipborne Applications in the Tropical Marine Boundary Layer. In A. Dabas, C. Loth, and J. Pelon, editors, *Advances in Laser Remote Sensing*, pages 463 – 466. Edition Ecole Polytechnique, Palaiseau, 2001.

[48] M. L. Nordeen, P. Minnis, D. R. Doelling, D. Pethick, and L. Nguyen. Satellite observations of cloud plumes generated by Nauru. *Geophysical Research Letters*, 28:631–634, 2001.

[49] Atmospheric Radiation Measurement (ARM) Program. Nauru Island Effect Study (NIES) IOP Science Plan. `http://www.arm.gov/docs/iops/2001/twp2001ieffect/NIES_Sciplan.pdf`, 2001.

[50] Atmospheric Radiation Measurement (ARM) Program. Southern Great Plains Site. `http://www.arm.gov/docs/sites/sgp/sgp.html`.

[51] D. D. Turner. DIAL/Raman Lidar Intercomparison Home Page. `http://engineering.arm.gov/~turner/working/dial_iop/`, 2000.

[52] Atmospheric Radiation Measurement (ARM) Program. Fall 2000 Water Vapor IOP. `http://www.arm.gov/docs/iops/2000/sgp2000fallwv/afteriop_fallwv2000.html`, 2000.

[53] ARM-Atmospheric Radiation Measurement Program. ARM-FIRE Water Vapor Experiment. `http://www.arm.gov/docs/iops/2000/sgp2000afwex/sgp2000fire.html`, 2000.

[54] J. E. M. Goldsmith, Forest H. Blair, Scott E. Bisson, and David D. Turner. Turn-key Raman lidar for profiling atmospheric water vapor, clouds, and aerosols. *Applied Optics*, 37:4979–4990, 1998.

[55] R. A. Ferrare, D. N. Whiteman, S. H. Melfi, K. D. Evans, F. J. Schmidlin, and D. O'C. Starr. A comparison of water vapor measurements made by Raman lidar and radiosondes. *Journal of Atmospheric and Oceanic Technology*, 12:1177–1195, 1995.

[56] E. V. Browell, S. Ismail, and W.B. Grant. Differential absorption lidar (DIAL) measurements from air and space. *Applied Physics B*, 67:399–410, 1998.

[57] D. Nagel, U. Leiterer, H. Dier, A. Kats, J. Reichardt, and A. Behrendt. High accuracy humidity measurements using the standardized frequency method with a research upper-air sounding system. *Meteorologische Zeitschrift*, 10:395–405, 2001.

[58] D. D. Turner, B. M. Lesht, S. A. Clough, J. C. Liljegren, H. E. Revercomb, and D. C. Tobin. Dry bias and variability in Vaisala RS80-H radiosondes: The ARM experience. *Journal of Atmospheric and Oceanic Technology*, 20:117–132, 2003.

[59] H. Linné, D.D. Turner, J.E.M. Goldsmith, T.P. Tooman, J. Bösenberg, K. Ertel, and S. Lehmann. Intercomparison of DIAL and Raman Lidar Measurements of Humidity Profiles. In A. Dabas, C. Loth, and J. Pelon, editors, *Laser Remote Sensing of the Atmosphere. Selected Papers of the 20th International Laser Radar Conference*, pages 293–298. Edition Ecole Polytechnique, Palaiseau, 2001.

[60] D. D. Turner, H. Linné, J. Bösenberg, S. Lehmann, K. Ertel, J. E. M. Goldsmith, and T. P. Tooman. Simultaneous Ground-Based Remote Sensing of Water Vapor by Differential Absorption and Raman Lidars, Presented at the International Geoscience and Remote Sensing Symposium (IGARSS 2000). `http://engineering.arm.gov/~turner/working/dial_iop/igarss2000.dial_rl.v2.ones_distiller.pdf`, 2000.

[61] J. Bösenberg. Personal Communication, 2001.

[62] V. Wulfmeyer and C. Walther. Future performance of ground-based and airborne water-vapor differential absorption lidar. I. Overview and theory. *Applied Optics*, 40:5304–5320, 2001.

[63] V. Wulfmeyer and C. Walther. Future performance of ground-based and airborne water-vapor differential absorption lidar. II. Simulations of the precision of a near-infrared, high-power system. *Applied Optics*, 40:5321–5336, 2001.

[64] P. Ricchiazzi, S. R. Yang, C. Gautier, and D. Sowle. SBDART: A research and teaching software tool for planeparallell radiative transfer in the Earth's atmosphere. *Bulletin of the American Meteorological Society*, 79:2101–2114, 1998.

[65] S. Ismail and E. V. Browell. Airborne and spaceborne lidar measurements of water vapor profiles: a sensitivity analysis. *Applied Optics*, 28:3603–3615, 1989.

[66] T. D. Raymond and A. V. Smith. Injection–seeded titanium–doped–sapphire laser. *Optics Letters*, 16(1):33–35, 1991.

[67] A. Kasapi, G. Y. Yin, and M. Jain. Pulsed Ti:sapphire laser seeded off the gain peak. *Applied Optics*, 35(12):1999–2004, 1996.

[68] J. C. Diels and W. Rudolph. *Ultrashort laser pulse phenomena*. Academic Press, San Diego, 1996.

[69] Jenoptik Laserdiode GmbH. Datasheet JOLD-x-xANC-1l actively cooled cw and qcw diode lasers. `http://www.jold.com`, 2002.

[70] Thales Laser Diodes. Datasheet TH-Q1401-A1 100W QUASI-CW LINEAR BAR ARRAY. `http://www.laser-diodes.thomson-csf.com`, 2002.

[71] Thales Laser Diodes. Datasheet TH-C1840-H CONDUCTIVELY COOLED CW LINEAR BAR ARRAY. http://www.laser-diodes.thomson-csf.com, 2002.

[72] Coherent Inc. Diode Lasers, Packaged Bars - Conduction Cooled Packaged Bars Datasheet. http://www.cohr.com, 2003.

[73] G. Poberaj, A. Fix, A. Assion, M. Wirth, C. Kiemle, and G. Ehret. Airborne all-solid-state DIAL for water vapour measurements in the tropopause region: system description and assessment of accuracy. *Applied Physics B*, 75:165–172, 2002.

[74] F. Balembois, F. Druon, F. Falcoz, P. Georges, and A. Brun. Performances of Cr:$LiSrAlF_6$ and Cr:$LiSrGaF_6$ for continuous-wave diode-pumped Q-switched operation. *Optics Letters*, 22:387–389, 1997.

[75] S. Lehmann. *Ein Heterodyn-DIAL System für die simultane Messung von Wasserdampf und Vertikalwind: Aufbau und Erprobung*. PhD thesis, Universität Hamburg, 2001.

[76] J. R. Ryan and R. Beach. Optical-absorption and stimulated-emission of neodymium in yttrium lithium-fluoride. *Journal of the Optical Society of America B*, 9:1883–1887, 1992.

[77] Positive Light. Datasheet Evolution diode-pumped, intra-cavity doubled, Q-switched Nd:YLF lasers. http://www.poslight.com/datasheets/Evolution-15_30.pdf, 2002.

[78] Photonics Industries. Datasheet DS Series Diode Pumped, GREEN Lasers. http://www.photonix.com.

[79] Quantronix. DARWIN 527nm DPSSL Green YLF laser. http://www.quantron.com, 2002.

[80] Thales Laser S. A. Datasheet Jade Solid State Nd:YLF Pulsed Laser. http://www.thales-laser.com.

[81] A. Ogino, M. Katsuragawa, and K. Hakuta. Single–frequency injection seeded pulsed Ti:Al_2O_3 ring laser. *Japanese Journal of Applied Physics 1*, 36:5112–5115, 1997.

[82] G. R. Morrison, C. P. Rahlff, M. Ebrahimzadeh, and M. H. Dunn. A high-average–power all–solide–state, single–frequency Ti:sapphire laser. In *Conference on Lasers and Electro–Optics, Vol. 9 of OSA Technical Digest Series*, pages 111–112, Washington, D. C., 1996. Optical Society of America.

[83] A. E. Siegman. *Lasers*, pages 815–817. University Science Books, Mill Valley, 1986.

[84] T. D. Raymond and A. V. Smith. Injection-seeded titanium-doped-sapphire laser. *Optics Letters*, 16:33–35, 1991.

[85] N. Zhavoronkov. Personal Communication, 2002.

[86] A. E. Siegman. *Lasers*, pages 413–422. University Science Books, Mill Valley, 1986.

[87] A. D. White. Frequency stabilization of gas lasers. *IEEE Journal of Quantum Electronics*, 1:349–349, 1965.

[88] T. W. Hänsch and B. Couillaud. Laser frequency stabilization by polarization spectroscopy of a reflecting reference cavity. *Optics Communications*, 35:441–444, 1980.

[89] S. W. Henderson, E. H. Yuen, and E. S. Fry. Fast resonance-detection technique for single frequency operation of injection seeded Nd:YAG lasers. *Optics Letters*, 11:715–717, 1986.

[90] T. Walther, M. P. Larsen, and E. S. Fry. Generation of Fourier-transform-limited 35-ns pulses with a ramp-hold-fire seeding technique in a Ti:sapphire laser. *Applied Optics*, 40:3046–3050, 2001.

[91] L. A. Rahn. Feedback stabilization of an injection-seeded Nd:YAG laser. *Applied Optics*, 24:940–942, 1985.

[92] D. Bruneau, P. Quaglia, C. Flamant, M. Meissonnier, and J. Pelon. Airborne lidar LEANDRE II for water-vapor profiling in the troposphere. I. System description. *Applied Optics*, 40:3450–3461, 2001.

[93] V. Wulfmeyer, J. Bösenberg, S. Lehmann, C. Senff, and St. Schmitz. Injection seeded Alexandrite ring laser: performance and application in a water vapor DIAL system. *Optics Letters*, 20:638–640, 1995.

[94] A. S. Moore, Jr., K. E. Brown, W. M. Hall, J. C. Barnes, W. C. Edwards, L. B. Petway, A. D. Little, W. S. Luck, Jr., I. W. Jones, C. W. Antill, Jr., E. V. Browell, and S. Ismail. Development of the Lidar Atmospheric Sensing Experiment (LASE) – An Advanced Airborne DIAL Instrument. In A. Ansmann, R. Neuber, P. Rairoux, and U. Wandinger, editors, *Advances in Atmospheric Remote Sensing with Lidar*, pages 281–288, 1996.

[95] G. Poberaj. Airborne Differential Absorption Lidar for Water Vapour Measurements in the Upper Troposphere and Lower Stratosphere in the Spectral Region around 940 nm (PhD Thesis). DLR Forschungsbericht 2000-43, DLR Oberpfaffenhofen, 2001.

[96] Melles Griot Inc. Laser Beam Measurement. `http://beammeasurement.mellesgriot.com/tut_m2.asp`, 2002.

[97] GKSS Institut für Küstenforschung. EVA-GRIPS. `http://w3.gkss.de/KSH/EVA_GRIPS`.

[98] J. R. Garratt. *The atmospheric boundary layer*. Cambridge University Press, Cambridge, 1992.

[99] C. Senff, J. Bösenberg, and G. Peters. Measurement of Water Vapor Flux Profiles in the Convective Boundary Layer with Lidar and Radar-RASS. *Journal of Atmospheric and Oceanic Technology*, 11:85–93, 1994.

[100] V. Wulfmeyer. Investigation of turbulent processes in the lower troposphere with water vapor dial and radar-rass. *Journal of the Atmospheric Sciences*, 56:1055–1076, 1999.

[101] V. Wulfmeyer. Investigations of Humidity Skewness and Variance Profiles in the Convective Boundary Layer and Comparison of the Latter with Large Eddy Simulation Results. *Journal of the Atmospheric Sciences*, 56:1077–1087, 1999.

[102] V. Bagnoud and F. Salin. Amplifying laser pulses to the terawatt level at a 1-kilohertz repetition rate. *Applied Physics B*, 70:S165–S170, 2000.

[103] Y. Nabekawa, T. Togashi, T. Sekikawa, S. Watanabe, S. Konno, T. Kojima, S. Fujikawa, and K. Yasui. All-solid-state high-peak-power Ti : sapphire laser system above 5-kHz repetition rate. *Applied Physics B*, 70:S171–S179, 2000.

[104] S. Ito, H. Ishikawa, T. Miura, K. Takasago, A. Endo, and K. Torizuka. Seven-terawatt Ti : sapphire laser system operating at 50 Hz with high beam quality for laser Compton femtosecond X-ray generation. *Applied Physics B*, 76:497–503, 2003.

[105] Positive Light. Datasheet Evolution-90, High average power DPSS Nd:YLF laser. `http://www.poslight.com/datasheets/Evolution-90.pdf`, 2003.

[106] Continuum. Datasheet Powerlite Precision II 9000. `http://www.continuumlasers.com/pdfs/Powerlite_Prec_II_9000.pdf`, 2002.

[107] M. Zavelani-Rossi, F. Lindner, C. Le Blanc, G. Cheriaux, and J. P. Chambaret. Control of thermal effects for high-intensity Ti : sapphire laser chains. *Applied Physics B*, 70:S193–S196, 2000.

Note: the validity of the cited URLs was last checked on January 11 2004.

MPI-Examensarbeit-Referenz:

Examensarbeit Nr. 1-79 bei Bedarf bitte Anfragen:
MPI für Meteorologie, Abtlg.: PR, Bundesstr. 55, 20146 Hamburg

Examensarbeit Nr. 80 November 2000	**Vertikalmessungen der Aerosolextinktion und des Ozons mit einem UV-Raman-Lidar** Volker Matthias
Examensarbeit Nr. 81 Dezember 2000	**Photochemical Smog in Berlin-Brandenburg: An Investigation with the Atmosphere-Chemistry Model GESIMA** Susanne E. Bauer
Examensarbeit Nr. 82 Juli 2001	**Komponenten des Wasserkreislaufs in Zyklonen aus Satellitendaten – Niederschlagsfallstudien-** Klepp Christian-Philipp
Examensarbeit Nr. 83 Juli 2001	**Aggregate models of climate change: development and applications** Kurt Georg Hooss
Examensarbeit Nr. 84 Februar 2002	**Ein Heterodyn-DIAL System für die simultane Messung von Wasserdampf und Vertikalwind: Aufbau und Erprobung** Stefan Lehmann
Examensarbeit Nr. 85 April 2002	**Der Wasser- und Energiehaushalt der arktischen Atmosphäre** Tido Semmler
Examensarbeit Nr. 86 April 2002	**Auswirkungen der Assimilation von Meereshöhen-Daten auf Analysen und Vorhersagen von El Niño** Sigrid Schöttle
Examensarbeit Nr. 87 Juni 2002	**Atmospheric Processes in a young Biomass Burning Plume - Radiation and Chemistry** Jörg Trentmann
Examensarbeit Nr. 88 August 2002	**Model Studies of the Tropical 30 to 60 Days Oscillation** **S**tefan Liess
Examensarbeit Nr. 89 Dezember 2002	**Influence of Sub-Grid Scale Variability of Clouds on the Solar Radiative Transfer Computations in the ECHAM5 Climate Model** Georg Bäuml
Examensarbeit Nr.90 Mai 2003	**Model studies on the response of the terrestrial carbon cycle to climate change and variability** Marko Scholze
Examensarbeit Nr.91 Juni 2003	**Integrated Assessment of Climate Change Using Structural Dynamic Models** Volker Barth

MPI-Examensarbeit-Referenz:

Examensarbeit Nr. 1-79 bei Bedarf bitte Anfragen:
MPI für Meteorologie, Abtlg.: PR, Bundesstr. 55, 20146 Hamburg

Examensarbeit Nr.92 Juli 2003	**Simulations of Indonesian Rainfall with a Hierarchy of Climate Models** Edvin Aldrian
Examensarbeit Nr.93 Juli 2003	**ENSO Teleconnections in High Resolution AGCM Experiments** Ute Merkel

ISSN 0938 - 5177